FABRICATION OF TUBULAR CERAMIC OXYGEN-ELECTROLYTE MEMBRANE REACTOR

YIN XIONG

NATIONAL UNIVERSITY OF SINGAPORE

2007

FABRICATION OF TUBULAR CERAMIC OXYGEN-ELECTROLYTE MEMBRANE REACTOR

YIN XIONG
(M.Sc., ZJU; M.Eng., NUS)

A THESIS SUBMITTED

FOR THE DEGREE OF DOCTOR OF PHILOSOPHY

DEPARTMENT OF CHEMICAL AND BIOMOLECULAR ENGINEERING

NATIONAL UNIVERSITY OF SINGAPORE

2007

ACKNOWLEDGEMENTS

I would like to express my sincere gratitude to my supervisor, A/Prof. Hong Liang, and my co-supervisor, Dr. Liu Zhao-Lin, for their invaluable guidance and suggestions, continual encouragement, great patience and support throughout the course of my study.

I would like to specially thank all the technical and clerical staff in the Department of Chemical & Biomolecular Engineering for their assistance in the set-up of experimental systems and in the use of materials characterization equipments. Thanks are also extended to Mr. Wang Ke and Ms. Zhang Xinhui for their supportive comments and cheerful assistance.

I am extremely grateful to my beloved family members for their love and support throughout the course of this program.

Finally, I would like to thank to National University of Singapore for granting me a research scholarship throughout this study period.

TABLE OF CONTENTS

Chapter 4 **Fabrication of asymmetric tubular membrane of $La_{0.2}Sr_{0.8}CoO_{3-\delta}/CeO_2$** **76**

Chapter 5 **Development of asymmetric tubular membrane of $La_{0.2}Sr_{0.8}CoO_{3-\delta}/Ce_{0.8}Gd_{0.2}O_{2-\delta}/CeO_2$** **102**

SUMMARY

The diminishing of world-wide petroleum oil resources and the increasing of the crude oil price highlight the gas-to-liquid (GTL) technologies. Due to its abundance and low cost, natural gas (mainly CH_4) has been widely attempted to produce liquid fuels or chemicals; however, the economic turns out to be the major challenge to this GTL process. Catalytic partial oxidation of methane (POM) with a ceramic oxygen-electrolyte membrane reactor (COMR) has the tremendous potential to convert methane economically into syngas (mixture of H_2 and CO, the precursor for final liquid products) economically. The major challenges for the commercialization of an asymmetric tubular COMR for POM include what is the low cost COMR fabrication method and how to retain stability of nickel catalyst through reducing the extent of coke formation. This thesis focuses on the developing of low cost methods to prepare asymmetric tubular COMR made of thin dense oxygen-electrolyte ceramic layer on thick porous ceramic tube surface, and investigating of the strategies to integrate the catalyst for POM with COMR.

This project has studied the viscous flow behavior of the ceramic-polymer paste, invented and characterized five types of low cost methods for the fabrication of COMRs, tested the function of the fabricated COMRs with the sweeping gas of pure He or CH_4/He mixture, proposed a new method to reduce the nickel surface coke formation, and performed a series of theoretical work to explain the experimental data and the methane dissociation mechanism. As a result, this work has

accomplished the following main breakthroughs: (i) analyzing of the interaction forces within the ceramic-polymer blend and developing of a new theoretical model which explains well the dependence of the measured viscous flow behavior of the ceramic-polymer blend on the ceramic volume concentration; (ii) developing and characterizing five types of low cost methods (i.e., vacuum assisted ceramic-ceramic composite slurry coating, green tube coating followed by co-firing, ceramic-metal composite dip coating followed by solution plugging, ceramic slurry coating followed by electroless silver plating, and two-steps colloidal suspension coating) to fabricate asymmetric tubular COMRs; (iii) demonstrating the feasibility of the fabricated COMRs for air separation using He as the sweeping gas or for methane reforming into syngas using CH_4/He as the sweeping gas; (iv) clarifying the high temperature bilateral diffusion of cations in YSZ-NiO composite (i.e., the anode or catalyst for POM), the reduction of NiO within the YSZ-NiO blend, and the collective action of NiO and YSZ upon exposing to methane gas; (v) solving the reductive thawing action of $CH_4/CO/H_2$ mixture to the membrane structure and the charcoaling effect on the nickel catalyst of POM with COMR; (vi) explaining the perovskite $La_{0.2}Sr_{0.8}CoO_{3-\delta}$ surface oxygen de-sorption and its bulk lattice distortion upon high temperature sintering successfully by the extended Hückel theory (EHT) and density function theory (DFT), respectively; and (vii) proposing of the POM mechanism with COMR, new methane 1st C-H cracking pathway, and the theoretical initial methane thermal sticking probability calculation method. In brief, both experimental and theoretical results on the asymmetric tubular COMR for POM process have been achieved.

NOMENCLATURE

Symbol	Description	Unit
a	spherical particulate radius in Eq. (2.21)	Å
A	constant in Eq. (3.8)	kJ/mol
A_H	Hamaker constant in vacuum in Eq. (3.1)	J
A_H^{eff}	effective Hamaker constant	J
A_n	coefficient in Eq. (2.17)	-
A_s	constant in Eq. (7.5a)	-
ABE	average metal-oxygen bond energy	eV
B	parameter in Eq. (3.10)	-
B_s	constant in Eq. (7.5a)	-
c_i	concentration	mol/m^3
D	outside diameter of sintered tube in Eq. (8.1)	cm
D_i	diffusion coefficient	m^2/s
D_0	outside diameter of extruded green tube in Eq. (8.1)	cm
E	activation energy	kJ/mol
E^0	energy barrier in Eq. (3.6)	kJ/mol
E_F	Fermi level energy	eV
f	impedance frequency	Hz
F	Faraday constant	C/mol
F_{CH4}^{in}	methane inlet flow rate	sccm
F_{CH4}^{out}	methane outlet flow rate	sccm
F_{CO}^{out}	CO outlet flow rate	sccm
F_{CO2}^{out}	CO_2 outlet flow rate	sccm
F_{H2}^{out}	H_2 outlet flow rate	sccm
FV	“free volume” of the lattice	m^3
G^{att}	the free energy of attraction per unit area	J/m^2

H	distance in Eq. (3.1)	m
h	Planck's constant	J-s
j_{in}	inlet gas flow rate	sccm
J_i	charge flux	$mol/(m^2 \cdot s)$
J_{O2}	oxygen permeation flux	$sccm/cm^2$
k	Boltzmann's constant	eV/K
k_0	constant in Eq. (3.6)	-
k'	proportional constant in Eq. (3.8)	-
k_1	constant in Eq. (3.6)	-
K	consistency modulus in Eq. (2.15)	-
K'	coefficient in Eq. (2.20)	-
K_r	constant in Eq. (3.6)	-
L	membrane thickness	m
L_D	dimensionless distance in Eq. (3.2)	-
m	Index in Eq. (2.15)	-
N	number of atoms within unit volume in Eq. (3.1)	m^{-3}
n	coefficient	-
n_e	concentration of electrons	mol/m^3
n_h	concentration of holes	mol/m^3
P_{O2}	partial oxygen pressure	atm
Q_{dl}	double layer constant phase element	F
Q_e	electrolyte constant phase element	F
Q_p	electrochemical polarization constant phase element	F
R	gas constant	$J/(mol \cdot K)$
R_{Ct}	electrode interface resistance	Ω
R_e	electrolyte resistance	Ω
R_p	electrochemical polarization resistance	Ω
R_s	radius of spherical particle	m
R(T)	reflection part in Eq. (8.3)	-
r_c	critical saddle point radius	Å
$S_0(E)$	methane initial dissociation sticking coefficient	-
$S_0(T)$	methane thermal sticking coefficient	-

S_C	carbon selectivity	%
S_{CO}	CO selectivity	%
S_{CO2}	CO_2 selectivity	%
S_{H2}	H_2 selectivity	%
sr	shrinkage rate of outside diameter of the ceramic tube	%
t	geometric Goldschmidt tolerance factor	-
T	temperature	K or ^oC
T_g	glass transition temperature	^oC
T_m	melting point	^oC
V_0	energy barrier in Eq. (7.8)	kJ/mol
$V_o^{\cdot\cdot}$	oxygen vacancy concentration	-
X_{CH4}	methane conversion	%
z_i	valence	-
Z'	real axis in Nyquist plot	Ω
Z''	image axis in Nyquist plot	Ω
Z_w	entanglement chain length	Å

Greek symbols

Symbol	**Description**	**Unit**
α	effective factor	-
α_0	electronic polarizability	C/m^2
ν	frequency	Hz
σ	shear stress	N/m^2
σ_h	conductivity of holes	S/cm
σ_i	electrical (ionic or electronic) conductivity	S/cm
σ_n	conductivity of electrons	S/cm
σ_o	oxygen ionic conductivity	S/cm
μ_i	electrical mobility	$cm^2/(V\cdot s)$
τ	applied stress	N/m^2
τ_0	yield stress	N/m^2

$\dot{\gamma}$	shear rate	s^{-1}
η_{rel}	relative viscosity	-
η	apparent viscosity	$N/(m^2 \cdot s)$
ϕ	solid powder volume fraction	-
ϕ_{eff}	effective solid loading in Eq. (2.21)	-
ϕ_{max}	maximum solid loading	-
δ	thickness of adsorbed layer in Eq. (2.21)	Å
ζ	vdw potential	J

LIST OF FIGURES

LIST OF TABLES

Chapter 1 Introduction

1.1 Background

As the diminishing of petroleum oil resources lots of endeavors have been made to establish a new technology to convert CH_4 into liquid fuels or other types of value-added chemicals. The major barrier to render methane be a rival to petroleum oil comes from concerns of economics. Conversion of methane directly into value-added chemicals still faces the issue of too low yields in the existing processes. Catalytic transferring methane into the synthesis gas (syngas, a mixture of CO and H_2), serving as a precursor to produce several end products, offers a very high production yield (> 90%); however, the cost to convert methane into syngas using existing technologies such as steam reforming, drying reforming, or conventional partial oxidation (co-feeding of methane and oxygen gases) is still too high to make this indirect route commercial feasible.

Partial oxidation of methane (POM) into syngas ($CH_4 + ½O_2 \rightarrow CO + 2H_2$) is mildly exothermic ($\Delta \boldsymbol{H}_{298}^{0}$ = -36 kJ/mol) and energy efficient; however, this process requires a large amount of pure oxygen which is traditionally generated by expensive cryogenic air separation process. A ceramic oxygen-electrolyte membrane reactor (COMR) is an appealing setup to couple air (or N_2/O_2) separation with POM process since this combination decreases the cost of syngas production significantly and makes it possible to build a house-sized methane conversion plant to replace the conventional billion-dollar big syngas factory. In addition to being used as the platform for the production of syngas, the COMR itself can also be used in air separation to obtain extremely pure oxygen and nitrogen, respectively.

Since the BP’s invention of the Electropox process, i.e., partially oxidizing methane into syngas (Mazanec et al., 1992) by COMR, lots of endeavors have been made to decrease the COMR fabrication cost and to improve the oxygen permeation and/or membrane stability by developing new ceramic oxide electrolytes that are also electron conductive. Low fabrication cost, easy to scale up, reliable stability, and high oxygen flux are basic attributes expected for a viable COMR. Unfortunately, to the best of our knowledge, no such a kind of COMR has been reported in literatures including patents so far. The asymmetric structure, in which a thin and dense oxygen electrolyte layer deposited on a thick and porous support, is the basic configuration to pursue both high oxygen flux and high stability. Compared with the disc mold, the tubular mold (i.e., plug flow reactor) is preferred for industrial applications because it is easy to be scaled up and requires for no high temperature ceramic sealant. Setting two ends out of the heating zone, the tubular structure avoids the usage of high temperature ceramic sealant since leakages and structural failure happen much more often at those joint points of a membrane reactor. Up to now, some technologies such as chemical vapor deposition (CVD), electrochemical vapor deposition (EVD), and sputtering have been used to produce the asymmetric tubular COMR with good quality but the equipment and fabrication costs are very high. To make the asymmetric tubular COMR be viable for industrial application low cost fabrication methods will have to be developed.

Integrating POM with COMR means to create interface between the two phases. At the interface oxygen anions supplied by COMR phase are consumed by the POM reaction. Nowadays, the mechanism of the POM at the interface with COMR is still not very clear. Nickel is the most common POM catalyst for a COMR due to its high efficiency and low cost. The 1st C-H bond cracking of methane on nickel surface is widely considered to be the rate-limiting step in POM process. Due to its industrial importance, the methane 1st C-H dissociation pathway on Ni(111) surface has been widely studied; however, all the reported activation energies from theoretical simulations were much higher than the experimental data measured by Lee et al. [1987] (51 kJ/mol) or Beebe et al. [1987] (53 kJ/mol). In order to diminish this discrepancy, a further theoretical study on POM mechanism based on COMR and the methane 1st C-H bond cracking on Ni (111) surface is expected. It is widely acknowledged that coke formation on the Ni(0) catalyst during the POM costs the catalytic activity. Before the commercialization of a nickel catalyzed COMR, the catalyst stability of the membrane reactor has to be solved.

1.2 Objectives of this thesis work

The scope of this thesis work includes (i) fabrication of asymmetric tubular COMR by means of wet chemistry to synthesize fine particles of ceramic oxygen-electrolyte, to formulate colloidal suspensions, and to perform ceramic coating; (ii) separation of oxygen from air on the COMR obtained, (iii) carrying out POM in conjunction with oxygen permeation via the fabricated COMR, and (iv) performing mechanism study on the POM process. The details of project execution are highlighted as follows:

1. Rehological study of the blend consisting of ceramic powder and polymer binder and the development of a proper theoretical mode that describes the effect of the volume fraction of ceramic powder on the blend's viscous flow behavior, which provides the theoretical basis of determining the composition of a ceramic-polymer blend prepared for extrusion of a ceramic object.

2. Development of asymmetric tubular COMRs by wet chemistry technologies, which contains vacuum assisted slurry coating, green tube surface coating, co-calcining technology, solution plugging, electroless metal plating, and modified colloidal suspension coating.

3. Characterization of the separation performance of COMRs using He or CH_4/He as the sweeping gas (i.e., for air separation or for methane partial oxidation into syngas) and examination of the catalytic stability of the imbedded POM catalyst for methane reforming into syngas.

4. Mechanism study of the methane reforming that occurs in the COMR where POM-catalyst was imbedded in the anodic layer, which includes (i) exploring the cracking pathway of the 1st C-H of methane, (ii) theoretical calculation of initial methane sticking coefficient at different temperature, and (iii) fitting the measured methane conversions at different temperatures with those obtained from the proposed methane partial oxidation mechanism.

1.3 Thesis organization

Chapter 2 gives a detailed review about the physical, chemical and thermal properties of the major oxide ion conductive ceramics investigated to date and their fabrication methods, viscous flow behaviors of the polymer-ceramic blend, interaction forces and extrusion of ceramic-polymer paste, POM into syngas, and POM process integrated with oxygen permeation through the COMR.

In Chapter 3 the topic of interest is the flow behavior of a ceramic-polymer blend since it has a direct relationship with the rheology of extrusion of the blend (or called paste) and thus yields the crucial impact on the quality of the fabricated ceramic objects. The rheology of the CeO_2-Polyethylene glycol blend was studied at different temperatures and shear rates and a new mathematical model, accounting for the dependence of the blend flow behavior on the volume fraction of ceramic powder in the extrusion paste, was established and found to be more precisely for describing the above dependence than previous models.

Chapter 4 presents the first successful method to develop a defect-free oxygen permeation membrane, $La_{0.2}Sr_{0.8}CoO_{3-\delta}$ (LSCO80)-CeO_2 composite, on a porous tubular support (or substrate) of CeO_2. This method involved formulation of colloidal suspension for slurry coating, performing slurry coating on the CeO_2 tube surface to generate a powder cake layer of LSCO80-CeO_2, and the post-coating calcinations to convert the LSCO80 powder coating into a consolidated ceramic membrane. There were three novel developments in this Chapter: firstly, the development of vacuum assisted slurry coating technology for largely enhancing the packing density of LSCO80-CeO_2 particles in the powder cake coating layer, it is necessary to reduce porosity and defects in the final sintered membrane; secondly, the development of an effective measure to buffer material stress generated in the LSCO80 membrane caused by mismatch of coefficient thermal expansion (CTE) between membrane and support, this measure was essential to attain a defect-free LSCO80 membrane; and thirdly, the development of a local structure model, which was isolated from the perovskite LSCO80 lattice and allowed to operate simulation by the extended Hückel theory (EHT), to describe the relationship between oxygen vacancy concentration and the energy barrier for the desorption of oxygen molecules from the sweeping side of membrane. The COMR of LSCO80-CeO_2/CeO_2 demonstrated desired air separation functionality.

In Chapter 5 the second successful method to develop a defect-free oxygen permeation membrane, LSCO80/$Ce_{0.8}Gd_{0.2}O_{2-\delta}$ (CGO20), was developed. Unlike the method developed in the preceding Chapter, this method utilized the co-sintering strategy by which a dense CGO20 layer was formed and intercalated at the same time in the surface layer of the tubular CeO_2 support in the course while the support was sintered. As CGO20 material has better oxygen permeation stability but is less reactive than LSCO80 at high temperature, a porous LSCO80 layer was then topped up on the CGO20 layer for promoting the oxygen flux. The air separation of this dual-layer membrane was tested and the effect of the sintering temperature on the membrane oxygen permeation was examined as well. Besides the experimental work, this Chapter also studied the LSCO80 lattice expansion phenomenon upon losing oxygen from the lattice by the density function theory (DFT), which provides a theoretical explanation for the observed crystalline distortion induced by high calcination temperature and the dependence of the membrane oxygen permeation on the LSCO80 sintering temperature.

Chapter 6 presents the third successful method to develop a defect-free oxygen permeation membrane, Ag(Pd)-doped $La_{0.2}Sr_{0.8}MnO_{3-\delta}$ (LSM80), via a pore plugging process. For the pore plugging process, a solution of the nitrate salts of LSM80 was led into tiny pores that were left behind in the sintered Ag(Pd)-LSM80 layer, and the salts staying in the pores were pyrolyzed in-situ to generate oxide powders. After repeating a few rounds of such maneuvering, the oxide powders accumulated inside the pores were sufficient to form dense plugs that sealed all the pores. The Ag(Pd) alloy was used to dope the LSM80 layer for raising electronic conductivity as well as to narrow down pore sizes in the sintered LSM80 layer to the extent so that the above solution plugging method can work. The Ag(Pd)-LSM80 membrane was developed on Y_2O_3 stabilized ZrO_2 (YSZ) tubular substrate. The impedance spectroscopic analysis was employed to study the chemical compatibility between the LSM80 and YSZ at high sintering temperature. The fabricated membrane revealed a reasonably high oxygen permeation flux within the temperature range from 600 ^{o}C to 900 ^{o}C.

In Chapter 7 the partial oxidation of methane (POM) was installed into COMR via the development of a new membrane fabrication technique. In such a dual-function membrane reactor the support of membrane in COMR must also be the support of the POM catalyst in the sweeping side, however more critically, the oxygen permeation membrane must be completely isolated from the sweeping stream (consisting primarily of CH_4, H_2, CO and He); otherwise the membrane is to be destroyed by the strongly reactive species (the former three types). To meet this requirement, the support must be divided into two co-annular layers, the one adjacent to the membrane has to be gas tight but also ionic and electronic conductive (i.e., O^{2-} and e^{-}) to serve as the electrolyte layer; and the one close to the sweeping side has to be sturdy enough to offer mechanical support to the entire membrane reactor but also to be porous to function as the support to POM catalyst, metallic nickel cluster, for ensuring adequate exposure of the catalytic sites to methane. The prime difficulty for introducing POM into COMR lies in therefore the construction of such a multifunctional structure, which is essentially an electrochemical cell. In this Chapter a novel method (i.e., the fourth successful method by following the previous list) was invented to attain the membrane reactor LSM80-CGO20/YSZ-Ag/YSZ-Ni, in which YSZ-Ni is a tubular structure with a porous and thick wall as the mechanical and catalytic support – the anode; YSZ-Ag is a dense (gas tight) and mixed conductive thin layer – the electrolyte; and bi-component composite LSM80-CGO20 is an oxygen-reactive layer, thin and porous on exterior surface, to function as the cathode. This membrane fabrication method entailed four installation stages to put together the above three components, of which the electrolyte layer was made by two states, namely forming YSZ scaffold by slurry coating and filling it up with Ag by electroless silver plating (ESP). The fabricated POM-COMR was proven to operate satisfactorily as designed by converting methane into syngas using oxygen anions permeated from air purging side. In addition, the bilateral diffusions of cations in YSZ-NiO composite, the reduction of NiO in the YSZ-NiO mixture, the collective action of NiO and YSZ, and the mechanism of methane reforming via the fabricated membrane reactor were also studied in this Chapter.

In Chapter 8 a different POM-COMR module from that demonstrated in the previous Chapter was developed. The key improvement made in this new module was on the YSZ electrolyte layer, which was made by slotting an electronic conducting strip (TiO_2-Pd) into the YSZ electrolyte layer instead of by filling the YSZ frame with silver metal by ESP. Precluding ESP is the advantageous aspect of this design over the previous one. In addition, to densify the YSZ electrolyte layer beyond the TiO_2-Pd strip, a two-step colloidal suspension coating approach (i.e. the fifth successful method by following the previous list) was invented. This invention proposes a convenient way to closing pores in a ceramic powder coating layer. As a result, the POM-COMR possessing the electrochemical cell structure, LSM80-CGO20/YSZ$\perp$(TiO_2-Pd)/YSZ-Ni, revealed satisfactory methane reforming reactivity and selectivity. Moreover, the stability of POM was studied and a new methane feeding scheme was proposed to maintain a stable POM output from the membrane reactor.

Chapter 9 reports the mechanism study of methane dissociation process using DFT. The calculated methane 1st C-H cracking energy barrier was compared with the experimental counterparts. A new method to calculate the initial methane thermal sticking coefficients at different temperatures was proposed and the calculated values were compared with the experimental data from literature. Further analysis of the proposed methane dissociation mechanism was used to clarify whether the dissociation is the H tunneling, “over barrier”, or reflection process. The method appropriate for simulating methane conversions at different high reaction temperatures was also developed and used to perform the fitting.

Finally, conclusions of this thesis and recommendations for future work are given in Chapter 10.

Chapter 2 Literature review

2.1 Oxide ion conductive ceramics

2.1.1 Electrical conductivity

Ceramics are commonly defined as the single-phase bodies that are neither metals nor organics (Rice, 2003). Many transition metal oxides (e.g., CoO, FeO, MnO_2, MoO_2, NiO, NbO, ReO_2, TiO and VO_2) exhibit electronic conductivity due to the unfilled *d* or *f* electron energy bands. The excitation of an electron across the bandgap (i.e., the energy difference between the conduction and valence band edges) results in an electron (e') in the conduction band and an electron hole ($h^{\cdot}$) in the valence band and the concentration of the electrons (n_e) within an intrinsic semiconductor is equal to that of its valence band holes (n_h). The Fermi level (E_F) of an intrinsic semiconductor is generally close to the middle of the bandgap (Chiang et al., 1997). The electron donors (n-type) or acceptors (p-type) are widely used to turn an intrinsic semiconductor into extrinsic by shifting its E_F from the middle of the bandgap to its conduction or valence band edge.

Small polaron mechanism (Anderson, 1992) is widely used to explain the p-type electronic conduction of transition metal oxides. The strong overlap of the empty or partly filled transition metal d orbitals (e_g and t_{2g}) with their neighboring O 2p orbital decreases the bandgap significantly as shown in Eq. (2.1).

$$M^{n+}O^{2-}M^{(n-1)+} \rightarrow M^{(n-1)+}O^{-}M^{(n-1)+} \rightarrow M^{(n-1)+}O^{2-}M^{n+} \qquad (2.1)$$

Lots of perovskite-type transition metal oxides, such as $La_xSr_{1-x}B_yB'_{1-y}O_{3-\delta}$ (e.g., B, B′ = Co, Fe, Mn, Cu, Ni), have p-type (or n-type) electronic conductivity at high temperatures in air (or reducing atmosphere) due to the mixed valence state of B or B′ (Wan et al., 2006; Huang & Goodenough, 2000). By selection of cations with only one valence state, Goodenough et al. (1992) obtained ABO_3 perovskite-type metal oxides with negligible electronic conductivity.

The oxide ion (O^{2-}) diffusion within a perfect ceramic crystal is very difficult. Nevertheless, the defects (e.g., Schottky, Frenkel, vacancy, or interstitial) can provide the diffusion with lower energy barrier (Chiang et al., 1997). Perovskite-type oxides, such as $La_xSr_{1-x}Mg_yGa_{1-y}O_{3-\delta}$ (Feng et al., 1996; Huang & Goodenough, 1998 & 2000), and fluorite-type metal oxides (e.g., $Y_xZr_{1-x}O_{2-\delta}$) with oxygen vacancies have high oxide ionic conductivity. The oxide ions transport via the thermally activated vacancy mechanism. The diffusion of vacancies due to the concentration gradient results in an equal counter-flux of lattice oxide ions. Kilner and Brook (1982) calculated the O^{2-} migration energy barrier through the A-A-B saddle point of ABO_3 perovskite-type oxides. The energy barrier was found to decrease with the increase of B cation size and decrease of the A cation size. Due to the outward relaxation of the larger A and smaller B cations at the saddle point, the migrating O^{2-} ion follows a curved route instead of a linear path (Cherry et al., 1995; Islam et al., 1996). The oxide ionic transport activation energy was found dependent on crystallographic-related parameters including (i) average metal-oxygen bond energy (ABE), (ii) “free volume” of the lattice (FV), and (iii) critical radius saddle point formed by A and B ions (r_c) (Cook and Sammells, 1991). The activation energy of O^{2-} diffusion increases as the increase of ABE and decrease of FV or r_c.

Electrical (ionic or electronic) conductivity (σ_i) is the charge flux through the testing sample under per unit electric field and is given by (Chiang et al., 1997)

$$\sigma_i \equiv \frac{J_i z_i e}{E} = c_i z_i e \mu_i \qquad (2.2)$$

in which E (V) is the applied electric field, J_i (mol/cm^2·sec), z_i, c_i (mol/cm^3) and μ_i (cm^2/V·sec) are the flux, valence, concentration, and electrical mobility (velocity per unit electric field) of species i, respectively.

The relationship between the conductivity (σ_i) and diffusion coefficient (D_i) of charged species i are usually related by the Nernst-Einstein equation (Maiya et al., 1997)

$$\sigma_i = \frac{D_i c_i}{RT}(z_i F)^2 \qquad (2.3)$$

where R is the gas constant, T is temperature in Kelvin, F is Faraday constant, and z_i = 2 for oxide ions.

When the membrane is thicker than its characteristic thickness (a value of 100 μm is often quoted for the perovskite-type oxides) the oxygen transport is controlled by the bulk diffusion through the membrane and the oxygen ion flux ($J_{O^{2-}}$) can be expressed by Wagner equation (Maiya et al., 1997)

$$J_{O^{2-}} = \frac{1}{8}\frac{RT}{F^2 L}\int_{\ln PO_2^{II}}^{\ln PO_2^{I}} \frac{\sigma_o \sigma_e}{\sigma_o + \sigma_e} d\ln P_{O2} \qquad (2.4)$$

where L is the membrane thickness, P_{O2} is the oxygen partial pressure, and σ_o and σ_e are the oxide ionic conductivity and electronic conductivity, respectively.

Equation (2.4) shows that, for the cases of the surface oxygen exchange rate being much higher than the bulk oxide ionic transport rate, the oxygen permeation linearly increases as the decrease of the membrane thickness; thus an asymmetric membrane structure with thin (10 ~ 50 μm) active dense layer provides much higher oxygen permeation than a symmetric dense membrane with typical thickness of around 1000 μm.

2.1.2 Classification and properties of oxygen ion conductive ceramics

Both mixed oxide ionic-electronic conductor (MIEC) and solid electrolyte (SE) can be used for oxide ion diffusion. The MIEC has both high O^{2-} conductivity and high electronic conductivity, while the SE has only high ionic conductivity and essentially no electronic conductivity (Goodenough, 2003; Akin and Lin, 2004). Table 2.1 shows some examples of the typical oxygen ion conductive ceramic materials. The perovskite-type and fluorite-type oxides as well as their mixture with electronically conductive metals or ceramics have tremendous potential for industrial oxygen separation, SOFCs or COMRs.

Table 2.1 Examples of the oxygen ionic-conducting ceramic materials

Type		Examples
Mixed (oxide) Ionic-Electronic Conductor (MIEC)	Perovskite-type (ABO_3)	$La_{1-x}Sr_xCo_{1-y}Fe_yO_{3-\delta}$
	Modified perovskite-type	$SrFeCo_{0.5}O_{3-\delta}$
	Brownmillerite ($A_2B_2O_5$)	$Sr_{1.4}La_{0.6}GaFeO_{5.3}$
	Fluorite-type (A_4O_8)	Doped ceria ($Ce_{1-x}Gd_xO_{2-\delta}$)
	Ruddlesden-Popper phase	$SrO(La_{0.7}Sr_{0.3}MnO_3)_2$
	Ceramic-ceramic composite	$Ce_{1-x}Gd_xO_{2-\delta}$ / $La_{1-x}Sr_xMnO_{3-\delta}$
	Ceramic-metal cermet	Stabilized zirconia / Pd
Solid Electrolyte (SE)	Fluorite-type (A_4O_8)	Doped zirconia or δ-Bi_2O_3
	Perovskite-related	$La_{1-x}Sr_xGa_yMg_{1-y}O_{3-\delta}$
	Brownmillerite ($A_2B_2O_5$)	$Ba_2In_2O_5$
	BIMEVOX	$Bi_2V_{0.9}Cu_{0.1}O_{5.35}$

2.1.2.1 Perovskite-type metal oxides

Many compounds with the ABO_3 stoichiometry (A is the large cation and B is the small cation) have perovskite-type crystal structure. Lanthanides and alkaline earth metals are examples of A metals. B elements include the transition metals, Al, Ga, and Ge. Figure 2.1 shows the crystal structure of an ideal cubic ABO_3 perovskite-type metal oxide.

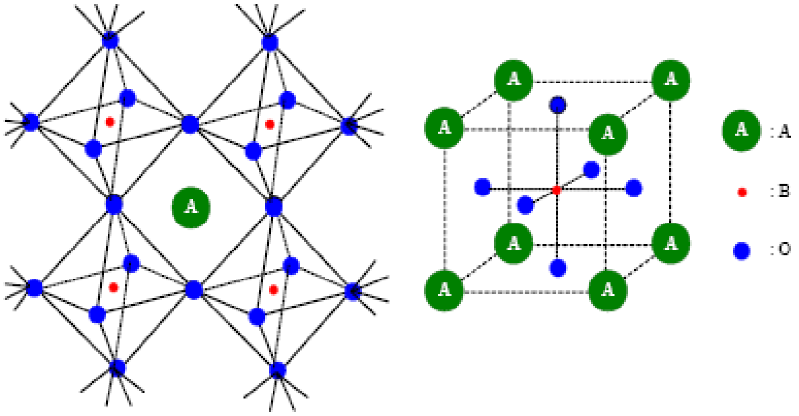

Figure 2.1 Schematic of the ideal ABO_3 perovskite structure

The larger A cation is surrounded by 12 nearest neighbor O^{2-}, while the smaller B cation occupies the center of a BO_6 octahedra. This structure can be imaged as a network of BO_6 with A cation in the cubic cavity (Schaak & Mallouk, 2002). Geometric Goldschmidt tolerance factor (t) defined by Eq. (2.5) was used to describe the relationship between the ionic radii (r) and the crystal symmetry of perovskite metal oxide at room temperature (Hayashi et al., 1999; Baran, 1990).

$$t \equiv \frac{r_A + r_O}{\sqrt{2}(r_B + r_O)} \tag{2.5}$$

An ideal cubic perovskite structure has the tolerance factor of unity and a distorted perovskite structure with lower vibration entropy has the t value slightly different from 1 (e.g., $0.75 < t < 1$). The stabilization energy of the ABO_3 perovskite-type oxide shows an excellent dependence of the tolerance factor (Yokokawa, 2003). Partial substitution of the lanthanide by a divalent ion enhanced the electrical conductivity considerably. For most of the perovskite-type metal oxides the tolerance factor was less than one, increasing the A site ionic radius pushes the t value approaching one and thus results in higher stability (Nakamura et al., 1979).

For an example, the phase stability of $Ba_{0.5}Sr_{0.5}Co_{0.8}Fe_{0.2}O_{3-\delta}$ is better than that of $SrCo_{0.8}Fe_{0.2}O_{3-\delta}$ since the radius of Ba^{2+} is larger than that of Sr^{2+} (Vente et al., 2006; Shao et al., 2001). Besides the A site metal, the B site element also has significant effect on the stability of a perovskite-type oxide. The stability under reducing atmospheres (in terms of the $-\log P_{O2}$ values) increases in the ordering of $LaNiO_3 < LaCoO_3 < LaMnO_3 < LaFeO_3 < LaCrO_3 \cong LaVO_3$ (Nakamura et al., 1979).

Partially substitution of the A-site or B-site metal of an ABO_3 compound results in numerous perovskite-type oxides and thus the electrical conductivity and the stability can be tailored by partially substitution of the three valence A ions (e.g., Y, La, Pr, Nd, Sm, Gd, etc.) with two valence ions (e.g., Ca, Sr, Ba, etc.) and/or partially change of B site element.

Substitution in the La^{3+} position of $LaCoO_3$ by alkaline earth metal ions such as Ca^{2+}, Sr^{2+}, and Ba^{2+} brings in oxygen vacancies, which are responsible for the oxygen transport. The structure of $La_{1-x}Sr_xCoO_{3-\delta}$ (LSCO) depends on its substitution degree. A rhombohedral structure was found at low substitution degree ($x < 0.5$), while at intermediate substitution degree ($0.5 < x < 0.6$) the LSCO has simple cubic structure and further increase of the substitution degree ($x > 0.65$) brings in local tetragonal ($a_P \times a_P \times 2a_P$) superstructure (20 -30 nm domain size) (James et al., 2004). At low x value the oxygen ionic conductivity increases as the increase of x value due to the increasing of mobile oxygen vacancy concentration ($V_o^{\cdot\cdot}$) or δ value; however, further increase of the x value may result in the immobilization of the oxygen vacancies (i.e., the formation of ordered oxygen vacancies and dopant-oxygen vacancy cluster) and thus decrease the oxygen ionic conductivity (James et al., 2005).

Teraoka et al. (1988) were the first to report the high ionic conductivity of the LSCF ($La_{1-x}Sr_xCo_{1-y}Fe_yO_{3-\delta}$) perovskites. The limited chemical and dimensional stability of the LSCF under large oxygen chemical potential gradients is a major issue for their applications. Balachandran et al. (1995 & 1997) reported the crack of LSCF membrane reactor upon the introduction of methane at 850 °C. It was believed that at reducing atmosphere the LSCF cubic phase transformed to new phase, which causes the lattice mismatch between the materials on the air-side and methane-side of the membrane and thus the fracture happens. Doping the LSCF with higher valence metal (such as Cr or Ti) (Kharton et al., 2001) or more stable trivalent cations (such as Ga^{3+} and Al^{3+}) (Patrakeev et al., 2002; Yaremchenko et al. 2004) leads to increased stability and decreased oxide ion conductivity. A "trade-off" between the conductivity and stability may exist within the doped LSCF perovskite-type oxides since high oxide ionic conductivity requires weak B-O bond which is easy to be reduced at low partial oxygen pressure (e.g., $P_{O2} < 10^{-17}$ atm).

Attempts to improve both the ionic conductivity and stability via substitution the A or B site have been reported (Tichy & Goodenough, 2002; Wang et al., 2003). $LaGaO_3$ has orthorhombic distorted perovskite structure at room temperature. High oxide ionic conductivity (~0.1 S/cm at 800 °C) can be obtained via doping the La or Ga site. $La_{1-x}Sr_xGa_{1-y}Mg_yO_{3-\delta}$ (LSGM) has been reported to have high O^{2-} conductivity (higher than that of stabilized zirconia and slightly lower than that of

Bi_2O_3 oxide) and near unity transference number ($t_o \equiv \sigma_o/\sigma \approx 1$) (Ishihara et al., 1994; Goodenough, 2003). Its oxide ion conductivity and transference number can be tailored by doping the Ga site with transition metals such as Fe, Co, or Cr (Ishihara et al., 1999; Baker et al., 1997). Nevertheless, the high cost and the high temperature volatilization of the Ga at reducing atmospheres as well as its low mechanical strength may limit the high temperature applications of the $LaGaO_3$-based perovskite-type oxides.

2.1.2.2 Fluorite-type oxide ion conductive materials

At high temperature (> 2300 °C) pure zirconia (ZrO_2) has the cubic fluorite structure in which a simple cubic structure consisting of eight oxide ions are located inside the face-centered cubic zirconium ions (Fig. 2.2). The cubic ZrO_2 is transformed into monoclinic structure at about 1100 °C and finally into tetragonal below 100 °C (Park & Blumenthal, 1989). The cubic structure can be stabilized to room temperature by doping ZrO_2 with larger aliovalent cations (e.g., Sc^{3+}, Yb^{3+}, Mg^{2+}, La^{3+}, Y^{3+} and Ca^{2+}), which also bring in oxygen vacancies located around the Zr^{4+} ions and thus oxygen ionic conductivity. Y_2O_3 stabilized ZrO_2 (YSZ) may be the most stable oxide ion conducting ceramic at both reducing and oxidizing atmosphere and it also has high mechanical strength; therefore, it has been widely employed as the electrolyte for SOFCs (Srinivasan et al., 1999; Steele, 2001), oxygen generation systems (Kim & Lin, 2000 b), and oxygen sensors. On one hand the yttrium substitution increases the oxygen vacancy concentration; on the other hand Y^{3+} reduces ion mobility by introduction strain into the cubic lattice (Irvine et al., 2000).

The YSZ with 8-15 mol% Y_2O_3 has the optimized oxygen ionic conductivity (about 0.15 S/cm at 1000 ^oC and 0.03 S/cm at 800 ^oC).

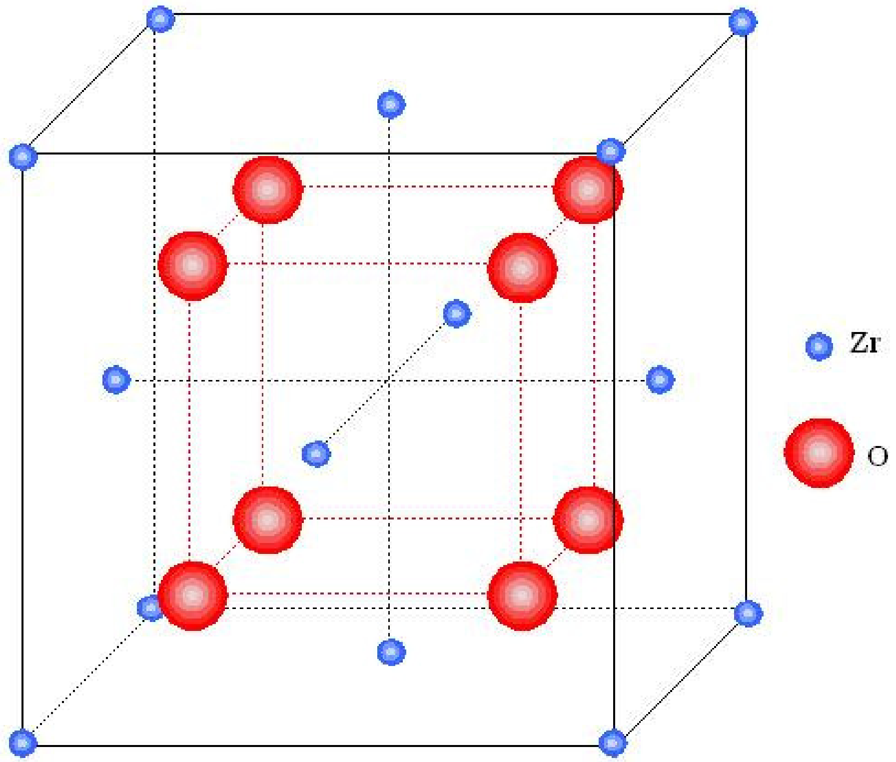

Figure 2.2 Schematic of the cubic fluorite-type ZrO_2 structure

Employing pure YSZ as the dense membrane layer for oxygen separation from air resulted in very low oxygen permeation due to its extremely low electronic conductivity (Lin et al., 1992). Park and Blumenthal (1989) reported the dependence of the oxygen ionic conductivity (σ_o, S/cm), the conductivity of electrons (σ_n, S/cm), and the conductivity of holes (σ_h, S/cm) of the 8 mol% Y_2O_3 stabilized ZrO_2 on the temperature (T) (1073 ~ 11323 K) and partial oxygen pressure (P_{O2}) (0.21 ~ 10^{-17} atm) as follows

$$\boldsymbol{\sigma}_{\boldsymbol{o}} = 1.63\times10^{2}\exp\left(\frac{-0.79\boldsymbol{eV}}{\boldsymbol{kT}}\right) \quad (2.6)$$

$$\sigma_n = 1.31\times10^{7}\exp\left(\frac{-3.88eV}{kT}\right)P_{O2}^{-\frac{1}{4}} \tag{2.7}$$

$$\sigma_h = 2.35\times10^{2}\exp\left(\frac{-1.67eV}{kT}\right)P_{O2}^{\frac{1}{4}} \tag{2.8}$$

where k (8.614×10^{-5} eV/K) is the Boltzmann's constant.

The oxygen ionic conduction of YSZ occurs via the vacancy mechanism and the oxygen vacancy is essentially controlled by the doping impurity ($Y_2O_3 \xrightarrow{ZrO_2} 2Y_{Zr}^{'} + 3O_o^{x} + V_o^{\cdot\cdot}$, in Kröger Vink notation (appendix A)) and the electrons ($O_o^x = 2e^{'} + V_o^{\cdot\cdot} + \frac{1}{2}O_2(g)$) or holes ($V_o^{\cdot\cdot} + \frac{1}{2}O_2(g) = 2h^{\cdot} + O_o^x$) trapped on the YSZ sub-lattices are introduced by thermal excitation and are strongly dependent on the temperature and oxygen partial pressure. At 850 °C the ionic conductivity of YSZ is about 4.6×10^{-2} S/cm, which is much higher than its electronic conductivity due to electrons at 10^{-18} atm P_{O2} (1.6×10^{-6} S/cm) or holes at 0.21 atm P_{O2} (5.1×10^{-6} S/cm). For an oxide ionic conductor (e.g., YSZ) membrane with very high ionic transference number ($t_i > 0.99$) the oxygen permeation flux (J_{O2-}) can simplified as

$$J_{O^{2-}} = \frac{\sigma_e RT}{8F^2L}\ln\left(\frac{P_{O2}^{I}}{P_{O2}^{II}}\right) \tag{2.9}$$

It can be seen from Eq. (2.9) that either the increase of its electronic conductivity or reducing the YSZ membrane thickness has to be executed to improve its oxygen permeation. The electronic conduction of YSZ can be enhanced by doping it with multivalent metal oxides, such as Tb (Han & Worrell, 1995) and Ti (He et al., 2004), or by addition of highly conductive noble metal (Chen et al., 1995 & 1996) to form the dual-phase composite. The percolation model has been used to explain the electronic conductivity of the doped YSZ and the low dopant percolation threshold (~ 3.6 mol % Ti^{4+}) (Swider & Worrell, 1996). Doping YSZ with TiO_2 can significantly improved its electronic conductivity under reducing atmosphere at elevated temperature, for an example, at 850 °C and reducing environment (P_{O2} ~ 10^{-18} atm) doping with 10 mol% TiO_2 improved the electronic conductivity (of 12 mol% YSZ) from about 1.6×10^{-6} S/cm to 7×10^{-3} S/cm; nevertheless the doped YSZ was still ionic conductivity predominate with transference number around 0.87.

CeO_2 and δ-Bi_2O_3 have the similar crystal structure as that of the ZrO_2. Doping CeO_2 with other types of oxides having different metal valency (e.g., La_2O_3, Sm_2O_3, Gd_2O_3, Yb_2O_3, Y_2O_3, Nb_2O_3, Ta_2O_5, and Pr_6O_{11}) has been studied by Zhao and Gorte (2003 & 2004). Ceria or doped ceria has high oxide ionic conductivity and high catalytic activity for hydrocarbon oxidation (Park et al., 2000). Gadolinium doped ceria has ionic conductivity up to 0.1 S/cm at 800 °C and is partially reduced at reducing atmosphere at temperatures above 600 °C ($Ce^{4+} \rightarrow Ce^{3+}$) resulting in significant electronic conductivity; however, its mechanical strength is much lower than that of the YSZ.

δ-Bi_2O_3 has the highest known oxide ion conductivity (2.3 S/cm at 800 °C) but it is only stable between 730 °C and its melting point (804 °C). Doping with other types of cations such as W^{6+}, Y^{3+}, Sm^{3+}, Er^{3+}, Ce^{4+}, and Gd^{3+} (Akin & Lin, 2004; Huang et al., 1996) can stabilize it to lower temperature. Doped δ-Bi_2O_3 exhibit ionic conduction higher than doped ZrO_2 or CeO_2 but most of them show extremely poor strength and stability under reducing atmosphere.

2.1.3 Fabrication methods

The ceramic powder fabrication techniques are usually categorized according to their synthetic reaction type (solid phase reaction, liquid phase reaction or gas phase reaction), the reaction chemistry (e.g., sol-gel synthesis, precipitation process, etc.) or the processing technologies (e.g., combustion, hydrothermal synthesis, microemulsion, etc.). Among those techniques, solid-state reaction method, co-precipitation, sol-gel, Pechini method, chemical vapor deposition (CVD) and physical vapor deposition (PVD) are widely employed.

The solid–state reaction (i.e., ceramic method) is a conventional method, in which the dry or wet grinding before and after high temperature heating of metal oxides, carbonates, hydroxides, cyanides or nitrates are involved (Tan et al., 2003; Flint & Slade, 1995). This method is very simple, cost cheap, and easy to control the overall chemical composition of the final product; however, it may be difficult to obtain a compositionally homogeneous product (Jin et al., 2002) and full conversion of the reactants is not guaranteed, although multi-grinding/heating method is reported to improve the uniformity of the final ceramics. The dense ceramic membrane prepared by the ceramic method has relatively lower oxygen permeation than the same membrane fabricated by other methods, which may produce more homogeneous membrane (Tan et al., 2003). The particle size produced by this method is generally larger than that produced by other technologies due to the required high sintering temperature and long sintering time.

Co-precipitation from the solution of metal salts, often nitrates, is one of the oldest methods to prepare perovsktie—type ceramics. Oxalic acid (Jitaru et al., 2000), citric acid (Liang et al., 2003), ammonium hydroxide (Lee, 2004), and $(NH_4)_2CO_3$ (Ge et al., 2001) have been used as the precipitating agents. Depending on the solution thermodynamics, homogeneous co-precipitation (in which the precipitate crystal has the same stoichiometric metal ratio as that of the solution) or non-homogeneous co-precipitation (in which the precipitated individual crystal has different stoichiometeric metal ratio each other) may be formed. Micro-emulsion (Lee et al., 2001; Giannakas et al., 2003) has been widely employed to improve the co-precipitation homogeneity and produce nano-size ceramic powders.

In a sol-gel route, the homogenization of the chemicals is achieved in the solution stage and the liquid structure is preserved by cross-linking in the followed gelling and curing steps, which may involve in drying (Hardy et al., 2004) or chemical reaction (Harizanov et al., 2004). Further heat treatment is used to remove the organic species, hydroxyls, and porosity. The major advantages of the sol-gel method include low sintering temperature (Cheng & Navrotsky, 2004) and capability to produce nano-sized particles (Zhang & Gao, 2004). Essentially, Pechini method (Pechini, 1967; Hong et al., 1999) is a type of sol-gel technology. Water-soluble chelating agents, such as EDTA, citric acid, lactic acid, tartaric acid, glycine and other organic ligands, are often used to prepare aqueous metal complexes. Water-soluble polymer (e.g., PVA) or polymer monomer (e.g., ethylene glycol) is typically added to form a gel or resin after evaporation of some amount of the water. An amorphous ceramic powder is resulted when the gel is subjected to calcining. Further heat treatment will result in crystalline ceramics.

2.1.4 Defect chemistry model

The defect chemistry model is widely used to explain the equilibrium oxide ionic or electronic conductivity of a metal oxide. With the help of Kröger Vink notation (appendix A), Ma et al. (1997) suggested the basic equations to build up the defect structure for an ABO_3-like system. That is, the equation describing the interaction between the defects and the surrounding partial oxygen pressure (Eq. 2.10), thermal generation of interstitial oxygen ions (Eq. 2.11), intrinsic thermal generation of electrons and holes (Eq. 2.12), valence change of the B ions (Eq. 2.13) and overall electrical neutrality (Eq. 2.14).

$$O_O^x \Leftrightarrow V_O^{\cdot\cdot} + 2e' + \frac{1}{2}O_2 \tag{2.10}$$

$$O_O^x \Leftrightarrow O_i'' + V_O^{\cdot\cdot} \tag{2.11}$$

$$nil \Leftrightarrow e' + h^{\cdot} \tag{2.12}$$

$$B_B^{\cdot} \Leftrightarrow B_B^x + h^{\cdot} \tag{2.13}$$

$$[e'] + 2[O_i''] = [h^{\cdot}] + 2[V_O^{\cdot\cdot}] + [B_B^{\cdot}] \tag{2.14}$$

Assuming that the concentrations of electronic defects were much smaller than those of ionic defects, Mizusaki et al. (1993) explained the equilibrium electrical conductivity of the $La_{1-x}Ca_xAlO_{3-\delta}$ system well. Kozhevnikov et al. (2003) analyzed the $La_{1-x}Sr_xCo_{1-z}Mn_zO_{3-\delta}$ series and found that the concentrations of n- (metal-like) and p-type (semiconductor-like) carriers were affected by the total oxygen vacancy concentration and temperature. Mitberg et al. (2000) studied the LSCO perovskite oxides and found that the cobalt disproportionation ($2Co^{3+} = Co^{2+} + Co^{4+}$) was dependent on the oxygen vacancy concentration and as the δ value decreased a p-to-n transition occurred.

2.2 Ceramic-polymer blend reheology and extrusion

A typical ceramic tube formation process via extrusion includes several steps in sequential as shown in figure 2.3. The porosity or relative density of the fabricated ceramic tube can be adjusted by the volume percentage of the solid particles in the ceramic-polymer blend or the sintering profile.

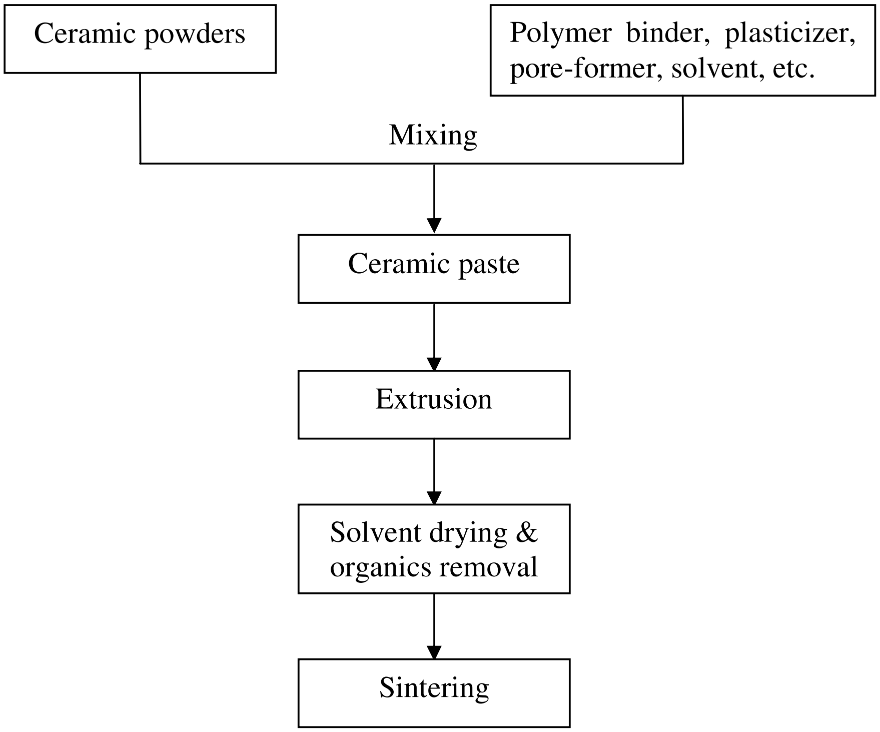

Figure 2.3 Schematic of the ceramic tube fabrication process

2.2.1 Rheology of ceramic-polymer blend

The flow behavior of ceramic-polymer blend has significant effect on extrusion process and thus the qualities of the extruded green tube and the final sintered ceramic tube. Unlike the extrusion of a polymer tube, ceramic extrusion encounters much larger abrasive force since the feedstock comprises a high content of ceramic solid powder(s) (30 ~ 50 vol.%) besides necessary organic additives, such as polymer binder, extrusion additives and others. The high ceramic loading has to be kept to assure the morphology of a consolidated ceramic object upon sintering. The ceramic-polymer blend has been realized to have different responses from the pure polymer melt to the applied shear stress; the experience came even from the blends with low solid-contents (Burbidge & Bridgwater, 1995).

One of the most popular models describing the dependence of the shear stress on the shear rate of the blend is the Herschel-Bulkley (HB) model (Rangarajan et al., 2000):

$$\boldsymbol{\tau} = \boldsymbol{\tau}_0 + \boldsymbol{K}\dot{\boldsymbol{\gamma}}^{\boldsymbol{m}} \qquad (2.15)$$

in which τ is the applied stress, τ_0 the yield stress accounting for the interactions between polymer-polymer, polymer-particle or particle-particle under very low shear rate, $\dot{\gamma}$ is the shear rate; K is the consistency modulus, and the index m is responsible for the high share rates. For the Bingham plastic flow, m equals to unity (Lewis, 2000). On the other hand, several mathematical models have been developed to describe the relationship between the relative viscosity (η_{rel}) of the blend and the solid powder content (ϕ). The most famous one should be regarded as the theoretical Einstein model (Lewis, 2000).

$$\eta_{rel} = 1 + 2.5\phi \tag{2.16}$$

The relative viscosity (η_{rel}) is defined as the ratio of the apparent viscosity (η) of the blend to the viscosity of the matrix without particle (η_0); ϕ is the volume fraction of solid in the blend. Anyway, Einstein relationship is valid only for very low solid loading systems ($\phi << 1$) and requires the solid particles to be hard and mono-dispersed spheres.

To date, there have been several empirical or semi-empirical formula, such as power series (Eq.2.17), Eilers equation (Eq. 2.18), Mooney model (Eq. 2.19) (Guyot et al., 2002) and Krieger-Dougherty Model (Rangarajan et al., 2000; Lewis, 2000) (Eq. 2.20), to describe the relationship between relative viscosity and volume fraction of solid particles. These models can be viewed as the modified forms of the Einstein's equation by adjusting the contribution of ϕ to η_{rel}. Nevertheless; these models do not furnish clear sense of physics and chemistry to the variations of the weigh of ϕ.

$$\eta_{rel} = 1 + 2.5\phi + \sum_{n=2} A_n \phi^n \tag{2.17}$$

$$\eta_{rel} = \left(1 + \frac{2.5\phi}{1 - \frac{\phi}{\phi_{\max}}} \right)^2 \tag{2.18}$$

$$\eta_{rel} = \exp\left(\frac{2.5\phi}{1-\dfrac{\phi}{\phi_{\max}}}\right) \qquad (2.19)$$

$$\eta_{rel} = \left(1-\frac{\phi}{\phi_{\max}}\right)^{-2.5\phi_{\max}} \qquad (2.20)$$

To endow the hard spheres certain sorts of surface characteristics (such as the polymer adsorption on the particle surface), the effective solid loading (ϕ_{eff}) has been used in place of ϕ in the above equations (Eq. 2.21).

$$\phi_{eff} = \phi\left(1+\frac{\delta}{a}\right) \qquad (2.21)$$

where δ is the thickness of adsorbed layer; *a* is the spherical particulate radius. For the hard sphere, δ is zero.

Interactions between polymers and solid particles are the root-cause of special rheological behavior of the ceramic-polymer composite, especially when polymer phase has a much smaller volume fraction than the solid particles (i.e., high solid volume loading). In the blend of ceramic powder and polymer melt, there are basically three factors shaping the interfacial interactions: firstly, the interfacial area between the ceramic particles and the polymer melt, with the same solid loading, the smaller the particles are, will be the more viscous of the blend (Guyot et al., 2002); secondly, affinity of functional groups bared by the polymer chains with the surface of the ceramic particles, which is the driving force of the adsorption of polymer chains on ceramic particles; and thirdly, the entanglement chain lengths (Z_w) of the polymers used; the Z_w involves flexibility as well as molecular weight distribution of polymer chains.

The interaction forces between ceramic particles include attractive van der Waals force, electrostatic attractive or repulsive interaction, steric force, depletion force and others. Understanding how theses forces work in the nano-particle systems has become the recent research focus. The van der Waals force is a universal force, which is generally regarded to be responsible for the agglomeration of the particles and the particle-polymer separation (Goodwin & Hughes, 1992), while electrostatic repulsion force is widely applied to increase the stability of the particle-polymer dispersion (Zhou et al., 2001). Combination of the van der Waals interaction with the electrostatic force has resulted in the very famous DLVO theory, which has been widely applied in colloidal systems. Through molecular design of the polymer chains, the steric repulsion caused by the adsorbed polymer chains onto the particle surface can prevent the particle aggregation.

In a polymer-solid particle blend wherein if non-adsorption occurs, the polymer chains are to be expelled from the space between two particles if the radius of the polymer gyration is larger than the distance due to the compression-caused high chemical potential. The exclusion of polymer molecules from the region leads to an unbalanced osmotic pressure; it then pushes the solid particles to join together known as depletion force. If the attractive depletion force is large enough, phase separation would occur in the blend (Lee & Robert, 1999; Sear 2001). In fact, adsorption of polymer chains onto the solid particles happens in major polymer-particle blends, and what matters is the adsorption intensity, which affects the rheology of the blend.

2.2.2 Ceramic-polymer paste extrusion

With respect to the preparation of polymer-ceramic blends to make ceramic green bodies via extrusion or molding, there are several approaches: (1) introduction of the desired ceramic powder into a polymer solution followed by removing the solvent (Croce et al., 1999) or into a polymer melt (Zanetti et al., 2002); (2) use of organometallic polymers as pre-ceramic matrix (Corriu et al., 2000); and (3) perpetrating polymerization at the surface of ceramic fine particles (Johnson et al., 1999). Of these methods, direct solution mixing is obvious a simple and practical way to prepare extrusion feedstock. The problem associated with this approach is the phase separation of the polymer from the ceramic powder, which will result in non-uniform flow of the extrusion stuff during extrusion and eventually cause defects in the finally obtained ceramic tube. Adding plasticizer, lubricant, and non-ionic surfactants is the general measure to overcome phase separation problem.

In generally, a ceramic paste has highly filled solid particles (~ 50 vol.%) in order to avoid crack formation during the organics removal or obtain high yield after post-consolidation steps. The paste should also be deformable and can retain their shape after deformation. Smaller powder particle size was reported to fabricate fully dense ceramics because they can be sintered at lower temperature (Liu, 1998). On the other hand, to make the ceramic with smaller particle size extrudable more binders need to be added because the powder has high specific surface area which adsorbs the additives necessary for extrusion (Du et al., 2000). It seems that to fabricate a highly dense ceramic tube a balance between the particle size and the amount of organic additives added may exist (Hatchwell et al., 1999).

Nowadays, lots of techniques, such as die pressing, casting, electrophoresis (Nakahira et al., 2003), biomimetics and extrusion, have been developed to shape the ceramic pastes. Extrusion has been widely suggested to fabricate a ceramic tube, because it can make green tube continuously without limiting the length of the tube. Burbidge & Bridgwater (1995) developed the equation to explain the dependence of the pressure gradient on the paste flow rate and the single screw extruder parameters. Benbow-Bridgwater model (Benbow et al. 1987) has been proposed and used to describe the extrusion pressure for a ram extrude. Anyway, the scientific understanding to the ceramic paste extrusion fundamentals was very limited and most of the studies were done in a “black art” approach. Failures may occur during the handling of the extruded green ceramic paste tube due to inadequate strength. Rumpf’s model (Uhland et al., 2001) was proposed to describe the strength of the randomly packed spheres with uniform size; however, due to the shape irregularity and size distribution of the actual ceramic powders, the particle volume fraction can be optimized only by experience.

Extremely care should be paid to the solvent drying and organics removal to avoid the crack formation. The drying process include three stages in sequential (Lewis, 2000): (i) constant rate period (CRP) in which the fluid is transported to the external surface(s) for evaporation via capillary force, (ii) first falling-rate period (FRP1) when evaporation occurs from the fluid menisci due to that the capillary-driven transport rate is lower than the surface fluid evaporation rate, and (iii) second falling-rate period (FRP2) when the liquid is removed from the body by vapor-phase diffusion. The binder physical properties and its distribution within a green ceramic tube play an important role in the kinetics of the binder removal process (Cima et al., 1989).

2.3 Ceramic oxygen-electrolyte membrane rector for partial oxidation of methane

2.3.1 Partial oxidation of methane into syngas

The natural gas (mainly methane) field is usually far away from the customer and its transport is quiet economically expensive as rarefied gas and not safety as compressed liquid (Lunsford, 2000). To avoid the high cost and hazardous pipeline transport, the natural gas is converted into value-added liquids directly or more frequently into intermediate gas (i.e., syngas) in-situ. Converting methane into liquid chemicals (e.g., methanol, alcohols, aldehydes, and higher hydrocarbons) could make the transportation safer and cheaper and thus have tremendous economic implications. Conversion of methane directly into liquids via metal oxide catalysts attracted lots of studies; however, it still faced the issue of either low yields or low selectivity (Zhu et al., 2005).

Catalytic oxidation of methane into methanol or methanol derivatives via intermediate methyl bisulfate (CH_3OSO_3H), a feedstock for methanol (Eq. 2.22), improved the yield significantly (Periana et al., 1993). Catalytic transferring methane into syngas (mixture of CO and H_2), a precursor to produce liquid fuels or other transportable liquid products, has very high production yield (> 90%). To date, steam methane reforming (SMR) is the most commonly utilized industrial process to coax methane into syngas, but this process is capital expensive and highly energy consumption due to its high endothermic nature ($\Delta H^0_{298} = +206$ kJ/mol) and the produced syngas has a too high H_2/CO ratio (Eq. 2.23) for the further methanol (Eq. 2.24) or Fischer-Tropsch (Eq. 2.25) synthesis (Lunsford 2000). Partial oxidation of methane (POM) with pure oxygen in the presence of a catalyst to syngas is mildly exothermic ($\Delta H^0_{298} = -36$ kJ/mol) and energy efficient and gives the H_2/CO ratio of 2 (Eq. 2.26), which is desired for the followed liquidize synthesis.

$$CH_3OSO_3H + H_2O \rightarrow CH_3OH + H_2SO_4 \quad (2.22)$$

$$CH_4 + H_2O \rightarrow CO + 3H_2 \quad (2.23)$$

$$CO + 2H_2 \rightarrow CH_3OH \quad (2.24)$$

$$nCO + 2nH_2 \rightarrow C_nH_{2n} + nH_2O \quad (2.25)$$

$$CH_4 + 1/2O_2 \rightarrow CO + 2H_2 \quad (2.26)$$

POM was first studied by Prettre et al. in 1946 using nickel as the catalyst. Since then, supported noble metals (e.g. Rh, Ru, Pd, Pt), support non-noble transition metals (e.g. Ni, Co, Fe), perovskite-type oxides ($LaMO_3$, M = Ni, Rh, Co, Cr) and some pyrochlore-type oxides (e.g. $La_2Ru_2O_7$) have been studied to catalyze POM. Nickel has been widely studied due to its low cost and high activity, although it favors the carbon formation and thus suffers from the deactivation when exposed to dry CH_4 (Lu et al., 2004; Gorte et al., 2004). Nowadays, mainly two types of mechanisms (i.e., two-steps mechanism and direct POM mechanism) were proposed to explain the POM process. The two-steps mechanism was first proposed by Prettre et al. in 1946. According to the two-steps mechanism, the methane was first totally oxidized into CO_2 and H_2O (Eq. 2.27) and the syngas came from the followed steam reforming (Eq. 2.23) or dry reforming (Eq. 2.28). The major experimental supports for the two-steps mechanism include the facts that a sharp temperature increase near to the methane entrance section of the catalyst bed due to the combustion reaction and zero CO and H_2 selectivity at low methane conversion (Dissanayake et al., 1991 & 1993). Based on the fact that high CO yield could be achieved even at residence time of 10^{-3} s or shorter, Hickman and Schmidt (1993) proposed the direct POM mechanism suggesting that the methane is directly dissociated into adsorbed carbon and adsorbed hydrogen at the catalyst surface (Eq. 2.29) and the syngas is produced by the surface carbon oxidation/desportion (Eq. 2.30) and hydrogen combination/desorption (Eq. 2.31). The significant discrepancy between the two mechanisms may be due to different experimental situations. The formation of CO_2 or CO was dependent on the C_{ads}/O_{ads} ratio. The observed CO_2 & H_2O and sharp temperature increase may be due to lower C_{ads}/O_{ads} ratio at the reactor inlet (Eqs. 2.32 & 2.33), whereas the experimental designed by Hickman and Schamidt (1993) have higher C_{ads}/O_{ads} ratio at the inlet resulting in the direct POM mechanism. It has been widely accepted that when a CH_4 molecule reacts with the pure nickel surface it is dissociated into C_{ads} and H_{ads} and the 1st methane C-H cracking is the rate determination step.

$$CH_4 + 2O_2 \rightarrow CO_2 + 2H_2O \qquad (2.27)$$

$$CH_4 + CO_2 \rightarrow 2CO + 2H_2 \qquad (2.28)$$

$$\mathrm{CH_4 \rightarrow CH_{4\,\mathit{ads}} \rightarrow C_{ads} + 4H_{ads}} \tag{2.29}$$

$$\mathrm{C_{ads} + O_{ads} \rightarrow CO_{ads} \rightarrow CO} \tag{2.30}$$

$$\mathrm{H_{ads} + H_{ads} \rightarrow H_{2\,ads} \rightarrow H_2} \tag{2.31}$$

$$\mathrm{C_{ads} + 2O_{ads} \rightarrow CO_{2\,ads} \rightarrow CO_2} \tag{2.32}$$

$$\mathrm{2H_{ads} + O_{ads} \rightarrow H_2O_{ads} \rightarrow H_2O} \tag{2.33}$$

Due to its industrious importance, the methane dissociation process has been widely studied. Molecular beam experiments found that the methane molecule can be activated by translational energy, vibrational energy, catalyst surface temperature, or methane gas temperature. Holmblad et al. (1995) found that the effect of surface temperature on Ni(100) was smaller than activation by translational or vibrational energy, which supported that the methane dissociation on transition metal surface was a direct process without involving in significant thermalization with the catalyst surface prior to reaction. Using pulsed laser and molecular beam techniques, Beck et al. (2003) observed the vibrational mode-specific CD_2H_2-Ni(100) reaction at catalyst surface temperature of 473 K. The observed mode-specific reaction was inconsistent with the "precursor" mechanism, an assumption widely accepted in statistical models. Nevertheless, the statistical models (Bukoski & Harrison, 2003; Abbott et al., 2003) based on the assumption that there exists complete intramolecular energy redistribution before dissociation occurs claimed to be able to explain existing experimental data.

To clarify the transition state and the activation mechanism for methane dissociation, quantum mechanic calculations were employed. Figure 2.4 showed the schematic of possible methane adsorption site on Ni (111) surface. The atop site was widely calculated as the most stable CH_4 adsorption location (Yang & Whitten 1992; Burghgraef et al., 1994; Kratzer et al., 1996); however, the energy difference between different physisorption sites were so small (Lai et al., 2005) that the actual CH_4 adsorption site still not very confident. Ferreira et al. (2003) found that the CH_4 molecule preferred to adsorb on the three-fold site of the Ni (111) with three H atoms pointing to three Ni atoms. Lee et al. (1987) proposed a pyramidal transition state configuration in which three hydrogen atoms and one carbon atom were within the same plane parallel and close to the nickel surface. Yang & Whitten (1991) studied the chemisorption of CH_3 on Ni (111) surface and found that the CH_3 radical adsorbs on the nickel 3-fold sites (fcc or hcp) preferably. The optimized methyl hydrogen plane was found to be parallel to the nickel surface with H's pointing toward the nearest Ni atoms, and Ni-C distance of 2.35 Å. Kratzer et al. (1996) also found that the three-fold site was most stable for CH_3 adsorption on Ni(111), but the C-H bonds have stretched into 1.18 Å and the HCH angle at around 100^o. Yang and Whitten (1989) found that CH_2, CH or H adsorbed on Ni(111) threefold or bridge sites strongly. Using DFT-GGA method Kratzer et al (1996) calculated the binding energy of H on Ni (111) fcc hollow site (277 kJ/mol) which was found close to the experimental data (264 kJ/mol).

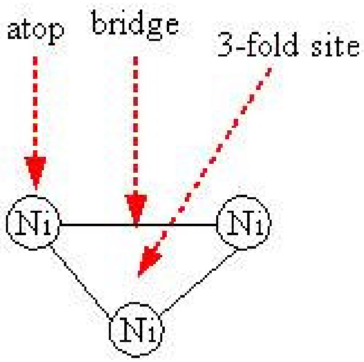

Figure 2.4 Possible methane adsorption sites on Ni (111) surface

Nowadays, all the simulated energy barriers for 1st methane C-H cracking were found to be much higher than the molecular beam experimental data measured by Lee et al. (51 kJ/mol) (Lee et al., 1987) and Beebe et al. (53 kJ/mol) (1987). Using Ab initio valence orbital configuration interaction calculations and cluster model Yang and Witten (1992) found the lowest methane dissociation energy barrier of 71 kJ/mol. Density functional theory (DFT) on a Ni_7-clsuter model resulted in a barrier of 214 kJ/mol and the barrier decreased to 121 kJ/mol for a Ni_{13}-cluster (Burghgraef et al., 1994). DFT calculations with 2-layer slab model resulted in a barrier of 127 kJ/mol (Bengaard et al., 1999) and a larger computational cell with 4-layer or 5-layer slab resulted in a lower barrier (~ 100 kJ/mol) (Kratzer et al., 1996; Bengaard et al., 2002). Those theoretical simulations essentially used the same methane 1st C-H cracking pathway that the molecular CH_4 adsorbed and dissociated on-top of a single Ni atom (1-fold or atop site) followed by the diffusion of the resulted CH_3 and H species in opposite 3-fold sites next to this Ni atom. During the whole reaction process, the C atom has to shift from the 1-fold site into the adjacent 3-fold site, which brought in high energy barrier since the mass of a C atom is much higher than an H atom. In addition, the calculations about the physical adsorption of a CH_4 molecule on the nickel surface found that the adsorption energies at different sites (atop, bridge, or 3-fold site) were very small and the adsorption energy difference at different sites was even less than the error bar of the employed calculation method, therefore, it is really not necessary for CH_4 to be adsorbed on the 1-fold site.

Because the energy required to directly crack the C-H bond of CH_4 was very high (~ 418 kJ/mol), the methane molecule must be distorted from its tetrahedral configuration before the dissociation took place. Three decades ago, Winters (1976) explained the kinetic isotope effect (the sticking coefficients ratio of CH_4 to CD_4) on tungsten surface via the hydrogen tunneling mechanism. Lee et al. (1987) ascribed the large magnitude of kinetic isotopic effect on Ni (111) into the hydrogen tunneling mechanism although the one-dimensional model was found difficult to explain the isotopic effect accurately. Luntz and Harris (1991 & 1992) argued that the tunneling mechanism with multi-dimensions can explain all the reported methane dissociation experimental results. Because the translational energy, vibrational energy and surface phonon were strongly coupled during the methane dissociation process, the tunneling mechanism has to use multi-dimensions to explain the experimental data accurately; nevertheless, the H tunneling mechanism suffers from the unknown potential barrier and height and at highly activated situations when the given energy was above the dissociation barrier the tunneling process became unimportant and the traditional transition state theory can provide an approximation to the dissociation process (Luntz, 1995).

The destruction of nickel catalyst was generally believed to be caused by carbon whisker (long carbon filaments) encapsulating the catalytic Ni particle. The filamentous carbon has high strength and may lead to the breakdown of the catalytic metal. The deposited carbon and the degraded catalyst may cause the blockage of the gas transport channels within the catalyst (Rostrup-Nielsen, 1993). The encapsulated graphitic carbon greatly inhibited the contact of Ni particles with methane and thus deactivated the catalyst. The nickel particle size and morphology have significant effect on the accumulated carbon yield before deactivation (e.g., larger spherical particles have lower carbon yield) (Li et al., 2006). The commonly accepted filament formation mechanism consists of: (1) formation of carbon adatoms on the nickel surface, (2) dissolution of the surface adsorbed C atoms into the nickel bulk lattice, and (3) carbon diffusion and precipitation in the form of filament (Larsen & Chorkendorff, 1999; Holstein, 1995). The driving force for carbon diffusion may be the carbon concentration gradient (Alstrup, 1988; Holstein, 1995). The rate-determining step of the coke formation was generally considered to be the carbon diffusion through the catalyst particle at low temperature and surface reactions may play an important role at high temperature. Several methods, such as doping the nickel surface with sulfur, Cu, and Au (Kratzer et al., 1996), have been proposed to delay the carbon filament formation via decreasing the carbon formation rate on the nickel surface. Addition of K^+ into the support was also found to improve the Ni stability (Juan-Juan et al., 2006).

2.3.2 Ceramic oxygen-electrolyte membrane reactor for methane partial oxidation into syngas

The ceramic oxygen-electrolyte membrane (COMR) has a thin or thick dense oxygen-electrolyte ceramic layer having both oxygen ionic and electronic conductivity (i.e., mixed conductivity) are recently becoming of great interest, inasmuch as their potentials as economical, clean, and efficient means of producing pure oxygen from air.

2.3.2.1 Oxygen permeation mechanism

The driving force for the oxygen transport through the COMR is the partial oxygen pressure difference at two sides of the membrane. Figure 2.5 showed the schematic diagram of oxygen transport mechanism through a COMR.

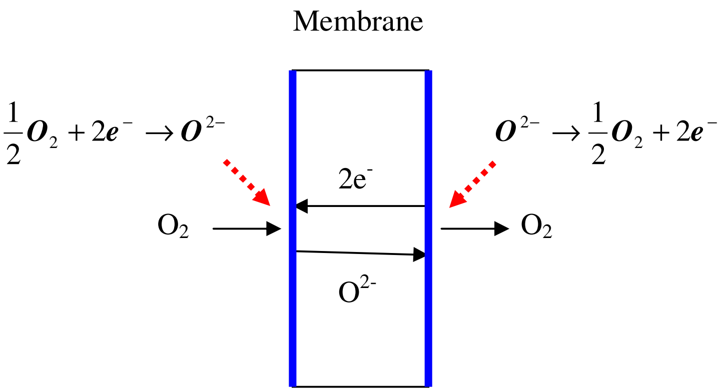

Figure 2.5 Oxygen transport mechanism through a COMR

At the upstream oxygen membrane interface, the oxygen is reduced by the surface electrochemical reduction ($\frac{1}{2}O_{2(g)} + V_O^{\cdot\cdot} + 2e' \rightarrow O_O^x$). Sirman & Kilner (1996) separated this surface oxygen incorporation process into three sequential elementary steps, i.e., adsorption ($\frac{1}{2}O_{2(g)} \rightarrow O_{ad}$), charge-transfer ($O_{ad} + 2e' \rightarrow O_{ad}^{2-}$) and incorporation ($O_{ad}^{2-} + V_O^{\cdot\cdot} \rightarrow O_O^x$). At the downstream membrane-gas interface, a reverse surface oxidation reaction takes place releasing the oxygen gas ($O_O^x \rightarrow \frac{1}{2}O_{2(g)} + V_O^{\cdot\cdot} + 2e'$). To maintain the electronic neutrality within the COMR, the negative electrons migrate along reverse direction to the oxygen ions. A dense COMR has nearly infinite permselectivity since other types of gases such as N_2, CO_2, and H_2 in the airside can not be reduced into ions and thus do not transport through the membrane.

From Eq. (2.4), one can see that the oxygen permeability is related to oxygen ionic and electronic conductivity; provided that the transport within the membrane is the rate determinate step. High conductivity normally results in high oxygen flux and for a given total conductivity (i.e., the summation of ionic and electronic conductivity) the oxygen flux is maximum when ionic and electronic transference numbers are equal (i.e., the transferred oxygen ions can be balanced immediately by the reversely migrated electrons).

2.3.2.2 Fabrication of asymmetric ceramic oxygen-electrolyte membrane

The asymmetric configuration of COMR (especially the tubular structure), in which a thin dense reactive oxygen-electrolyte membrane layer is coated on the surface of a thick porous support, has become the desired model in pursuit of both high oxygen permeability and membrane stability. Decreasing thickness of the reactive membrane until to its characteristic length would enhance the oxygen permeability significantly. A thin active membrane layer could be kinetically favorable to maintaining the chemical stability of membrane at reducing environment since the limited bulk oxygen transport rate is responsible for the unwanted chemical reductions at the membrane surface.

The technologies to deposit a thin dense ceramic film on the surface of a dense or porous substrate have been reviewed by Will et al. (2000). The methods coating a dense ceramic layer on a dense or porous substrate surface can be classified by the nature of the employed materials, i.e., gas phase methods such as chemical vapor deposition (CVD) (Abrutis et al., 2004), physical vapor deposition (PVD) (Besland et al., 2006), electrochemical vapor deposition (EVD) (Isenberg, 1981), spray pyrolysis (Setoguchi et al., 1990) and laser ablation (Endo et al., 2000), liquid phase processes such as sol-gel (Chen et al., 1994), and solid phase methods such as colloidal suspension coating (Lenormand et al., 2005), electrophoretic deposition (EPD) (Kaya et al., 2005), screen-printing (Chu, 1992) and tape casting (Montinaro et al., 2006). Generally, the gas phase techniques have high deposition quality but need expensive equipment or process, while the liquid or solid phase methods are economical but have poor deposition quality or poor repeatability due to the large shrinkage associated with the removal of liquid phase or solvent. To obtain a dense film, the low-cost liquid or solid phase methods usually need to go through a subsequent co-firing process, after which the coated thin layer becomes dense.

The porosity of the anode should be around 30 vol.% at least to allow the diffusion of the gas to the reaction interface (Boaro et al., 2003). The conventional Ni-YSZ anode can be fabricated by simply reducing the NiO into metallic Ni after high temperature sintering of the NiO-YSZ cermet. At high NiO loading (≥ 50 wt.%), the required porosity of the Ni-YSZ anode can result from the reduction of NiO powders (Du & Sammes, 2004). Kim et al. (2002) fabricated highly porous Cu-YSZ by leaching the nickel out of the Ni-YSZ cermet with nitric acid followed by Cu impregnation. A porous YSZ substrate can also be formed by sintering the mixture of YSZ and pore former (such as graphite and PMMA) (Gorte et al., 2004). Gorte et al. (2002 & 2004) and Lu et al. (2002) fabricated Cu-YSZ cermet via impregnation of the porous YSZ layer with aqueous $Cu(NO_3)_2$ solution. The Cu-based anode can eliminate the carbon formation (Park et al., 1999 & 2000) and has high sulfur tolerance (He et al., 2005), which are the two major issues for Ni-based anode for the application as SOFCs.

Dip coating is a conventional technique to prepare a thin layer of dense ceramic membrane (0.1 ~ 100 μm) on a porous ceramic support (Gu & Meng, 1999). When a dry porous ceramic support is dipped into and subsequently withdrawn from a ceramic suspension, a wet ceramic cake, whose thickness is proportional to the square root of the dipping time (Pan et al., 2003), can be formed due to the capillary force caused by the porous substrate. After the solvent evaporation, organic materials burning off, and ceramic sintering, a layer of ceramic membrane is achieved; however, additional chemical or physical treatment (Hong & Chua, 2002; Hong et al., 2001) is often necessary to turn this thin layer gas-tight. It has been reported that the metals or their alloys, whose melt point is close to the sintering temperature, facilitate densification of the ceramic membrane and thus improve the mechanical properties of the resulted membranes (Hong et al., 2001). It is also reported that an under-pressure in the fiber bore during dipping can increase the thickness of the coated ceramics (Pan et al., 2003).

Compared to asymmetric tubular ceramic membrane, planar structure is technically easier to realize, however the planar membranes has limited application prospective in terms of having difficulties for scaling up and significant edge leakage effect (Du & Sammes, 2004). Since Siemens Westinghouse's work to assemble a SOFC by laying a dense YSZ oxygen electrolyte membrane, via the expensive electrochemical vapor deposition (EVD) procedure, on a tubular porous cathodic support (Isenberg, 1981), looking for cost-effective techniques to achieve the same goal has been a challenge to the development of commercial COMR. The vacuum-assisted spray deposition method forming a dense ceramic layer on a tubular porous support has been developed (Ritchie et al., 2001) despite it is highly energy consuming due to the involved multiple-sintering steps. Cracks are easy to form during the drying or sintering process for the dip coating technique (Du & Sammes, 2004). The sol-gel coating technique (Puetz et al., 2003) is a low temperature process with relatively low fabrication cost, but it is very difficult when using this method to be rid of crack formation or nano-sized pores in a coating layer during drying and burning treatment, especially when such a coating is developed on a tubular support. In conclusion, it is still a challenge to obtain an asymmetric tubular COMR with low cost method.

2.3.2.3 Ceramic oxygen-electrolyte membrane reactor coupling air separation and methane reforming

The POM process requires large quantities of pure oxygen which was traditionally generated by expensive cryogenic process. A COMR coupling the N_2/O_2 separation with methane reforming decreases the POM cost significantly and makes it possible to build house-sized methane conversion plants to replace the conventional billion-dollar big syngas plant (Amato, 1993). Figure 2.6 shows how an asymmetric COMR converts methane into syngas. In the porous cathode, the oxygen gas is reduced into O^{2-}, which selectively diffuses through the non-porous oxygen electrolyte and reacts with the CH_4 gas in the porous catalyst-containing anode. The electrons accumulated at the anode need to be transported into the cathode via the electrolyte as shown in Fig. 2.6. For a SOFC, the dense electrolyte layer is only oxide ion conductive and the electrons are transported through external circuit.

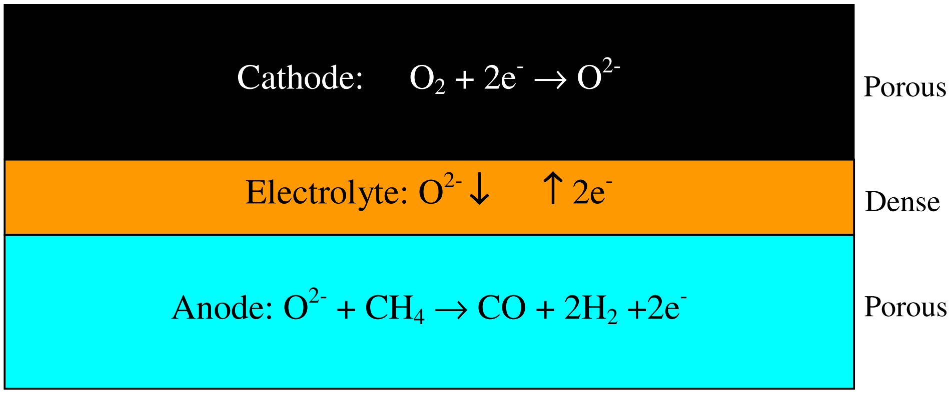

Figure 2.6 Schematic diagram of an asymmetric COMR

The concept of COMR for catalytic reforming of methane into syngas has been proposed in early 1990s. Lots of studies in this area have been done by Air Products, BP-Amoco and Praxair, in hundred-million-dollar projects (Lin, 2001). Since the BP's invention of the Electropox process, a COMR partially oxidizing methane into syngas (Mazanec et al., 1992), endeavors have been tried to improve the POM yield or stability, to decrease the COMR fabrication cost by synthesis new active membrane materials or developing new membrane structures or fabrication methods. Good stability, high oxygen flux, and low fabrication or material cost are basic requirements for a viable COMR. Unfortunately, materials having both high oxygen flux and stability have not been found so far and a "trade-off" between the oxygen permeation and the stability may exist. Most of the MIECs with high oxide ionic conductivity (e.g., $La_xSr_{1-x}Co_yFe_{1-y}O_{3-\delta}$ perovskite-type oxides) are thermodynamically unstable under reducing environment. Some MIECs, such as $SrFeCo_{0.5}O_{3-\delta}$, $Ba_{0.5}Sr_{0.5}Co_{0.8}Fe_{0.2}O_{3-\delta}$, $La_xSr_{1-x}Fe_yGa_{1-y}O_{3-\delta}$ and $La_2Ni_{0.9}Co_{0.1}O_{4+\delta}$, were reported to have high stability; however, their stability, especially the stability under industrial application condition, remains to be further confirmed.

$SrFeCo_{0.5}O_{3-\delta}$ includes several phases such as 236, perovskite-phase, rock-salt, and spinel phases (Ma & Balachandran, 1997; Mitchell et al., 2002). Balachandran et al. (1995 & 1997) demonstrated an extruded $SrFeCo_{0.5}O_{3-\delta}$ membrane tube for POM over 1000 h at 850 ^{o}C in small lab scale; however, the phase composition of the material was found to depend significantly on its synthesis route and conditions (Deng et al., 2004). $Ba_{0.5}Sr_{0.5}Co_{0.8}Fe_{0.2}O_{3-\delta}$(BSCF) was studied by Shao et al. (2000) and Wang et al. (2003). The fabricated BSCF was used to fabricate a symmetric COMR and demonstrated to be a good candidate membrane material for air separation (Shao et al., 2000). After catalyzing POM at 850 ^{o}C for 500 h no crack within the COMR was found (Shao et al., 2001; Wang et al., 2003); however, the H_2-TPR analysis showed that the BSCF itself is unstable under the reducing environment (Shao et al., 2001). K_2NiF_4 structure type $La_2Ni_{2-x}B_xO_{4+\delta}$ (B = Co, Cu, Fe, or other types of transition metals) compounds have relatively high stability due to their nature of oxygen excess. Kharton et al. (2004) reported that the stability of $La_2Ni_{0.9}Co_{0.1}O_{4+\delta}$ satisfied the POM process up to 800 ^{o}C; however, La_2NiO_4 was found to decompose into La_2O_3 and Ni upon exposing to CH_4 at high temperature (Zhu et al., 2003).

In conclusion, the materials with both high mixed (O^{2-} and e^{-}) conductivity and stability still have not been found. The fabrication of asymmetric tubular COMR presents a good way to obtain both high oxygen permeation and stability; it is still a challenge to fabricate an effective asymmetric tubular COMR using low cost methods.

Chapter 3 Rheological study of ceramic-polymer blend

In this Chapter the CeO_2-polyethylene glycol (PEG) blend was selected to study the viscous flow behavior of ceramic-polymer composite under low shear rates. The blend containing as high as 41.6 vol.% of CeO_2 can still exhibit Bingham plastic response. Hence, the relative viscosities (η_{rel}) of the CeO_2–PEG mixtures with various volume fractions of CeO_2 (ϕ) could be obtained at different temperatures, and these data were then used to simulate the rheological model developed. The model was created by assuming that there are two primary forces governing the rheological behavior of the blend, i.e., the van der Waals attractive forces among CeO_2 particles and the adsorption of PEG segments on the surface of CeO_2 particles. The simulation turned out that this model matches more precisely the experimental data than the three widely quoted models. Furthermore, the CeO_2-PEG interactions have also been examined by scanning electron microscopy (SEM), X-ray diffraction (XRD), Fourier transform infrared spectroscopy (FTIR), and differential scanning calorimetry (DSC).

3.1 Introduction

Extrusion is the most widely employed technique to produce green ceramic-polymer tube (Section 2.2.2 of Chapter 2). Rheology of a polymer melt including ceramic particles is far cry from that of the pristine polymer phase. Viscous behavior of a ceramic-polymer blend has significant effect to the extrusion process and the quality of an extruded green tube. The details of the ceramic-polymer blend rheology and the interactions between polymer and ceramic particles have been reviewed in Section 2.2.1 of Chapter 2. Up to now, several empirical or semi-empirical models describing the relationship between the relative viscosity (η_{rel}) of the blend and the solid powder volume fraction (ϕ) have been developed. The most widely used models include Eilers' equation (Eq. 2.18 in Chapter 2), Mooney model (Eq. 2.19 in Chapter 2), and Krieger-Dougherty Model (Eq. 2.20 in Chapter 2). These commonly used models were found fitting poorly with our measured experimental $\eta_{rel} \sim \phi$ data; therefore, a new mathematical model based on the two important interactions, i.e., PEG adsorption on the ceramic powder surface and the van der Waals (vdw) attractive forces between the powders, was proposed and used to fit the experimental data in this study.

There are several approaches which have been developed to prepare a ceramic-polymer paste (Section 2.2.2 of Chapter 2). In this work the solution mixing process, in which the polymer was dissolved in D.I. water and mixed with ceramic powder followed by drying, was chosen to prepare the CeO_2-PEG blends mainly due to the fact that it is a simple and effective way to the preparation of extrusion feedstock. Environmental friendly PEG has a low and sharp melting point, surfactant-like property and ease of being burned out, these are also the merits of a desired polymer binder (Venkatarman et al., 2001). In addition, ceria or doped ceria has high oxide ionic conductivity (Section 2.1.2.2 of Chapter 2). Therefore, the CeO_2-PEG blend was selected as a model system to study the rheology of the ceramic-polymer composite.

3.2 Experimental

3.2.1 Chemicals

Cerium (IV) oxide (CeO_2) powder with average particle size of about 4.8 μm was purchased from Strem Chemicals (USA). PEG15000 (polyethylene glycol, average M_w: 15000, Merck), PEG400 (polyethylene glycol, average M_w: 400, Nacalai Tesque, Inc.) and Tween®-80 (polyoxyethylene-20 sorbitan monolaurate, Aldrich) were used as binder, plasticizer and lubricant, respectively. All the above chemicals were used as received.

3.2.2 Preparation of CeO_2-PEG blend

Solution mixing method was employed to fabricate the CeO_2-PEG blends. At room temperature, CeO_2 powder (200 g/l) was dispersed in an aqueous solution containing PEG400 and Tween®-80 under continuous magnetic stirring (~ 600 rpm). After mixing for 20 min, the resulting suspension was added into aqueous PEG15000 solution (20 g/l) with stirring. The slurry was stirred (~ 600 rpm) at room temperature for 4 h followed by heating to 80 ^{o}C and evaporating the water till when the magnetic stirring became stuck. The concentrated slurry turned was manually stirred with glass rod while it was cooled down to room temperature. The remaining wet CeO_2-PEG solid was dried under vacuum for at least 72 h at room temperature to obtain the desired blend for rhelogical study. Several CeO_2-PEG compositions were formulated by varying the content of CeO_2, which are listed in Table 3.1. The rheological study (shear stress vs. shear rate) was carried out by examining only the blends without containing the surfactant Tween®-80.

Table 3.1 Composition of the CeO_2-polymer pastes

Chemical	Function	Content[a]
CeO_2	Ceramic powder	1-80 wt.% (0.18-41.6 vol.%)
PEG400	Plasticizer	5 wt.% of CeO_2
PEG15000	Binder	Variable
Tween®-80	Lubricant	Variable

[a] The mass densities of CeO_2 (ρ = 7.3 g/cm^3) and PEG (ρ = 1.3 g/cm^3) were used to calculate vol.% of CeO_2.

3.2.3 Rhelogical investigation

Measurements of the steady-state viscosity were performed by using a Brookfield viscometer (Brookfield DV—II). The fabricated CeO_2-PEG blend was loaded in a tubular aluminum sample holder, which was then placed in the accessory micro-oven. The measurement was conducted at temperatures above the melting point of PEG.

3.2.4 Differential scanning calorimetry studies

DSC analysis of the CeO_2-PEG blend was performed on the METTLER TOLEDO STAR DSC-821 scanning calorimeter in the temperature range from 25 to 100 ^{o}C. The measurement procedure included heating the sample to 100 ^{o}C (at the rate of 10

^{o}C/min), and subsequently cooling it down to 25 ^{o}C (at the rate of -10 ^{o}C/min) to ensure all the samples under investigation have the same thermal history. The DSC data (T_g and T_m) were collected from the second scanning.

3.2.5 Other instrumental characterizations

XRD analysis was employed to examine the crystallization behavior of CeO_2-PEG mixture. The analysis was carried out on a SHIMADZU XRD-6000 diffraction meter using Cu-K_α radiation (λ = 1.54056 Å) with the scanning speed of 2.5 ^{o}/min. The scanning angle was set from 10 and 80 degree. The adsorption of PEG on CeO_2 was identified by the infrared spectra of PEG obtained from a Bio-Rad FTIR FTS135 spectrometer. For this characterization, only PEG15000 was employed to form the blend with CeO_2. The morphology of the CeO_2-PEG blend was observed on a SEM instrument (JEOL JSM-5600).

3.3 Results and discussion

3.3.1 Adsorption and van der Waals attractive forces in CeO_2-PEG blend

When the content of CeO_2 powder in the blend was raised to the comparable or higher level than that of PEG phase, the PEG phase becomes a jacket of CeO_2 particles (Fig. 3.1). This phenomenon shows that PEG wets CeO_2 surface well and hence a thorough mixing of both achieves readily. Likewise, XRD (Fig. 3.2) characterization proved that the crystallinity of PEG phase dropped drastically even at a rather low volume fraction of CeO_2, i.e. $\phi = 7.1$ vol.%. It could be ascribed to the strong adsorption tendency of PEG segments onto the surface of CeO_2 particles, namely the orderly folding of PEG chains (crystallization) became difficult in the adsorption layer.

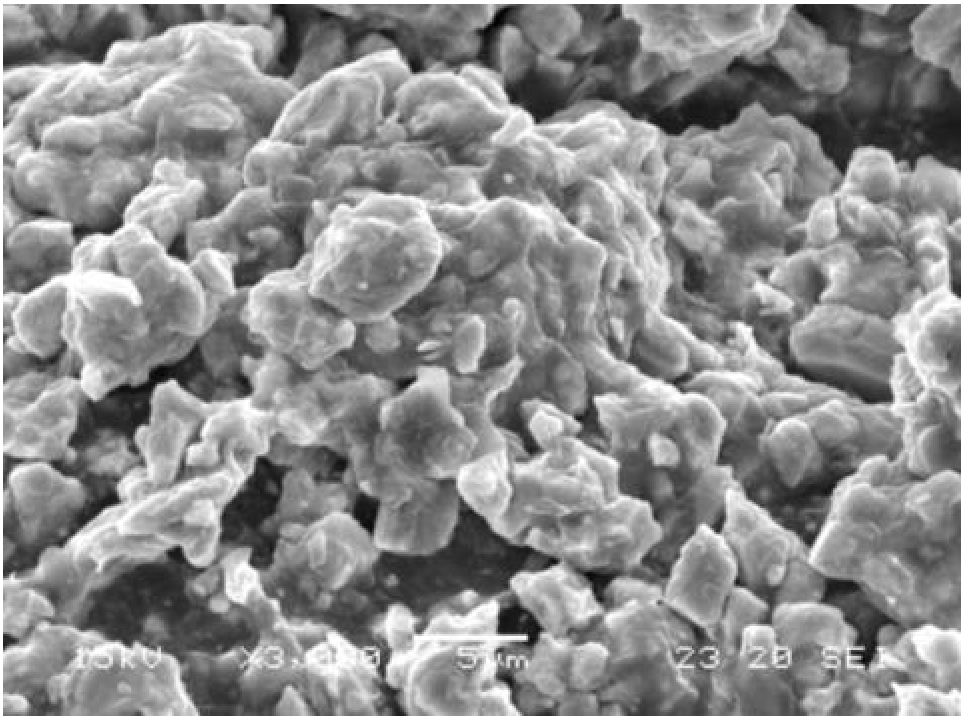

Figure 3.1 SEM of PEG-CeO_2(50 vol.%) blend

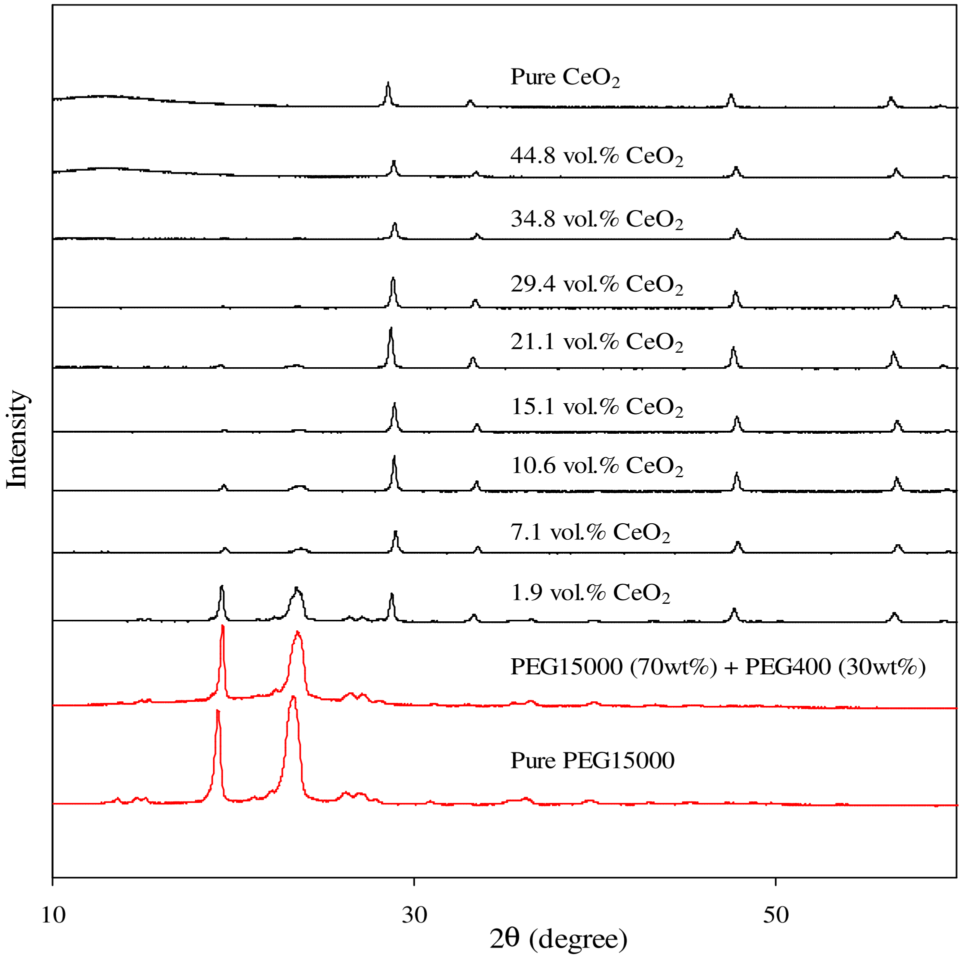

Figure 3.2 XRD of the CeO_2-PEG blends with different CeO_2 loadings

From the SEM image (Fig. 3.1), the rifts between particles were smaller than the sizes of CeO_2 particles. With this aspect ratio, the vdw attractive forces between CeO_2 particles became inevitable. As far as this type of surface-surface interaction is concerned, Myers (1991) used an ideal model to describe the situation: two identical spheres of radius R_s are separated in vacuum by a distance H, when $H/R_s << 1$, the free energy of attraction per unit area is approximated by

$$\Delta G^{att} = -(A_H R_s/12H)[1 + (3/4)H/R_s + \text{higher terms}] \qquad (3.1)$$

where $A_H = (3/4)h\nu\alpha_0^2\pi^2N^2$ is the Hamaker constant in vacuum (α_0 is the electronic polarizability of the atoms, $h\nu$ is related to the first ionization potential of the atoms, and N is the number of atoms in unit volume of the spheres.) When the two particles (surface) are separated by a medium, $A_H{}^{eff}$ is used in lieu of A_H to approximate such a more complex system, where $A_H{}^{eff}$ takes a mathematic form including the Hamaker constants of the two phases. Despite the fact that Eq. (3.1) could describe far precisely from the free energy existing between CeO_2 particles in the blend due to geometric and compositional irregularities, it still does not lose the sense of being the ground for studying real systems. The free energy of inter-particle attraction is a crucial factor affecting the rheological responses of the composition with high CeO_2-loadings (ϕ) to shear stress.

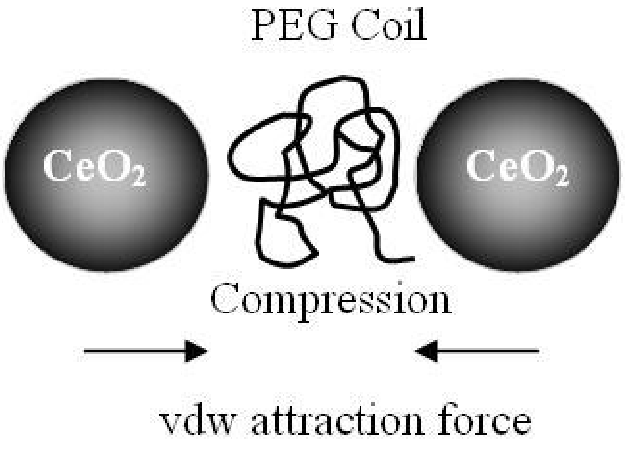

Figure 3.3 Schematic illustration of compressive effect on PEG coils

The inter-particle attraction is considered to generate compressive force on the PEG chains (Fig. 3.3). FTIR spectra of the PEG-CeO_2 mixtures furnish the evidence to this theoretical inference (Fig. 3.4). The useful information from the FTIR analysis is the vibration absorption band of the C-O-C bond at 1112 cm^{-1}; this band became blunt when the CeO_2 loading reached 7.1 vol.% from 1.9 vol.%, and after that, the band resumed somewhat its original shape with the increasing of CeO_2 content. This phenomenon can be understood by both the effects of inter-particle attraction and adsorption of PEG on CeO_2 surface. Under the compression of CeO_2 particles, the bond angle of C-O-C of PEG segments would engage a certain extent of deformation, which caused changes in its stretching modulus and therefore in the shape of C-O-C IR absorption band. Although the compression on PEG became more severe with increasing ϕ of CeO_2 particles, the PEG molecules adsorbed on CeO_2 surface, on the other hand, countered the deformation of bond-angles due to the “fixation” effect. The number of adsorbed PEG molecules increased with increasing CeO_2 loading in the blend, and as a result, the IR band of C-O-C vibration reflected the molecular conformation of this portion of molecules, which look more like free PEG molecules.

In addition to the XRD investigation, coherent message about structural changes of the PEG phase due to adsorption on CeO_2 particles can also be acquired from the DSC analysis. The two blends composed of 41.6 vol.% CeO_2 and the PEG phase (consisting of PEG15000 and PEG400) were employed as the typical samples to exhibit the occurrence of strong physical adsorption (Fig. 3.5). Compared with the single PEG phase (a mixture of PEG15000 and PEG400), the PEG phase in both blends displayed higher melting temperatures. It was an indication that the adsorption “bonding” restricted segment motions, e.g. rotations and creeps of PEG macromolecules, as what the “fixation” refers to above. Moreover, the two different preparation procedures (solution versus fusion) also gave rise to different thermal response of the PEG phase, which revealed that the solution blending procedure resulted in a more thorough mixing blend because of higher T_g, which is ascribed to the existence of higher PEG-CeO_2 interface in the blend.

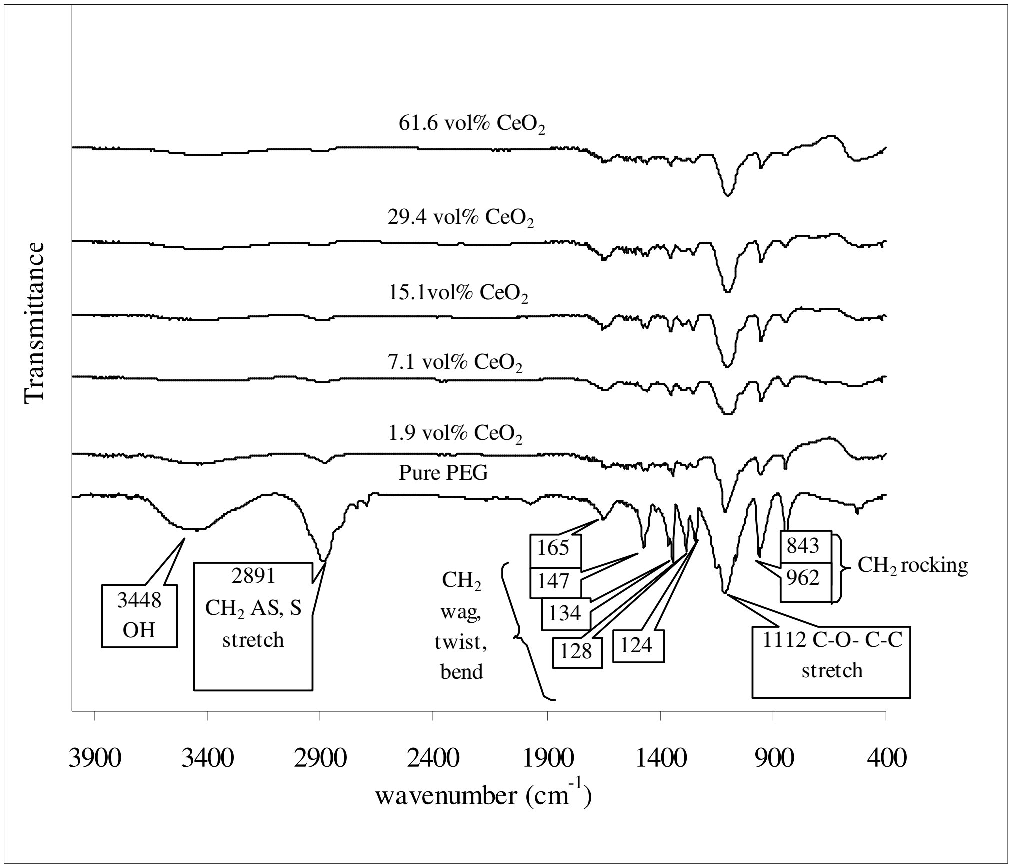

Figure 3.4 FTIR of CeO_2-PEG blends with different CeO_2 loadings

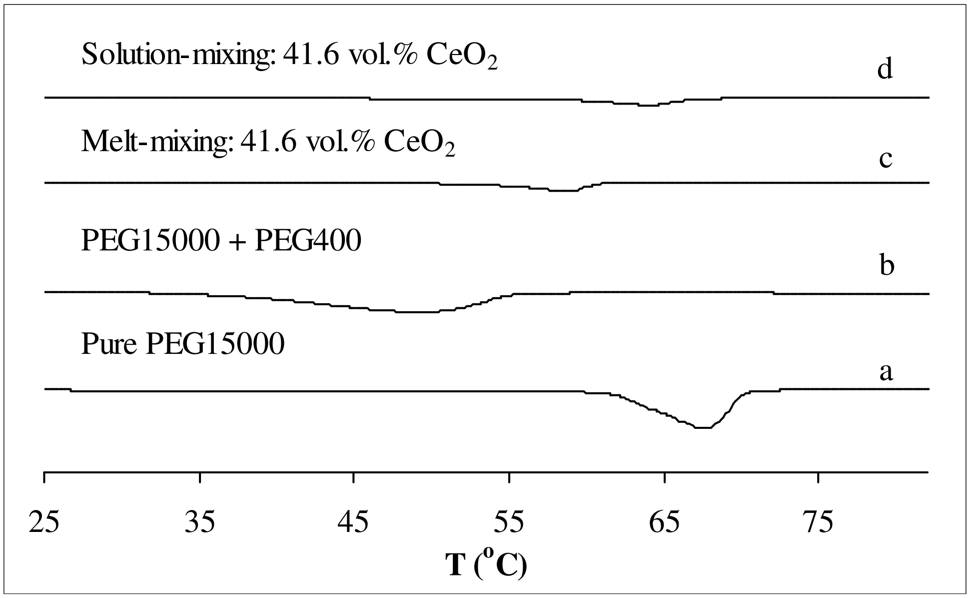

Figure 3.5 DSC of: (a) pure PEG; (b) PEG15000 (80 vol.%)-PEG400 blend; (c) mixture of PEG blend and CeO_2 (41.6 vol.%) made by melt mixing method; (d) mixture of PEG blend and CeO_2 (41.6 vol.%) made by solution mixing method

3.3.2 Relative viscosity of the PEG-CeO_2 blend

The shear stress (σ)-strain rate ($\dot{\gamma}$) relationship of the melts of CeO_2-PEG blends with different ϕ of CeO_2 all displayed Bingham fluid behavior within the low shear stress range at various temperatures (Figs 3.6 a-c). With respect to temperature effect, the sample containing 21.1vol.% of CeO_2 showed a steady reduction of viscosity with raising temperature (Fig. 3.6a). With respect to the effect of CeO_2 loading at a fixed temperature, the higher the CeO_2 content the greater the viscosity was observed as expected; for this study two temperature points (140 °C and 160 °C) were examined (Figs 3.6 b & c). It is worthy to note that the viscosity of the blend containing 41.6 vol.% of CeO_2 became somewhat smaller than that of the blend with 21.1 vol.% of CeO_2 at 160 °C. This apparent drop in shear stress caused by raising temperature from 140 °C to 160 °C is deemed as the squeezing effect due to presence of the vdw attractive forces among CeO_2 particles. At 160 °C, the PEG phase became easier to free from inter-particle spaces in the blend with the higher CeO_2 content under the compression. In other words, the particle phase separation caused by raising temperature lowered down the activation energy of viscous flow. The trend revealed in this study represents a common fact that the mixing extent between a ceramic powder and a polymer phase decreases with increasing the ceramic content.

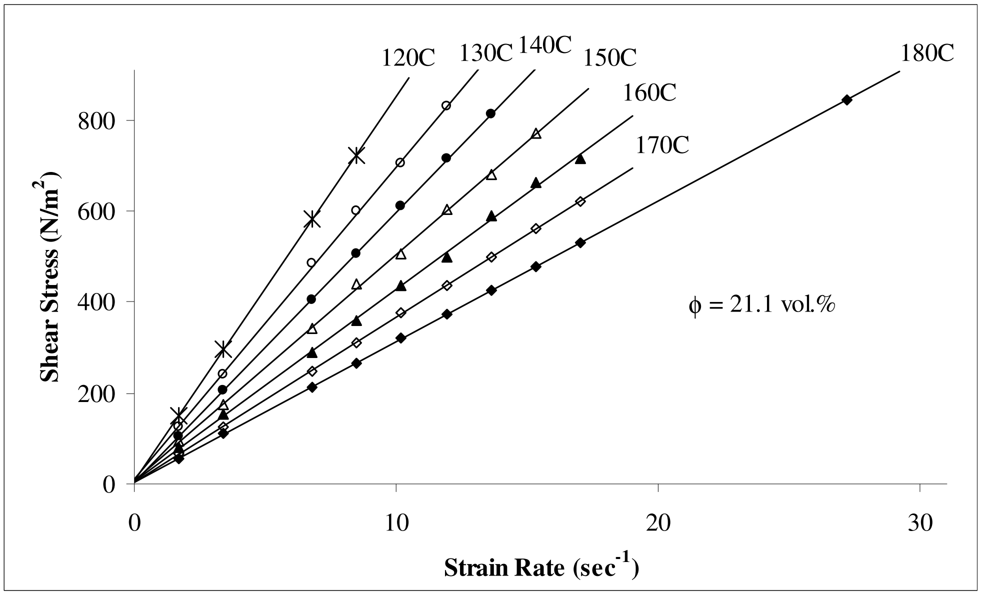

(a)

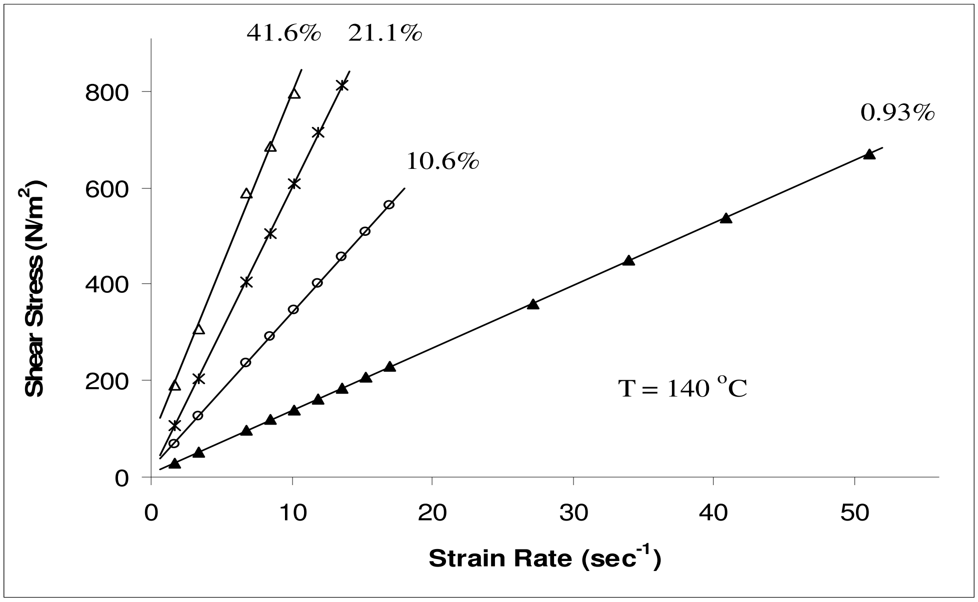

(b)

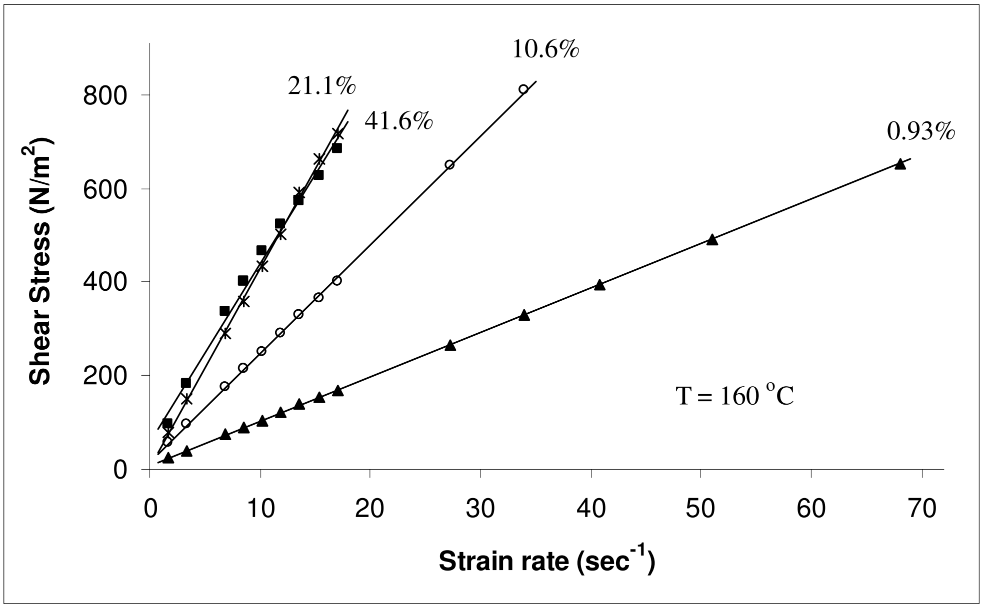

(c)

Figure 3.6 Dependence of shear stress (σ) on shear rate ($\dot{\gamma}$): (a) the PEG-CeO_2 (21.1 vol.%) blend at different temperatures (b) different CeO_2 loading at 140 °C; (c) different CeO_2 loading at 160 °C

The temperature dependence of apparent viscosity of the blend melt obeyed satisfactorily the Arrhenius relation (obtained based on seven or eight temperature points in the range of 100 ~ 180 ^{o}C). The activation energy barrier of viscous flow did not vary noticeably with the CeO_2 loadings below roughly 25 vol.% (Fig. 3.7), which meant that there was a slippery PEG layer between CeO_2 particles before this ϕ value. A sensible explanation would be the adsorption of PEG on CeO_2 particle surface, which induced free volumes surrounding particle surface through irregular screwing up of PEG chains (Fig. 3.8a). The further climbing up of the activation energy symbolized the formation of a physical network (Fig. 3.8b), in which the CeO_2 particles behaved as cross-linking points to make the viscous flow take place collectively.

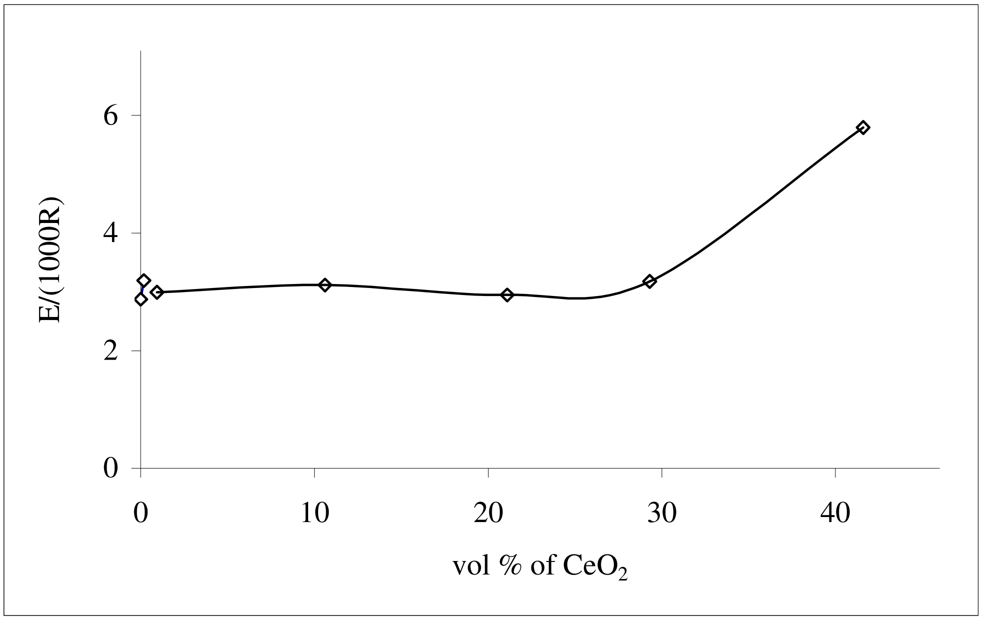

Figure 3.7 Dependence of the activation energy of viscous flow on the CeO_2 loading

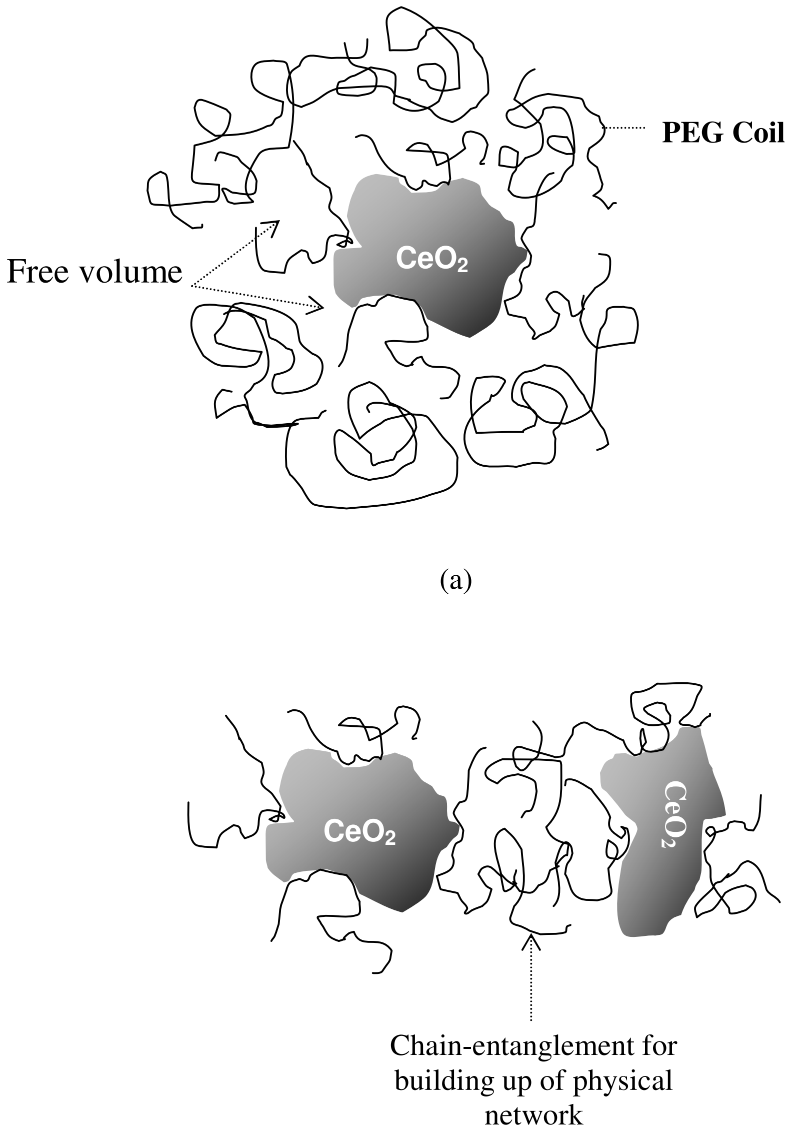

(a)

(b)

Figure 3.8 Schematic illustration of: (a) the generation of free volume at the interfacial boundary between PEG and CeO$_2$ particles; (b) the formation of the physical network due to adsorption

A mathematical model is established to express the rheological behavior of the CeO$_2$-PEG blend. The volume fraction of ceramic particles (ϕ) could be expressed by a simple mathematic formula that assumes the ceramic particles be hard spheres with identical radius of R and stacked with simple cubic structure:

$$\phi = \frac{\frac{4}{3}\pi}{\left(2 + \mathrm{L_D}\right)^3} \tag{3.2}$$

However, since CeO$_2$ particles have irregular shapes and are poly-dispersed, to satisfy the model, these irregular particles can be equivalent to a certain number of spheres with radius r on the basis of the unchanged surface area. As noted above, the H value is the boundary distance between two adjacent balls, $\mathrm{L_D}$= H/$\mathrm{R_s}$ is a dimensionless quantity signifying effective distance for vdw attractive forces. Equation (3.2) can thus be rewritten as:

$$\mathrm{L_D} = \left(\frac{4\pi}{3\phi}\right)^{\frac{1}{3}} - 2 \tag{3.3}$$

The Arrhenius relation was considered as a pertinent and succinct theoretical model to describe the particle effect on viscosity. Equivalently, this concept is applied hereby to express the relative viscosity $\eta_{\mathrm{rel}}^{vdw}$ of the CeO$_2$-PEG blend due to the vdw attraction force among CeO$_2$ particles:

$$\eta_{rel}^{vdw} = \frac{\eta}{\eta_0} = \frac{\boldsymbol{k}_1 \exp\left(\frac{\boldsymbol{E}}{\boldsymbol{RT}}\right)}{\boldsymbol{k}_0 \exp\left(\frac{\boldsymbol{E}_0}{\boldsymbol{RT}}\right)} = \boldsymbol{K}_r \exp\left(\frac{\Delta \boldsymbol{E}^{vdw}}{\boldsymbol{RT}}\right) \tag{3.4}$$

where E^0 is the energy barrier to the flow of Bingham plastic of the single PEG melt (comprising PEG15000 and PEG400), E is the energy barrier to the Bingham flow of the PEG (melt)-CeO_2 blend, k_1, k_0, and K_r are constants. Therefore, ΔE^{vdw} reflects the contribution of particle-particle interactions at a given temperature.

In the high-particle-loading blend, the vdw attractive forces act in the same way as the cross-adsorbed PEG chains to strengthen the network (or elastic) property of the blend, and then to impede the flow of PEG melt. From this perspective, ΔE^{vdw} can be correlated with the vdw attraction. Hamaker model (Hsu et al., 2003; Wennerström, 2003) describes the vdw potential (ζ) between two particles by the simple form:

$$\zeta = -\frac{A_H}{{L_D}^n} \tag{3.5}$$

in which A_H and L_D have been defined before, n is the parameter determined by the shape of particles.

$$\Delta E^{vdw} = -k'\zeta = \frac{k' A_H}{{L_D}^n} = \frac{A}{{L_D}^n} \tag{3.6}$$

The contribution of the particle-particle attraction component to retarding the viscous flow can be approximated by the linear relation between ΔE^{vdw} and ζ, k' is the proportional constant and has also the significance of the number of particle-particle pairs per unit volume. Combination of Eqs (3.3), (3.4) and (3.6) enables the vdw attraction to be mathematically related to the relative viscosity for the high CeO_2-loading blend.

$$\eta_{rel}^{vdw} = \exp\left\{ \frac{A}{\left[\left(\frac{4\pi}{3\phi} \right)^{\frac{1}{3}} - 2 \right]^{n} RT} \right\} \tag{3.7}$$

It is known that Einstein equation (Eq. 2.16) describes the hydrodynamic effect of the mono-dispersed hard spherical particles possessing a low volume fraction in the continuous medium. Since the CeO_2 particles used in the present real system are neither spherical ball nor mono-dispersed, the Einstein equation has to be modified by redefining its second terms:

$$\eta_{rel}^{ad} = 1 + B\phi \tag{3.8}$$

where B is the parameter including the effect of the surface area of CeO_2 particles which are the absorbent of PEG segments and therefore the cross-linking point of the physical networks formed. The physical cross-linking gives rise to a strong hydrodynamic drag on the flow of PEG melt (Fig. 3.8b). Moreover, B value also embraces the influences of irregular shape and different sizes of the CeO_2 particles on the viscosity. The superscript “ad” symbolizes the contribution of adsorption to the elastic component of the flow.

Consequently, the total relative viscosity (η_{rel}) of the blend should include both η_{rel}^{vdw} (Eq. 3.7) and η_{rel}^{ad} (Eq. 3.8) terms, which are corresponding to ΔE^{vdw} and ΔE^{ad}, respectively:

$$\eta_{rel} = \eta_{rel}^{ad} + \eta_{rel}^{vdw} - 1 = \exp\left\{ \frac{A}{\left[\left(\frac{4\pi}{3\phi} \right)^{\frac{1}{3}} - 2 \right]^{n} RT} \right\} + B\phi \qquad (3.9)$$

Fitting the model (Eq. 3.9) with experimental data ($\eta_{rel} \sim \phi$ at an assigned T and n) by using the linear least square method, we were able to determine the numerical values of A and B (Table 3.2). The fitted value of B is much higher than the corresponding parameter in the Einstein equation (Eq. 2.16). In contrast to the original Einstein model that considers only the mechanical resistance of individual hard spheres to the flow of the continuous fluid, the B value obtained from the simulation reflects the real resistance to the viscous flow due to the adsorption of a polymer layer on particles as well as the formation of the physical network. Values B determined at the three different temperatures (140, 150 and 160 ^{o}C) were rather similar. On the other hand, value A decreased sharply with increasing temperature, which suggests that the vdw attractive forces in the blend with a high ϕ are susceptible to temperature, in connection this conclusion with the preceding interpretation to the $\sigma - \dot{\gamma}$ response of the blend with $\phi = 41.6\%$ (in Fig. 3.6*c*), it is likely that agglomeration of CeO_2 particles due to loss of the PEG layer separating them is the reason for the reduction of A values.

Table 3.2 Parameter values of different models under different temperature

Model & Parameter		140 °C	150 °C	160 °C
Eilers (ϕ_m)		0.7546	0.8441	0.9678
Modified Eilers	k	3.2605	2.9257	2.6429
	ϕ_m	1	1	1
Mooney (ϕ_m)		0.7344	0.7801	0.8367
Modified Mooney	k	3.4023	3.1750	2.9653
	ϕ_m	1	1	1
Krieger-Dougherty (ϕ_m)		0.4825	0.5016	0.5265
Modified Krieger-Dougherty	k	4.4944	4.2085	3.9280
	ϕ_m	1	1	1
Our model (n=1)	A	15.9297	11.6915	4.8772
	B	14.8997	14.5144	14.4867
Our model (n=2)	A	111.273	85.5952	39.9812
	B	12.8593	13.0951	13.923

Figure 3.9 shows the experimental data and the simulated curves based on Eq. (3.9). This model fits well the experimental data. In comparison with the other three well-known models, they depart away from the experimental data more noticeably (Fig. 3.10). Table 3.2 lists numerical values of the parameters of these three models, which were obtained from simulating the experimental data. Each model had both single and double parameter forms; the latter one came from replacing the number of 2.5 with the parameter k, which was introduced as the crowding factor. This substitution led to the modified (or two-parameter) Eilers (Eq. 3.10), Mooney (Eq. 3.11) (Guyot et al., 2002) and Krieger-Dougherty Models (Eq. 3.12) (Quemada & Berli, 2002), respectively.

$$\eta_{rel} = \left(1 + \frac{k\phi}{1 - \frac{\phi}{\phi_{max}}}\right)^2 \tag{3.10}$$

$$\eta_{rel} = \exp\left(\frac{k\phi}{1 - \frac{\phi}{\phi_{max}}}\right) \tag{3.11}$$

$$\eta_{rel} = \left(1 - \frac{\phi}{\phi_{max}}\right)^{-k\phi_{max}} \tag{3.12}$$

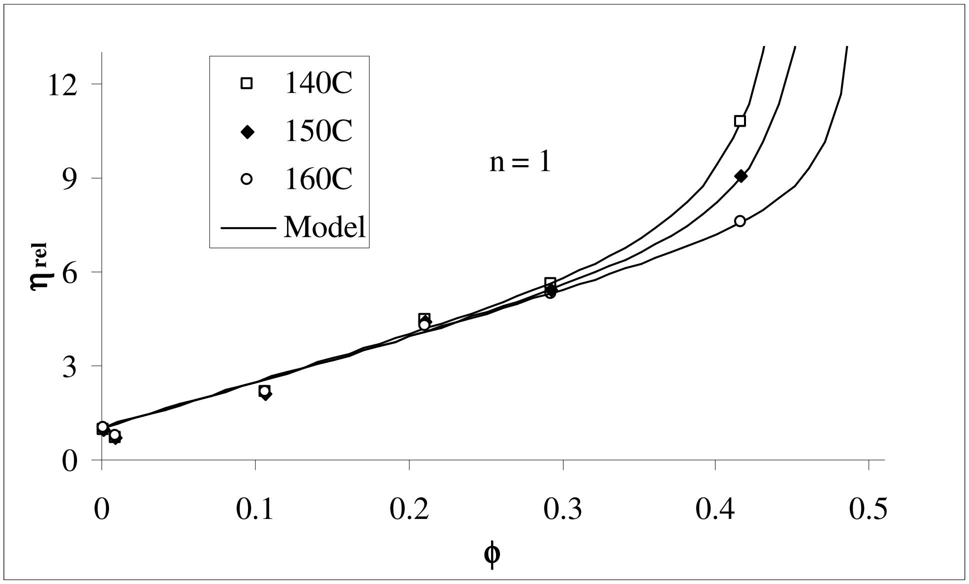

(a)

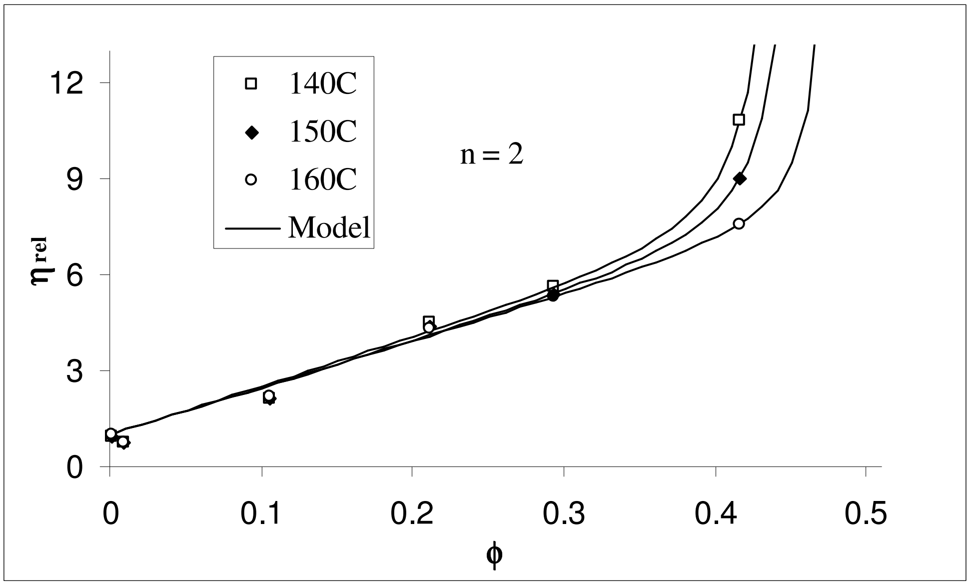

(b)

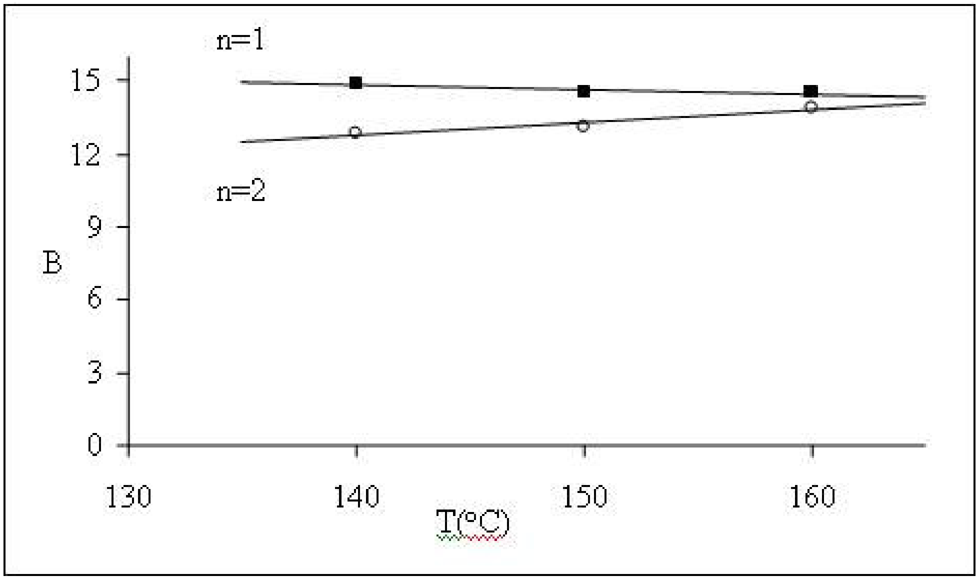

(c)

Figure 3.9 Demonstration of the fitting results of the model developed to the experimental $\eta_{rel} \sim \phi$ data at different temperatures: (a) the model assuming spherical CeO_2 particle shape (n = 1); (b) the model assuming rod-like CeO_2 particle shape (n = 2); (c) dependence of the simulated parameter value B on temperature

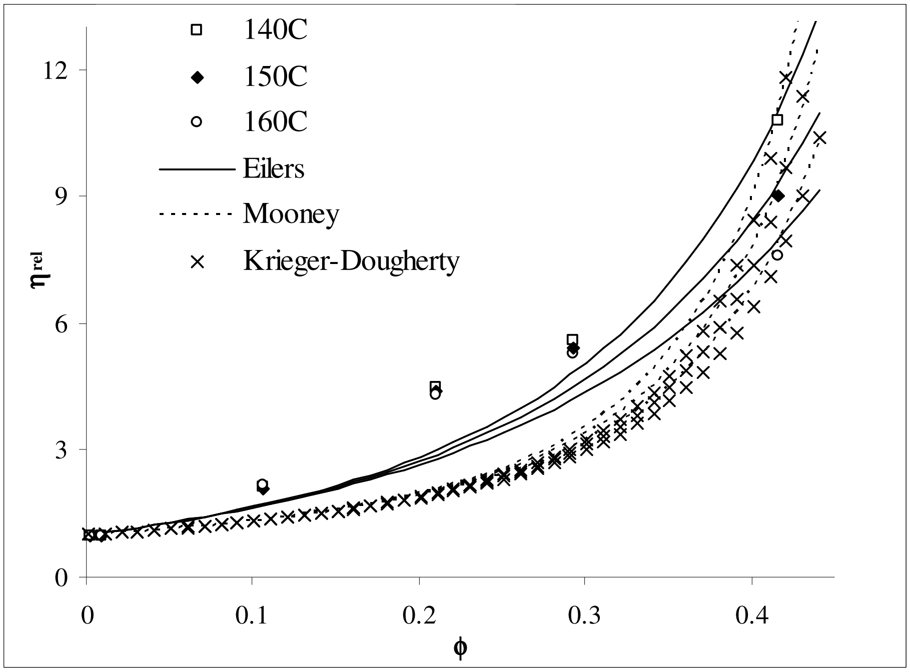

(a)

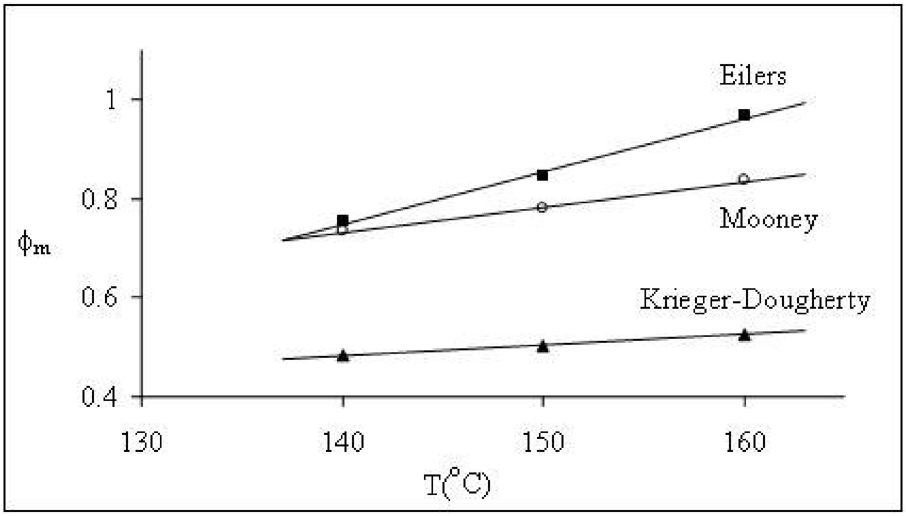

(b)

Figure 3.10 (a) Comparison of the fitting results of the three common models with the experimental $\eta_{rel} \sim \phi$ data at different temperatures. (b) Dependence of simulated parameter ϕ_m value on temperature

The modified models fit the experimental data slightly better than their corresponding un-modified models within the range of $0 < \phi_{\max} \leq 1$ (Fig. 3.11). A comparison among figures 3.9, 3.10 and 3.11 found that the model described by Eq. (3.9) portrays more closely the real roles of CeO_2 particles in affecting the viscous flow of PEG melt in the blend. The roles are divided as two respects: the vdw attractive forces among CeO_2 particles and the physical network that is contingent upon the adsorption of PEG segments on CeO_2 particle surface.

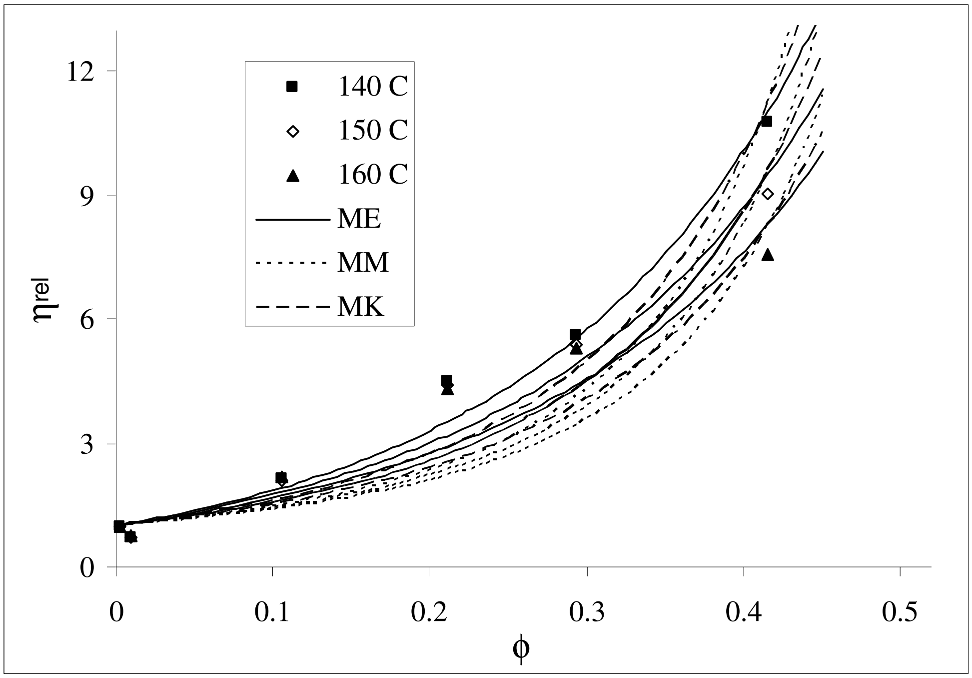

(a)

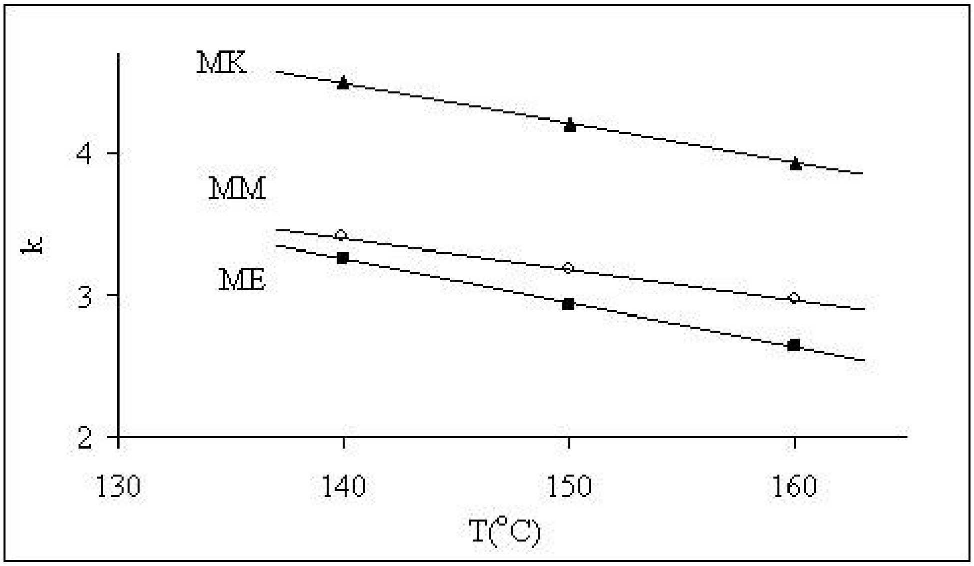

(b)

Figure 3.11 (a) Comparison of the fitting results of the modified Eilers (ME) model, modified Mooney (MM) model and modified Krieger-Dougherty (MK) model with the experimental $\eta_{rel} \sim \phi$ data at different temperatures. (b) Dependence of simulated parameter k value on temperature

3.3.3 Surfactant effect

Non-ionic surfactants bearing hydrophilic polyoxyethylene oligomer blocks have often been used as the de-flocculation reagent for fine ceramic oxide powders (Koke & Modigell, 2003). This particular functionality is attributed to the adsorption of the hydrophilic moiety on the metal-oxide particles through the Lewis acid-base interaction or hydrogen bonding. In this way, the surfactant molecules would form one or more adsorption layers on oxide particles (Fig. 3.12) depending upon the amount of surfactant used. Tween®-80 was employed in this work as the plasticizer for the PEG-CeO_2 (41.6 vol.%) blend to reduce its low temperature extrusion viscosity. The viscosity flow activation energy of the blend decreased quickly before

2 wt.% and level off after that (Fig. 3.13). This phenomenon can be understood from the multi-adsorption structure laid out in Fig. 3.12, firstly, the hydrophobic block of Tween®-80 leads to a hydrophobic slippery layer, which is responsible for the decrease of melt viscosity; secondly, only the most inner slippery layers play the primary role in lubricating the flow of PEG melt as these hydrophobic layers feel the greatest torque.

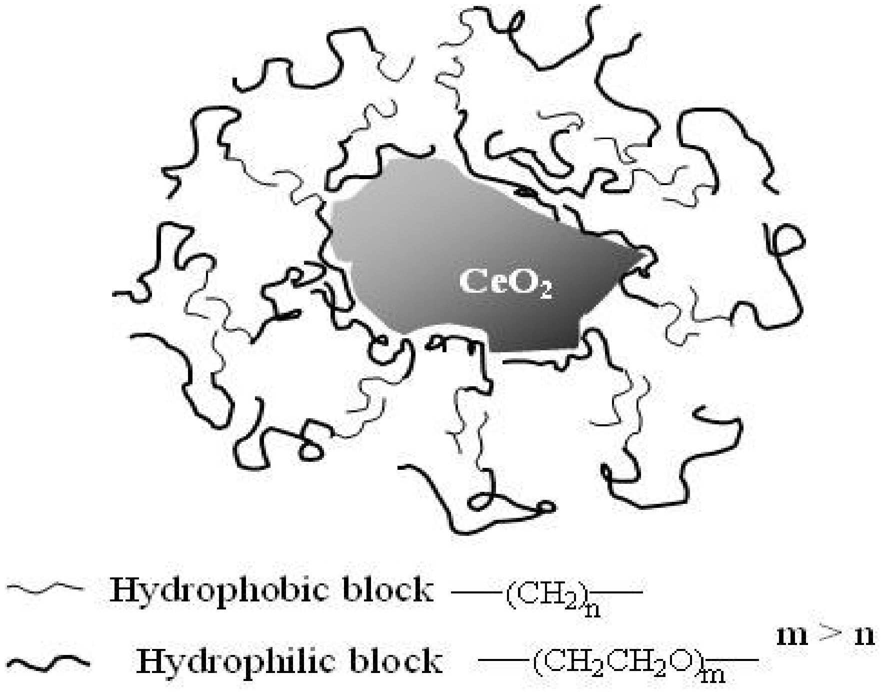

Figure 3.12 Schematic illustration of the multi-layer adsorption of Tween®-80 molecules on CeO_2 particles

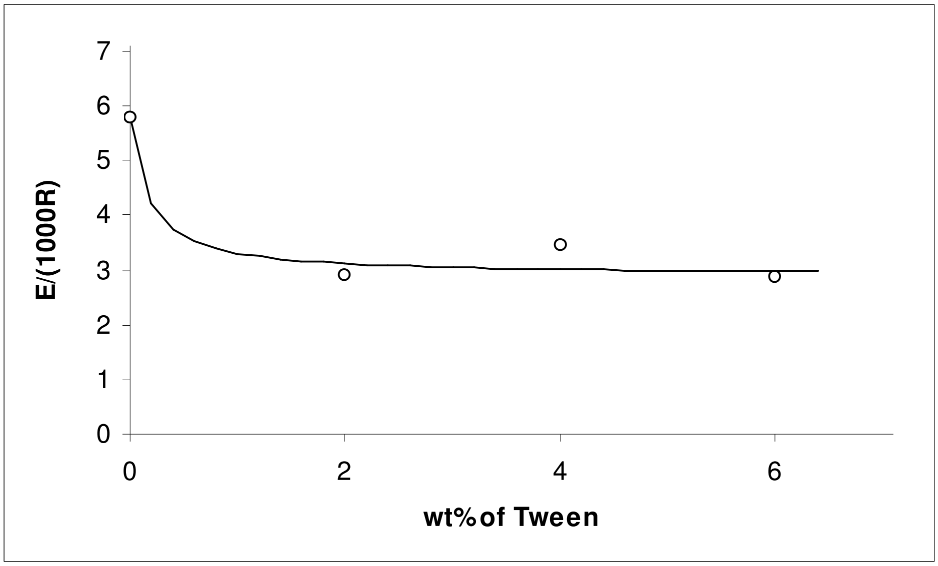

Figure 3.13 Lubricating effect of Tween®-80 on the viscous flow of PEG-CeO_2 (41.6 vol.%) blend

3.4 Conclusions

The CeO_2-PEG blends prepared via mixing CeO_2 fine powder with an aqueous solution of PEG and then removing water is an appropriate system, because of the thorough mixing extent, for the study of particle effects on viscous flow of the PEG melt under low shear rates. The XRD and DSC analyses of the resultant blends differentiated by the loading of CeO_2 proved the occurrence of strong adsorption of PEG chains on CeO_2 particle surface. The adsorption led to formation of a physical cross-linking network, especially in the high CeO_2-loading blends. On the other hand, the characteristic infrared absorption band of the PEG (ν_{C-O-C}) undergo changes in its shape with increasing ϕ value, which was ascribed to the existence of inter-particle van der Waals attractive forces among CeO_2 particles. These two fundamental interactions (adsorption and vdw attraction) are considered as the prevalent forces in such a polymer-ceramic blending system. A mathematic model expressing the relative viscosity (η_{rel}) as the function of ϕ, T, and the geometry/surface states of CeO_2 particles (n/B) was established on the basis of the Einstein equation and the Arrhenius relationship. In this mathematic model, the activation energy of viscous flow consists of two parts, the barrier due to the presence of vdw attractive forces ($\Delta E^{vdw} \sim \eta_{rel}^{vdw}$) and the barrier due to formation of the physical network ($\boldsymbol{\Delta E^{ad} \sim \eta_{rel}^{ad}}$). In parallel, under the low shear rates, the blends display Bingham flow behavior with respect to a series of ϕ at temperatures above the melting point of PEG. This mathematic model could more precisely match the experimental $\eta_{rel} \sim \phi$ data within the designated range of shear rates and temperatures by comparing with the three commonly used models. An additional study was also carried out to understand non-ionic surfactant effect on lowering down the melt viscosity of the blends. The concept of slippery hydrophobic shell is proposed to explain the fact that there is a lowest critical concentration of surfactant.

Chapter 4 Fabrication of asymmetric tubular membrane of $La_{0.2}Sr_{0.8}CoO_{3-\delta}/CeO_2$

The present work reports the formation of a complete gas-tight thin $La_{0.2}Sr_{0.8}CoO_{3-\delta}$ (LSCO80)-CeO_2 (1:1 by vol.) layer on the outer surface of a porous CeO_2 support by the means of vacuum assisted ceramic-ceramic composite slurry coating. The oxygen permeation flux tests showed a low activation energy barrier (~ 30 kJ/mol) of the whole electrochemical reaction in the temperature range from 400 to 900 ^{o}C. In addition, the surface de-sorption (or the anodic) process of the oxygen has been simulated using the extended Hückel theory (EHT).

4.1 Introduction

Mixed conductive perovskite-type materials, e.g., $La_{1-x}Sr_xCoO_{3-\delta}$ (LSCO), have been widely investigated to develop oxygen-transport solid electrolyte membranes (Section 2.1.2.1 of Chapter 2). An effective method to boost the oxygen permeation flux is to reduce the membrane thickness via employing the asymmetric structure in place of the single-bulk membrane structure (Eq. 2.4 in Section 2.1.1 of Chapter 2). However at the present stage fabrication of a dense thin dense layer of perovskite-type oxide on a thick porous tubular support with low cost method is still a technological challenge to the endeavor (Section 2.3.2.2 of Chapter 2). The chance of success for the generation of dense and thin oxygen permeable membrane layer on a porous ceramic tube of different material via traditional high temperature sintering process is slim due to the two problems: large surface pore sizes of the underlying porous support and a big CTE mismatch between the thin dense layer and the thick porous support. The former one impedes the formation of a complete dense layer and the latter one introduces cracks or de-lamination when the membrane is subjected to thermal cycle.

This Chapter reports a simple wet chemistry method (i.e., vacuum assisted ceramic-ceramic composite slurry coating) to solve the above problems. The asymmetric structure studied in the present work consists of a composite membrane and a porous CeO_2 tubular support. The LSCO80-CeO_2 (1:1, v/v) is used to form the composite membrane and this simple membrane composition brings about a drastic change in both membrane cohesion and adhesion strength. The oxygen permeation flux through the constructed asymmetric tubular membrane is measured and the experimental activation energy is found in a good agreement with the theoretical simulation results by using the EHT.

4.2 Experimental

4.2.1 Fabrication of tubular porous CeO_2 support

A mixture of 30 g polymers and extrusion additives (Table 4.1) and 170 g CeO_2 powder (average particle size: ~ 4.8 μm, Strem Chemicals (USA)) were dispersed in 1000 ml deionized water under continuous stirring (~ 600 rpm) at room temperature. After mixing at room temperature for 12 h, the slurry was heated up to 80 ^{o}C to thicken the slurry with stirring till the mechanical stirring became ineffective. Pouring down the slurry into a 1000 ml plastic beaker and stirring the concentrated slurry via glass rod until it was cooled down to room temperature. The resulting wet polymer-CeO_2 solid was dried for 5 days at room temperature to obtain the desired blend containing ca. 5 wt.% water. The blend was extruded into a green tube through an extruder (ThermoHaake PolyDrive). The temperature range of extrusion zone was set from 40 to 45 °C with screw rotation rate of 30 rpm and applied torque of 5 Nm. After drying for one week at room temperature, the extruded green tube was heated in a Carbolite furnace using a very slow heating rate to burn out the organics and then to sinter the packed CeO_2 particles. Figure 4.1 shows the entire heating program applied to generate a consolidated but porous CeO_2 tube. Figure 4.2 shows a green tube which has the dimension (OD: 1.2 cm, ID: 0.9 cm and length 38 cm) and its counterpart after sintering (1600 °C for 1 h) which has the dimension (OD: 1.0 cm, ID: 0.73 cm and length of 32 cm). The shrinkages in the length, OD & ID directions are 15.8%, 16.7%, and 18.9%, respectively.

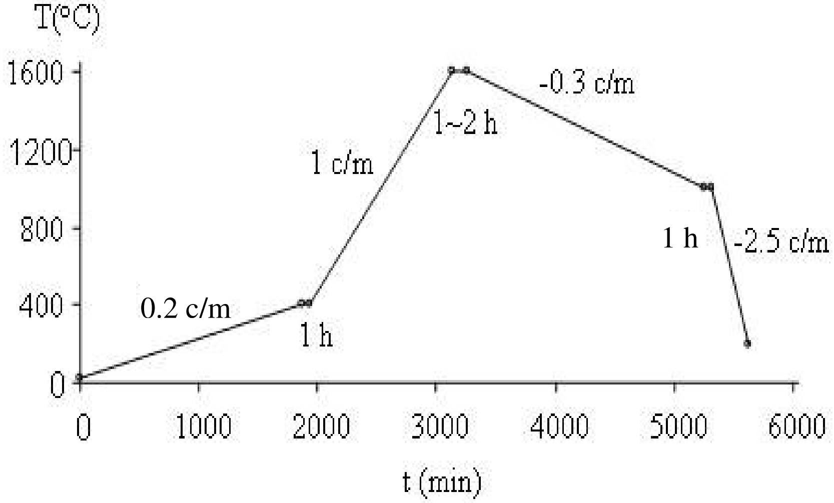

Figure 4.1 Calcination profile of the green CeO_2 tube (c/m = °C/min)

Table 4.1 Organics added in the extrusion feed for the CeO_2 tube

Organic	Mass percentage of different components		
	Lubricant (wt.%)	Extrusion aid (wt.%)	Pore-former (wt.%)
PEG200	6.7	-	-
PEG400	10	-	-
Tween®-80	10	-	-
PEG15000	-	37	-
PEG20000	-	6.7	-
PVP10000	-	-	10
HEC90000	-	-	6.7
HEC250000	-	-	6.7
HEC720000	-	-	3.8
HEC1300000	-	-	3.8

PEG: Poly(ethylene glycol) (Merck)

(PEG200 represents the PEG with average molecular weight of 200)

Tween®- 80: Polyoxyethylene(20) sorbitane monooleate

PVP10000: Poly(N-vinyl pyrrolidone) (average molecular weight: 10000, Sigma)

HEC: Hydroxyethylcellulose (Aldrich)

(HEC90000 represents the HEC with average molecular weight of 90000)

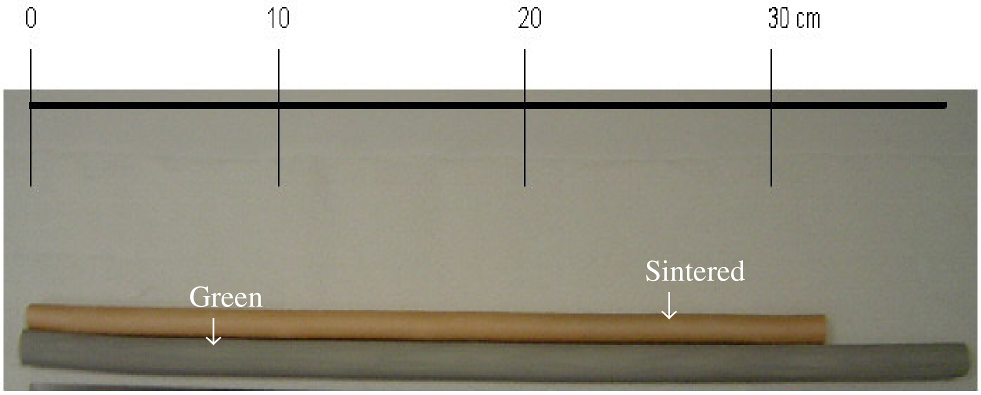

Figure 4.2 Photograph of the green and sintered (1600 °C for 1 h) tubes

4.2.2 Preparation of ultra fine LSCO80 powder

Stoichiometric amount (La^{3+} : Sr^{2+} : Co^{3+} = 1 : 4 : 5 in molar ratio) of $La(NO_3)_3{\cdot}6H_2O$ (99.9%, Aldrich), $Sr(NO_3)_2$ (99.9%, Aldrich), and $Co(NO_3)_2{\cdot}6H_2O$ (99.9%, Aldrich) were dissolved in an EDTA (ethylenediaminetetraacetic acid, Aldrich)-ammonia aqueous solution (pH 8~9) with stirring. The molar ratio of the total metal ions to EDTA was 1:1. A dark-brown solution was obtained, and a small amount of polyvinylalcohol (PVA) (Aldrich) (5 wt.% of EDTA) was dissolved in the solution. Gelation occurred by accompanying with evaporation of the water at 80-100 ^{o}C. The organic component in the gel was burned out at 400 ^{o}C for 2 h, leaving a black powder. The black powder was calcined under purging of air (100 l/h) at 900 ^{o}C for 2 h in a Carbolite furnace, resulting in the LSCO80 powder. The LSCO80 powders were grounded and sieved through a 45 μm pore size sieve.

4.2.3 Fabrication of asymmetric tubular membrane

The ceramic suspension was obtained by adding ceramic powder (LSCO80 or LSCO80/CeO_2 (1:1, v/v) mixture) into an organic solution containing a variety of additives. Toluene-methylethyl ketone mixture (1:1, v/v) was used as the solvent and the final suspension consisted of 150 g/l ceramic powder, 6.25 g/l polyvinylbutyral resin (Butiva-79, Monsanto), 6 ml/l fish oil, 3 ml/l dibutyl phthalate, and 3 ml/l Span-80. It was followed by ball-milling the suspension formed with zirconia balls (Fisher Scientific) for 3 days to generate an ink-like dispersion. The ball-milling procedure could only break up soft agglomerations of elementary particles (that join together by van der Waals attractive forces or weak mechanical interlocks) rather than elementary particles. While applying the suspension to the external surface of porous CeO_2 tube by brushing or spraying, one end of the tube was blocked with epoxy resin and the other end was vacuumed, and as a result, a highly packed and uniform LSCO80-CeO powder layer was formed on the outer tube surface. After drying at room temperature overnight, the coated CeO_2 tube was heated slowly (at the heating rate of 0.5 ^{o}C/min) to 400 ^{o}C and held on for 1 h, and after that, the calcinations temperature was raised to 1200 ^{o}C by the rate of 1.0 ^{o}C/min and held on there for 2 h to allow formation of a dense LSCO80-CeO_2 composite membrane on the porous CeO_2 tube surface.

4.2.4 Instrumental characterizations

The pore size distribution was measured via mercury porosimeter (Micromeritics AutoPore III). XRD analysis (SHIMADZU XRD-6000, Cu Kα radiation with wavelength of 1.54056 Å and scanning rate of 2.5 ^{o}/min) was employed to examine the crystalline phases. The morphologies of the LSCO80 powder and the different sections of the asymmetric tube were investigated on a scanning electron microscopy (SEM) instrument (JEOL JSM-5600) or field emission scanning electron microscopy instrument (FESEM) (JEOL JSM-6700F). The CTEs of the composite (1-y)LSCO-80/yCeO_2 specimens (y = 0-1) in the temperature range from 25 to 900 ^{o}C were measured on a thermal mechanical analyzer (TMA 2940, TA Instruments). To minimize the happening of bulk voids as they affect the measurement accuracy of CTE, we sintered the samples ($y \leq 0.5$) at 1200 ^{o}C for 3 h and the pure CeO_2 sample at 1600 ^{o}C for 3 h to assure a maximum densification (> 92%).

4.2.5 Oxygen permeation test

The setup for assessing oxygen permeation flux is shown on Fig. 4.3. Two ends of the fabricated asymmetric ceramic membrane (1.0 cm OD X 0.73 cm ID X 10 cm length) were linked with two alumina tubes (1.91 cm OD X 1.27 cm ID X 35 cm length) using ceramic sealant (CERAMABOND 813-A, Aremco Prodducts Inc., USA). Helium was used as the sweep gas to check if any the leakage of the membrane module as well as to establish chemical potential difference of oxygen across the membrane. The volume percentage of oxygen (O_2%) in the outlet He-O_2 stream of the membrane tube was quantified using gas chromatography (GC) (PerkinElmerARNEL, Clarus 500). The GC analysis also showed no detectable content of N_2 in the He stream. The oxygen permeation flux (J_{O2}, sccm/cm^2) was then calculated by the formula:

$$J_{O2} = \frac{j_{in} \times O_2\%}{\pi D_O L} \tag{4.1}$$

in which j_{in} (sccm) is the inlet gas flow rate, D_o (cm) and L (cm) are the out surface diameter and length of the membrane tube, respectively. The tubular membrane was placed in the center of a split furnace (Nabertherm, with T_{max} = 1100 ^{o}C) that has a 35-cm long heating zone. As the membrane used is far shorter than the heating zone length, the temperature gradient along the membrane at the all temperature points (450–900 ^{o}C) could be neglected.

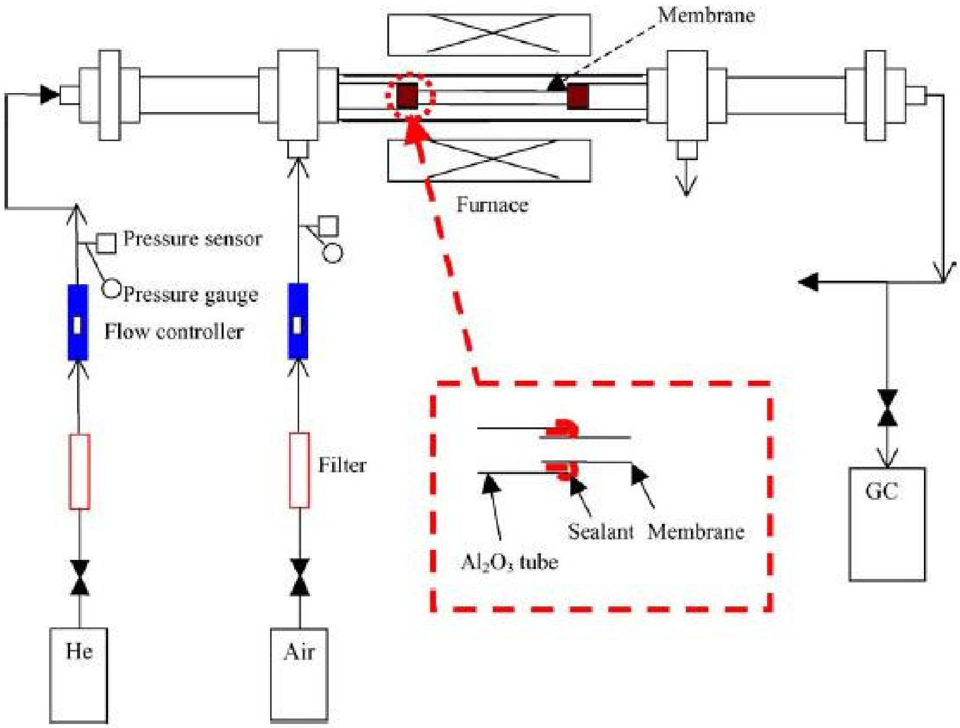

Figure 4.3 Schematic of assembled membrane module for oxygen permeation testing

4.3 Results & discussion

4.3.1 Structural aspects of porous CeO_2 tube

The porosity and surface pore size of a tubular ceramic support have significant effect on the quality of the thin dense membrane layer coated on the support surface. Larger porosity is expected to render the anodic side of membrane be more exposed to the feed inside the tube in order to achieve a higher oxygen permeation flux. The desired support porosity is within the range of 20 ~ 30%, which provides enough exposure to the sweep gas and satisfied mechanical strength to the COMR. Formation of uniform and small surface pore sizes in the support is even more significant to ensure a thin and dense membrane to be fabricated. The trait (porosity and pore size distribution) of a sintered tube counts very much on both the type and amount of the polymers used to formulate the blend of polymer and ceramic powder for extrusion. The CeO_2 powder–organic blend for extrusion (Table 4.1) contains 15 wt.% of the organic phase, of which four functions can be assigned respectively. The organic phase is classified into the three main categories according to their functionalities. PEG is used as the extrusion aid because of its low melting point and flexible chain motions (Chapter 3). HEC offers strong hydrogen bonding with surface oxygen atoms of CeO_2 particles and it is much more bulky than PEG, and therefore was employed as binder and porogen.

Another critical condition affecting porosity and surface pore sizes is the sintering temperature and its duration. The CeO_2 tubes obtained from sintering at 1600 °C for 1 and 2 h, respectively, show rather different porosity and total pore area (Table 4.2). The outer surface SEMs of the sintered tubes are shown in Figure 4.4. The tube sintered for 1 h has both higher pore numbers per unit surface area and average pore size than the tube sintered for 2 h.

Table 4.2 Effect of sintering time on the porosity of the CeO_2 tube

S-time*	Total pore volume (ml/g)	Total pore area (m^2/g)	Average pore radius (μm)	Porosity (%)
1 h	0.034	0.04	1.5	23
2 h	0.0072	0.01	1.1	5

* Sintering time at 1600 °C

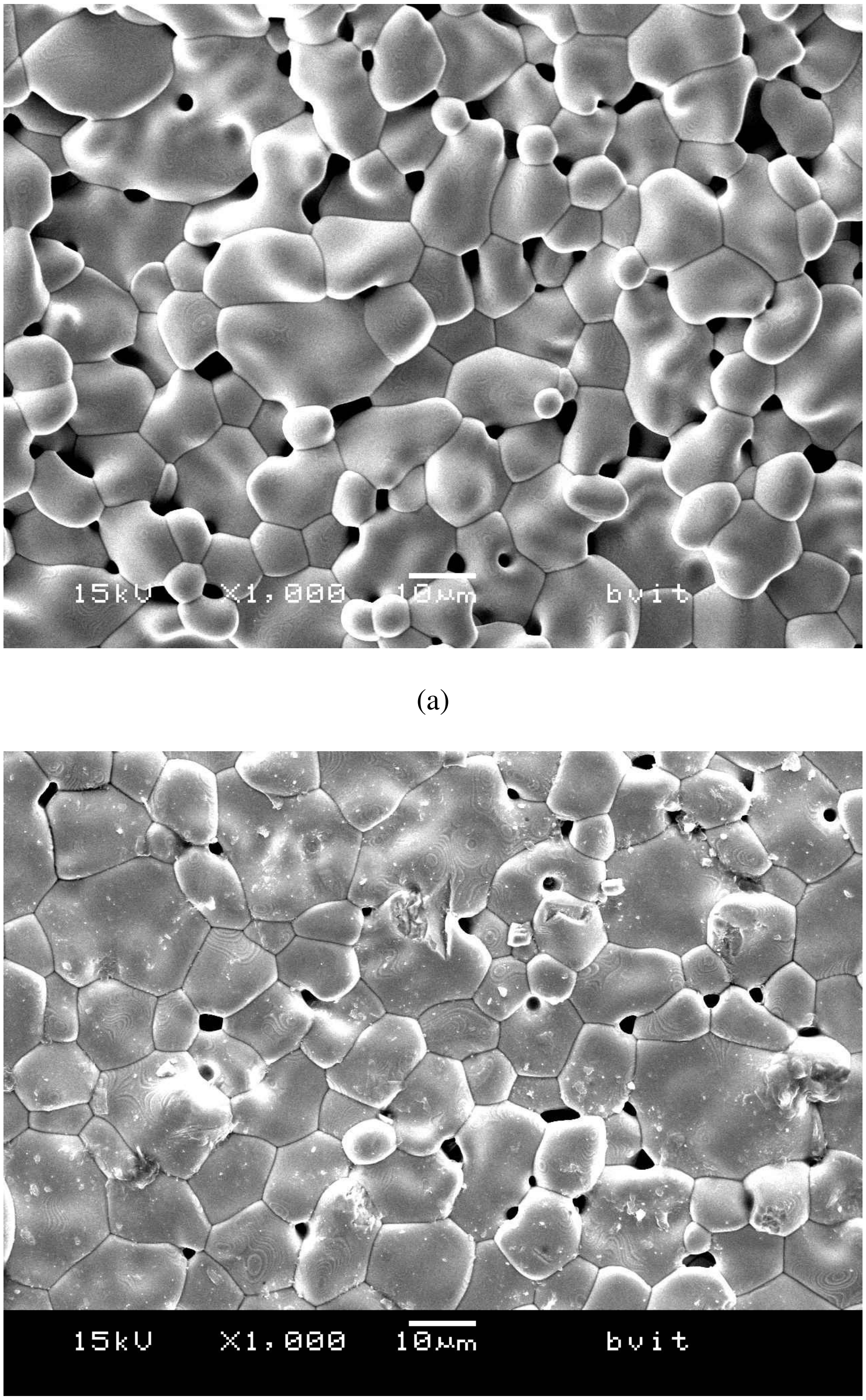

(a)

(b)

Figure 4.4 Outer surface SEMs of the CeO_2 tubes after sintering at 1600 °C for: (a) 1 h; (b) 2 h

4.3.2 Fabrication of a thin and dense LSCO80/CeO_2 composite membrane

The fabricated LSCO80 powder shows a certain extent of aggregation and consists of sub-micron particles with irregular shape (Fig. 4.5). The XRD indicates that the LSCO80 possesses a single cubic perovskite structure with lattice of 3.835 Å (Fig. 3.6a). Since the LSCO80 particle size is much smaller than the surface pore sizes of CeO_2 (Fig. 4.4a), direct conventional ceramic dip coating procedure, i.e., dipping porous CeO_2 tube into the LSCO80 slurry without vacuum for 5 seconds (the vacuum will suck the submicron LSCO80 particles from the support outside into the inside and thus fail the coating process) and then sintering at 1200 ^{o}C for 2 h, results in the porous LSCO80 layer with the thickness of about 5 μm (Fig. 4.7). Increasing the thickness of the LSCO80 coating layer by longer dipping time or multi-dipping procedure did not help close the pores, and lots of visible cracks within the coated LSCO80 layer were found when the thickness of the LSCO80 layer becomes larger than about 10 μm, which is caused by a severe CTE mismatch between the LSCO80 membrane and the underlying CeO_2 support. Decreasing the sintering temperature to 1100 ^{o}C or lower with the same sintering duration, poor adhesion between the LSCO80 membrane and the CeO_2 support was found. This outcome indicates that an insufficient sintering temperature or duration causes poor wetting of LSCO80 on the CeO_2 surface. Therefore, plugging the surface pores on the CeO_2 tube and eliminating material cracks in the LSCO80 membrane due to CTE mismatch are crucial to the accomplishment of a gas-tight membrane.

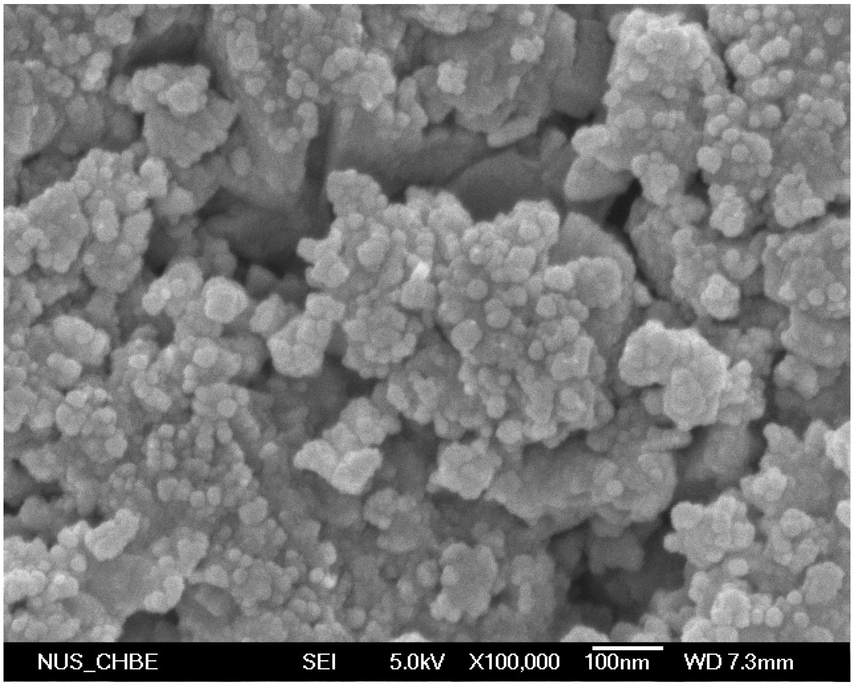

Figure 4.5 FESEM of the fabricated LSCO80 sub-micron particles

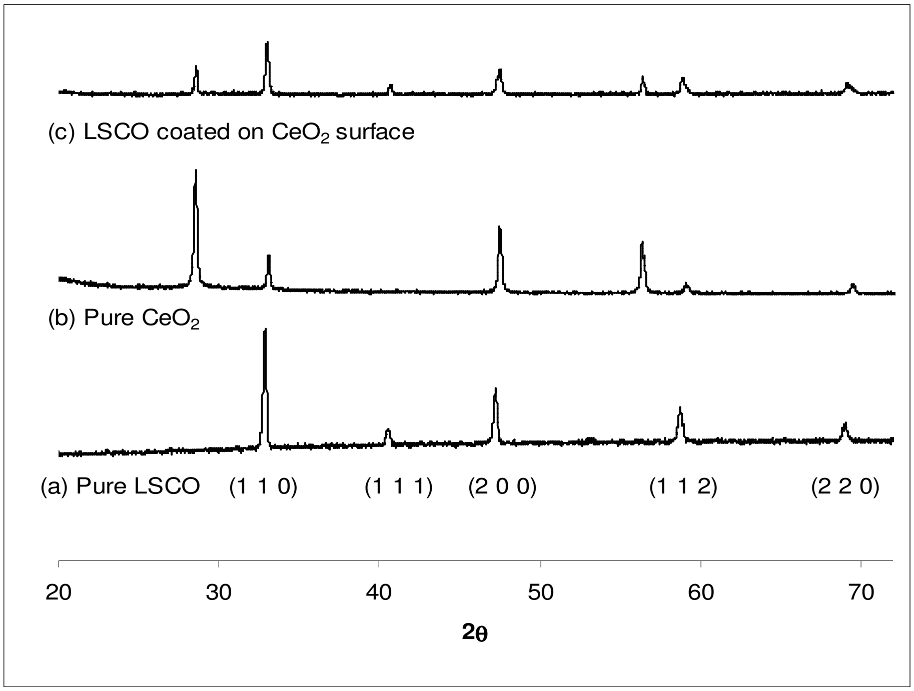

Figure 4.6 XRD profiles: (a) pure LSCO80 (sintering at 1200 °C for 2 h); (b) pure CeO_2; (c) LSCO80 coated CeO_2 tube (sintering at 1200 °C for 2 h)

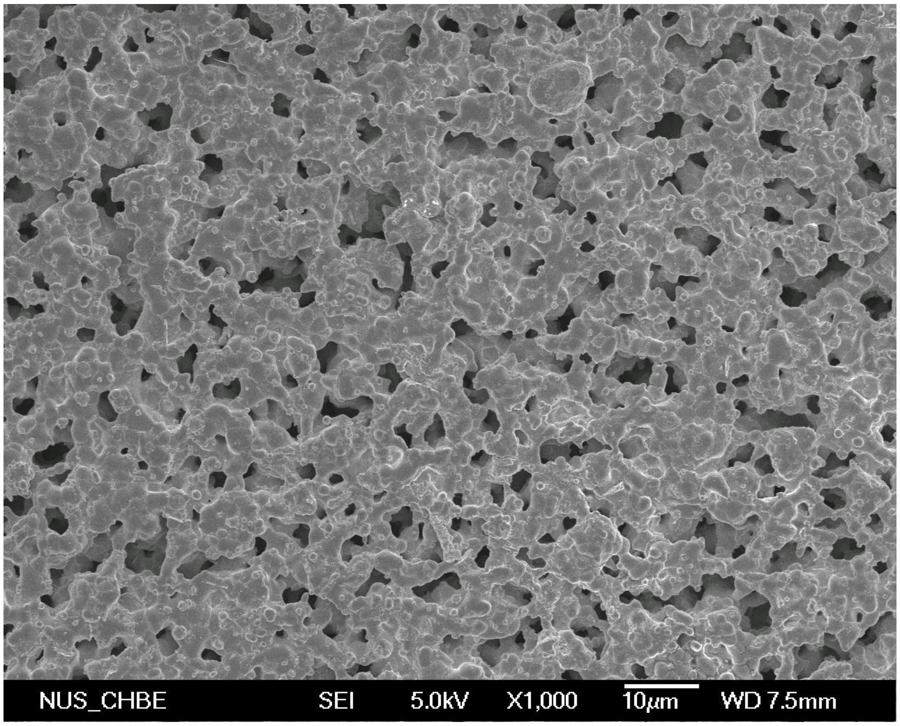

Figure 4.7 Outside surface FESEM of the coated pure LSCO80 layer on the CeO_2 surface after sintering at 1200 °C for 2 h

We found that incorporation of CeO_2 fine powder into LSCO80 coating (e.g., by a volume ratio of 1:1) using vacuum-assisted coating could basically meet the above two requirements. As a result, a dense LSCO80/CeO_2 composite membrane (~ 10 μm) was generated on the porous CeO_2 tube outer surface. The presence of CeO_2 particles (with average particle size of about 4.8 μm) in the coating layer prior to sintering has two roles, i.e., blocking large surface pores of CeO_2 tube and buffering the stress generated in the continuum of LSCO80 phase (Fig. 4.8). The second function is profound because of two reasons: firstly, the continuum of LSCO80 is embedded by so many CeO_2 particles and hence the LSCO80 phase itself is in effect a network structure and thus possesses better plasticity than the stuffing counterpart; secondly, the CeO_2 particles in the composite membrane do not bind with each other to form rigid connects because they undergo no sintering while LSCO80 particles merge together at 1200 °C, and on the other hand, Fig. 4.9a shows that LSCO80 wets CeO_2 particles well. The ceria particles look like covered by a smooth layer of LSCO80 and no structural discontinuity happens between the two phases. It is supposed that this intimate connection has the relation with similar crystallographic parameters that both LSCO80 and CeO_2 possess. LSCO80 has the perovskite structure with the axial length of ca. 3.8 Å, while CeO_2 has cubic fluorite structure with the axial length of ca. 3.4 Å.

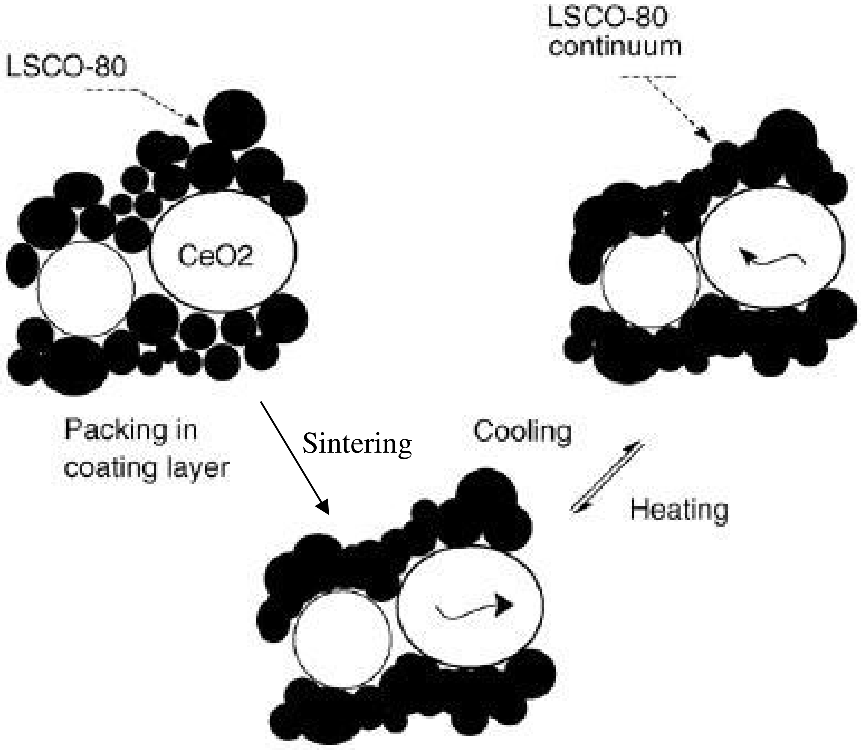

Figure 4.8 Illustration of how CeO_2 particulate filler install stress buffering

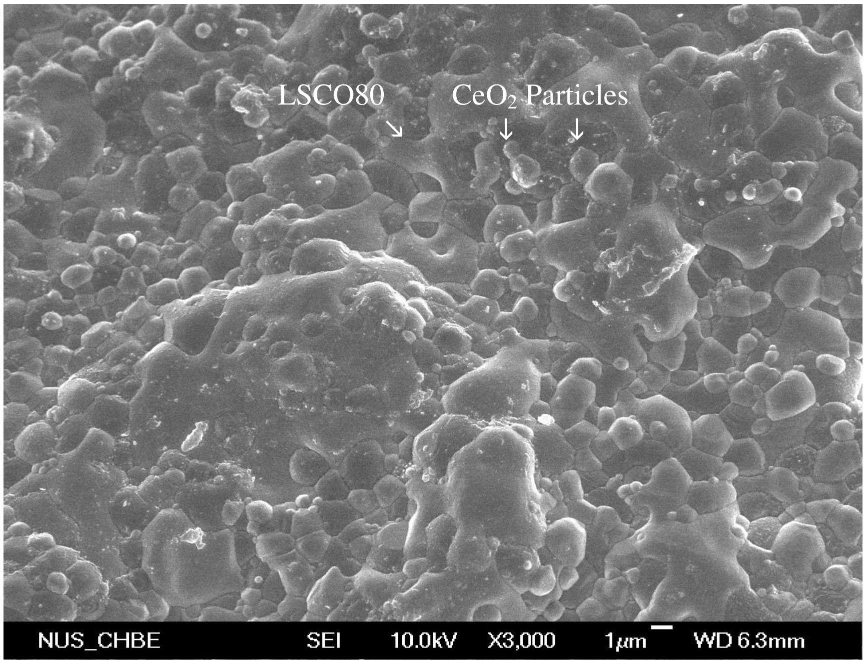

(a)

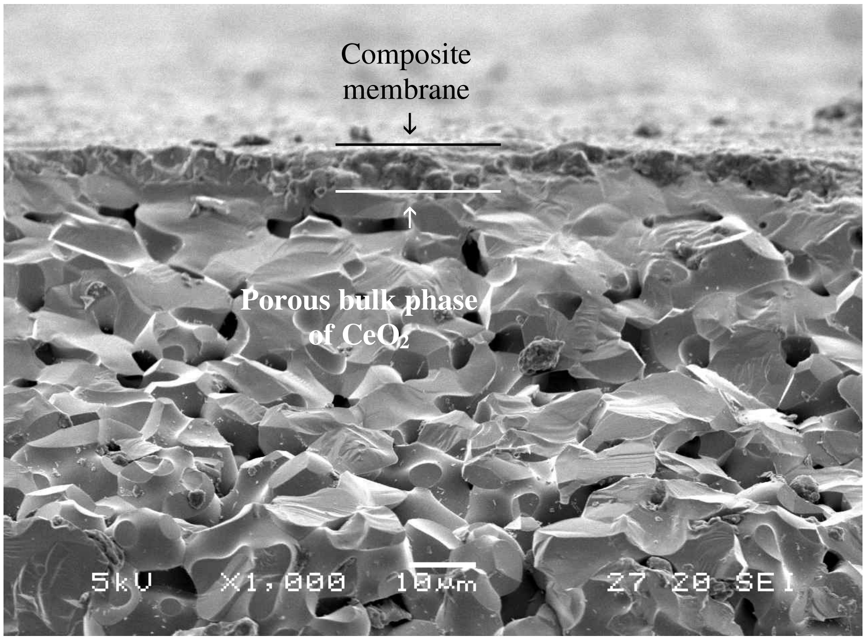

(b)

Figure 4.9 The fabricated asymmetric tubular ceramic membrane: (a) outside surface FESEM of coated dense thin layer; (b) cross-sectional SEM

Figure 4.8 is the schematic diagram that illustrates how ceria particles dispersed in LSCO80 phase function to buffer thermal stress. It has been well known that hard ceramic particles in a continuous phase can act as a barrier to crack propagation or the movement of dislocation (Okada, 2003). The fracture toughness (of a ceramic composite) increases with an increase in the volume fraction of the hard particles via the mechanisms of crack bowing, crack deflection, micro-cracking, or bridging. The CeO_2 particles in LSCO80 indeed reduce the CTE mismatch between the LSCO80 and the underlying CeO_2 porous support (Fig. 4.10). An apparent drop in CTE happens in the volume fraction range of ceria from 25 to 50%. The relation between a variety of physical properties and volume fraction of particulate fillers often displays the percolation threshold in this range of volume fraction, which means that, in the present case, the stress buffering action becomes significant only when the CeO_2 particles are approaching in physical contact as illustrated in Fig. 4.8. It also needs to note that although we used 50 vol.% CeO_2 to fabricate LSCO80/CeO_2 composite membrane, this may not be the optimal CeO_2 content in terms of maximizing the concentration of oxygen vacancies in LSCO80 but causing nil cracks and adequate toughness in the membrane. Actually, this vacuum-assisted ceramic-ceramic composite technology can also be used to fabricate other types of COMRs provided that the selected ceramic-ceramic composite contains the ceramic powder having the particle diameter comparable with the support surface pore size and the CTE of the composite is close to that of the support. According to the cross-sectional view the reactive layer (LSCO80/CeO_2 after sintering at 1200 ^{o}C for 2 h) has a thickness of about 10 μm (Fig. 4.9b), and its XRD pattern (Fig. 4.6c) indicates that no solid phase reaction happened between LSCO80 and CeO_2 during co-sintering stage.

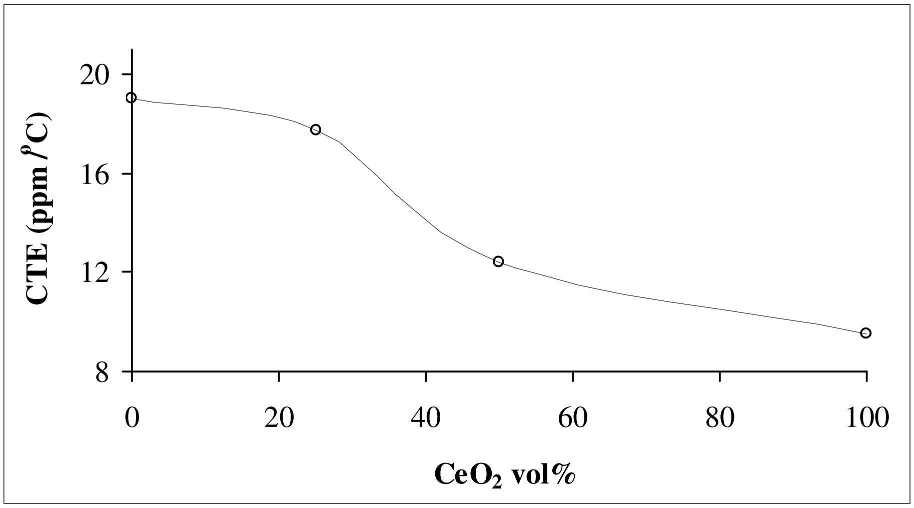

Figure 4.10 Dependence of the CTE of LSCO80/CeO_2 composite upon the CeO_2 concentration

4.3.3 Oxygen permeation flux and oxygen surface de-sorption simulation

Figure 4.11 shows the dependence of the oxygen permeation flux on the measurement temperature. The asymmetric membrane based on the higher porous CeO_2 tube (Fig. 4.11a) gave rise to a higher oxygen permeation flux than that based on the lower porosity support (Fig. 4.11b). Since the dense composite membrane layer (~10 µm in thickness) is much thinner than the critical thickness of LSCO80 (~ 80 µm) (Chen et al., 1997), it is rational to take the surface oxygen exchange as the controlling step in the oxygen permeation process. Indeed, the activation energies of both membranes (ca. 30 kJ/mol) are lower than the activation energy observed from the permeation process predominated by the bulk oxygen ion transport step (~ 100 kJ/mol) (Bouwmeester & Burggraaf, 1997). Moreover, with regard to the asymmetric membrane setup used in the present work, the outer surface where adsorption of oxygen takes place is much more exposure (to air stream) than the inner surface where the oxygen desorption takes place. Therefore, the oxygen desorption in helium-purging side can be accounted for the bottleneck of the oxygen permeation flux. The two $\log J_{O_2} \sim 1/T$ linear relations show similar slopes, which means that the oxygen de-sorption energy has not much to do with the discrepancy in the surface porosity of the two CeO_2 tubes. The difference in J_{O_2} between them was solely due to the different inner surface area exposed to helium purging stream.

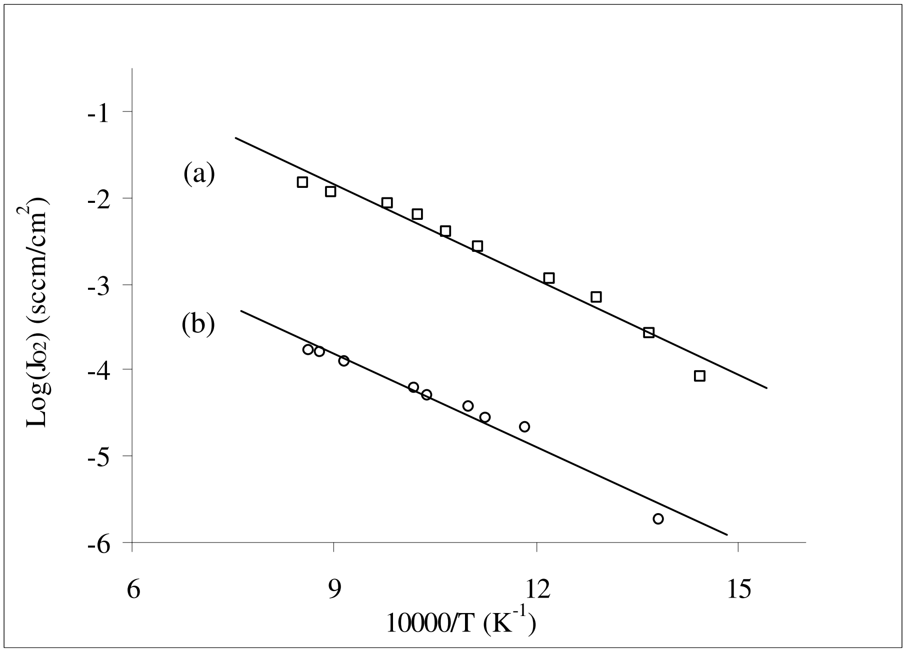

Figure 4.11 Dependence of oxygen permeation flux on temperature of the membrane with the support porosity of: (a) 23%; (b) 5%

The surface oxygen exchange mechanism in the purging side is widely regarded as containing three consecutive steps:

Step 1: $O_O^x \rightarrow O_{ad}^- + V_{\ddot{O}} + e^-$

Step 2: $O_{ad}^- \rightarrow O_{ad} + e^-$

Step 3: $O_{ad} \rightarrow \frac{1}{2}O_2(g)$

The oxygen de-sorption can happen in the form of α de-sorption (Co^{4+} is reduced to Co^{3+}) or β de-sorption (Co^{3+} is reduced to Co^{2+}), depending upon the valence state of the cobalt ions close to the desorbed surface lattice oxygen atom (Yamazoe & Teraoka, 1990). Up to date, the surface oxygen exchange mechanism is still not thoroughly understood, especially in the explanation of the dependence of the exchange rate upon the apparent oxygen pressure. Due to the nonlinear oxygen chemical potential gradient cross the membrane, the oxygen vacancy gradient should also be nonlinear across the membrane, and it is very difficult to experimentally assess the oxygen potential gradient and the oxygen vacancy concentration gradient across the membrane. Therefore, computational simulation of the surface exchange by using experimental parameters as reference is of importance to clarify the proposed mechanism.

Extended Hückel Theory (EHT) (Appendix B), a one-electron semi-empirical MO (molecular-orbital) method, is simple but suffers from its poor treatment of electron-electron repulsions and nuclear-nuclear repulsions (Stoneham, 1985; Levine, 2000). However, when employed to calculate those systems where weak (or constant) electron overlap and nucleus-nucleus repulsion exist, EHT is effective and could offer satisfactory results. A suitable case for this may be the conversion of lattice oxygen to physically adsorbed oxygen atom at the surface of purging side as it involves a low energy perturbation and de-sorption would not happen otherwise. Different from the oxygen ion bulk transport that must go through the “A-A-B” (lattice point of perovskite cell) type saddle point (Cook & Sammells, 1991; Sammells et al., 1992; Cherry et al., 1995; Kilner & Brook, 1982), which involves a huge electron orbital overlap and nuclei interactions, the surface oxygen de-sorption process deals with a crystal cluster consisting of a number of perovskite unit cells (e.g. $nLa_{0.2}Sr_{0.8}CoO_{3-\delta}$), in which much weaker electron overlap and nuclei interactions than oxygen ion transport in the bulk phase occur because oxygen ions do not go through the saddle point at the surface, and the oxygen ions having weaker interactions with the crystal lattice would take priority to undergo de-sorption.

The EHT calculation was done via the software of Arguslab (version 4.0) (http://www.arguslab.com; Thompson & Zerner, 1991; Thompson et al., 1994; Thompson & Schenter, 1995; Thompson, 1996) with the STO 6G basis sets and EHT constant (K) of 1.75. Figures 4.12a~d show the cluster models with different oxygen vacancy ($20[La_{0.2}Sr_{0.8}CoO_3]$, $20[La_{0.2}Sr_{0.8}CoO_{3-0.05}]$, and $20[La_{0.2}Sr_{0.8}CoO_{3-0.1}]$) that were designed for the calculation, of them Fig. 4.12a shows the arrangement of the Sr^{2+} and La^{3+} ions for the $20[La_{0.2}Sr_{0.8}CoO_3]$ cluster model. To make the 3-D Figs. 4.12 (b~d) easy to see, the La and Sr ions in the cluster are not drawn but they are included in the EHT calculation. The arrow in the Fig. 4.12a indicated the desorbed oxygen atom and the de-sorption direction (vertical to the cluster surface).

During the de-sorption process, an oxygen anion leaves its original surface location and thus the distance between the oxygen anion's location and its original surface coordination neighbors (Δr) will increase. At the same time, the whole cluster energy will change due to the variation of the coulomb interaction and the distortion of the cluster geometry. The energy difference (ΔE) is thus defined as the change in the cluster energy accompanying with de-sorption. Figure 4.13 shows the dependence of the calculated energy difference (ΔE) on the de-sorption distance (Δr). ΔE increases as the increase of Δr until when the interactions between the desorbing oxygen and the cluster become negligible (Δr ~ 3 Å).

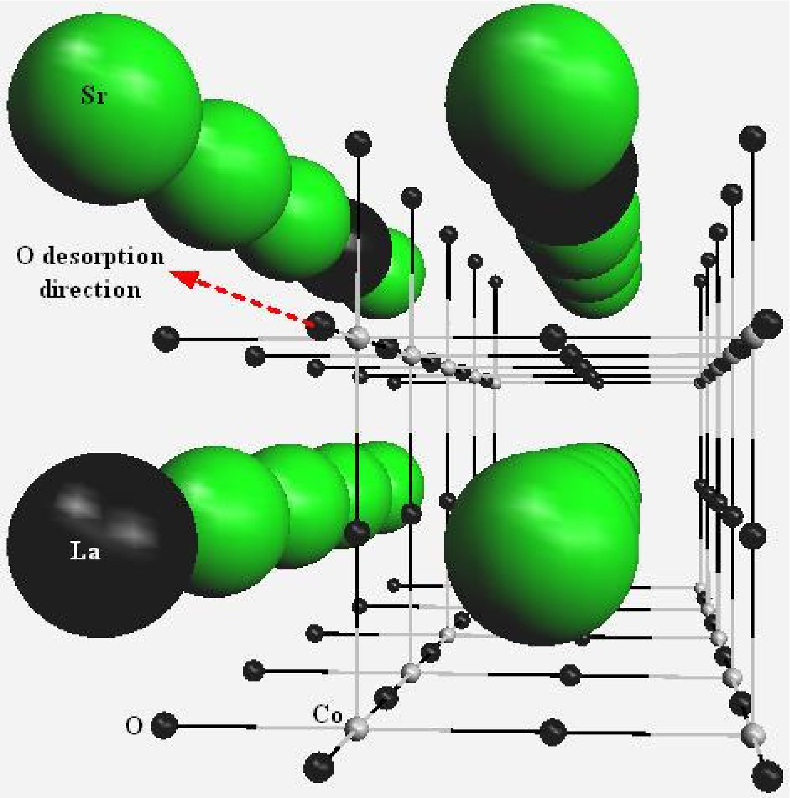

(a) $20[La_{0.2}Sr_{0.8}CoO_3]$

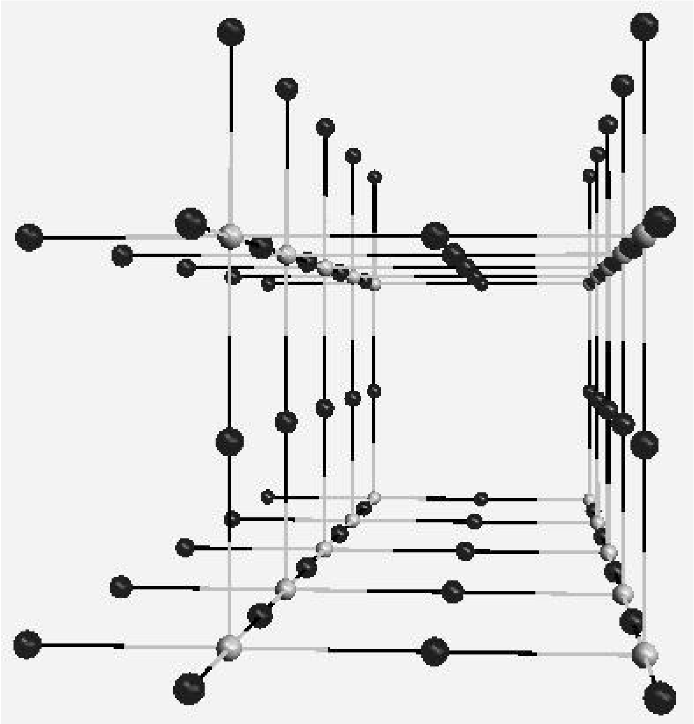

(b) $20[La_{0.2}Sr_{0.8}CoO_3]$

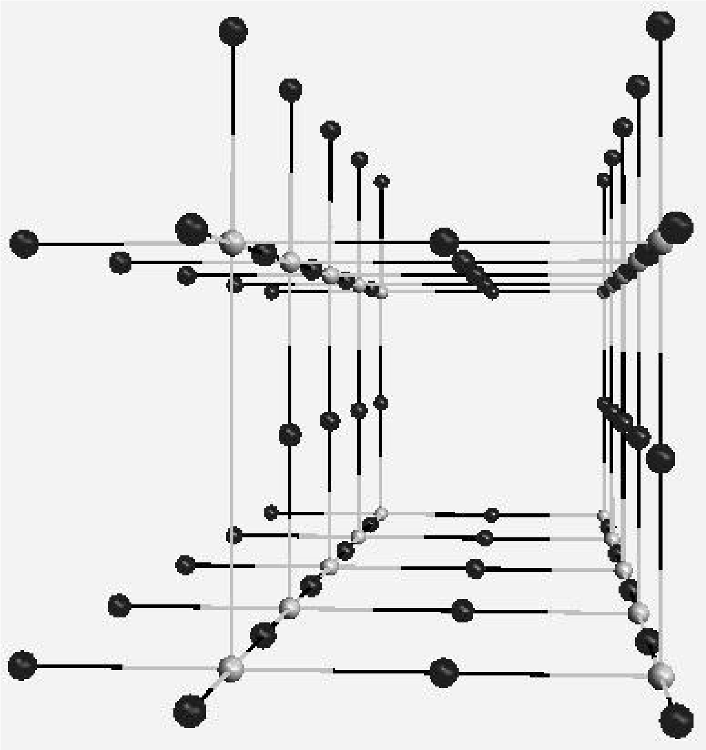

(c) $20[La_{0.2}Sr_{0.8}CoO_{3-0.05}]$

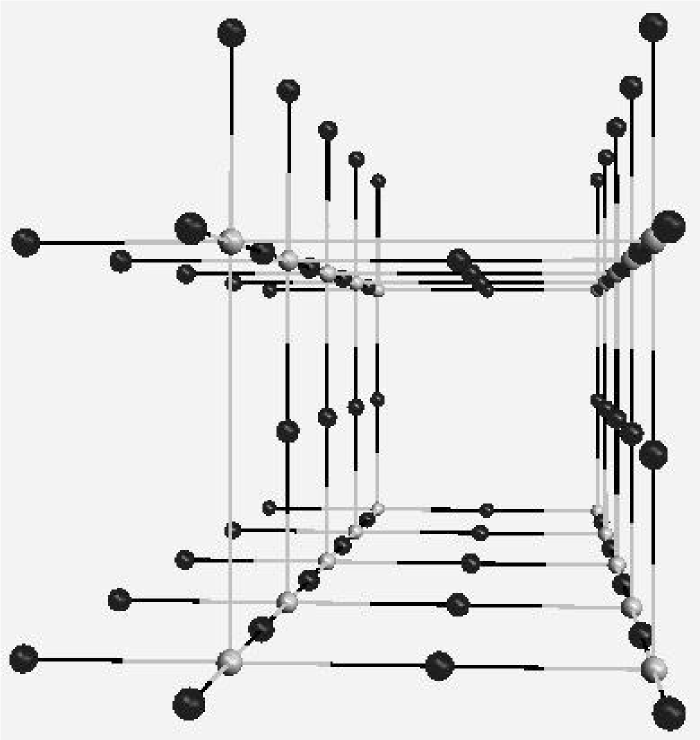

(d) $20[La_{0.2}Sr_{0.8}CoO_{3-0.1}]$

Figure 4.12 Cluster models ($20[La_{0.2}Sr_{0.8}CoO_{3-\delta}]$) for EHT calculation: (a) $\delta = 0$ with Sr^{2+} and La^{3+} drawn in the figure; (b) $\delta = 0$; (c) $\delta = 0.05$; (d) $\delta = 0.1$

Once the lattice oxygen released electron(s) during the de-sorption process, it will migrate from the oxygen lattice position and rest at the crystal surface as the radical species $O^{\cdot}_{ad}$, therefore, the de-sorption distance is about the diameter of an oxygen anion (~ 3 Å) (Fig. 4.14). Figure 4.15 shows the linear dependence of the calculated surface exchange activation energy (E_a) on the surface oxygen vacancy concentration (δ). Based on the different δ values (0 to 0.1, corresponding to $La_{0.2}Sr_{0.8}CoO_{3-\delta}$), the calculated activation energies fall into the range from 29 kJ/mol to 34 kJ/mol, which embraces the experimental value of 30 kJ/mol. The increase of the surface oxygen vacancy concentration on the permeate side lifts the de-sorption activation energy threshold. By decreasing oxygen fugacity in the purging side, the oxygen vacancy concentration will increase correspondingly, and this will in turn increase the de-sorption activation energy. In other words, the oxygen fugacity in the feeding stream influences the surface exchange process via changing the surface oxygen vacancy concentration.

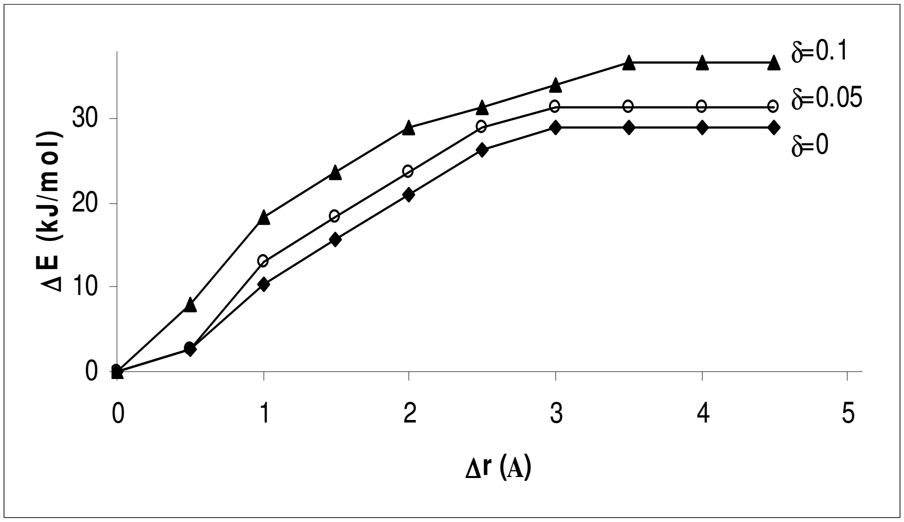

Figure 4.13 Dependence of the calculated potential energy barrier upon de-sorption distance

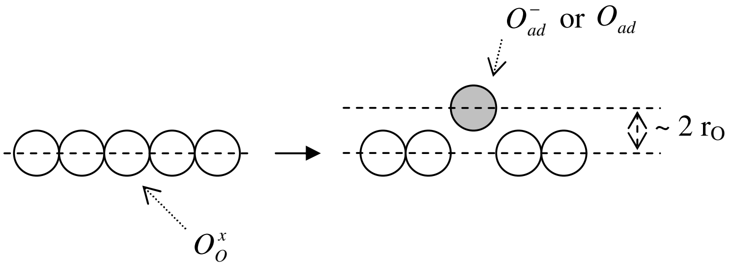

Figure 4.14 Schematic diagram of the de-sorption of an oxygen atom

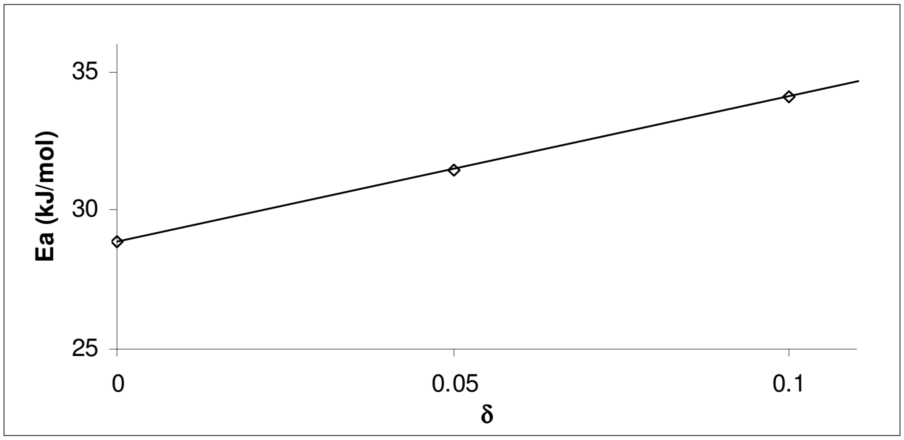

Figure 4.15 Dependence of the calculated surface oxygen de-sorption activation energy on the surface oxygen vacancy concentration

4.4 Conclusions

The asymmetric tubular membrane reactor composed of the porous CeO_2 support and the dense $La_{0.2}Co_{0.8}SrO_{3-\delta}/CeO_2$ composite membrane (~10 μm) has been successfully fabricated. As a result, the oxygen permeation fluxes within the temperature range of 400 ~ 900 °C show lower activation energy than the oxygen ion bulk transport controlled perovskite oxides. The presence of CeO_2 particles in the membrane layer plays the crucial role in achieving the gas-tight composite membrane, which is the prerequisite of undertaking electrochemical oxygen separation. It is suggested that the ultra fine CeO_2 particles in the membrane gives rise to and upholds a LSCO80 network that buffers the thermal-induced stress effectively. The porosity of the porous support has almost no influence on the measured activation energy value, although it shows a significant effect on the oxygen permeation flux, which implies that the surface oxygen exchange on the permeate side is likely the rate-limiting mechanism when measuring the permeation via inert gas sweep method.

Computational simulation of the surface oxygen de-sorption process by employing EHT has also been performed. The calculated activation energy value is very close to the experimental outcome, which suggests that EHT may be an appropriate simple method to investigate the surface adsorption/de-sorption. According to the computational simulation, the oxygen de-sorption activation energy is surface oxygen vacancy concentration dependent and the oxygen partial pressure has influence on the surface exchange process due to the fact that the surface oxygen vacancy concentration is oxygen partial pressure dependent.

Chapter 5 Development of asymmetric tubular membrane of $La_{0.2}Sr_{0.8}CoO_{3-\delta}/Ce_{0.8}Gd_{0.2}O_{2-\delta}/CeO_2$

The asymmetric tubular ceramic oxygen-electrolyte membrane, $Ce_{0.8}Gd_{0.2}O_{2-\delta}$ (CGO20)/CeO_2, has been successfully fabricated by means of the green tube slurry coating followed by co-sintering. To promote oxygen flux at relatively lower separation temperatures, a thin layer of $La_{0.2}Sr_{0.8}CoO_{3-\delta}$ (LSCO80) was deposited on the outer surface of CGO20/CeO_2. The outcome of density function theory (DFT) simulation shows that the LSCO80 bulk lattice undergoes expansion upon losing oxygen, which provides a theoretical explanation for the crystalline distortion induced by high calcination temperature.

5.1 Introduction

To date, realization of industrially viable asymmetric tubular ceramic oxygen-permeable membranes with high oxygen permeation still face economical or fabrication technological challenge, i.e., high preparation costs incurred by multiple-sintering steps or by employing physical or chemical vapor deposition means, and the technological difficulties to get rid of cracks in ceramic membranes during preparation and operation processes (Adler, 2004). Decreasing active membrane separation layer thickness is an effective way to boost the membrane oxygen permeability.

Cubic fluorite type ceria-based materials have drawn vital attentions due to their higher ionic conductivities than the stabilized zirconia and better stability at reducing atmosphere than the perovskite type La-Sr-Co-Fe oxides. The properties of the doped or pure ceria have been thoroughly studied and proven to be the mixed ionic/electronic conductors (Section 2.1.2.2 of Chapter 2). The oxygen ionic conductivity of the ceria-based oxides comes from the occurrence of Ce^{3+} ions or doping ions with lower valences (e.g., Gd^{3+}, Sm^{3+}, Ca^{2+} & Mg^{2+}) since these low-valence metal ions induce oxygen vacancies (Zhao & Jorte, 2004; Zhang et al., 2004b). At low oxygen partial pressure or reducing atmosphere the ceria-based oxides are *n*-type semiconductors, while when the oxygen partial pressure goes to about 1 bar the electronic conductivity turns into *p*-type in the temperatures range of 600 ~ 800 ^{o}C (Mogensen et al., 2000). Besides mixed-conducting property, the doped-ceria has very similar coefficient of thermal expansion (CTE) to pure CeO_2 or another type of doped ceria, therefore the ideal support for doped-ceria membrane is pure CeO_2 or doped ceria, and also the green body of both can be co-fired to save energy and time.

The doped-ceria has by far been used almost exclusively as the anode and electrolyte materials for intermediate temperature solid oxide fuel cells (IT-SOFCs). However, the aforementioned properties also offer the doped-ceria materials a great potential of being as oxygen permeable ceramic membranes without expensive external circuit for air separation and for catalytic reforming of natural gas when coupled with a partial oxidation catalyst system. In this chapter, a dense $Ce_{0.8}Gd_{0.2}O_{2-\delta}$ (CGO20) membrane on a porous CeO_2 tubular support is configured for performing oxygen separation from air. On this basis, since the perovskite $La_{1-x}Sr_xCoO_{3-\delta}$

(LSCO) is regarded as a highly reactive oxide ion transport material (Section 2.1.2.1 of Chapter 2), the CGO20 membrane is further topped up with a thin LSCO80 ($La_{0.2}Sr_{0.8}CoO_{3-\delta}$) coating layer to augment oxygen permeability. In addition, a theoretical analysis using density function theory (DFT) has been carried out to assess the experimental results.

5.2 Experimental

5.2.1 Preparation of ultra fine ceramic powders and coating suspensions

(a) Stoichiometric amount of metal nitrate salts of $Ce(NO_3)_3{\cdot}6H_2O$ (99%, Aldrich) and $Gd(NO_3)_3{\cdot}6H_2O$ (99.9%, Aldrich) by 4:1 molar ratio; or (b) $La(NO_3)_3{\cdot}6H_2O$ (> 99.9%, Aldrich), $Sr(NO_3)_2$ (> 99.9%, Aldrich), and $Co(NO_3)_2{\cdot}6H_2O$ (> 99.9%, Aldrich) by 1:4:5 molar ratio were dissolved respectively in an EDTA-ammonia aqueous solution (pH 8~9) with stirring. The molar ratio of metal ions to EDTA was 1:1 in these two batches. A dark-brown solution was obtained, and a small amount of polyvinylalcohol (PVA, 87-89% hydrolyzed, Mw: 13,000-23,000, Aldrich) (ca. 5 wt.% of EDTA) was then dissolved in the solution. Gelation occurred while both solutions were concentrated at 80 ~ 100 ^{o}C. The resulting metallo-organic gels underwent pyrolysis and finally combustion at 400 ^{o}C, leaving metal oxide powders. CGO20 powder was calcined under air (100 l/h) purging at 750 ^{o}C of 1 h, and LSCO80 powder was calcined under air purging at 900 ^{o}C of 2 h in a Carbolite furnace. After this, the two kinds of powders were grounded and sieved through a 45 μm pore size sieve. The coating suspension was formulated by adding 15 wt.% of ceramic powder (CGO20 or LSCO80) into an organic solution containing a variety of additives similar to those used in Section 4.2.3 of Chapter 4. It was followed by ball-milling the slurry formed with zirconia balls (Fisher Scientific) for 3 days to generate the ceramic ink-like suspension. The primary particle sizes of these two powders were found to fall in submicron or even nano range (Fig. 4.5 in Chapter 4 & Fig. 5.1).

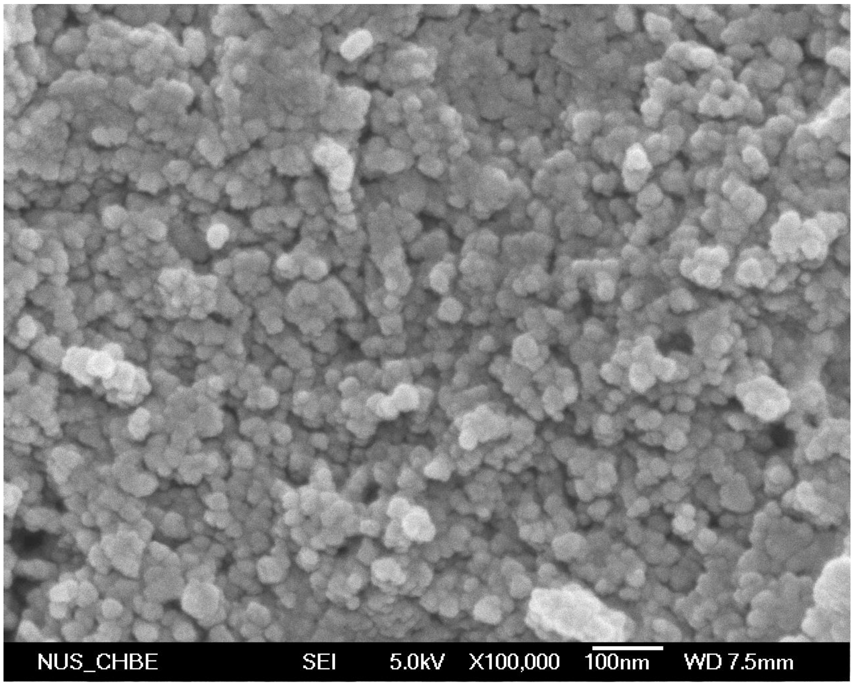

Figure 5.1 FESEM of the fabricated sub-micron CGO20 powders

5.2.2 Fabrication and sintering of green composite tube

A mixture of 30 g polymers or organic additives (Table 4.1 in Chapter 4) and 170 g CeO_2 powder were used to fabricate a green CeO_2 tube. The preparation and extrusion of the ceramic-polymer blend have been described in Section 4.2.1 of

Chapter 4 in details. After drying for one week at room temperature, the green CeO_2 tube was brushed on exterior surface with the CGO20 colloidal suspension and dried for overnight at room temperature. The dried green composite tube was heated in a Carbolite furnace using a very slow heating rate (0.1 ^oC/min) to 400 ^oC and dwelled for 1 h to burn off the organics, and the next dwell at 1600 ^oC was reached by 1 ^oC/min, where the tube was sintered for 1 h. The LSCO80 suspension was applied to the surface of CGO20 membrane as the second COMR coating layer and brought to sintering at different temperatures (1100 ^oC ~ 1300 ^oC) for 3 h since LSCO80 coating gains sufficient adhesion strength and remains stable in this temperature range.

5.2.3 Impedance spectroscopic analysis

Yttria stabilized (15 mol.%) zirconia (YSZ) cylindrical disks were prepared by sintering pellets of YSZ (99.9% Aldrich) at 1400 ^oC for 3 h. The LSCO80 disks were made by sintering 3 h at different temperatures (1100, 1200 and 1300 ^oC), and CGO20 disk was made by sintering 3 h at 1600 ^oC. All the as-pressed pellets have approximate diameter of 1.6 cm and the sintered pellets have the diameter between 1.3 cm and 1.5 cm. The specimens were carefully polished to make sure of a smooth surface before the impedance measurement.

Figure 5.2 showed the cell configuration for the impedance measurement. An Al_2O_3 sample holder was designed to fasten the disks together via screwing the holder. The packed electrochemical cell was placed in a furnace and connected to the Solartron

1260 impedance analyzer. The impedance measurements (over the frequency from 70 Hz to 3×10^7 Hz) were taken in the temperature range of 600 ~ 900 °C.

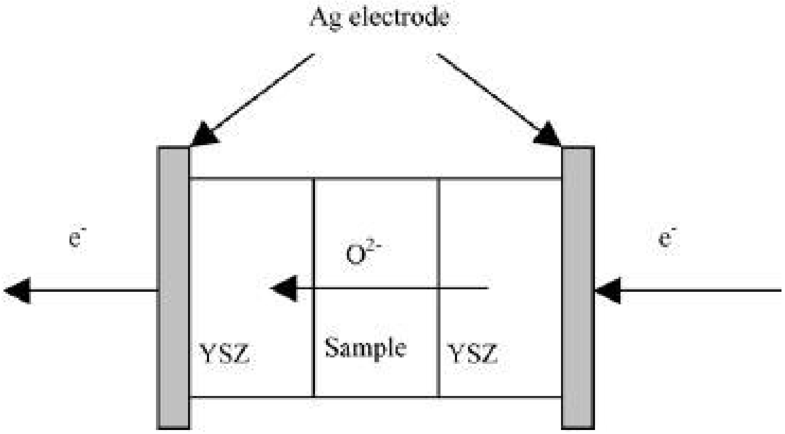

Figure 5.2 Schematic of the electrochemical cell configuration

5.2.4 Oxygen permeation test and instrumental characterizations

The setup for assessing oxygen permeation flux has been described in Section 4.2.5 of Chapter 4. XRD analysis (Section 4.2.4 of Chapter 4) and SEM (or FESEM) (Section 4.2.4 of Chapter 4) were employed to examine the crystalline phases and the morphologies, respectively.

5.3 Results & Discussion

5.3.1 Structural stability of the ceramic powders

The XRD patterns of the LSCO80 powder (Fig. 5.3a), the CGO20 powder (Fig. 5.3b), and a mixture of LSCO80 (30 wt.%) and CGO20 (70 wt.%) (Fig. 5.3c) are determined at room temperature to investigate influence of calcinations temperature on their crystal structures. The samples were sintered at different temperatures for 3 h. For LSCO80, crystal grains of perovskite phase grow with increasing calcinations temperatures from 1000 ^{o}C to 1200 ^{o}C, and the crystal structure undergoes a slight variation when calcinations temperature is pushed up to 1300 ^{o}C. The major peaks shift a bit to the low two-theta or the high *d* spacing direction, which represents an increase in lattice length along a particular crystallographic direction (e.g., at 1100 ^{o}C the *d* value of (110) is about 3.735 Å, while at 1300 ^{o}C it increases to 3.844 Å). In addition, the peaks of (111) and (220) faces disappear after the sample was sintered at 1300 ^{o}C. It has been found that the perovskite $La_{1-x}Sr_xCoO_{3-\delta}$ ($x > 0.65$) contained certain amount of the local tetragonal ($\boldsymbol{a}_p \times \boldsymbol{a}_p \times 2\boldsymbol{a}_p$) supstrucutre, which has very small domain size such that it is very difficult to be detected by XRD (James et al., 2004). It seems that the content of the local tetragonal superstructure increases as the sintering temperature increases. On the other hand, the CGO20 exhibits the stable fluorite structure at temperature from 760 ^{o}C to 1600 ^{o}C. The calcination of the mixture of LSCO80 and GCO20 at 1300 ^{o}C produces no new XRD peaks, indicating that interfacial reactions between these two material phases are negligible.

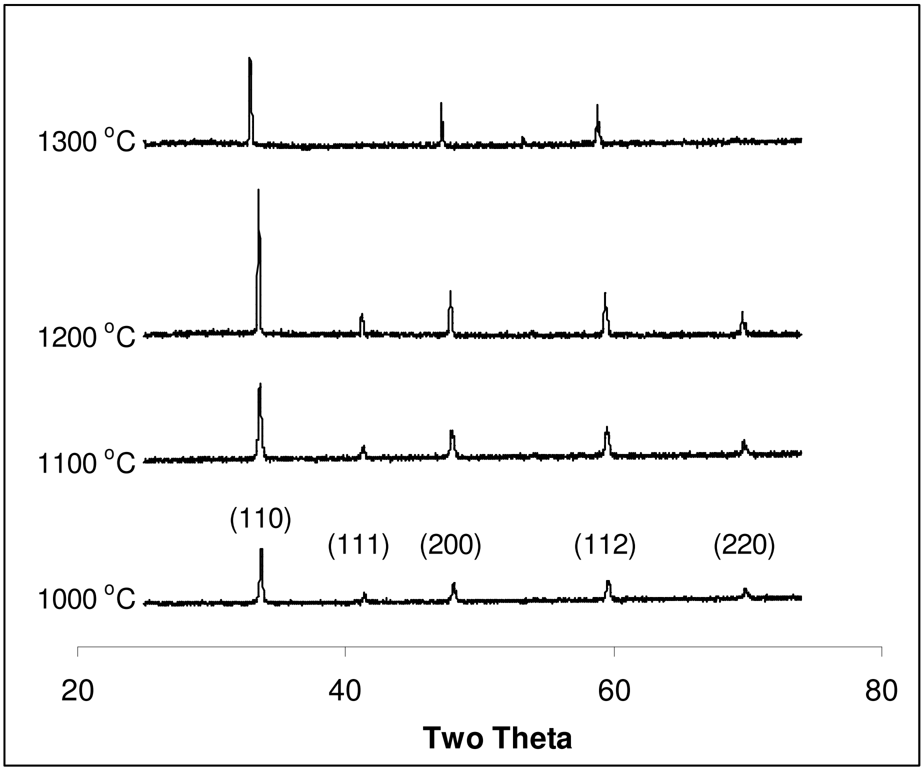
1300 °C
1200 °C
1100 °C
1000 °C
(110)
(111)
(200)
(112)
(220)
20
40
60
80
Two Theta

(a)

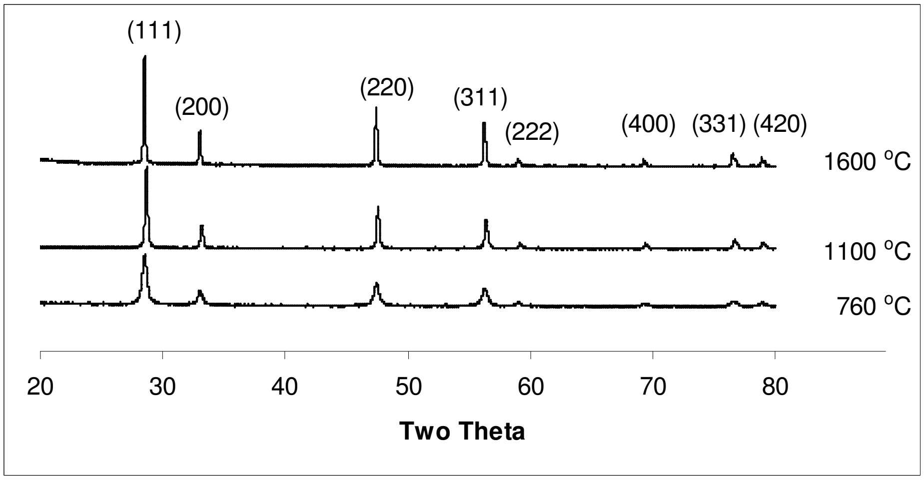
(111)
(200)
(220)
(311)
(222)
(400)
(331)
(420)
1600 °C
1100 °C
760 °C
20
30
40
50
60
70
80
Two Theta

(b)

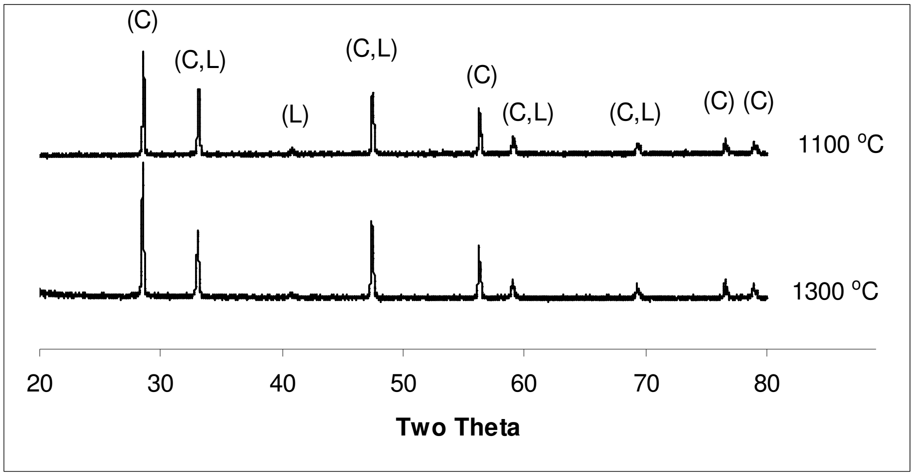

(c)

Figure 5.3 XRD profiles of the ceramic powders after sintering for 3 h at different temperatures: (a) LSCO80; (b) CGO20; (c) mixture of LSCO80 and CGO20 (C stands for CGO20 and L stands for LSCO80)

5.3.2 Influence of CGO20 loading on the co-sintered CGO20/CeO_2 structure

The bulk morphology of the co-sintered CGO20/CeO_2 tube at near exterior surface is found to change clearly with the loading of the CGO20 on CeO_2 tube, which is the amount (g) of CGO20 used to coat per exterior surface area (cm^2) of CeO_2 green tube (Figs 5.4 a & b). It can be seen that with a low loading (i.e., 0.001 g CGO20/ cm^2 CeO_2 green tube) the co-sintering brings about a porous structure from the exterior surface to the bulk (Fig. 5.4a). However, when the loading is increased to 0.005 g CGO20/cm^2 CeO_2 green tube, a triple-layer structure, namely porous/dense/porous (Fig. 5.4b), is generated. Since the mean particle size of CGO20 in the coating suspension (Fig. 5.1) (~ 30 nm) is much smaller than that of the CeO_2 powder (~ 4.8 μm) used to make the support, a large portion of CGO20 particles are likely to slip into interstices of CeO_2 particles while the polymer binders are burning out. As there is a much higher amount of polymers in the green body of CeO_2 support than in the CGO20 coating layer, given a very slow heating rate, it takes an even longer time of combustion to remove the organic component in the bulk of CeO_2 tube than in the CGO20 coating layer, and therefore during this process smoke coming out would continuously shuffle fine CGO20 powders seating on the top and juggle them with gaps generated in the CeO_2 support. This filling is driven by capillary attractive action. Consequently, a significant part of CGO20 particles are moved down into the CeO_2 phase due to this "sieving and filling" action. Only when the CGO20 residing on the ceria tube is over a certain loading level, i.e., 0.005 g CGO20/cm^2 CeO_2 green tube, were the CGO20 particles sufficient to form a packing layer slightly underneath the exterior surface of the CeO_2 support. Too high a CGO20 loading is undesirable as it will result in thick dense film layer and would ultimately reduce oxygen permeability. Furthermore, in the high temperature stage up to 1600 ^{o}C, there must have been a diffusion of Gd(III) ions from CGO20 towards the neighboring CeO_2 to form the $Ce_{1-x}Gd_xO_{2-\delta}$ ($x < 0.2$) solid solution. At the same time, a large extent of CeO_2 tube shrinkage (15 ~ 20%) strongly pushed the densification of $Ce_{1-x}Gd_xO_{2-\delta}$ phase trapped inside the porous CeO_2 bulk phase.

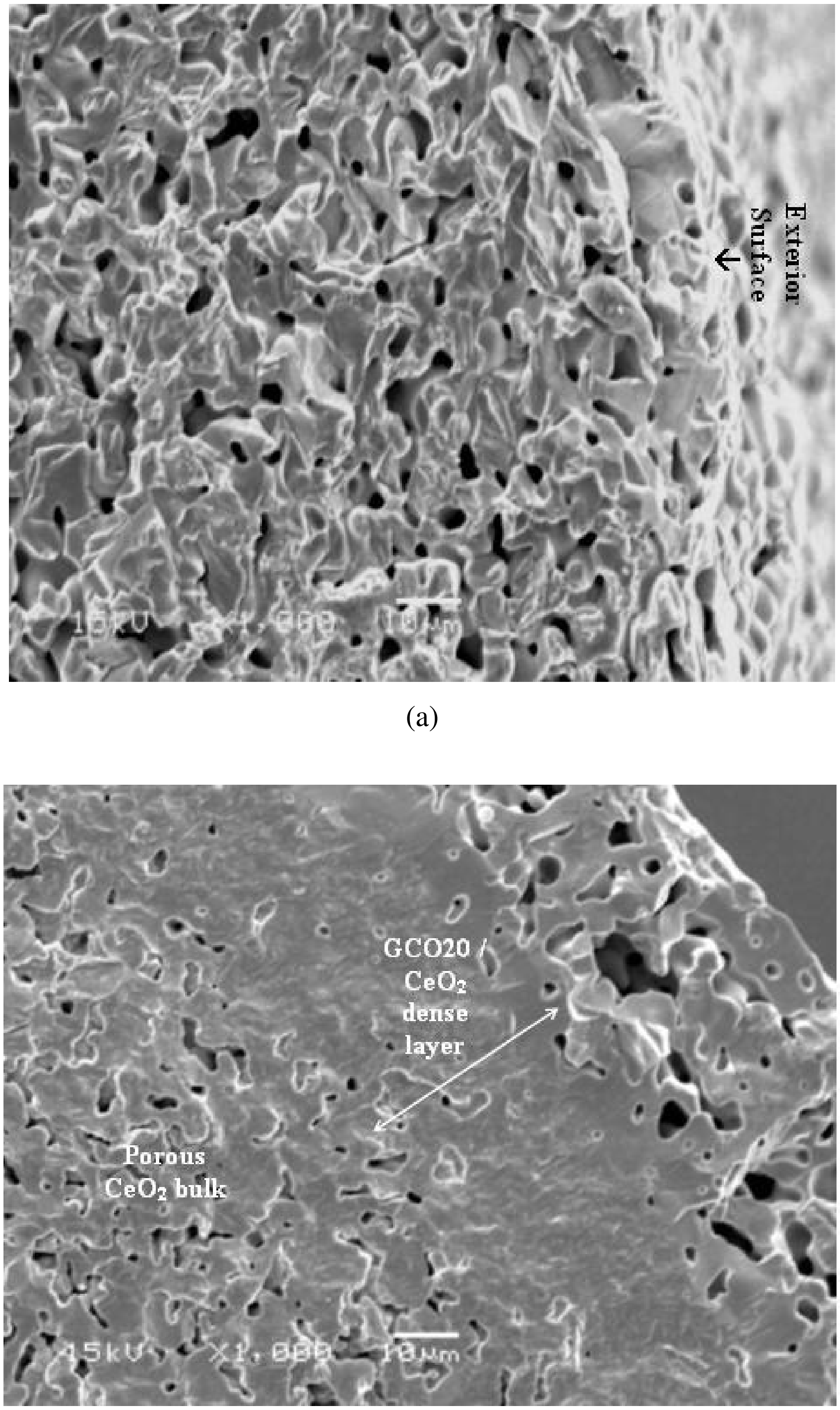

(a)

(b)

Figure 5.4 Cross-sectional SEMs of the co-fired CGO20/CeO_2 tubes with different CGO20 loadings (g /cm^2 CeO_2 green tube): (a) 0.001; (b) 0.005

The exterior surface of the sintered CGO20/CeO_2 tube (Fig. 5.5a) is less porous than the cross sectional part beneath the surface (Fig. 5.4b). The higher sintering degree at surface is caused by the thermodynamic tendency to reduce the surface energy. A thin layer of LSCO80 was added to the sintered CGO20/CeO_2 surface (the image of Fig. 5.5a, namely 0.005 g CGO20/cm^2 CeO_2 green tube) to promote oxygen permeability. This combination is feasible since both LSCO80 and CGO20 do not react with each other at the high temperatures (Fig. 5.3c). It turned out that the LSCO80 coating layer became less rough with increasing of the sintering temperature and in the end realized dense grain-boundary morphology at 1300 ^oC (Figs 5.5 b-d) (LSCO80-1100 means that the coated LSCO80 is sintered at 1100 ^oC for 3 h).

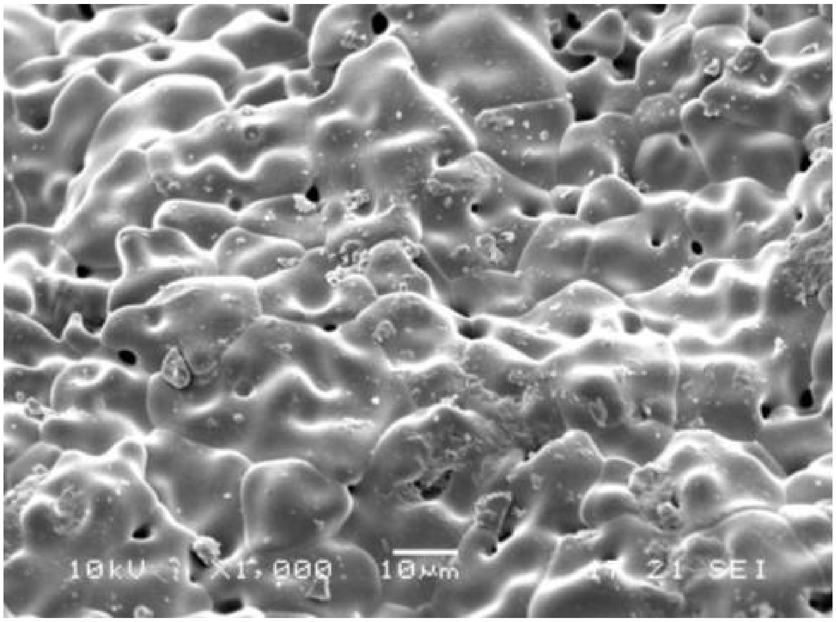

(a)

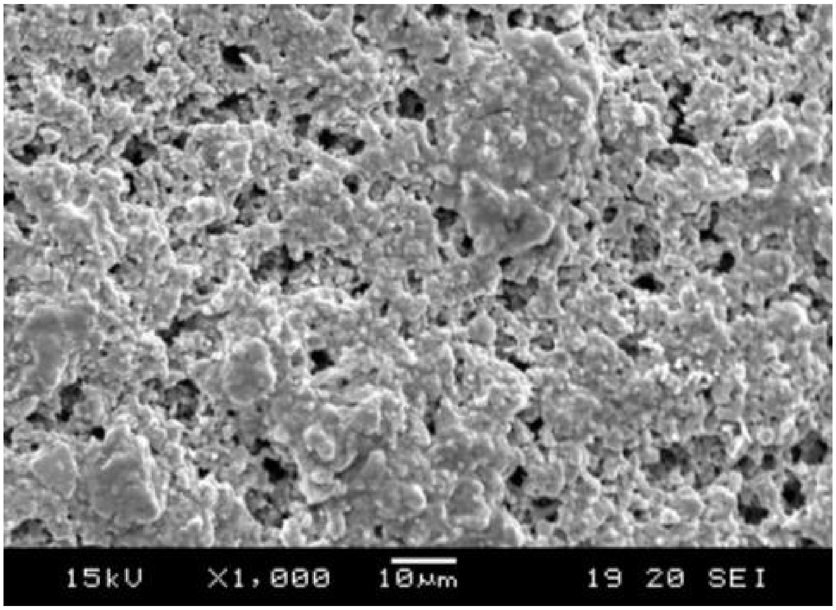

(b)

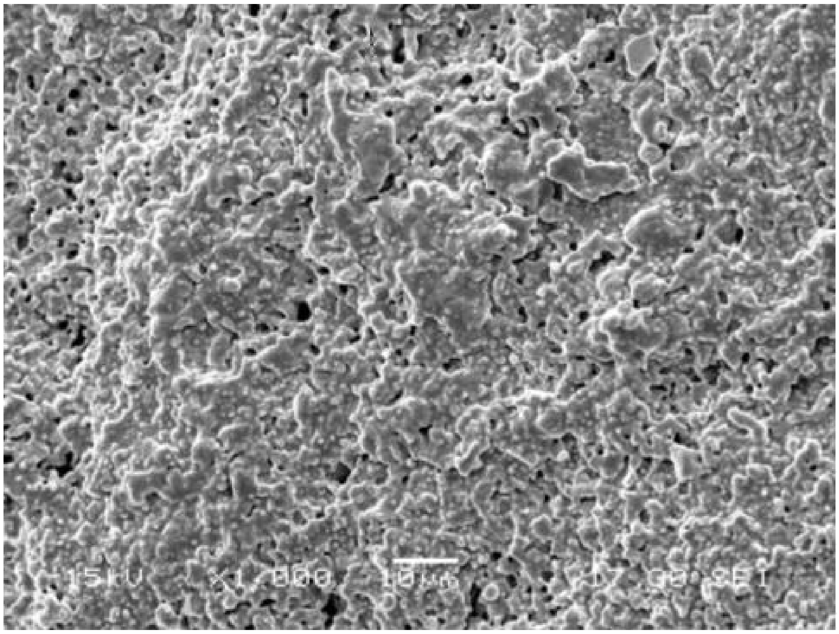

(c)

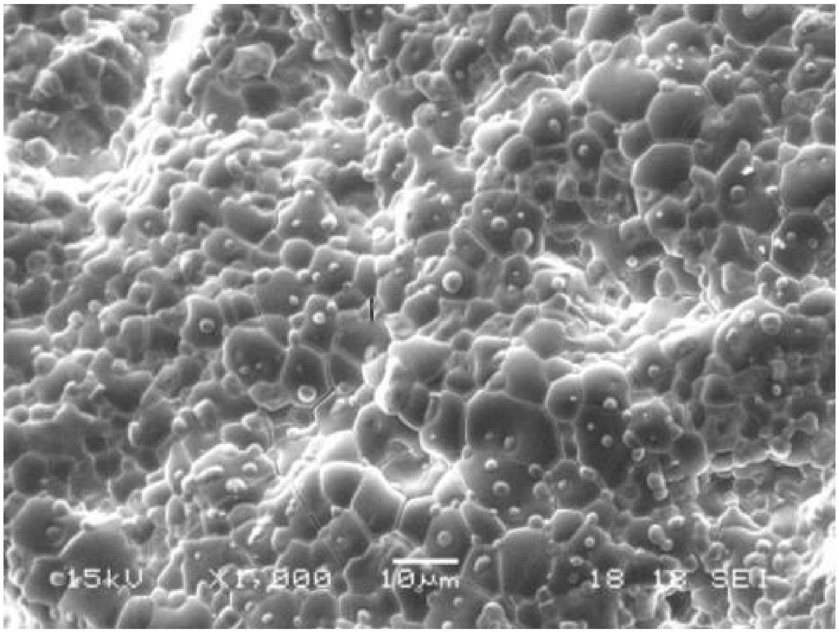

(d)

Figure 5.5 Outer surface SEMs of the fabricated membranes: (a) CGO20; (b) LSCO80-1100; (c) LSCO80-1150; (d) LSCO80-1300

5.3.3 Oxygen permeation through the dual-layer asymmetric membrane

Figure 5.6 shows the oxygen permeation flux of the four types of the fabricated asymmetric tubular membranes at different measurement temperatures. The membrane indicated as LSCO80-1100 (the LSCO80 coating layer was calcined at 1100 °C for 3 h and the resulting surface characterized by Fig. 5.5b) displays a higher oxygen permeability in a broad temperatures range (below 830 °C) and lower permeation activation energy than the membrane of CGO20/CeO_2 (Fig. 5.5a). The porous LSCO80 layer functions to facilitate the surface oxygen exchange or the chemical reduction of oxygen molecules, because LSCO80 has higher (oxygen ionic and electronic) conductivity and faster surface oxygen exchange rate than CGO20.

Nevertheless, adsorption of oxygen molecules becomes more difficult with increasing temperature of the testing system, and hence the surface exchange becomes less important than the bulk oxygen ion transport to the oxygen permeation outcome. As a result, these two factors trade off at 830 °C.

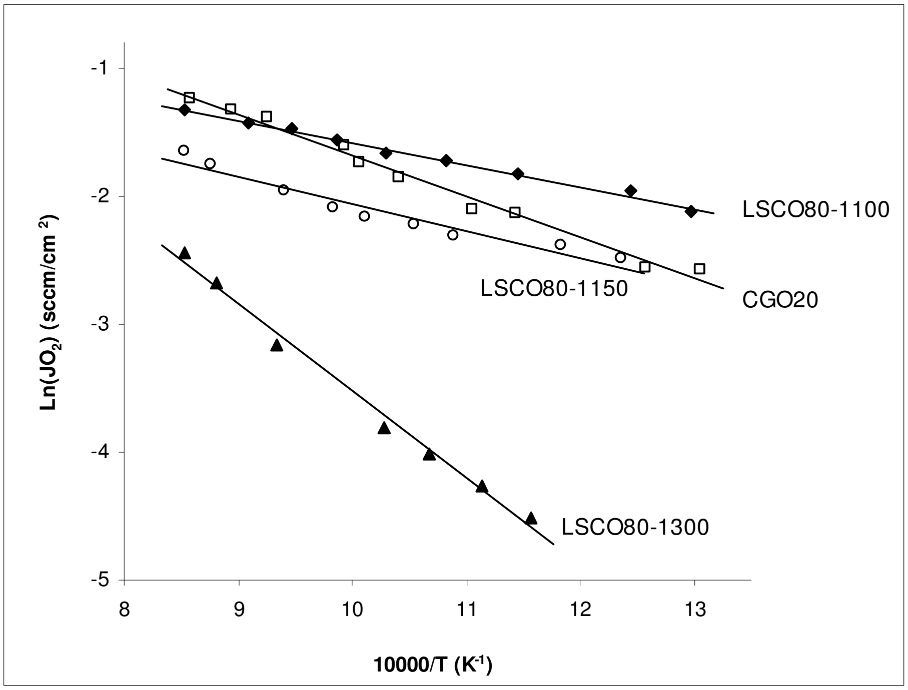

Figure 5.6 Temperature dependence of the oxygen permeation of the respective fabricated membranes

When the LSCO80 topping layer becomes less rough or less porous (Fig. 5.5c) because of the increase in grain sizes driven by the higher sintering temperature, this layer functions counter-productively, namely the oxygen permeability of this double-layer membrane is lower than the single layer (CGO). The reason for this is that the population of oxygen adsorption sites located at grain boundary area, imperfections, steps, and grooves reduces with increasing sintering extent, on the other hand, diffusion of oxygen ions is often much faster at grain boundary than through the bulk diffusion of a grain (Bouwmeester, 2003). This is because the boundary region has higher oxygen vacancy concentrations and therefore permits higher oxygen ion mobility, namely, there is an intrinsic correlation between the equilibrium surface oxygen exchange rate and the bulk oxygen vacancy diffusion rate (James et al., 2004). Consequently, the conversion of fractal surface to a less rough surface diminished the total oxygen diffusion activity within the LSCO80 layer and resulted in lower oxygen permeation and higher activation energy. Sintering of the LSCO80 coating at 1300 ^{o}C yielded a denser and smoother surface (Fig. 5.5d) relative to the other two obtained from the lower sintering temperatures; this membrane reveals a big drop in oxygen permeability compared with the other three membranes. Besides the dull surface morphology, an increase in the content of the local tetragonal superstructure in the LSCO80 perovskite structure as shown in its XRD pattern (Fig. 5.2a) would also likely contribute to this outcome. As far as the reduction procedure of oxygen at the membrane is concerned, oxygen molecules firstly undergo disassociating adsorption on the LSCO80 surface and generate surface-polarizing species O^{n-}, which is then incorporated into the CGO20 layer through mainly two pathways (Adler, 2004), either migrating to the triple-phase (LSCO80-CGO20-oxygen gas) boundary (TPB), where it is reduced to O^{2-}, or being reduced to O^{2-} in the LSCO80 bulk and then drifting toward the LSCO80/CGO20 interface.

5.3.4 Oxygen conductivity of LSCO80 and CGO20 – impedance investigation

The oxygen ionic conductivity measurement offers a complementary approach to the study of oxygen permeability. The electronic conduction is blocked by YSZ, which has negligible electronic conductivity in nature (Fig. 5.2), and the measurement reflects only oxygen ionic conductivity (Fig. 5.7*a*). On the experimental impedance spectrum obtained, the low frequency end of the arc (e.g. $R_{C_t} \cong 2600\ \Omega$ / 59.9 kHz at 700 °C), which assesses the resistance to mass transfer of O^{2-} ions at the interface of electrode and is therefore the measure of oxygen ionic conductivity, shifts to the low ohmic resistance direction with increasing the measurement temperature. It follows the generic trend that ionic conduction in a solid electrolyte is temperature-propelled. For an example, the assembly YSZ/LSCO80/YSZ exhibits $R_{C_t} \cong 750\ \Omega$ at 800 °C but $R_{C_t} \cong 250\ \Omega$ at 900 °C, in which LSCO80 makes the main contribution to oxygen ionic conduction (Liu & Hong, 2003).

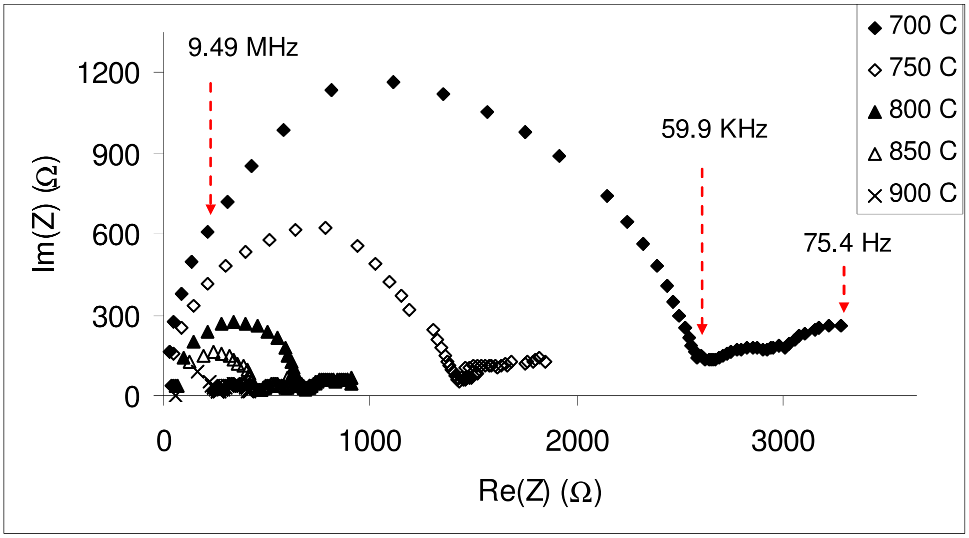

(a)

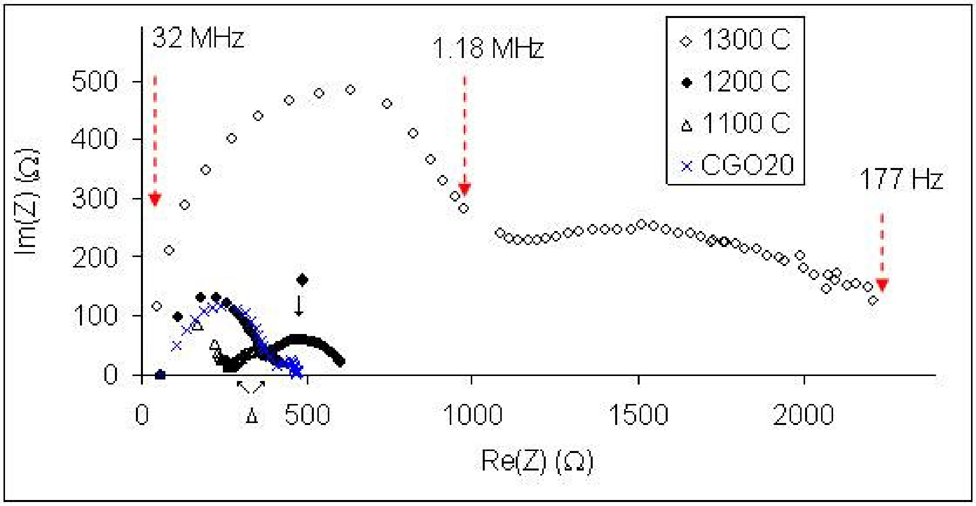

(b)

Figure 5.7 Complex impedance plots: (a) temperature effect on the O^{2-} ionic conduction in LSCO80 pellet, which was made by sintering at 1100 °C for 3 h prior to the measurement; and (b) effect of sintering extent of the LSCO80 pellet on the O^{2-} ionic conduction in it, the measurement was conducted at 900 °C

As concluded above according to the oxygen permeation testing result, increasing sintering temperature of LSCO80 (from 1100 °C to 1300 °C) will push down the oxygen ionic conduction rate because of the merging of grains, which results in less boundary conduction. This trend could also be replicated by the means of impedance analysis. The measurement was performed at 900 °C (Fig. 5.7*b*); the difference in R_{Ct} caused by increasing sintering temperatures from 1100 °C to 1200 °C is about 250 Ω versus 400 Ω. In contrast to these two specimens, sintering at 1300 °C leaves LSCO80 a much greater R_{Ct}. This big gap is consistent with the oxygen permeation measurement (Fig. 5.6), wherein membrane LSCO80-1300 shows a clearly lower O_2 permeability; that decrease is ascribed to the earlier structural distortion. The oxygen ionic conductivity of CGO20 sintered at 1600 °C for 1 h has also been assessed at the same conditions; it locates at somewhat behind that of LSCO80 sintered at 1200

^{o}C for 3 h. In comparison with the oxygen permeation testing result, the CGO20/CeO_2 membrane performs better than the dual-layer membrane LSCO80-1150 (Fig. 5.6). This reverse order might be due to the fact that oxygen ions need to pass the dual layer junction in the LSCO80-1150 membrane.

5.3.5 Simulation of the oxygen surface exchange of LSCO-80

This work also attempts to apply density functional theory (DFT) (Payne et al., 1992) to approximately describe the ground-state perovskite lattice parameter of LSCO80. Two super-cells (models *a* and *b* in Fig. 5.8) are coined in this study to simulate the ground-state equilibrium lattice length. Figure 5.8*a* represents the $La_{0.125}Sr_{0.875}CoO_{3-\delta}$ crystal without any oxygen vacancy (i.e., $\delta = 0$) whereas Fig. 5.8*b* contains presumably the maximum oxygen vacancy number with $\delta = 0.125$. In order to find the ground-state equilibrium lattice constant of the cubic LSCO lattice, the total-energy calculations at different lattice length (using model *a*) are performed; the results construct a smooth curve (Fig. 5.9). The minimum value of the total energy gives out the ground-state equilibrium lattice length *d* of about 4.4 Å in model *a* and 4.8 Å in model *b*. This theoretical result is obtained from the ground state approximation; it could be extended to describe the structure distortion at the high temperature caused by elimination of surface lattice oxygen (Sitte et al., 2002; Bucher et al., 2001). One also expects on the basis of this result the generation of composition stress in a thick LSCO membrane as long as there is a gradient of oxygen vacancy concentration from surface to bulk, which would bring about structural cracks.

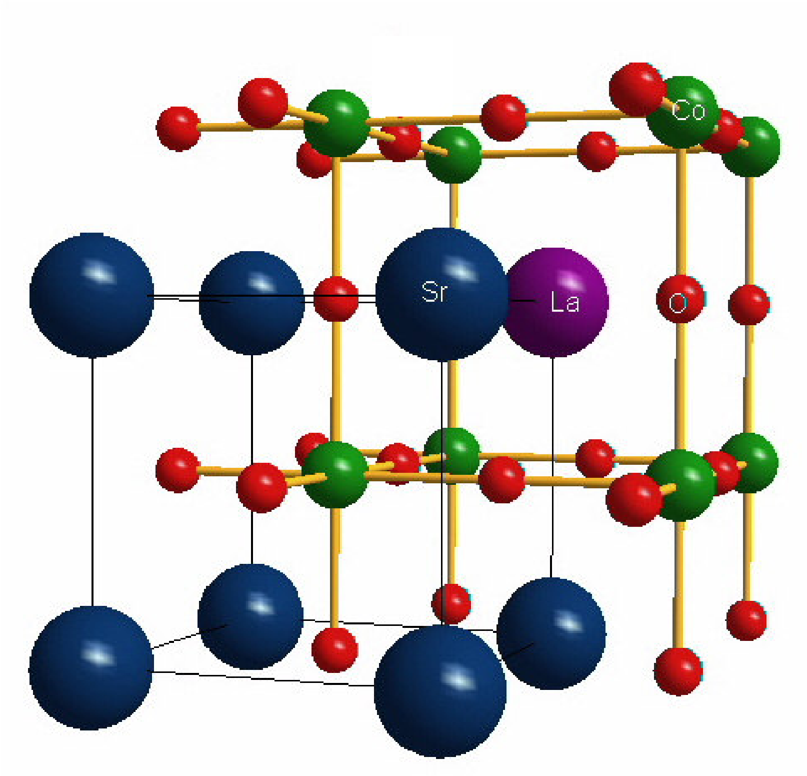

(a)

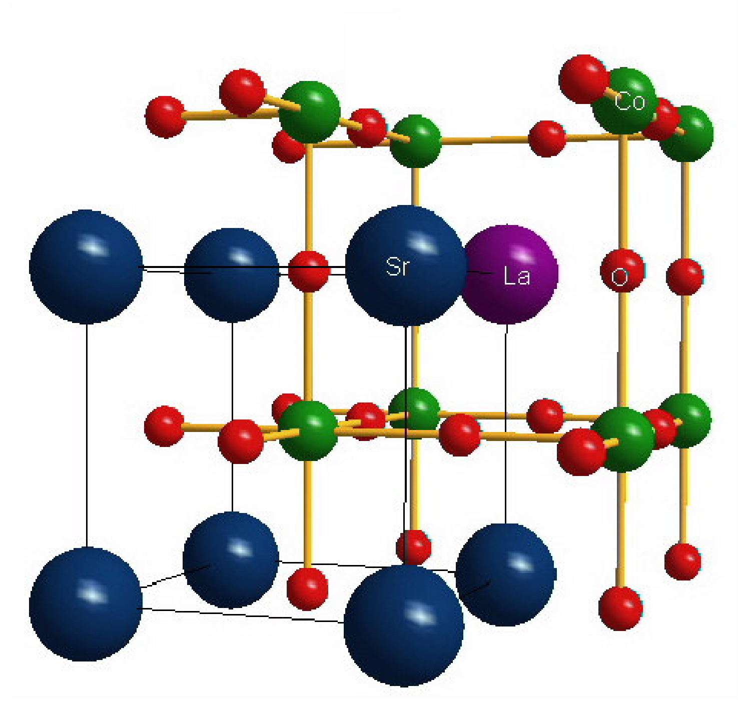

(b)

Figure 5.8 Cluster models: (a) $LaSr_7Co_8O_{24}$; (b) $LaSr_7Co_8O_{23}$

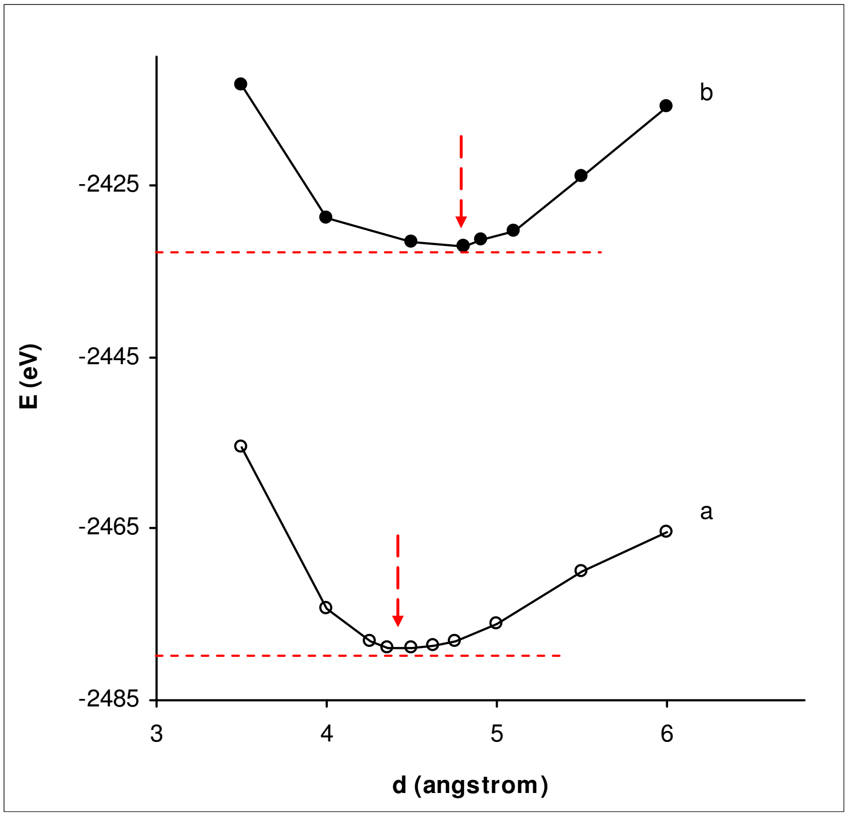

Figure 5.9 Dependence of the calculated ground-state energy of the cubic LSCO80 on its crystal lattice length

5.4 Conclusions

A dual-layer oxygen transport membrane $La_{0.2}Sr_{0.8}CoO_{3-\delta}/Ce_{0.8}Gd_{0.2}O_{2-\delta}$ (LSCO80/CGO20) has been prepared on a tubular CeO_2 support via a two-step procedure: (1) coating CeO_2 green-body tube with a thin CGO20 powder layer and carrying out co-sintering at 1600 °C for 1 h to form an asymmetric membrane structure CGO20/CeO_2; (2) coating a layer of LSCO80 on CGO20/CeO_2 and sintering it 3 h to realize the dual layer configuration. In step 1, the CGO20/CeO_2

displays a unique sintered structure with a dense CGO20 layer being embedded slightly below the porous tube surface. In step 2, the LSCO80 layer exhibits three different surface morphologies resulted from varying its sintering temperature (at 1100, 1150 and 1300 °C respectively), which correspondingly give rise to three oxygen permeation activation energy values. Only the one with the lowest sintering temperature could lead to a better oxygen permeation performance than the single-layer membrane CGO20/CeO_2 because of its very rough surface morphology. The XRD analysis shows that the perovskite LSCO80 and the cubic fluorite CGO20 are stable at the above three sintering temperatures. However, the highest temperature causes tetragonal distortion in this oxide. Impedance measurement also shows that the reverse effect of the LSCO80 sintering temperature on the oxygen ionic transport and the surface oxygen exchange. The density function theory has been applied to simulate the equilibrium ground-state lattice length of LSCO having different oxygen vacancies. The calculated lattice length increases with increasing the oxygen vacancy concentration.

Chapter 6 Crafting $La_{0.2}Sr_{0.8}MnO_{3-\delta}$ membrane with dense surface from porous YSZ tube

This work reports a low cost method (i.e., ceramic-metal composite dip coating followed by solution plugging) to fabricate a thin gas-tight mixed conductive membrane, i.e., $La_{0.2}Sr_{0.8}MnO_{3-\delta}$ (LSM80)-Ag(Pd), on the porous Y_2O_3 stabilized ZrO_2 (YSZ) tube surface. The Ag(Pd) alloy component promotes not only electronic conductivity and mechanical strength but also reduction of both porosity and pore sizes in the layer (~10 μm thick) where it dopes. The porous structure in this layer could then be closed through a solution coating procedure, by which ingress of an aqueous solution containing stoichiometric nitrate salts of La^{3+}, Mn^{3+} and Sr^{2+} to the pore channels takes place firstly and the mixture of nitrate salts left after drying is subjected to pyrolysis to generate tri-metal oxides in-situ.

6.1 Introduction

As a POM reactor or a SOFC, the COMR is required to possess both high oxygen permeability and chemical stability in the reducing atmosphere at high reaction temperature (800 ~ 900 ^{o}C). These two major features are crucial to real applications (Figueiredo et al., 2004; Armstrong et al., 2001). A “trade off” may exist between the material oxide ionic conductivity and stability. Fortunately, the oxygen permeability can be improved by decreasing the thickness of the nonporous oxygen-electrolyte membrane layer until its characteristic thickness since that the oxygen permeation flux is inversely proportional to the membrane thickness (Eq. 2.4). An asymmetric membrane structure provides the possibility to offer both high oxygen permeation and membrane stability by making the thin nonporous selective layer with the ceramic materials with high stability under reducing atmosphere.

This work proposes a new type of low-cost wet chemistry method that combines dip coating and solution coating methods for the fabrication of an asymmetric COMR. $La_xSr_{1-x}MnO_{3-\delta}$ (LSM), Ag(Pd) and YSZ were selected as the membrane materials due to their high chemical, mechanical, and thermal stability in the reducing atmosphere. The Ag(Pd) alloy component promotes not only electronic conductivity and mechanical strength but also reduction of both porosity and pore sizes in the layer where it dopes. An asymmetric structure was designed to achieve high oxygen permeability. Perovskite-type LSM has been well known to be the porous cathode in conjunction with YSZ electrolyte in SOFCs, because they have excellent chemical compatibility and rather close TECs (Wandekar et al., 2005). LSM has relatively a high electronic conductivity but a low oxygen ionic conductivity while YSZ is almost a pure oxygen electrolyte. It was reported that the oxygen diffusivity of LSM can be significantly improved by forming a composite with YSZ, and the composite has a higher effective oxygen surface exchange coefficient than either component (Ji et al., 2005). An alternative design based on using these two materials is attempted in the following work, in which the main technical progress achieved is the implantation of a dense LSM-Ag(Pd)-YSZ membrane layer on porous YSZ tube by means of a simple approach and the fabricated membrane exhibits oxygen permeability at the level it should reach at the designated temperature point.

6.2 Experimental

6.2.1 Fabrication of porous tubular YSZ support

The details about the preparation of a ceramic-polymer blend for the extrusion of ceramic tube were described in Chapter 4. Table 6.1 lists the recipe of YSZ-polymer blend for extrusion. The extruded tube is placed in a Carbolite furnace and heated up (by 1 ^{o}C/min) to 400 ^{o}C and dwelled there for 1h to burn off the polymers, and then the calcinations temperature is raised to 1400 ^{o}C (by 2 ^{o}C/min) and held for 30 min to carry out sintering in the YSZ bulk. The sintered YSZ tube is porous (Fig. 6.1) with a porosity of about 31%.

Table 6.1 Chemical composition of the YSZ-polymer composite

Component	Function	Content (wt%)
15 mol.% Y_2O_3 stabilized ZrO_2 (YSZ)	Ceramic	80
Hydroxyethyl Cellulose (HEC) (Mw: 90000)	Pore-former	6
Polyethyleneglycol (PEG) (Mw: 15000)	Binder	12
Polyvinylpyrrolidone (PVP) (Mw: 10000)	Extrusion aid	2

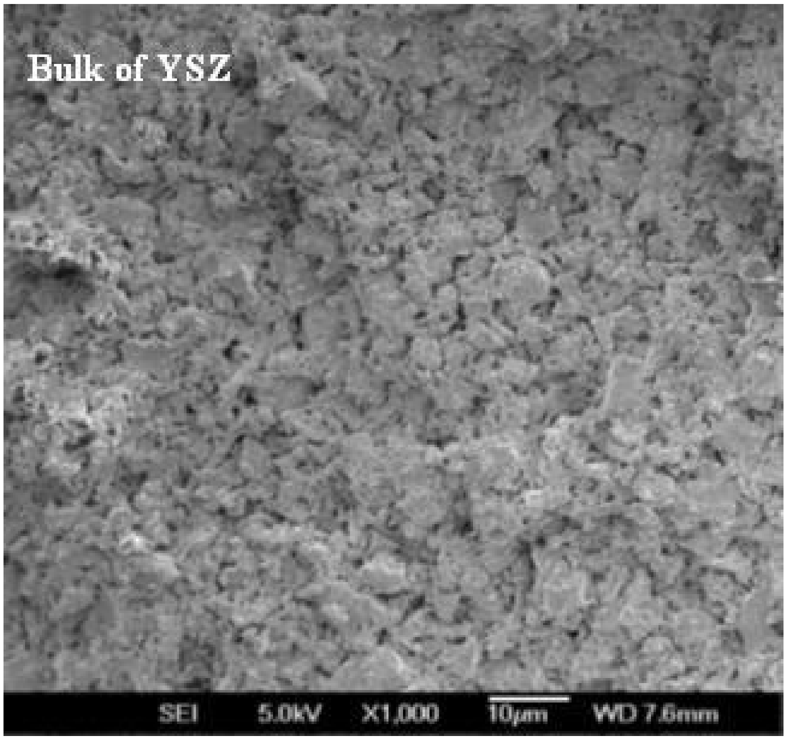

Figure 6.1 Cross-sectional view of the sintered porous YSZ support

6.2.2 Synthesis of fine LSM80 powders and formulation of colloidal suspensions

A Stoichiometric amounts of the three metal salts ($La(NO_3)_3{\cdot}6H_2O$, $C_4H_6O_4Mn{\cdot}4H_2O$ and $Sr(NO_3)_2$) are dissolved in an aqueous solution of $(NH_4)_4$-EDTA (ethylenediamine-tetraacetic acid, 98%, Aldrich) (pH 8~9) with 1:1 of the metal ions to EDTA molar ratio. Polyvinylalcohol (PVA, 87-89% hydrolyzed, Mw: 13,000-23,000, Aldrich) (5 wt.% of EDTA used) is then added and dissolved in the above solution. A gel-like substance is obtained after the solution became thick at 80 ^{o}C and the gel is thereafter subjected to burning at 350~400 ^{o}C to form a composite of the metal oxides. The powder is finally calcined at 900 ^{o}C for 1 h under air flow (100 l/h) in a Carbolite furnace to convert the oxide composite to the perovskite-type

$La_{0.2}Sr_{0.8}MnO_{3-\delta}$ (LSM80). The LSM80 powders are grounded and sieved through a 45-μm pore size sieve, which comprise primarily submicron particles (Fig. 6.2).

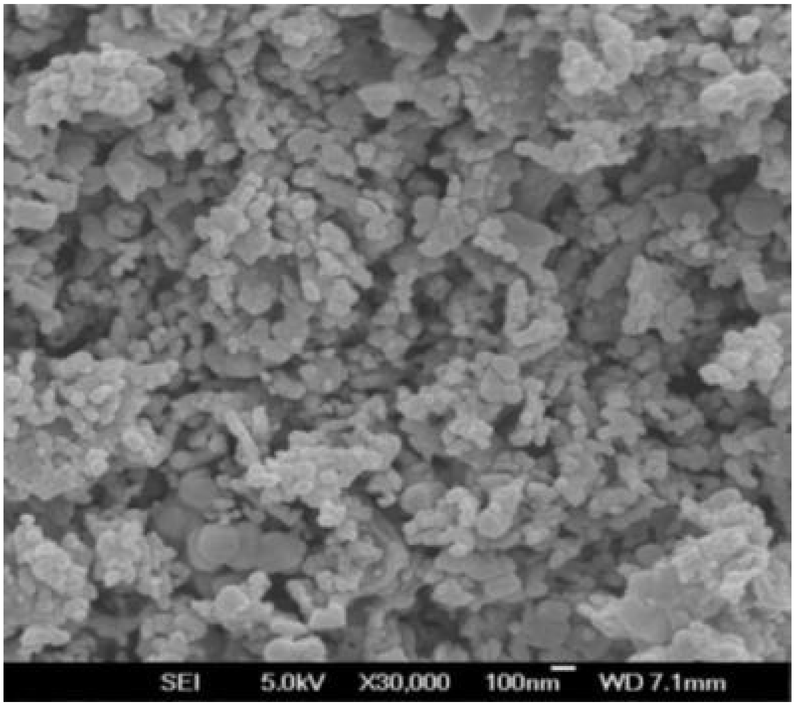

Figure 6.2 Micrograph of the calcined LSM80 fine powders

B A given amount of LSM80 fine powder (5.71 g) is suspended in an aqueous solution (1 l) containing $Pd(NO_3)_2$ (0.12 g), $AgNO_3$ (0.8 g), and PVA (0.71 g). After evaporating off the water at 80 °C, the residue is calcined at 350~400 °C to decompose the nitrates and calcined at 750 °C for 1 h and the product is a fine powder comprising Ag(Pd) alloy-coated LSM80 particles, i.e. Ag(Pd)-LSM80. According to the composition of feed, the dual phase Ag(Pd)-LSM80 contains approximately Ag (8.1 wt.%), Pd (0.9 wt.%) and LSM80 (91 wt.%).

C The colloidal suspension of either LSM80 or Ag(Pd)-LSM80 is formulated via the procedure described in chapter 4. The ink-like colloidal suspension consisting of 150 g/l LSM80 or Ag(Pd)-LSM80 powder, 6.25 g/l polyvinylbutyral (Butiva-79), 6 ml/l fish oil, 3 ml/l dibutyl phthalate and 3 ml/l Span-80. A mixture of toluene and methylethylketone (v/v=1:1) was employed as the solvent. The resulting suspensions are ready to perform dip-coating.

6.2.3 Asymmetric tubular membrane preparation

A The porous YSZ tube is blocked at one end with epoxy resin and dipped into the LSM80 (or Ag(Pd)-LSM80) colloidal suspension for 1 min and pull out, and this causes the formation of a thin LSM80 or Ag(Pd)-LSM80 powder-packing layer due to capillary force after drying under ambient condition. The coated tube is brought to burning at 400 ^{o}C for 1 h to eliminate organic additives, and this is followed by calcinations at 1300 ^{o}C for 3 h to sinter the asymmetric coating layer; consequently an asymmetric membrane, LSM80-YSZ or Ag(Pd)-LSM80-YSZ, is obtained.

B To completely close the surface pores existing in the above two membranes, the Ag(Pd)-LSM80-YSZ tube is coated by spraying an aqueous solution containing the three metal salts $La(NO_3)_3$ (0.2M), $C_4H_6O_4Mn$ (1M), and $Sr(NO_3)_2$ (0.8M). After coating, the tube is first dried at 80 ^{o}C and subsequently heated at 350 ^{o}C for 1 h to decompose the trapped nitrates. This coat-dry-heat process is repeated for five times and finally, the tube is calcined at 1300 ^{o}C for 1 h to form a gas-tight LSM80(S)-Ag(Pd)-LSM80-YSZ membrane. However, it is impossible through this procedure to close pores in membrane LSM80-YSZ.

6.2.4 Structural and oxygen permeation assessments of the asymmetric tubular membrane

Figure 6.3 shows the schematic of the setup to check room temperature gas leakage (using N_2 as the sweeping gas) and high temperature oxygen permeation (He as the sweeping gas) of the membrane. The details of the system were described in chapter 4 (Fig. 4.3). For carrying out electrochemical impedance study, round disks, which are made of pristine YSZ or an equal-mass mixture of LSM80 and YSZ, are prepared by sintering the respective powder-packing pellets at 1300 ^{o}C for 3 h. A minicell of Al_2O_3 is designed to fasten the disk together with two Ag electrodes via screwing the holder. This electrochemical cell is placed in a furnace and connected to the Solartron 1260 impedance analyzer for conducting impedance measurements (over the frequency from 500 Hz to 20 MHz) in the temperature range of 400~870 ^{o}C. Figure 5.2 in Chapter 5 showed the schematic diagram of the impedance analysis.

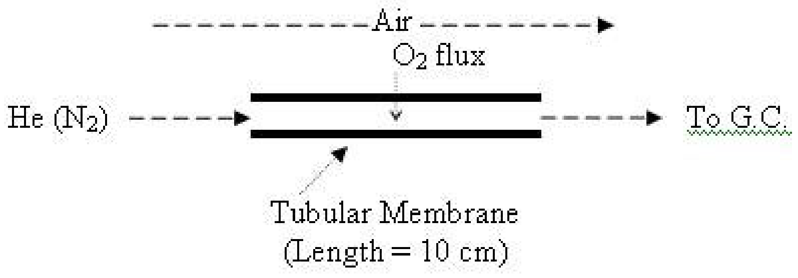

Figure 6.3 Schematic of the setup for checking gas leakage and assessing oxygen permeation

X-ray diffraction (XRD) patterns of the various specimens were described in Chapter 3. Both surface and cross-sectional images of membrane are taken on a field emission scanning electron microscope (JSM-6700F, FESEM).

6.3 Results and Discussion

6.3.1 From porous YSZ support to dense LSM80 surface

In contrast to the asymmetric electrolyte/cathode assembly in SOFC, the desired configuration for COMR requirement is to attach a thin and dense MIEC membrane layer to a thick and porous YSZ support. Despite the fact that YSZ and LSM materials have similar TECs and good chemical compatibility, it is still not ready to realize a dense LSM membrane, which partially merges with the YSZ support underneath through a single step of coating on the porous YSZ support with a somewhat rough and porous surface (Fig. 6.4). Therefore, on such a surface, deposition of a LSM80 particle-packing by using the specially formulated colloidal dispersion (section 6.2.2 A) would be an appropriate way to generate a consolidated membrane. However, the resulting LSM80 membrane through sintering has not yet been dense and contains lots of pin holes as shown in Fig. 6.5a.

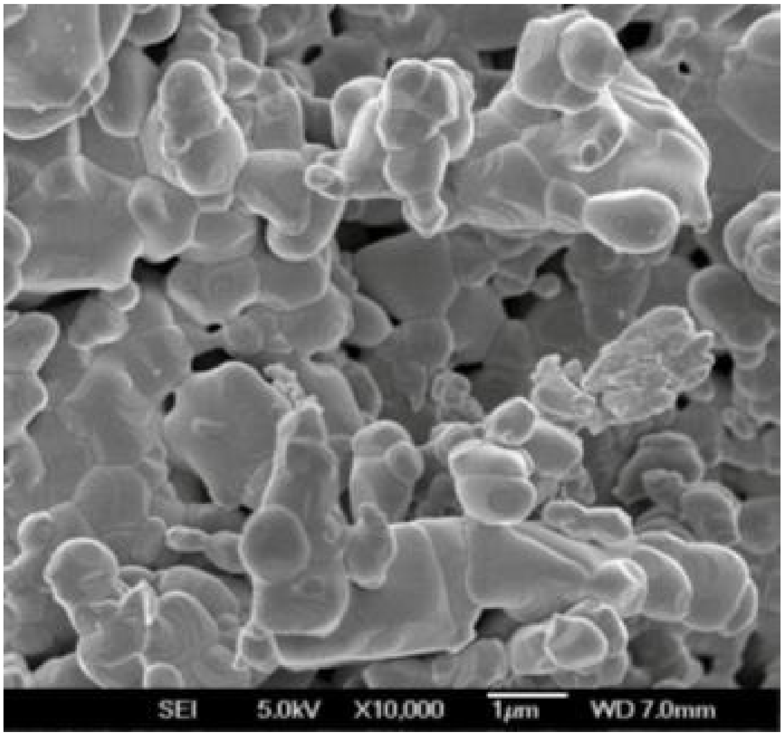

Figure 6.4 The external surface morphology of the sintered YSZ tube

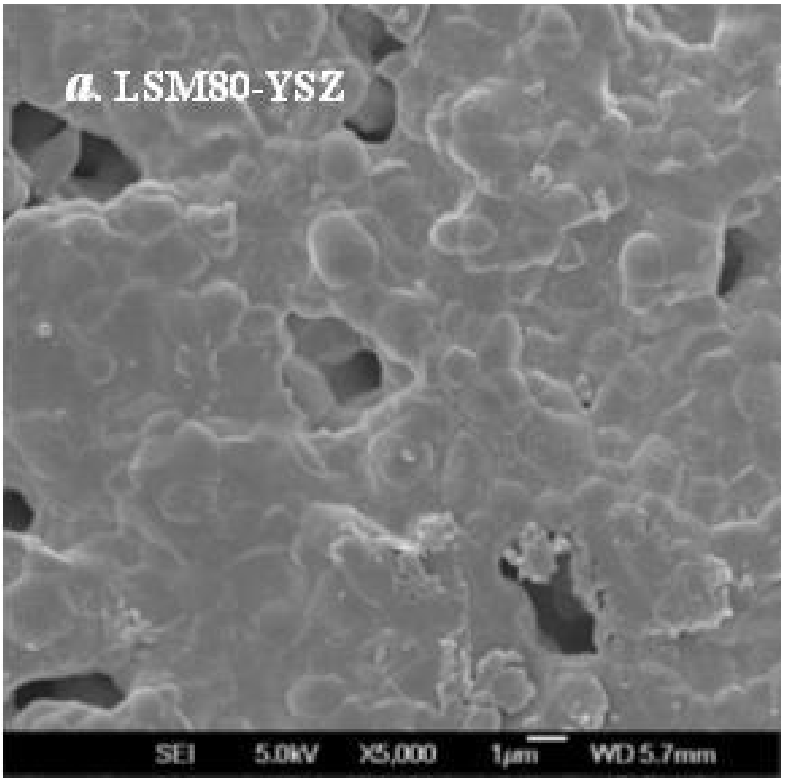

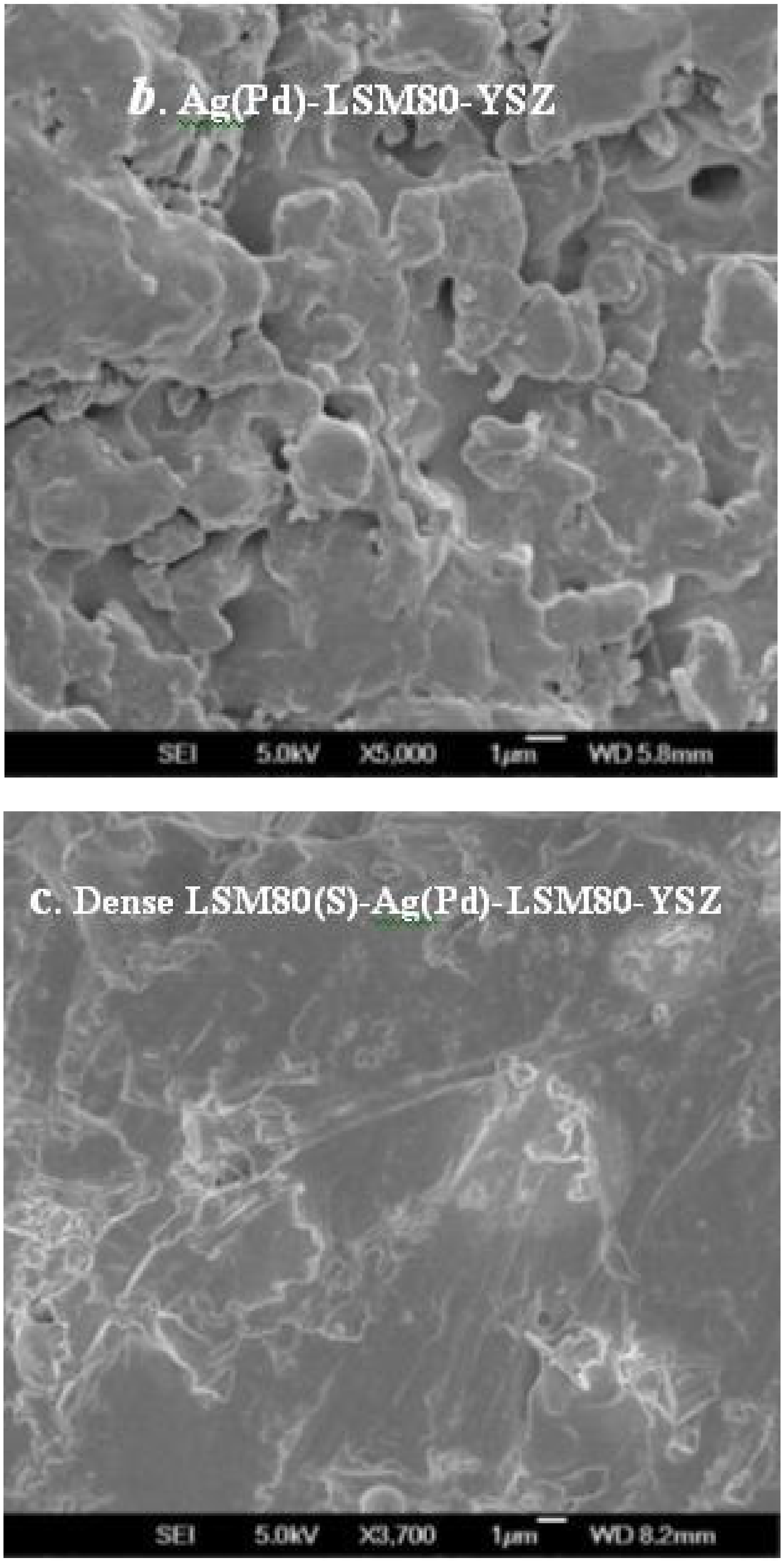

Figure 6.5 The surface morphologies of the three membranes as indicated

In the course of sintering, the pores with negative surface curvature are thermodynamic unstable and tend to grow (Chiang et al., 1997). The LSM80 fine powder, shown in Fig. 6.2, comprises particles from 10 nm to 200 nm, having the average particle diameter around 50 nm. It is unavoidable to form domains of different powder packing density as the agglomeration tendency is greater among smaller particles. Consequently, formation of uneven domains is the root cause leading to the negative surface curvature pores, which would end up with pinholes after sintering at high temperature. Incorporating a metal alloy Ag(Pd) (Ag/Pd = 9:1 by wt.), which has melting point well below the sintering temperatures of LSM80 and YSZ, into the ceramic phase by a content of 9 wt.% causes a decrease in the numbers of pin-holes (Fig. 6.5b). It is supposed that Ag(Pd) alloy functions as a binder to help consolidation of LSM80 particles and as a pinhole filler after sintering. Unfortunately, the 9 wt.% alloy content is still not enough to eliminate all the pin-holes and further increasing of the alloy content will cause coefficient of thermal expansion mismatch between the Ag(Pd)-LSM80 coating layer and the YSZ support.

Alternatively, plugging the surface pores through using the salt precursor as described in section 6.2.3 could satisfactorily closes pinholes in the Ag(Pd)-LSM80 membrane and realize a dense surface layer, LSM80(S)-Ag(Pd)-LSM80, as displayed in Fig. 6.5c. It is worthy to note that such a pore-plugging approach based on solution coating can be applicable only on the substrate with small pore sizes. The Ag(Pd)-LSM80 membrane is a transition layer that has a thickness of about 10 μm (Fig. 6.6) and offers a suitable porous structure for making this pore-closing approach viable. The energy-dispersive x-ray analysis of the outside surface of the LSM80(S)-Ag(Pd)-LSM80 membrane (Fig. 6.5c) at different locations showed that besides the elements of Ag, Pd, Zr and Y, the membrane surface also has the La, Sr and Mn elements with uniform local molar ratio close to 1:4:5 as designed.

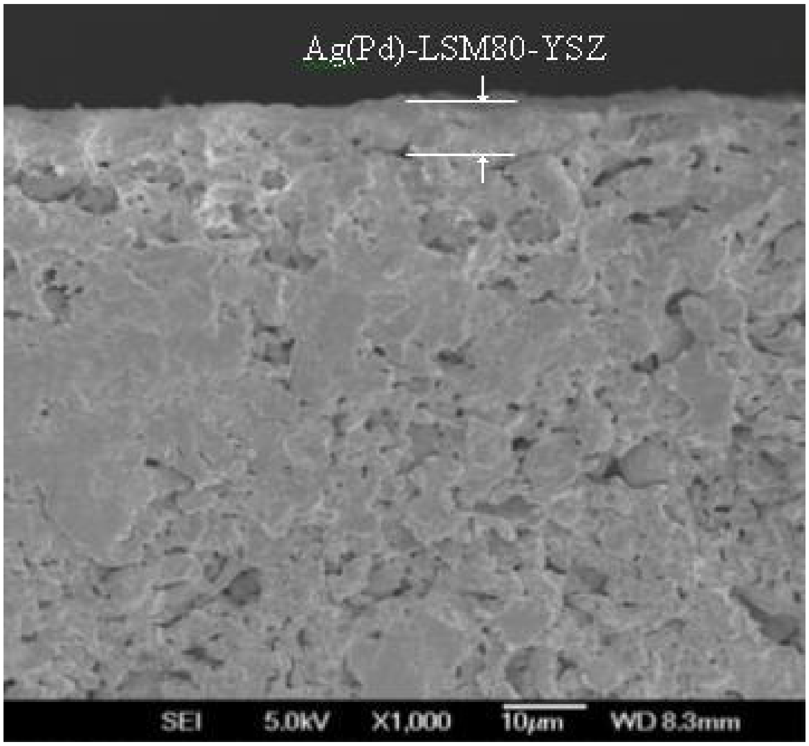

Figure 6.6 Cross-sectional view of the Ag(Pd)-LSM80-YSZ membrane

The gas leakage tests of the porous YSZ tube, porous LSM80-YSZ membrane, porous Ag(Pd)-LSM80-YSZ membrane and dense LSM80(S)-Ag(Pd)-LSM80-YSZ membrane are performed at room temperature (section 6.2.4, Fig. 6.3). The O_2% by volume in the outlet gas stream decreases with increasing the sweeping gas (N_2) flow rate (Fig. 6.7). This is considered to be a result of the enhancement of nitrogen fugacity, which brings about a reverse flow of N_2 towards airside. Furthermore, the O_2% is higher in the outlet stream from LSM80-YSZ membrane than that from Ag(Pd)-LSM80-YSZ membrane, showing the dual roles of the Ag(Pd) component in the membrane as stated above. The O_2% of the dense LSM80(S)-Ag(Pd)-LSM80-

YSZ membrane is zero in the whole testing range, indicative of the success of the salt-precursor plugging approach, which leads to a gas-tight exterior side of Ag(Pd)-LSM80-YSZ membrane. In brief, gas leakage testing results are consistent with those based on the electron microscopy displayed in Fig. 6.5.

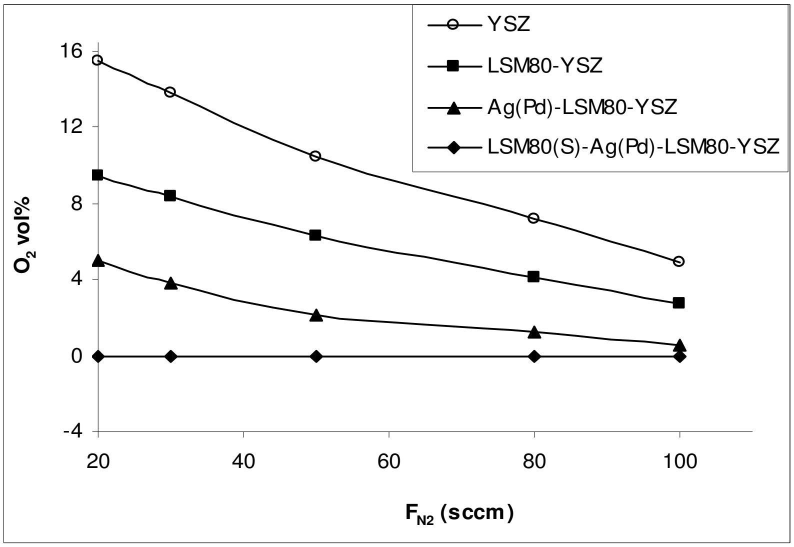

Figure 6.7 The air leakage extents through different membranes with the change of sweeping gas flow rate at room temperature

6.3.2 Chemical and electrochemical features of the LSM-YSZ interface

The chemical compatibility of LSM80 and YSZ was examined by sintering a pellet made of the two oxides (1:1 by wt.) at 1300 °C. Compared with the XRD patterns of the pristine LSM80 and YSZ, an extra peak (at $2\theta = 31.44^o$), although very weak, appears on the XRD pattern of the sintered pellet (Fig. 6.8). This peak, belonging to neither perovskite LSM80 nor cubic YSZ, is therefore attributed to a minor phase derived from the interfacial reaction between LSM80 and YSZ at the calcination temperature. The chemical compatibility between the LSM with YSZ was extensively investigated (Barbucci et al., 2005; Brant & Dessemond, 2000) and it was widely accepted that at the LSM-YSZ interface, the insulating pyrochlore-type $La_2Zr_2O_7$ (LZO) or perovskite-type $SrZrO_3$ (SZO) layer is formed at high sintering temperatures (≥ 1100 °C) due to the relatively fast diffusion rate of La^{3+} or Sr^{2+} into the YSZ lattice. Nevertheless, Sahu et al. (2004), however, discovered that even sintering neither LZO nor SZO was found at the LSM-YSZ interface even when sintering at 1400 °C for 6 h. This discrepancy is likely due to different LSM compositions and the related preparation methods. Because the diffusion of La^{3+} or Sr^{2+} into YSZ phase to form insulating LZO or SZO phase is driven by the chemical potentials of La^{3+} and Sr^{2+} at the LSM-YSZ interface, a homogeneous LSM composition should favour lowering down such diffusion tendency and similarly, a high Sr doping extent should favour formation of SZO.

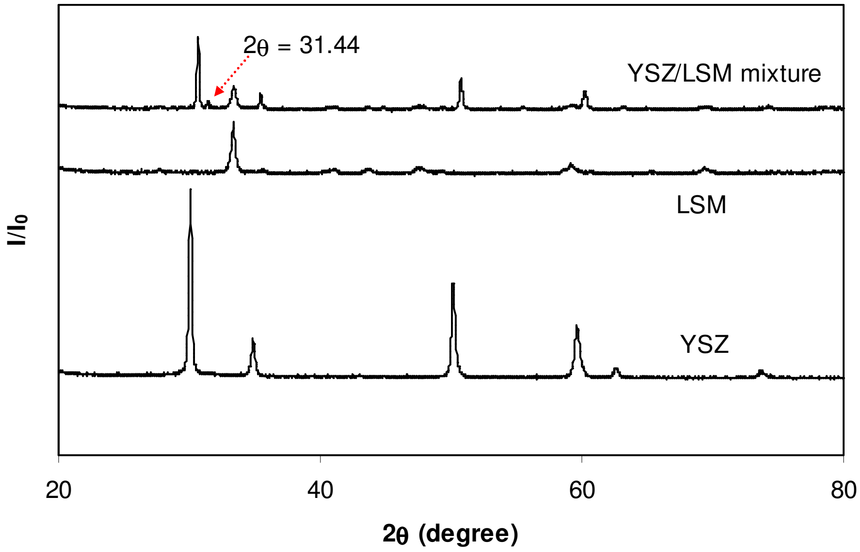

Figure 6.8 XRDs of pure YSZ, pure LSM80, and 1:1 wt mixture of LSM80 and YSZ after calcinations at 1300 °C for 3 h

The experimental impedance spectra (EIS) of the pristine YSZ and YSZ-LSM80 (1:1 wt) pellets (obtained from sintering at 1300 ^{o}C) are shown in Figs. 6.9 a & b, in which the spectra are expressed by Nyquist diagram, i.e., imaginary part (Z´´) is plotted against real part of the impedance (Z´). The Nyquist plots of YSZ are approximately interpreted by an equivalent circuit as shown in Fig. 6.10a (Mitterdorfer & Gauckler, 1999). R_o is the sum of ohmic resistors due to electric connection including electrode ohmic resistance and contact resistance at interfaces. The high frequency impedance ($f > 0.01$ MHz) is attributed to the resistance (R_e) and constant phase element (Q_e) of the YSZ electrolyte; while the low frequency regime of the Nyquist plot is related to the electron transfer at the electrode (R_{ct} & Q_{dl}).

The electrical conductivity of the YSZ-LSM80 composite (Fig. 6.9b) is much higher than that of the pure YSZ. The equivalent circuits as shown in Fig. 6.10b is used to explain the EIS of YSZ-LSM80 composite, where L is the inductance that is taken into account because of the existence of magnetic Mn^{3+} ion, R_s the overall ohmic resistance (Jørgensen et al., 1999; Leng et al., 2004) including the electrolyte resistance and electric connection resistance and could be determined by the first intercept of the "arc" with the real axis (Z´), while R_p and Q_p are the electrochemical polarization resistance and its corresponding constant phase element, respectively, and R_p could be determined from the second intercept (Fig. 6.9b). Compared with YSZ, LSM80-YSZ displays a distorted Nyquist plot due to the occurrence of electronic conduction across the continuous LSM80 phase in the testing disk. This can also be evidenced by the weak response of its impedance to the increasing of temperature showed in Fig. 6-9b.

In contrast to the YSZ-LSM80 mixture, the impedance of YSZ (e.g. R_s+R_p value) shows an apparent temperature-dependency due to its ionic conduction nature. As a reference, the pristine LSM80 also manifests very similar R_s+R_p values with increasing of temperature (Fig. 6.9c). It is important to note that LSM80-YSZ and LSM80 possess very similar R_s+R_p values at all the temperature points examined, which implies that tiny occurrence of the insulating phase (e.g., LZO or SZO) at the interface between LSM80 and YSZ affects very litte the charge transfer though the LSM80 phase.

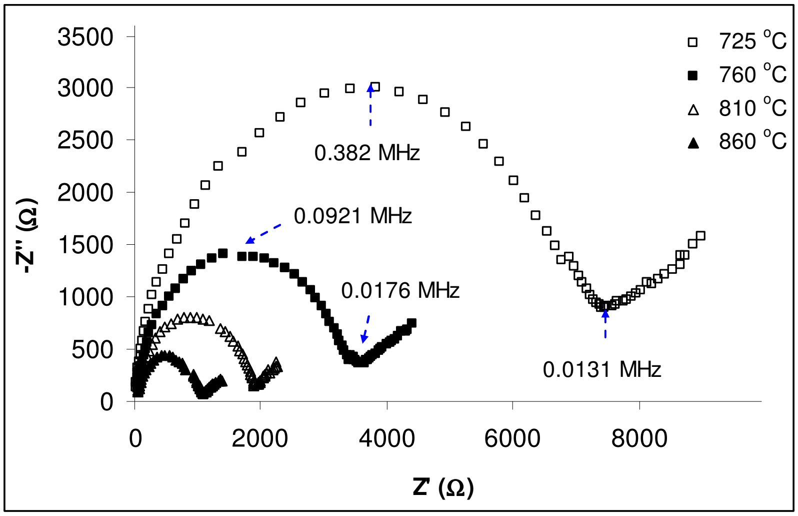

(a)

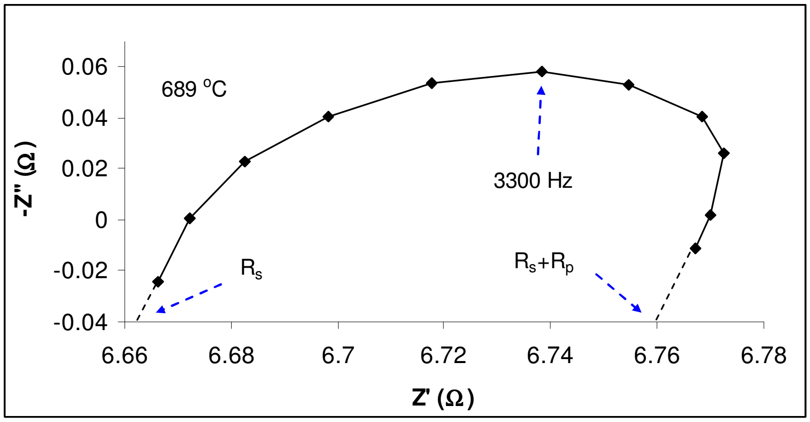
0.06
0.04
0.02
0
-0.02
-0.04
-Z'' (Ω)
689 °C
3300 Hz
R_s
R_s+R_p
6.66
6.68
6.7
6.72
6.74
6.76
6.78
Z' (Ω)

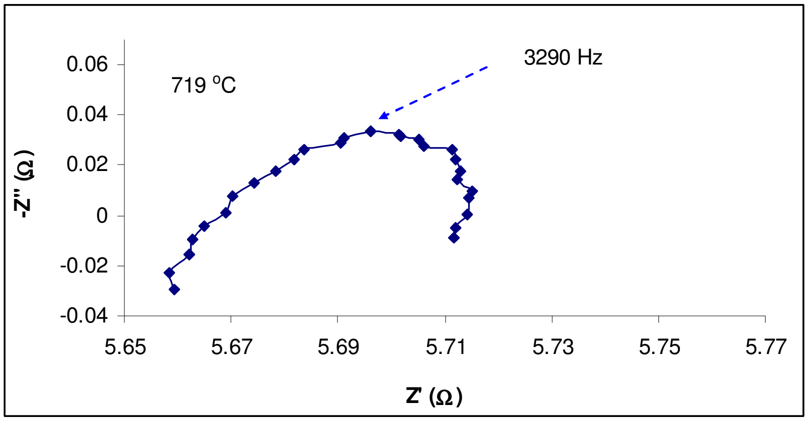
0.06
0.04
0.02
0
-0.02
-0.04
-Z'' (Ω)
719 °C
3290 Hz
5.65
5.67
5.69
5.71
5.73
5.75
5.77
Z' (Ω)

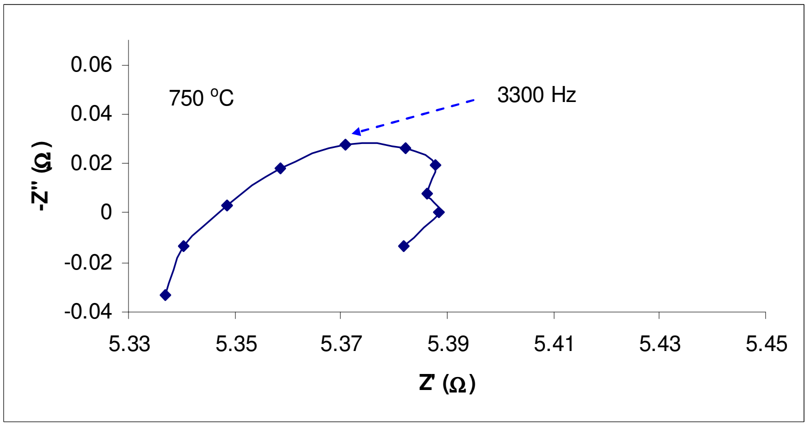
0.06
0.04
0.02
0
-0.02
-0.04
-Z'' (Ω)
750 °C
3300 Hz
5.33
5.35
5.37
5.39
5.41
5.43
5.45
Z' (Ω)

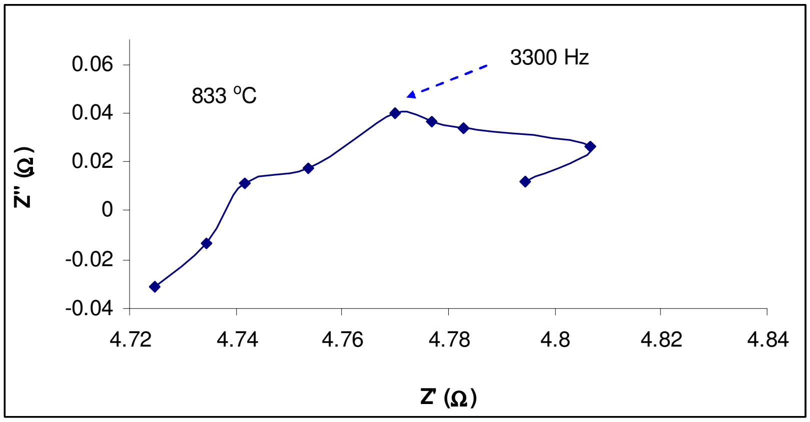

(b)

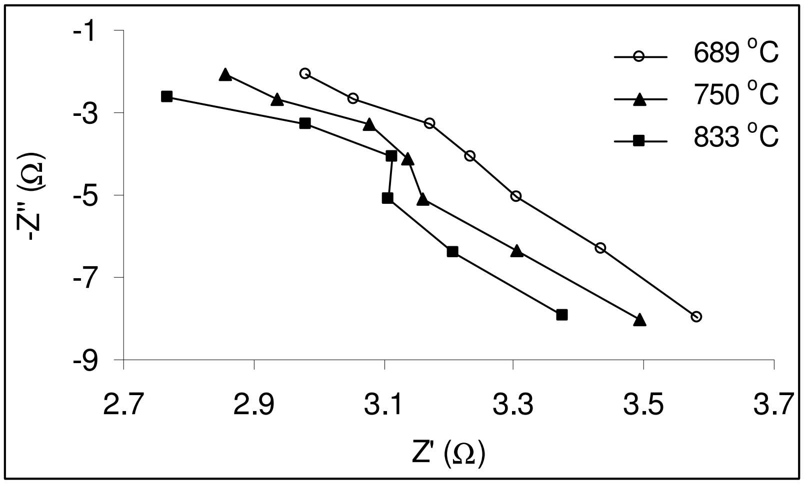

(c)

Figure 6.9 Nyquist diagrams at different measurement temperatures of: (a) YSZ; (b) 1:1 wt mixture of LSM80 and YSZ; (c) pure LSM80

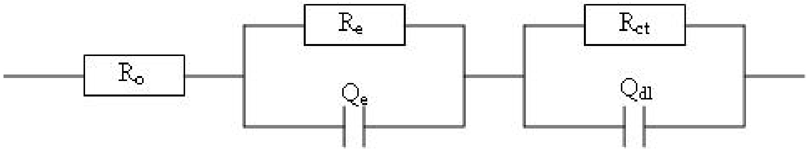

(a)

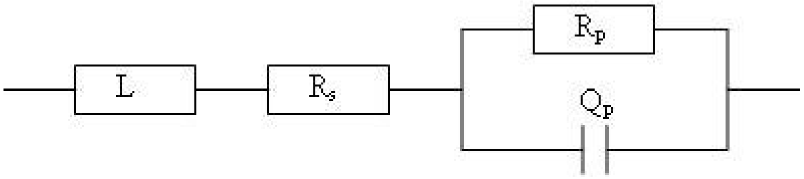

(b)

Figure 6.10 Equivalent circuit models for the EIS of: (a) YSZ; (b) mixture of LSM80 and YSZ

Figure 6.11 shows the temperature effect on the charge transfer in the bulk of electrolyte and at the electrode-ceramic interface, respectively. YSZ displays as expected the typical relationship of solid ionic conduction trend, but LSM80 is prevailed by its electronic conducting behaviour that shields the ionic conduction so as the R_s of LSM80 undergoes basically no reduction with increasing temperature. For YSZ-LSM80 mixture, the ionic conduction component in both of its bulk conduction (R_s) and the charge transfer at electrode (R_p) increases with increasing temperature, and the trend of the later one is clearer than the former one. This result states that a tiny occurrence of the insulating phases (e.g., LZO or SZO) at the interface between LSM80 and YSZ does not bar ion transfer through the YSZ phase. In the tubular membrane, LSM80(S)-Ag(Pd)-LSM80-YSZ, the interface between LSM80 and YSZ has similar structure and properties to the YSZ-LSM80 mixture. The separation of oxygen from air through the tubular membrane has been carried out in the temperature range from 600 to 900 ^oC (Fig. 6.12). The oxygen permeation flux experiences a big increase when the separation temperature is raised from 800 to 900 ^oC. According to the above electrochemical impedance analysis, it is suggested that O^{2-} ions transfer through LSM80 is a rate determining step and a useful oxygen flux could be achieved only when the operation temperature hits 900 °C.

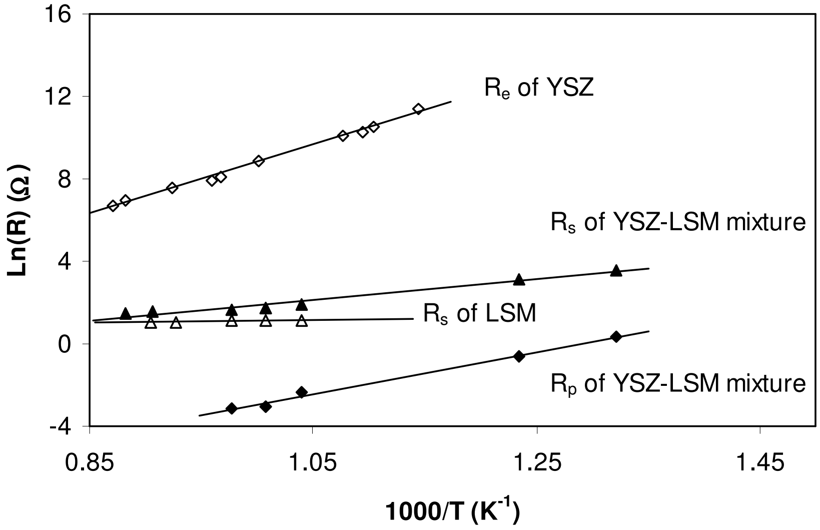

Figure 6.11 The temperature-dependent charge transfer behaviors of YSZ, LSM80, and their composite

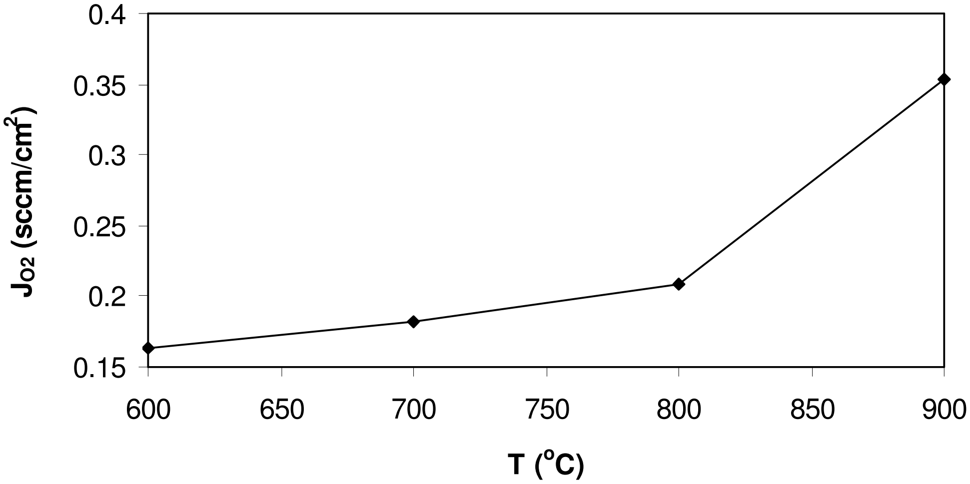

Figure 6.12 Dependence of oxygen permeation flux on temperature

6.4 Conclusions

In this chapter, a porous YSZ tube with mean pore diameter around 1 μm and porosity of 31% was made through extrusion and sintering at 1400 °C for 30 min. The target of this work is the fabrication of an asymmetric oxygen electrolyte membrane, LSM80-YSZ. To achieve the gas-tight state in the reactive LSM80 layer, two steps were employed, which are, firstly, implementation of dual phase metal-ceramic composite coating, Ag(Pd)-LSM80, and secondly, plugging surface pores of the coating layer by the salt-precursor approach. The presence of Ag(Pd) (ratio = 9:1) alloy (9 wt.%) in the LSM80 phase reduces its porous feature. This is essential to assure success of the subsequent pore-closing step. The chemical compatibility and charge transport behavior at the interface between LSM80 and YSZ were investigated. The analysis results show that the occurrence of minor interfacial species generated from sintering the two oxides at 1300 °C does not affect the oxygen ionic conductivity at the interface. The oxygen permeation of the asymmetric LSM80(S)-Ag(Pd)-LSM80-YSZ membrane gains an apparent increase when operation temperature is raised from 800 to 900 °C, reaching to 0.35 $sccm/cm^2$.

Chapter 7 Asymmetric tubular LSM80-CGO20/YSZ-Ag/YSZ-Ni(O) membrane reactor for partial oxidation of methane

This work reports a successful instance of assembling of an asymmetric tubular LSM80-CGO20/YSZ-Ag/YSZ-Ni(O) membrane reactor by the means of ceramic slurry coating followed by electroless silver plating. Very high methane conversion, CO selectivity, and H_2 selectivity were achieved within the COMR. It was also found that mutual diffusion of Ni^{2+} and Zr^{4+} ions happened at the interface between the YSZ and NiO phases, and the migration of Ni^{2+} towards the interface and the bulk of YSZ affected performance of POM. This result is attributed to a retreating action of lattice oxygen ions from the $Ni_{1-\delta}O$ phase by YSZ phase or in versa.

7.1 Introduction

Conversion of natural gas (mainly CH_4), an abundant fossil fuel, into value-added chemicals has nowadays attracted great efforts due to its telling economic implications. Direct conversion of methane into liquid chemicals over specific catalyst systems has still faced the issue of either low yield or low selectivity. Catalytic transferring methane to syngas, the key precursor leading to liquid fuels or other transportable liquid products, has a very high production yield. To date, steam methane reforming (SMR) is the most commonly utilized industrial process to transform methane into syngas, but this process is capital expensive and energy consuming due to its high endothermic nature. On the contrary, catalytic partial oxidation of methane (POM) with pure oxygen is a mild exothermic reaction and the syngas produced has the H_2/CO ratio of 2, which is desired for the reactions liquefying light olefins.

The POM requires a large quantity of pure oxygen which is traditionally generated from the expensive cryogenic air separation process. Integrating the N_2/O_2 separation and methane reforming in a COMR will cut the cost of POM significantly and make it possible to build the house-sized methane conversion plants to replace the conventional billion-dollar big syngas plants. It has been discussed in Chapter 2 (literature review) that an asymmetric tubular COMR is the desired membrane reactor module for POM, because it can offer both high oxygen permeation flux and high stability, and it is easy to be scaled up and no need for high temperature sealant. One of the major challenges for POM using an asymmetric tubular COMR is how to fabricate the COMR by a low cost method. In this work, a novel design of low cost COMR utilizing POM to drive oxygen permeation was reported. The asymmetric tubular COMR attained consists of the three co-axial annular layers of different ceramic materials and structure: porous $La_{0.2}Sr_{0.8}MnO_{3-\delta}$ (LSM80)-$Ce_{0.8}Gd_{0.2}O_{2-\delta}$ (CGO20) / dense YSZ–Ag composite / porous YSZ-Ni(0) composite. This structure was crafted by means of combining the conventional low cost ceramic slip coating-sintering technique with the low cost electroless silver plating technique.

7.2 Experimental

7.2.1 Membrane reactor fabrication

The fabrication procedure for making the tubular membrane reactor is shown in Fig. 7.1, in which submicron powders of LSM80 (Section 6.2.2 of Chapter 6) and CGO20 (Section 5.2.1 of Chapter 5) were fabricated in house and submicron YSZ (8 mol.% Y_2O_3 doped) powder was purchased from Stanford Material Corporation (U.S.A.). The NiO (50 wt.%)-YSZ mixture was fabricated by suspending a given amount of the YSZ powder in an aqueous solution containing $Ni(NO_3)_2$ ($\geq$ 98%, Nacalai Tesque, Inc. (Japan)) (1 mol/l), EDTA (1 mol/l) and PVA (87-89% hydrolyzed, Mw: 13,000-23,000, Aldrich) (15 wt.% of YSZ), and followed by drying and calcination. Details about the preparation of polymer-ceramic mixture, green tube extrusion, fine ceramic powder fabrication, and ceramic sintering were reported in Chapters 4 & 6. After precalcinating the NiO-YSZ-polymer green tube at 1000 ^{o}C (by 1 ^{o}C/min) for 2 h, the resultant porous NiO-YSZ tube possessed sufficient mechanical strength for withstanding a coating layer on it. A YSZ slurry was formulated (150 g of the YSZ in an organic solution comprising of Butiva-79 (6.25 g), Span-80 (3 ml), fish oil (6 ml), dibutyl phthalate (3 ml) and toluene-methylethyketone (v/v = 1:1, 1 l)) for coating the exterior side of the NiO-YSZ tube with a thin layer of YSZ, and subsequent sintering of the coated tube at 1450 ^{o}C for 4 h produced a solid tube with double porous layer YSZ/NiO-YSZ, and the NiO-YSZ inner layer attained a mixing extent of the two at micron range (Fig. 7.2)..

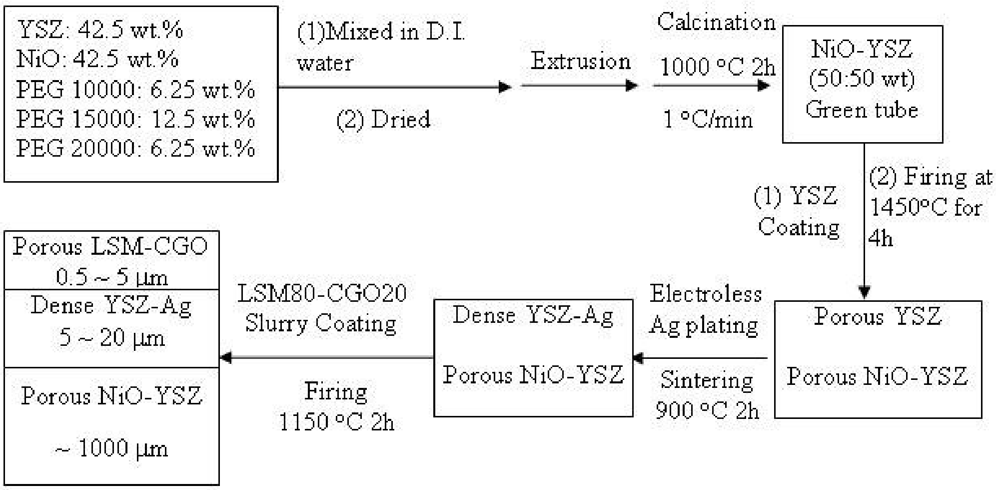

Figure 7.1 Flow chart illustrating the fabrication of the membrane reactor

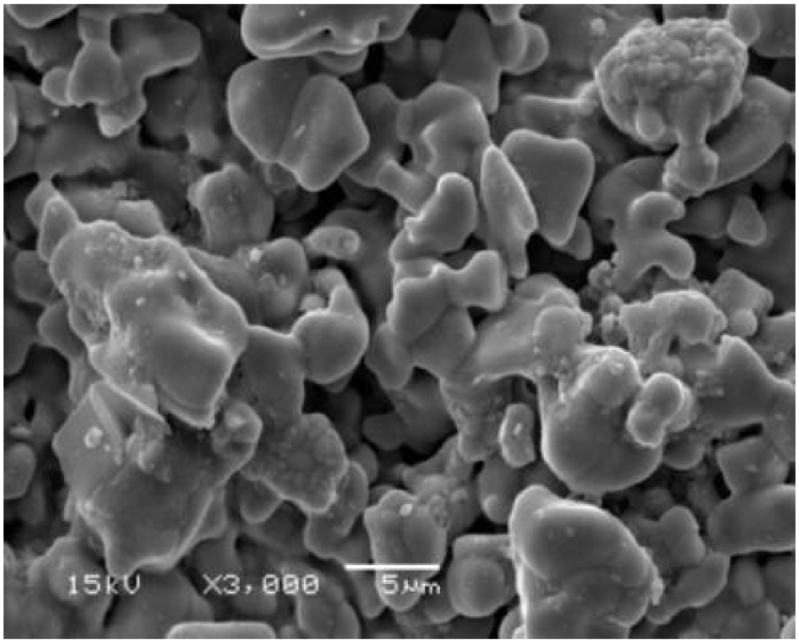

(a)

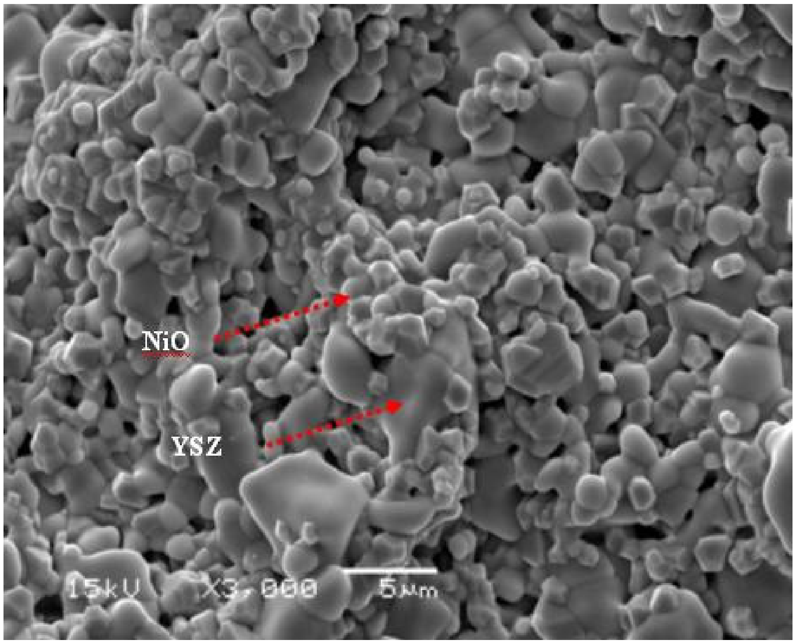

(b)

Figure 7.2 SEM images of: (a) porous YSZ; (b) porous NiO-YSZ

An electroless silver plating (ESP) solution (1 l, pH = 11) was formulated by mixing $AgNO_3$ (0.112 mol), HCHO (0.093 mol), ammonia (25%) and D.I. water. The porous YSZ/ NiO (50 wt.%)-YSZ tube was dipped into the ESP solution for a few seconds to allow the external YSZ pores to be filled with the ESP solution. After wiping the surface attached ESP solution away, the tube was placed in an oven at 60 ^{o}C for 1 h to carry out silver deposition inside the pore channels of the YSZ layer. The exterior surface layer of the tube then became dense (confirmed by N_2 permeation test) after repeating a few rounds of the filling-and-plating manipulations. As the ESP solution is unstable, only the fresh ESP solution was appropriate for the filling-plating purpose. In the last step, a powder coating layer was developed on the exterior surface of the tube by brushing on it a colloidal dispersion. It contained 15 wt.% of LSM80 and CGO20 fine particles (1:1 by wt.) and the organic additives that were the same as those used to formulate the YSZ slurry in toluene-MEK. The LSM80/CGO20 powder coating layer was then subjected to calcinations as shown in Fig. 7.1. Finally, the triple-layer membrane structure was realized according to the microscopic investigation (SEM, JEOL JSM-5600), in which the thickness of the porous Ni(0)-YSZ tube wall, the dense YSZ-Ag layer and the porous LSM80-CGO20 layer were about 1mm, 5~10 μm and 0.5~2 μm, respectively.

7.2.2 Characterizations of the NiO-YSZ mixture

Temperature programmed reduction (TPR): The NiO-YSZ powder obtained from calcinations at 1450 ^{o}C for 4 h was placed in a quartz tube connected with a thermal conductor detector (TCD) (Shimadzu, GC-8A). Before TPR the sample (100 mg) was pretreated with Ar gas at 700 ^{o}C for 1 h. After cooling down to room temperature, the TPR was carried out under the reducing atmosphere of H_2 (2.5 sccm) and Ar (47.5 sccm), and the temperature was increased from 25 ^{o}C to 800 ^{o}C with the heating rate of 10 ^{o}C/min. X-ray powder diffraction (XRD) analysis was carried out as described in Chapter 4. The X-ray photon spectroscopy (XPS) was carried out on an instrument (Kratos Axis His, Manchester, U.K.) equipped with the Al Kα X-ray source (1486.6 eV) by using the takeoff angle of 90^{o} with pass energy of 40 eV.

7.2.3 Coupling air separation with POM reaction

The membrane reactor setup has been illustrated in Section 4.2.5 of Chapter 4. The reactor was continuously purged with He while it is heated up to the designated reaction temperature. After that, the NiO-YSZ inner, was connected to a feeding drift comprising of CH_4 (10 sccm, F_{CH4}^{in}) and He (20 sccm), and to the external cathodic side, viz. the LSM80-CGO20 layer, an air flow (100 sccm) was introduced. The outlet stream from the interior side of reactor was led into an on-line gas chromatograph (Clarus 500, PerkinElmer ARNEL) for composition analysis, and the outlet gas flow rates of CH_4 (F_{CH4}^{out}), CO (F_{CO}^{out}), H_2 (F_{H2}^{out}) and CO_2 (F_{CO2}^{out}) were then determined by multiplying the total outlet gas flow rate with the respective mole fraction. The methane conversion (X_{CH4}), CO selectivity (S_{CO}), CO_2 selectivity (S_{CO_2}) and H_2 selectivity (S_{H2}) were calculated by the formulas as follows

$$X_{CH4} = \frac{F_{CH4}^{in} - F_{CH4}^{out}}{F_{CH4}^{in}} \times 100\% \qquad (7.1)$$

$$S_{CO} = \frac{F_{CO}^{out}}{F_{CH4}^{in} - F_{CH4}^{out}} \times 100\% \qquad (7.2)$$

$$S_{CO2} = \frac{F_{CO2}^{out}}{F_{CH4}^{in} - F_{CH4}^{out}} \times 100\% \qquad (7.3)$$

$$S_{H2} = \frac{0.5F_{H2}^{out}}{F_{CH4}^{in} - F_{CH4}^{out}} \times 100\% \qquad (7.4)$$

The carbon selectivity (S_C) was estimated from the measured S_{CO} and S_{CO2} ($S_C = 100\% - S_{CO} - S_{CO2}$).

7.2.4 Methane thermal decomposition over NiO, YSZ and NiO-YSZ composites

When methane undergoes thermal decomposition on nickel catalyst, the reaction produces the syngas with a very high H_2/CO ratio. It can be utilized to probe the methane pyrolysis mechanism which happens in the POM process. Metal oxide (NiO 1 g, or NiO-YSZ (1:1 by wt.) composite 2 g, or YSZ 1 g) was placed in the middle of a quartz tube (ID = 8 mm) and heated up to 850 ^{o}C. After purging the quartz tube with He (20 sccm) for 0.5 h, a diluted methane stream (CH_4 10 sccm / He 10 sccm) was introduced into the quartz tube, and the CH_4 reacted with the lattice oxygen from NiO or YSZ.

7.3 Results and Discussion

7.3.1 Bilateral diffusions of cations in YSZ-NiO composite

As described in section 7.2.1, YSZ-NiO composites with different NiO contents were prepared through solution impregnation and co-calcination at 1450 ^{o}C for 4 h. The XRD angular positions of the characteristic peaks of the NiO and YSZ phases were listed in Table 7.1. The 2θ parameters of YSZ shift to higher values (representing contraction of lattice) with increasing the NiO content up to 33.4 wt.% (Fig. 7.3). This trend could be explained as diffusion of Ni^{2+} ions into the YSZ lattice. It is believed that doping the Zr^{4+} (0.84 Å) lattice site by smaller Ni^{2+} (0.78 Å) ions was responsible for the contraction of YSZ lattice, which was primarily a size adjusting effect. The dissolution of nickel ions in the ZrO_2 matrix at a low NiO content was previously reported by Dongare et al. (2004). We observed however in this study that a further increase in the NiO content to 50 wt.% brought about reversely an expansion of YSZ lattice, i.e. exhibiting a set of 2θ values slightly smaller even than that of the native YSZ. We deem that ionic size effect instigated this backward structural adjustment. In fact, there was a coincident diffusion of Zr^{4+} ions into NiO phase and its impact became more influential to the YSZ lattice with increasing NiO content. Since departure of Zr^{4+} ions from the YSZ phase promoted the Y/Zr ratio in its bulk and led to, therefore, an expansion of lattice because Y^{3+} is bigger than Zr^{4+}. Hence, these two opposite effects on the lattice size of YSZ, namely entering of Ni^{2+} ions and leaving of Zr^{4+} ions, caused the YSZ phase experience a contraction and followed by an expansion change. We also found that XRD pattern of the YSZ phase resumed to native after the NiO phase was reduced to Ni(0) by methane, such change could be attributed to the exclusion of Zr^{4+} ions from the NiO phase upon its chemical reduction.

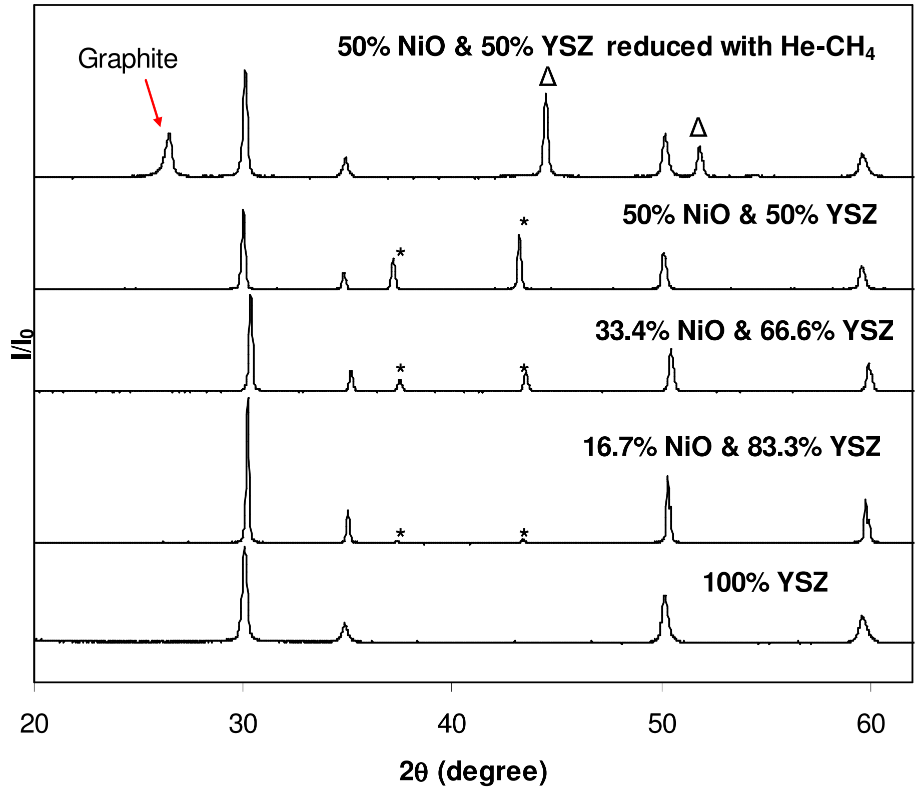

Figure 7.3 XRD patterns of the Ni(O)-YSZ composites with different Ni(O) contents. (the * indicates the NiO peaks and the $^{\Delta}$ the Ni peaks)

On the other hand, the YSZ phase also affected the lattice parameter of NiO phase in the composite (Table 7.1). The existence of the Ni^{3+} in NiO was reported to account for the color change of the NiO happened in its sintering process (Gavalas et al., 1984). It was possible that oxygen-ion conductive YSZ facilitated the oxidation of Ni^{2+} into Ni^{3+} via supplying O^{2-}. When a certain amount of Ni^{3+} was generated in the NiO lattice (due to calcination at 1450 ^{o}C), a reduction in the lattice parameter (i.e. increasing of 2θ values) was the outcome as expected. Besides happening in the NiO phase (33.4 wt.% in the composite), the lattice contraction should also occur in the NiO phase of 16.7 wt.% in the composite with respect to pristine NiO. Nevertheless, similar to the YSZ phase in the composite, when the content of the NiO phase reached to 50 wt.% a lattice expansion (i.e. decreasing of 2θ values) of it was observed. As aforementioned, the doping of Zr^{4+} ion in the NiO phase was furthered in the equi-mass composite, and the lattice expansion of NiO was triggered by the lodging of bigger Zr^{4+} ions in the lattice site of Ni^{2+}.

The XPS peak of NiO, Ni-2p3/2, was used to probe structural environments of the NiO phase in the composite, and the Ni-2p3/2 of native NiO, prepared also by calcinations at 1450 ^{o}C, was employed as the reference (Fig. 7.4). The Ni-2p3/2 peak consists of two partially overlapping sub-peaks with binding energy of (~ 854 eV) and (~ 856 eV), respectively. The high BE-peak was assigned to Ni^{3+} species whereas the low-BE peak to Ni^{2+} (Otsuka et al., 1989; Badyal et al., 1990). For composite, NiO(16.7 wt.%)-YSZ, a very weak Ni-2p3/2 profile was observed. It is an indicative of a significantly high dispersion of the NiO phase in the YSZ phase, and the NiO bulk phase should contain the highest concentration of Ni^{3+} ion due to the dominant YSZ surroundings. In composite, NiO(33.4 wt.%)-YSZ, the ratio of high-BE peak to low B-E peak (viz. Ni^{3+}/Ni^{2+}) is greater than that of the native NiO, which reflected the effect of YSZ on promoting the oxidation of Ni^{2+} to Ni^{3+}.

Table 7.1 The XRD angular positions (2θ) in Fig. 7.3

Compound	2θ (degree)					
	of YSZ				of NiO	
Pure YSZ	30.1	34.9	50.2	59.6	-	-
NiO (16.7 wt.%)/YSZ	30.2	35.0	50.3	59.8	37.2	43.2
NiO (33.4 wt.%)/YSZ	30.4	35.2	50.5	59.9	37.5	43.5
NiO (50 wt.%)/YSZ	30.0	34.8	50.1	59.6	37.3	43.4
NiO (50 wt.%)/YSZ reduction with CH_4	30.1	34.9	50.2	59.6	-	-

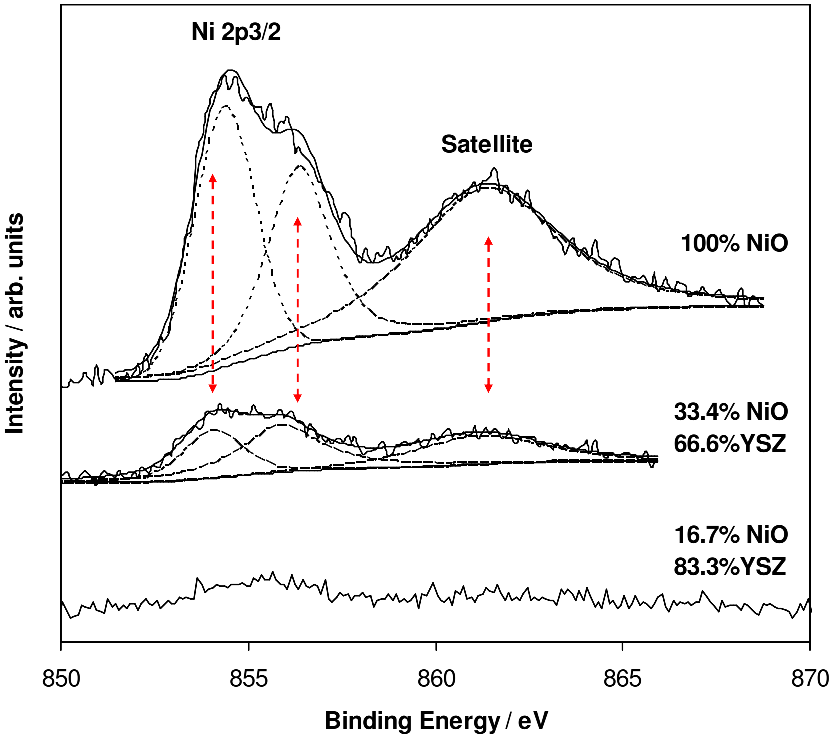

Figure 7.4 XPS of Ni 2p3/2 core level of the NiO-containing specimens

7.3.2 TPR of NiO-YSZ composite

The NiO-YSZ composite shows a TPR profile consisting of three peaks whose temperatures vary with the loading of NiO in the composite (Fig. 7.5). Peak I (the beginning peak) appears earlier with the increasing of NiO loading and is considered to be due to the reduction of the bulk NiO phase. Peak I reflects in effect how easy could the bulk NiO phase be reduced. The composite with a higher YSZ content exhibited a higher reduction temperature since the bulk NiO phase contained higher concentration of Ni^{3+} and Zr^{4+} species. Furthermore, peak II (the interim peak) could be attributed to the reduction of NiO located at the NiO-YSZ interfacial regions and peak III (emerging at the highest temperature) to the reduction of Ni^{2+} dissolved in YSZ phase. Both peak II and peak III followed the same trend in terms of peak position: NiO (50 wt.%) > NiO (16.7 wt.%) > NiO (33.4 wt.%). It could also be understood as the magnitude of activation energy barrier for reducing Ni^{2+} at the above two specific locations. In this context, the equi-mass composite (i.e. NiO of 50 wt.%) had the most intimate interfacial boundary amid the three composites. In light of the relative intensity of peak II in a TPR profile, since it stands for the allocation of Ni^{2+} ions at the interface in a particular composite, NiO (50 wt.%) is estimated to have the highest percentage of interfacial Ni^{2+} ions, and this is followed by NiO(16.7 wt.%) and then NiO(33.4 wt.%). The reduction temperatures of peak III also displayed the same order as mentioned just now. Such a consistency was because, in principle, a greater interfacial concentration of Ni^{2+} ions would favor diffusion of the ions deeper into the YSZ bulk phase, and therefore these Ni^{2+} ions were more difficult to reduce relative to those that are nearby to the interfacial boundary. In short, a high concentration of interface-located Ni^{2+} is a desired feature for POM catalysis, which will be elaborated in the following sections.

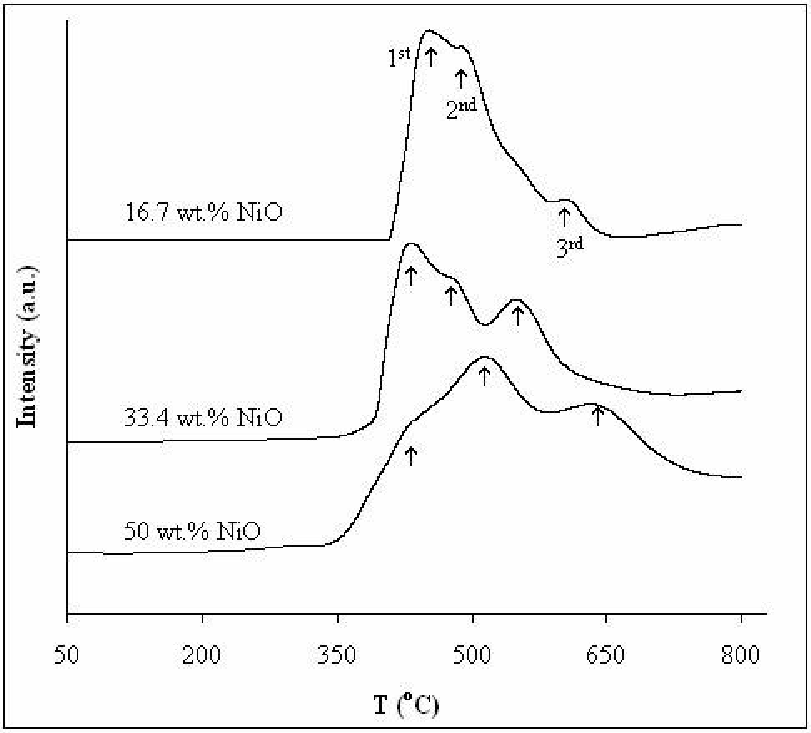

Figure 7.5 TPR of the NiO-YSZ composites with different NiO loadings

7.3.3 Characterizations of dual functional tubular membrane reactor

7.3.3.1 Fabrication of membrane reactor

As illustrated in Fig. 7.1, a thin layer of YSZ powder was coated on the pre-calcined NiO-YSZ tube via dip-coating. The resulting tube was co-fired (at 1450 °C for 4 h) and a shrinkage rate of around 20% and the overall porosity of about 10% were acquired in the tubular body after sintering. The thickness of the sintered YSZ layer was about 8-10 μm (Fig. 7.6). This thickness suited the design for attaining a dense

Ag-YSZ layer through electrolessly depositing of Ag in the porous channels of the YSZ layer. Furthermore, a highly porous LSM80-CGO20 layer was laid out on the Ag-YSZ layer using conventional slurry coating/sintering methods to form the cathode. To confirm whether or not the YSZ-Ag layer developed (Fig. 7.7a) was entirely gas-tight to nitrogen but not oxygen, the NiO embedded in the inner layer of the tube was reduced (with purging a stream of H_2 (10 sccm)-He (20 sccm) at 900 ^{o}C for 2 h) prior to the air permeation test to make the inner layer (Ni-YSZ) more porous (Fig. 7.7b vs. Fig. 7.2b). Moreover, the presence of Ni in the inner layer is one of the key structural features in the ultimate membrane reactor. The air permeation test was conducted at 900 ^{o}C using He (20 sccm) as the sweeping gas and revealed an oxygen flux but nil N_2 flux through the triple-layer tubular reactor, confirming that the Ag-YSZ layer was gas-tight.

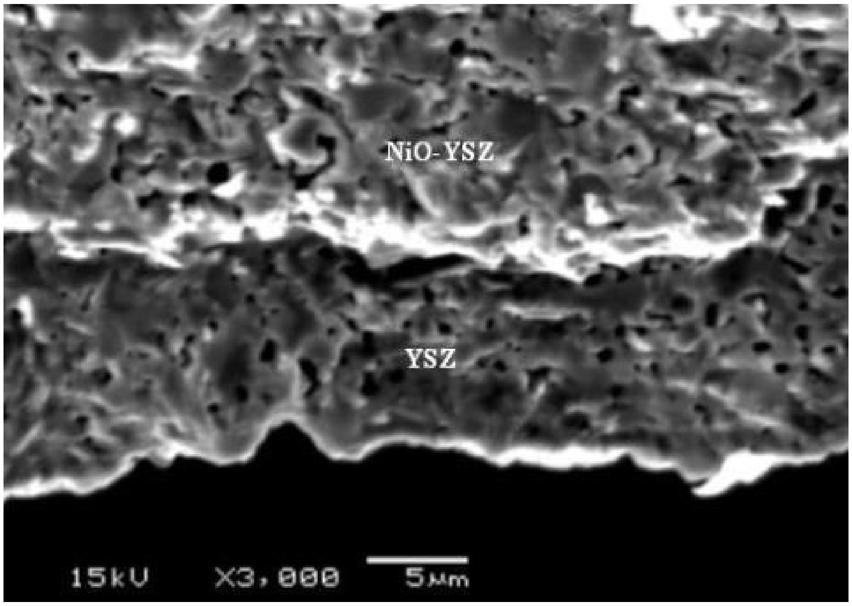

Figure 7.6 Cross-sectional SEM of the YSZ/NiO(50 wt.%)-YSZ tube generated from co-sintering at 1450 ^{o}C for 4 h

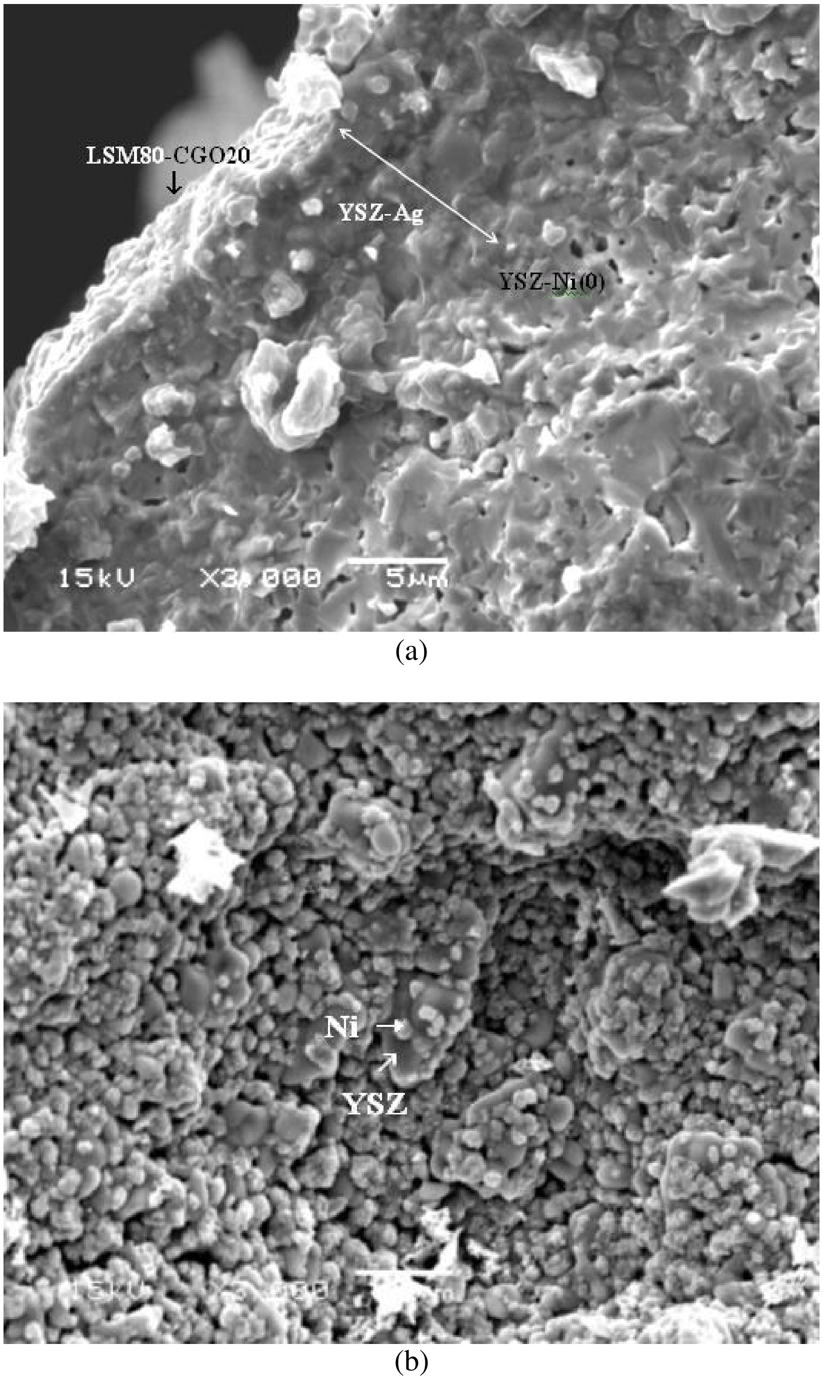

(a)

(b)

Figure 7.7 SEM of (a) a cross-section; (b) the inner Ni-YSZ surface

7.3.3.2 Partial oxidizing of methane by the permeated oxygen stream

The methane conversion (X_{CH_4}) in the tubular membrane reactor LSM80-CGO20/Ag-YSZ/NiO-YSZ was increased with lifting the operation temperature. The chemical selectivity of CO (S_{CO}) and H_2 (S_H) evaluated by Eqs. (6.2) & (6.4) also displayed an increasing trend with the uprising of methane conversion (in the stable reaction period) (Fig. 7.8). The NiO in the composite was reduced to metallic Ni(0) by CH_4 in the initiation period and CO_2 and H_2O were produced. The propagation of metallic Ni(0) sites gained momentum with increasing temperature and therefore the selectivity for CO or H_2 increased steadily to the stable levels. At the same methane flow rate, a higher reaction temperature favored to shorten the initiation period. As an example, when the POM was carried out at 700 ^{o}C in the membrane reactor, it took more than 1 h to realize the stable selectivity of H_2/CO (Fig. 7.9). In addition, the reaction temperature had a significant impact on the outcomes of POM, to perform this study, an overall reaction time of 2 h was applied. At 900 ^{o}C (20 sccm He and 10 sccm CH_4), a very high methane conversion (97%), CO selectivity (94%) and H_2 selectivity (96%) were obtained. Compared with the turnout from the reaction at 700 ^{o}C, it can be concluded that a reaction temperature above 800 ^{o}C is needed for achieving technically useful selectivities for CO and H_2.

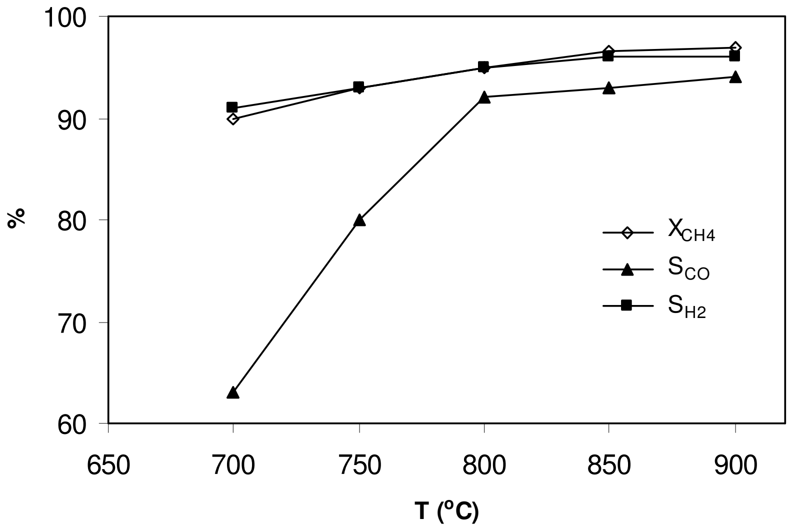

Figure 7.8 Temperature-dependent methane conversion, CO selectivity and H_2 selectivity based on a feeding stream consisting of 20 sccm He and 10 sccm CH_4

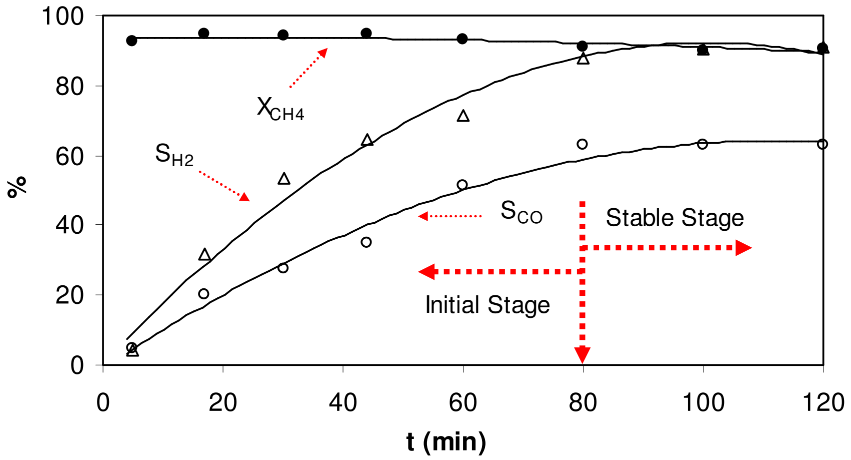

Figure 7.9 The relationships of the methane conversion, CO selectivity and H_2 selectivity with reaction time at 700 °C

7.3.3.3 Collective action of NiO and YSZ

The thermal decomposition of methane on the three designated catalysts, NiO (1 g), YSZ (1 g), and NiO-YSZ (2 g, w/w = 1), respectively, is a study aiming at the unique role of NiO-YSZ interface in catalytic POM (Fig.7.10 a-c). On both the NiO and the NiO-YSZ catalysts the methane conversion (X_{CH4}) was very high (> 91 %) over the entire process of reaction. However these two catalysts gave rise to significantly different ratios of $S_{CO2}/S_{CO.}$ The ratio was around 4:1 on the NiO but below 0.15:1 on the NiO-YSZ after 50 min, this result suggests that the NiO catalyst may supply a higher surface concentration of lattice oxygen ion $[O]_s$ than the NiO-YSZ catalyst after initiation period, i.e., the YSZ enhances the transport of lattice oxygen within the NiO phase.

Compared with the NiO and the NiO-YSZ, a very low X_{CH4} (< 7 % after 35 mins) was presented on the pristine YSZ. But it was very interesting to note that the converted portion of CH_4 totally yielded CO and H_2O. It was reported that methane was selectively oxidized by the YSZ surface lattice oxygen ions (Zhu et al., 2005). Initially some methane was converted to CO_2 due to the large amount of surface $[O]_s$ and the production of CO_2 fell rapidly to almost nil after about 35 min. After that, CH_4 was exclusively oxidized to CO at the YSZ surface. It is also noteworthy that H_2 and C were absent from the product stream of oxidation from very beginning. Based on these experimental facts methane likely undergoes a complicated thermal decomposition process on YSZ surface involving multiple intermediates (e.g., formaldehyde, formate and carbonate) as proposed by Zhu et al. (2004).

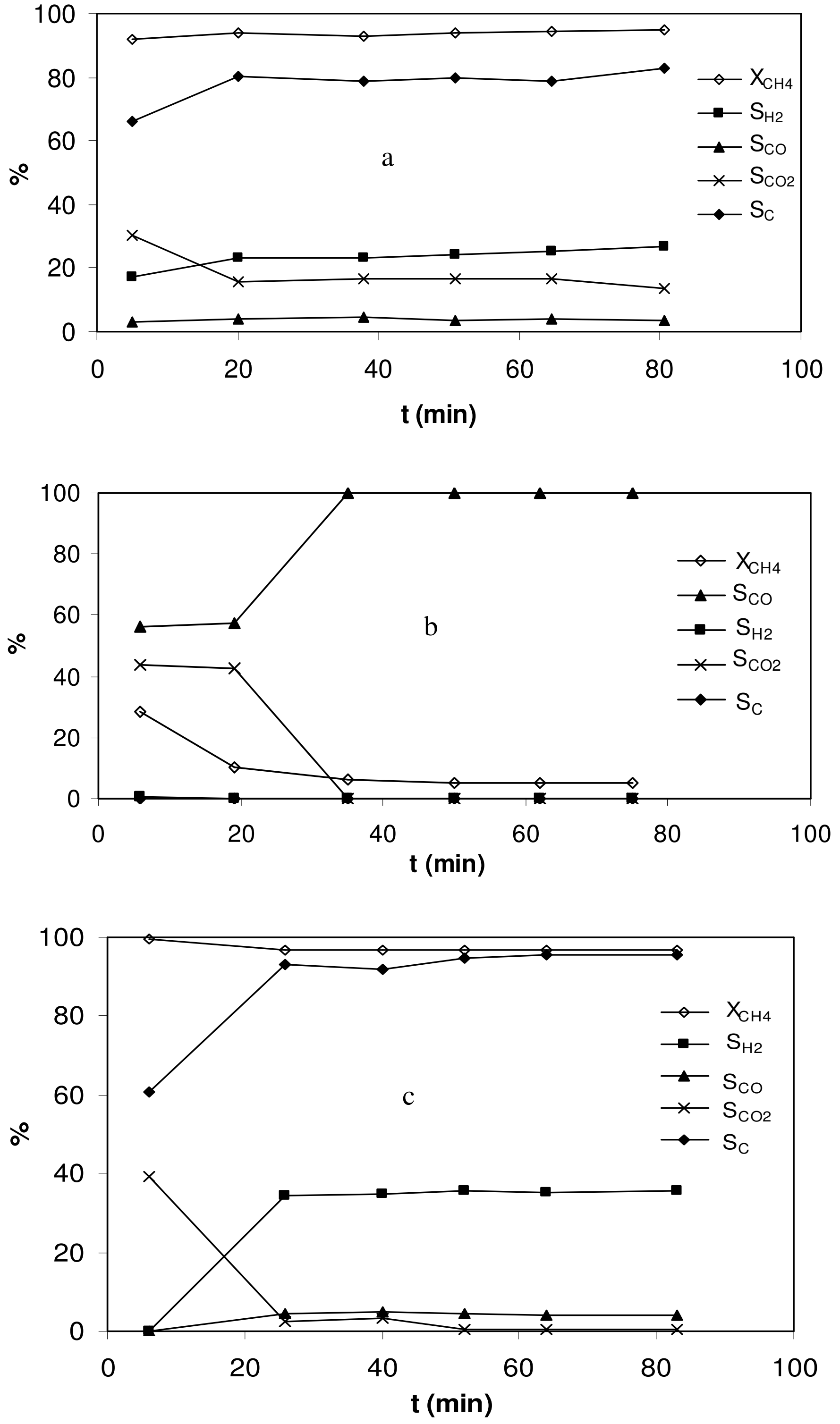

Figure 7.10 Thermal decomposition of methane: (a) on pure NiO (1 g); (b) on pure YSZ (1 g); (c) on NiO (50 wt.%)-YSZ composite

The ratio $S_{H2}/(S_{CO2}+S_{CO})$ varied with time and the outputs collated from the three catalytic pyrolysis systems of methane were plot in Fig. 7.11. In this chart the ratio of NiO-YSZ catalyst was far greater than the sum of the ratios from native NiO and YSZ. Regarding the discrepancy in the ratio $S_{H2}/(S_{CO2}+S_{CO})$ or in S_{CO2}/S_{CO} as indicated above, it implied a difference in the chemical potential of lattice oxygen $[O]_s$ in the two catalysts. As the conversion of methane on the YSZ was much lower than that on the NiO, it is rational to believe that methane dissociated primarily at the $Ni_{1-x}O$ surface.

The XPS results (Fig. 7.4) showed that YSZ facilitated the oxidation of Ni^{2+} to Ni^{3+} in the presence of air at high sintering temperature. Alternatively, the YSZ could also acted as a reservoir for lattice oxygen $[O]_s$ and imposed an attractive chemical potential to the $[O]_s$ in the neighboring catalytic $Ni_{1-x}O$ sites, which was generated from the reduction of NiO-YSZ in CH_4/He atmosphere. As a result, there was a fugacity equilibrium of $[O]_s$ between $Ni_{1-x}O$ sites and YSZ, which lowered down the chemical potential of $[O]_s$ in $Ni_{1-x}O$ sites relative to that in the pure NiO, and in accordance a higher $S_{H2}/(S_{CO2}+S_{CO})$ ratio was turned out. In another word, the YSZ phase functions as an oxygen pump to accelerate the oxygen transport within the $Ni_{1-x}O$ phase.

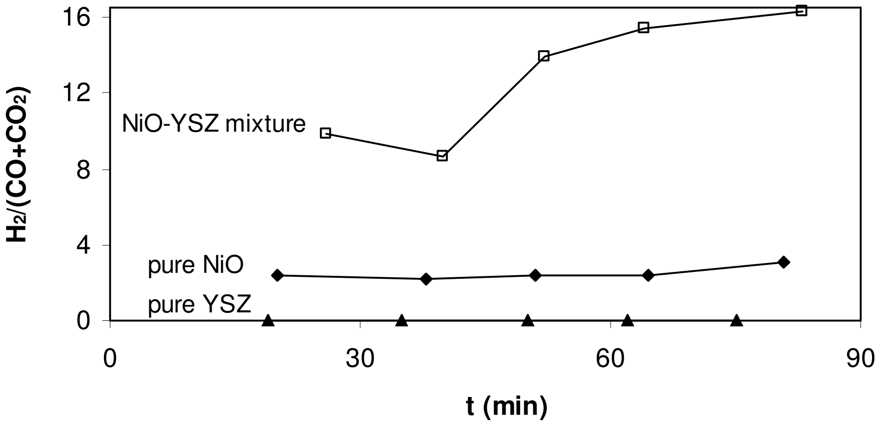

Figure 7.11 The POM $H_2/(CO+CO_2)$ ratio on the three oxides: (a) pure NiO; (b) pure YSZ; (c) NiO(50 wt.%)-YSZ composite

The trends shown in the above two figures could lead to the following conclusive remarks: CH_4 was oxidized by the lattice oxygen ($[O]_s$) at the surface of NiO to form CO_2 and H_2O (Eq. 7.5), while the surface NiO sites were reduced to Ni(0) atomic clusters correspondingly. Furthermore, the methane molecules adsorbed on the Ni(0) sites of the clusters ($CH_4 \xrightarrow{Ni} [CH_4]_s$) were thermally decomposed into adsorbed species: C ($[C]_s$) and H ($[H]_s$) via the reaction step ($[CH_4]_s \xrightarrow{Ni} [C]_s + 4[H]_s$). CO and CO_2 were synthesized from the reaction of the $[C]_s$ with $[O]_s$ at the catalyst surface. At the same time, H_2O and H_2 were produced as well. The selectivity of CO_2, CO, C and H_2 are dependent upon the X_{CH4} and the chemical potential of $[O]_s$. A higher X_{CH4} value and a lower $[O]_s$ potential favor the formation of C and H_2, while a lower X_{CH4} value and higher $[O]_s$ concentration result in higher CO_2% and CO% (e.g., on the pristine YSZ).

A careful analysis of Fig. 7.8 found that at low reaction temperature (e.g., 700 ^oC) the CO selectivity is low (< 65%) while both the H_2 selectivity and methane conversion are high (> 85%). This experimental fact suggested that the POM process using a COMR is very complicated and is surface oxygen chemical potential dependent and membrane temperature dependent. It may be the reason why the two major POM mechanisms (i.e., two-steps mechanism and direct methane dissociation mechanism) debated for so long time. Based on the above studies, this work suggested that the actually POM process may involve in at least three major overall reactions as follows:

$$\boldsymbol{CH}_4 + 4[\boldsymbol{O}]_s \rightarrow \boldsymbol{CO}_2 + 2\boldsymbol{H}_2\boldsymbol{O} \qquad (7.5)$$

$$\boldsymbol{CH}_4 + 2[\boldsymbol{O}]_s \rightarrow \boldsymbol{CO}_2 + 2\boldsymbol{H}_2 \qquad (7.6)$$

$$\boldsymbol{CH}_4 + [\boldsymbol{O}]_s \rightarrow \boldsymbol{CO} + 2\boldsymbol{H}_2 \qquad (7.7)$$

Eq. (7.5) represents the methane total combustion reaction in the case of low x value of $Ni_{1-x}O$ and Eq. (7.7) is equivalent to the direct POM mechanism when the surface oxygen concentration is low. Eq. (7.6) explains the case of middle x value, which may be the major reaction at low temperature within the fabricated COMR in this work (Fig. 7.8). As the increase of the membrane temperature, the methane reforming mechanism in Eq. (7.7) turns to be the dominant one, and thus the COMR results in high methane conversion, high CO selectivity and high H_2 selectivity.

7.4 Conclusions

An asymmetric tubular oxygen-permeable ceramic membrane POM reactor has been fabricated, which was equipped with a cathode layer (< 10 μm), the composite of

LSM80 and CGO20 oxides, and with an anodic layer (~ 1000 μm), the composite of YSZ and Ni(0). These two electrodes sandwiched a dense electrolyte layer (5-10 μm) composed of YSZ and Ag(0). The anode is a catalytic layer over which POM takes place and functions in addition as a structural support to the reactor. This membrane reactor successfully coupled the oxygen separation from the air with partial oxidation of methane and realized a high conversion of CH_4 and high selectivity for CO and H_2.

A series of studies involving XRD, XPS, TPR, and methane thermal decomposition have been conducted to understand the bilateral cation diffusion between the NiO and YSZ phases. The $Ni_{1-x}O$ located at the interface derived from reduction of the NiO by CH_4 revealed unique POM catalytic performance. This study suggested that the POM process was very complicated and involved in at least three major reactions as the change of the surface oxygen chemical potential or the membrane reaction temperature.

Chapter 8 Asymmetric tubular LSM80-CGO20/YSZ⊥TiO_2-Pd/YSZ-Ni(O) membrane reactor for partial oxidation of methane

This Chapter reports a new asymmetric tubular ceramic membrane reactor consisting of three layers (i.e., the porous $La_{0.2}Sr_{0.8}MnO_{3-\delta}$ (LSM80)-$Ce_{0.8}Gd_{0.2}O_{2-\delta}$ (CGO20) cathode layer, the dense YSZ⊥Pd-TiO_2 electrolyte layer, and the porous YSZ-Ni anode layer). In order to realize the dense electrolyte layer, a novel two-step colloidal suspension coating technology has been proposed. The fabricated membrane reactor was used to test the partial oxidation of methane (POM) under different temperatures. At reaction temperature of 850 ^{o}C very high methane conversion (>90%), CO selectivity (> 90%) and H_2 selectivity (>80%) were achieved. In addition, the methane reforming catalyst stability was studied and a new cyclic feeding process was proposed to improve the catalyst stability within the fabricated membrane reactor.

8.1 Introduction

Oxygen ionic conductive ceramics were widely studied in solid oxide fuel cells (SOFCs) and ceramic oxygen-electrolyte membrane reactors (COMRs). In a SOFC or COMR the dense oxide ion conductive ceramic layer, which is impervious to molecular gas, transports the O^{2-} from the cathode (P_{O2} ~ 0.21 atm) to the oxygen-lean side (or anode) (P_{O2} ~ 10^{-21} atm). High oxide ion permeate rate and stability under high oxygen pressure gradient are desired for the dense O^{2-} conductive layer. Unfortunately, up to now those materials with high oxide ion conductivity (such as La-Sr-Fe-Co perovskites) were found unstable under such high oxygen chemical potential gradient, while the stable ceramics (such as Y_2O_3 stabilized ZrO_2) had relatively lower oxide ion conductivity (Section 2.1.2 of Chapter 2). The asymmetric COMR structure, in which a thin dense ceramic layer coated on a thick porous support surface, has the great potential to achieve both high oxygen permeability and membrane stability. How to fabricate an asymmetric tubular COMR with low cost method is still a challenge before its commercialization (Section 2.3.2.2 of Chapter 2). Sol-gel technology, spray pyrolysis, chemical solution deposition (CSD), and ceramic powder processing methods required low-cost equipments. The dense layer should be thick enough to cover the underlying large micron-sized pores. To achieve the a dense and crack-free ceramic film with a thickness above 5 μm, the sol-gel, spray pyrolysis or CSD has to be repeated many times and thus became very time- and labor-intensive. Net shape technology (Jasinski et al., 2005; Petrovsky et al., 2004) was reported to decrease the sol-gel or CSD process times in achieving the dense ceramic film with thickness larger than 1 μm.

Ceramic powder processing methods, especially the colloidal deposition technology, were widely employed to fabricate a dense ceramic film upon a planar disk support surface. Du and Sammes (2004) fabricated an anode-supported tubular structure via vacuum-assisted dip coating and co-firing. In this work, a new two-steps colloidal suspension coating technology has been developed to obtain an asymmetric tubular membrane with the structure of thin dense YSZ (~ 10 μm)/thick porous YSZ-NiO (~ 1000 μm). An asymmetric membrane reactor for the methane partial oxidation into syngas was prepared using the developed technology and tested for the catalytic reaction at different temperatures. The POM stability due to coke formation on the catalyst surface is also one of the major issues for the commercialization of an effective COMR due to the very high possibility of the coking formation when reforming methane into syngas. In this work, the POM stability has also been studied.

8.2 Experimental

8.2.1 Synthesis of fine ceramic powders

The NiO fine powder was produced via pyrolysing the pre-ceramic gel comprising $Ni(NO_3)_2$ (98%, Nacalai Tesque) and polyvinylalcohol (PVA, 87-89% hydrolyzed, Mw: 13000-23000, Aldrich) (5 wt.% of the nickel nitrate) at 800 ^{o}C for 2 h. The details of the fabrication process have been described in Section 4.2.2 of Chapter 2. $La_{0.2}Sr_{0.8}MnO_{3-\delta}$ (LSM80) (Section 6.2.2 of Chapter 6) and $Ce_{0.8}Gd_{0.2}O_{2-\delta}$ (CGO20) (Section 5.2.1 of Chapter 5) fine powders were also prepared in house.

8.2.2 Fabrication of porous tubular support

The NiO powder and yttrium(III) stabilized zirconia fine powder (sub-micron YSZ containing 8 mol.% of Y_2O_3, Strem Chemicals) (1:1 by weight) were used to form the ceramic-polymer blend for extrusion. The polymer composition has been given in Section 6.2.1 of Chapter 6 (Table 6.1) and the preparation and extrusion of the ceramic-polymer blend have been detailed in Section 4.2.1 of Chapter 4. The extruded YSZ-NiO green tube comprising about 80 wt.% ceramic powders. The green tube was first slowly heated up in a Carbolite furnace to 400 ^{o}C (by 1 ^{o}C/min) and dwelled for 1 h to burn off the organic component, and then the temperature was raised to the precalcination temperature (1000 ^{o}C, by 1 ^{o}C/min) to form a partial sintered ceramic tube, which had very porous structure but free-standing, as the substrate for development of the functional layers on it.

8.2.3 Preparation of colloidal suspensions

Three types of ceramic fine powders were used to formulate colloidal suspension in this work, which were (1) YSZ, (2) a mixture of TiO_2 (Degussa PS-25) and Pd (1.0 ~ 1.5 μm, Aldrich) with the weight ratio of 1:1; and (3) a mixture of LSM80 and CGO20 with the weight ratio of 1:1. These powders were dispersed respectively in a specially formulated organic medium which contained organic binder and other additives and the resulting suspensions were milled by zerconia balls to obtain an ink-like colloidal dispersion. The detailed formulation has been described in Section 4.2.3 of Chapter 4. Besides organic-solvent based suspensions, water-borne suspensions which were free of polymer binder were fabricated by ball-milling the suspension of the respective ceramic powder 2 wt.% in D.I. water for 3 days.

8.2.4 Characterization of the fabricated tubes

The shrinkage rate (sr) of outside diameter (D) of the sintered tube was estimated by the formula, where D_o the initial diameter of the extruded green tube

$$sr = \left(1 - \frac{D}{D_o}\right) \times 100\% \tag{8.1}$$

The surface and cross-sectional morphologies were examined by scanning electron microscopy (SEM) (JEOL JSM-5600) with an energy dispersive X-ray (EDX) to determine the spatial dependent compositions. The porosity of the fabricated porous tubes was measured by simple Archimedes' method (Shaojai and Mäntylä, 2001).

8.2.5 Fabrication of membrane reactor

8.2.5.1 Formation of dense YSZ electrolyte layer

Figure 8.1 shows a unique tactic to prepare an asymmetric tubular COMR that was composed of the triple cylindrical layers. The YSZ-NiO core layer made by extrusion and precalcination of the green tube via a heating program with setting 1000 ^{o}C as the highest temperature and the dwelling time of 2 h, had the thickest wall (~ 1000 μm) and porous structure, and the other two coaxial layers, namely YSZ and LSM80-CGO20, were formed respectively onto the YSZ-NiO tube by coating it with colloidal suspension and subsequently by calcination the coated structure. For applying the colloidal suspension, in contrast to the conventional coating procedure as shown by path (a) in Fig. 8.1, a novel coating procedure labeled by (b) was designed in this work with the aim of achieving a dense YSZ layer. For more specifically, this new coating procedure consisted of two operation steps. Firstly, the organic colloidal suspension of YSZ was applied by brushing (or dip coating) to the porous YSZ-NiO tube to form a layer of YSZ powder "cake" which contains organic additives of ca. 10.8 wt.%. This coated tube was then subjected to calcination (by heating rate of 1 °C/min) at 900 °C for 2 h to obtain the tubular structure YSZ/YSZ-NiO, where the YSZ coating layer is still very porous. Secondly, the water-borne YSZ suspension which was totally free of organic additives was applied by brushing on the YSZ layer and the object was calcined at 1450 °C for 4 h to accomplish the tubular structure YSZ/YSZ-NiO, where the YSZ layer was totally dense but the YSZ-NiO substrate remains porous.

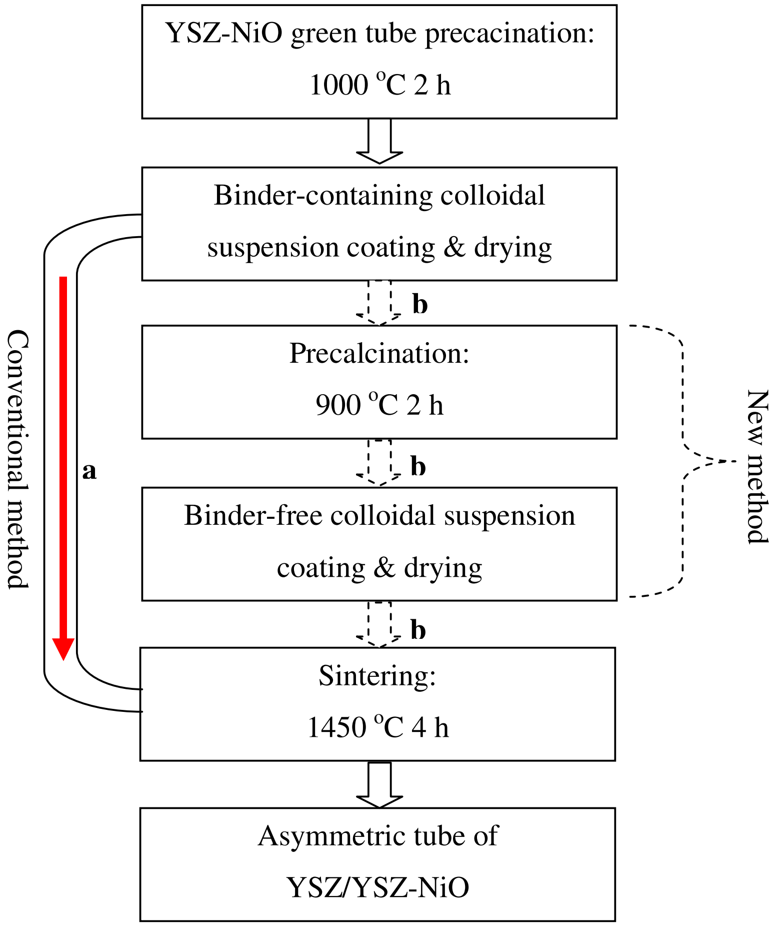

Figure 8.1 Schematic of the asymmetric ceramic tube fabrication process: (a) conventional colloidal suspension coating method; (b) novel two-steps colloidal suspension coating method

8.2.5.2 Slotting in an electron conductive TiO_2-Pd belt in the dense YSZ layer

Introducing an electron returning pathway into the electrolyte YSZ layer is essential to allow the negative charge injected into the anode layer (YSZ-Ni) to be able to return to the cathode layer (LSM80-CGO20) for sustaining generation of oxygen anions O^{2-}. A narrow belt of TiO_2-Pd belt was slotted in the YSZ layer. For doing so, a straight trench (of ~ 2.5 mm wide) along the axial direction was scratched in the coated YSZ-organic layer produced by the first step of procedure (b) as mentioned above. Over this trench a layer of powder cake of TiO_2-Pd (1:1 by wt.) was laid down by using the colloidal suspension formulated and the TiO_2-Pd layer became dense in the second stage of calcination at 1450 ^{o}C. The resulting structure is termed as YSZ⊥TiO_2-Pd/YSZ-NiO.

8.2.5.3 Formation of porous LSM80-CGO20 cathode layer

A porous LSM-CGO20 layer (1:1 by weight) was deposited on the dense YSZ⊥TiO_2-Pd electrolyte layer as the cathode. The organic LSM80-CGO20 colloidal suspension (with organic phase) was employed to form a powder cake layer via brush coating, and the coated object was subjected to calcination at 1200 ^{o}C for 2 h to form the cathode layer. As such, a triple layer cylindrical membrane reactor as depicted in Fig. 8.2 was realized, in which both LSM-CGO20 and YSZ⊥TiO_2-Pd layers were all about 10 μm thick.

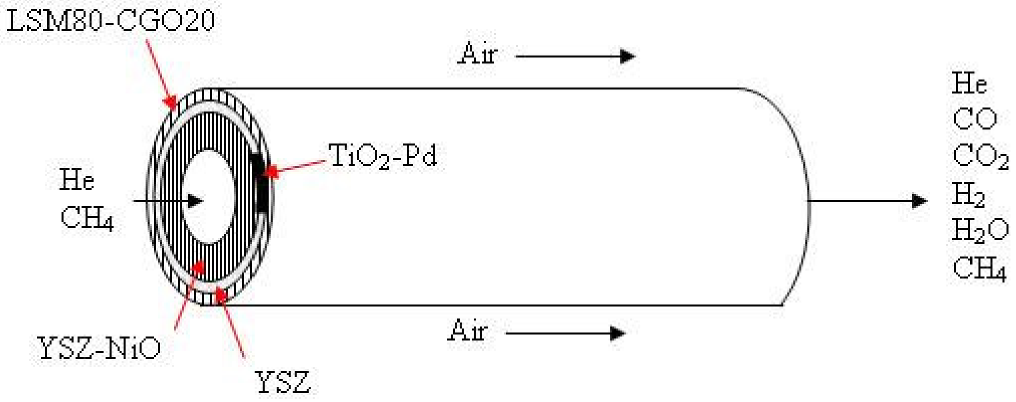

Figure 8.2 Schematic of the fabricated COMR for POM

8.2.6 Operating the membrane reactor for partial oxidation of methane

The details of the methane reforming reactor setup were reported in Section 4.2.5 of Chapter 4. The exterior surface area of membrane reactor was about 10 cm^2. The membrane reactor was heated to the designated reforming temperature and then a steam of H_2 gas (30 sccm) was allowed to pass through the tube for 40 min. During this period of time, reduction of NiO to Ni(0) in the inner side of the tube, namely the YSZ-NiO thick wall, was completed. After that methane gas (5 sccm) diluted with 30 sccm He for the safety concern was introduced into the reactor. The products of methane reforming were detected by an on-line gas chromatograph (Clarus 500, PerkinElmer ARNEL). The methane conversion (X_{CH4}), CO selectivity (S_{CO}), and H_2 selectivity (S_{H2}) were calculated by the Eqs (7.1), (7.2) and (7.4) in Section 7.2.3 of Chapter 7.

8.3 Results and Discussion

8.3.1 Shrinkage and densification study

To obtain an asymmetric tube with desired qualities the shrinkages of the two layers should be close to each other; otherwise, delamination or crack may be introduced after co-firing the structure at high temperature. Figure 8.3 showed the *sr* (Eq. 8.1) of YSZ and YSZ-NiO tubes at different sintering temperatures. The *sr* of the YSZ tube was smaller than that of YSZ-NiO tube at the corresponding sintering temperatures due to likely the retarding effect of NiO phase on the sintering.

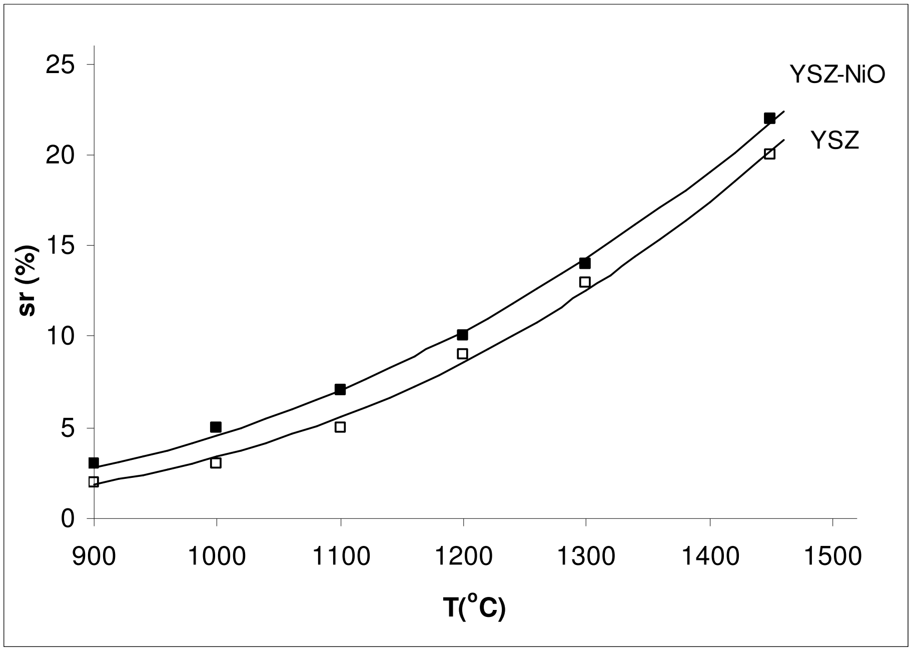

Figure 8.3 Dependence of the shrinkage rate (sr) of the YSZ and YSZ-NiO tubes on the sintering temperature

Figure 8.4 showed the porosity of the above two tubes. The difference in porosity between the two tubes was almost close to 5% before the sintering temperature of 1200 °C, but the difference tended to minimize with increasing sintering temperature. Both tubes exhibited almost the same porosity of about 19% after being sintered at 1450 °C for 2 h. Increase the sintering time from 2 h to 4 h at 1450 °C decreased the porosity of the YSZ-NiO tube to 16%. Figure 8.5 showed the SEMs of the exterior surfaces of the YSZ-NiO and YSZ tubes sintered at 1200 °C & 1300 °C for 2 h. Pure YSZ displayed a greater sintering tendency than YSZ-NiO because NiO powders blocked consolidation of the coexisting YSZ phase. The large extent of sintering produced a lot of dead holes inside the YSZ tube, which could not easily be measured by Archimedes method and accounted for the lower measured porosities of the pure YSZ tube at sintering temperature below 1200 °C. The fact that pure YSZ prefers to consolidate is very important to form a dense electrolyte layer.

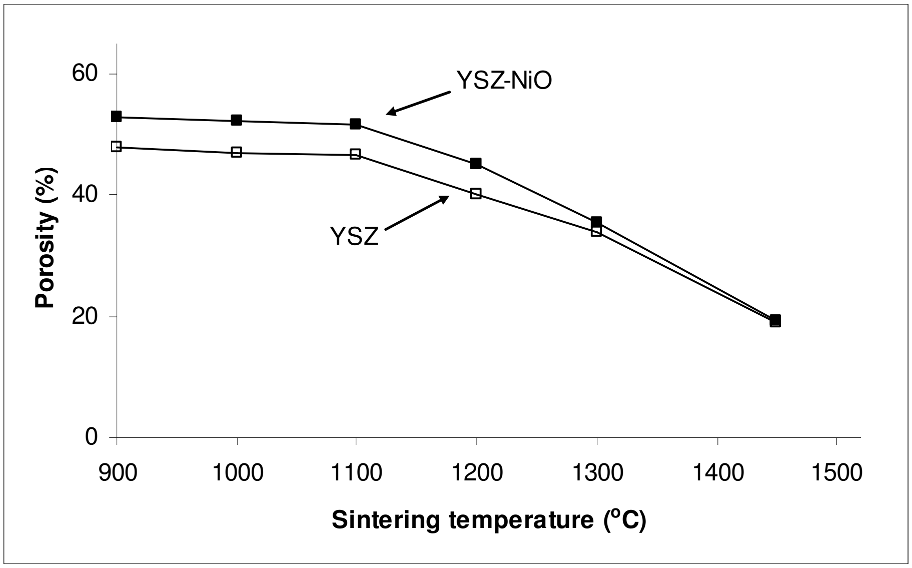

Figure 8.4 Dependence of the porosity of the YSZ and YSZ-NiO tubes on the sintering temperature

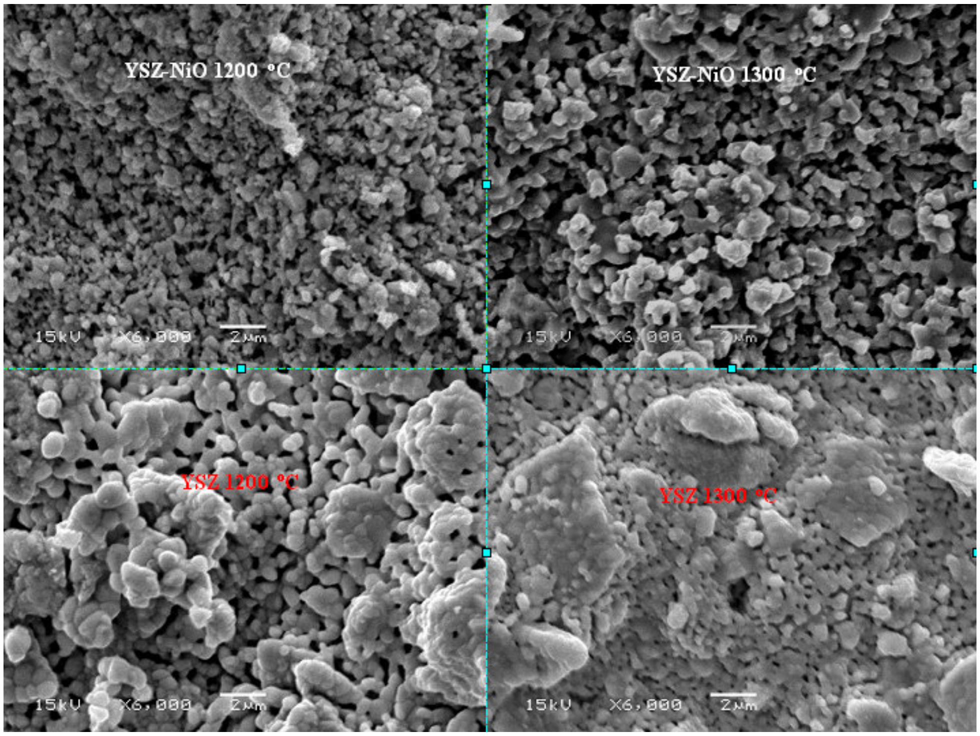

Figure 8.5 SEMs of the outside surfaces of the YSZ and YSZ-NiO tubes sintered at different temperatures

8.3.2 Fabrication of asymmetric YSZ/YSZ-NiO tubes

The exterior surface of the tubular YSZ/YSZ-NiO structure of the YSZ coating layer generated from the first stage (Section 8.2.5.1) was still very porous (Fig. 8.6a). In comparison, a higher particle packing density could be obtained from putting the second YSZ coating layer onto the above YSZ porous layer by using the binder-free YSZ colloidal suspension and calcining the object again at 900 ^{o}C for 2 h (Fig. 8.6b). We also found that the precalcination temperature for the YSZ-NiO tube was crucial to the development of further coating layers on it. Too low a precalcination temperature (< 800 ^{o}C) would result in a very weak tube and not suitable for further handling, whereas too high a precalcination temperature (> 1200 °C) would bring about a large shrinkage (Fig. 8.3) and close a lot of surface pores which are essential for forming YSZ powder cake layer in the following coating process. The optimal precalcination temperature was between 900 °C and 1100 °C, and we used 1000 °C to obtain a partially sintered YSZ-NiO tube, which possessed adequate mechanical strength for coating manipulation as well as surface porosity for supporting a powder cake layer formed by coating with the organic colloidal suspension.

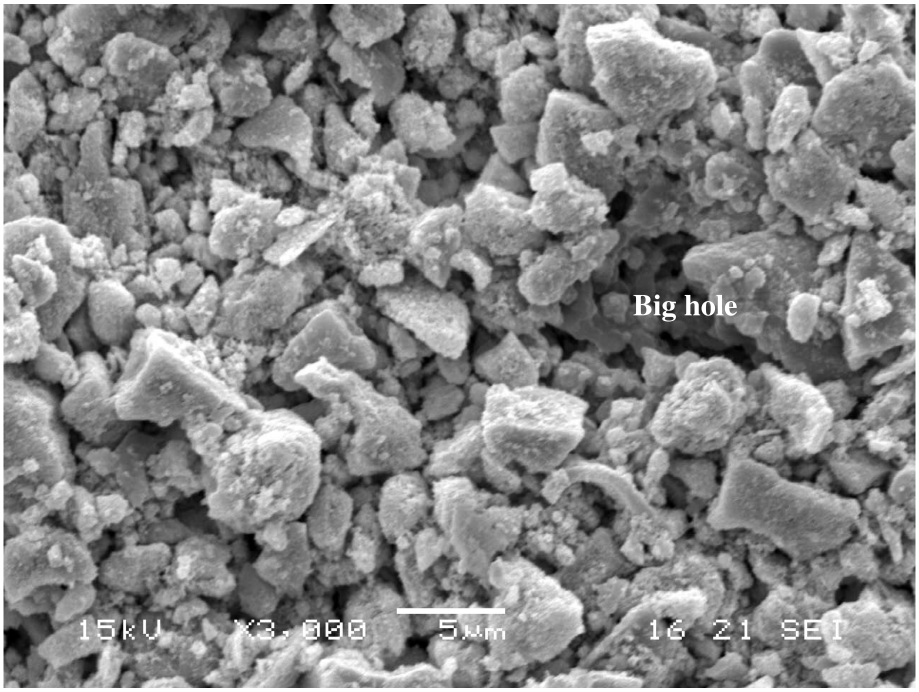

(a)

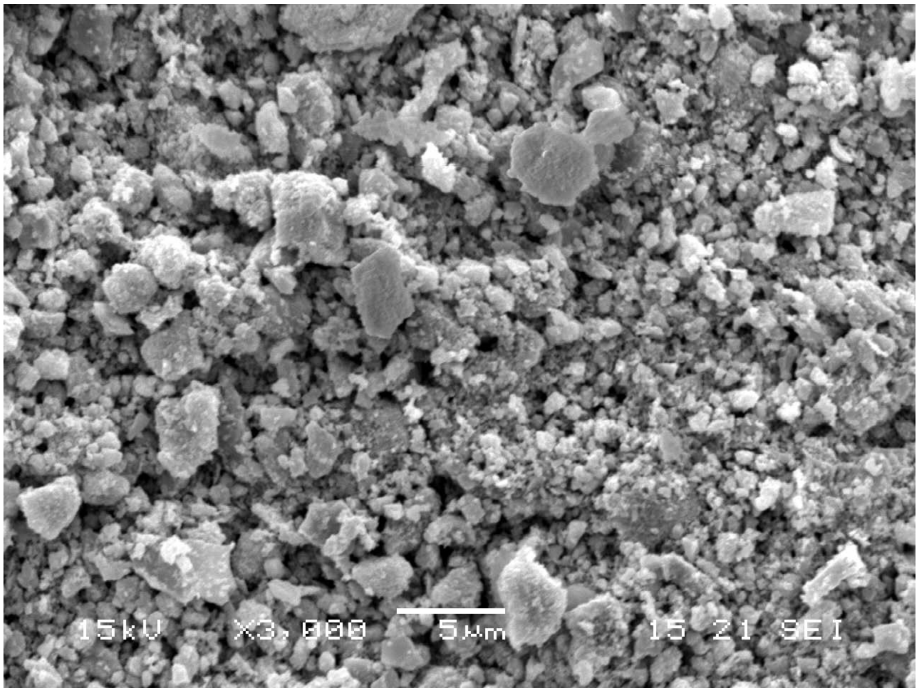

(b)

Figure 8.6 SEMs of the tube outside surface: (a) after conventional colloidal suspension coating and sintering at 900 ^{o}C for 2 h; (b) after two-steps colloidal suspension coating and sintering at 900 ^{o}C for 2 h

The dry powder cake layer of YSZ from the organic coating consisted of YSZ particles of around 81 vol.% and organic additives taking up the rest of space. The drying of the coating layer and later on burning off the organic additives were responsible for the generation of large pores, voids or cracks (Lewis 2000; Cima et al., 1989). In addition, the thickness of the powder cake layer (or powder loading by mg/cm^2) made by increasing times of coating of the organic suspension affected the matrix structure of YSZ layer after sintering at 1450 ^{o}C for 2 h (Fig. 8.7a-c). It was found that the powder loading of 6 mg/cm^2 achieved the least cracking YSZ matrix (Fig. 8.7a) even though some pinholes and cracks in micron range couldn't be avoided. These defects were the results of the unevenly packed YSZ powders in the YSZ layer as shown in figure 8.6a. While being calcined at high temperature, some pores within the YSZ layer had negative surface curvature and were thermodynamic unstable and tend to grow (Chiang et al., 1997) and finally formed the pinholes. The drying of coating layer made from colloidal suspension and the removing of organic additives have been widely studied and were found to be very complicated (Lewis, 2000; Chiu & Cima, 1993). Generally, a thicker coated layer favours crack formation at the drying and organic removal stages. Increasing the amount of the coated YSZ particles would worsen the situation (Figs. 8.7 b & c).

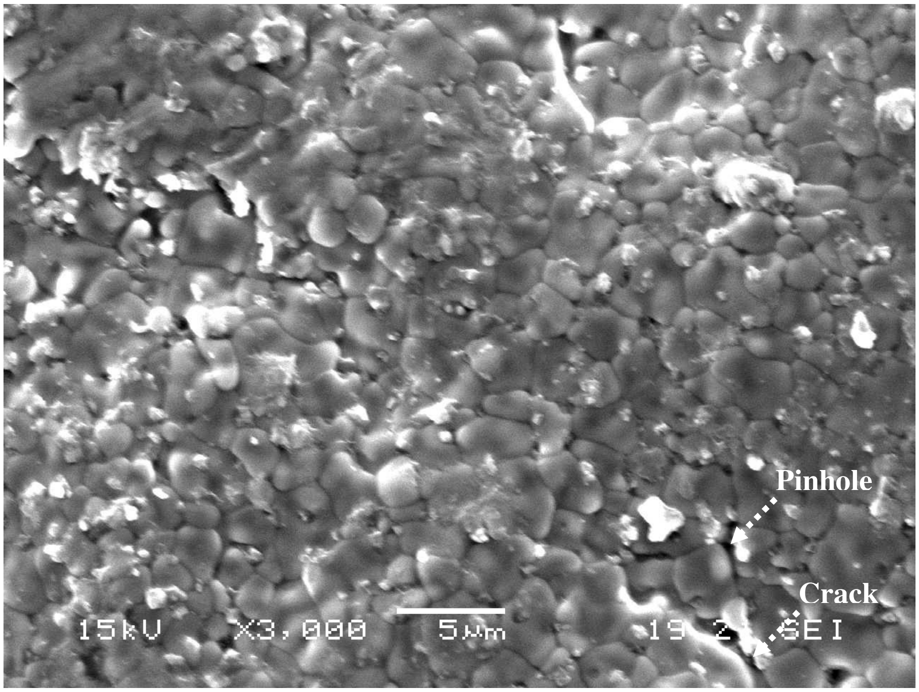

(a)

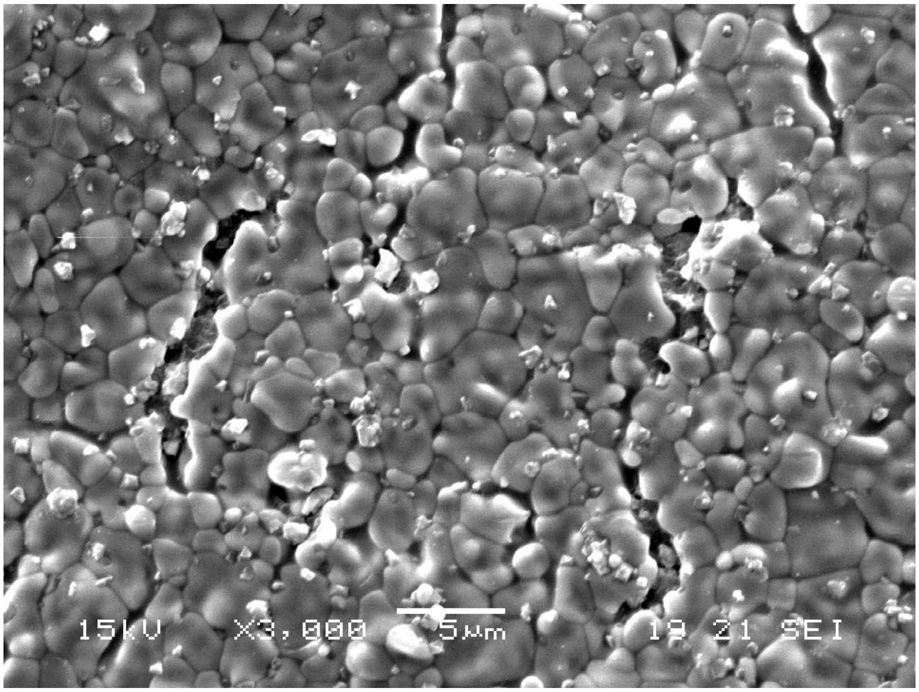

(b)

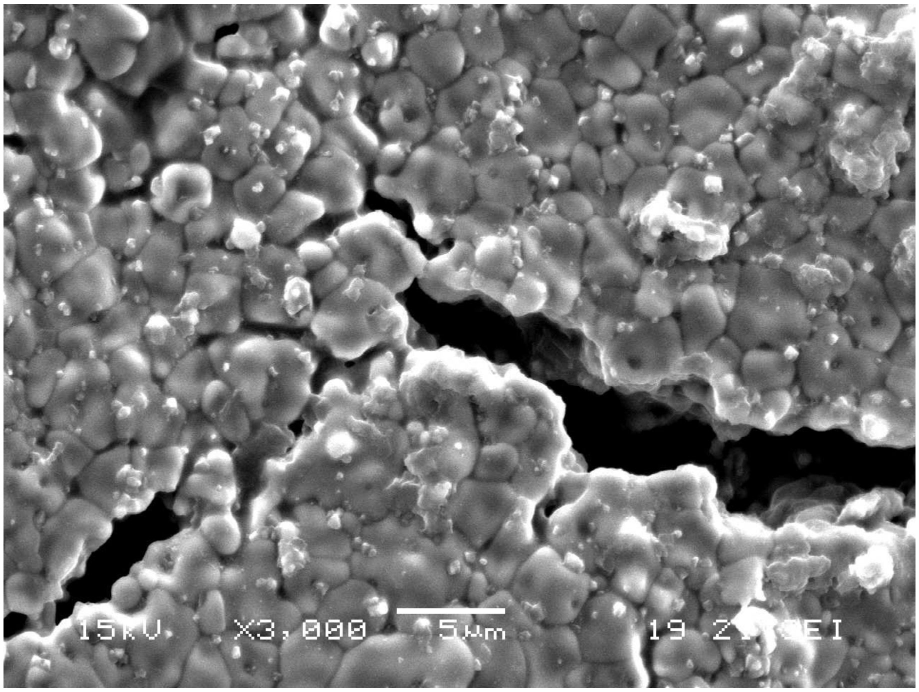

(c)

Figure 8.7 SEMs of the YSZ outside surface fabricated via traditional colloidal deposition method: (a) 6 mg coated YSZ powders/cm^2 outside tube surface; (b) 12 mg coated YSZ powders/cm^2 outside tube surface; (c) 24 mg coated YSZ powders/cm^2 outside tube surface

To get rid of pinholes and cracks a two-step coating method was developed. It means that an additional coating aims at filling the big pores or cracks left in the precalcined YSZ layer was to pursue. The colloidal suspension used to carry out the second coating was organic binder-free so there was no problem of removing the organic binder. A comparison of Fig. 8.6a with Fig. 8.6b showed the effect that big pores existing in the former matrix were filled by small YSZ particles in the latter matrix that is the prerequisite for achieving a defect-free matrix when sintered at 1450 °C. Figure 8.8 gives a schematic of how the two-steps method functions. At the 1st step the coated YSZ particles are deposited onto the porous YSZ-NiO surface to provide a framework with designed thickness. At the 2nd step the YSZ particles are filled into the YSZ large pores or cracks resulting in a compact uniform YSZ layer.

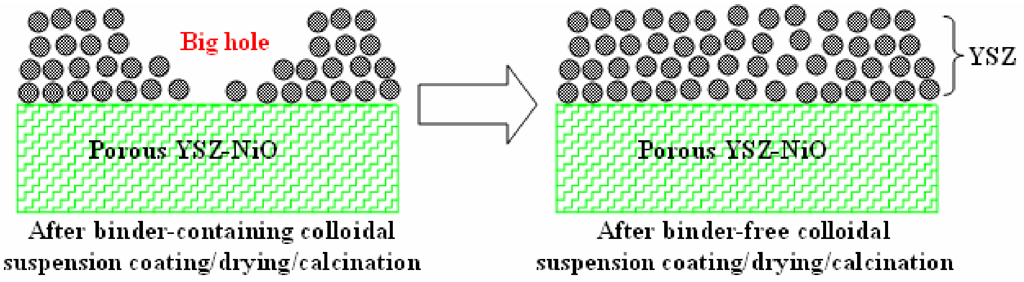

Figure 8.8 Schematic of the removal of voids or cracks by the invented two-steps YSZ coating technology

After sintering at 1450 °C for 2 h, the YSZ layer made by the two-step procedure was dense and crack-free (Fig. 8.9a). This pure YSZ layer was stable at the reducing atmosphere. Fig. 8.9b is the SEM showing that the YSZ layer was intact after the tube went through reduction of NiO at 850 °C for 30 min under 20 sccm H_2 gas flow. Even under such harsh reducing environment the YSZ layer was still dense and crack-free.

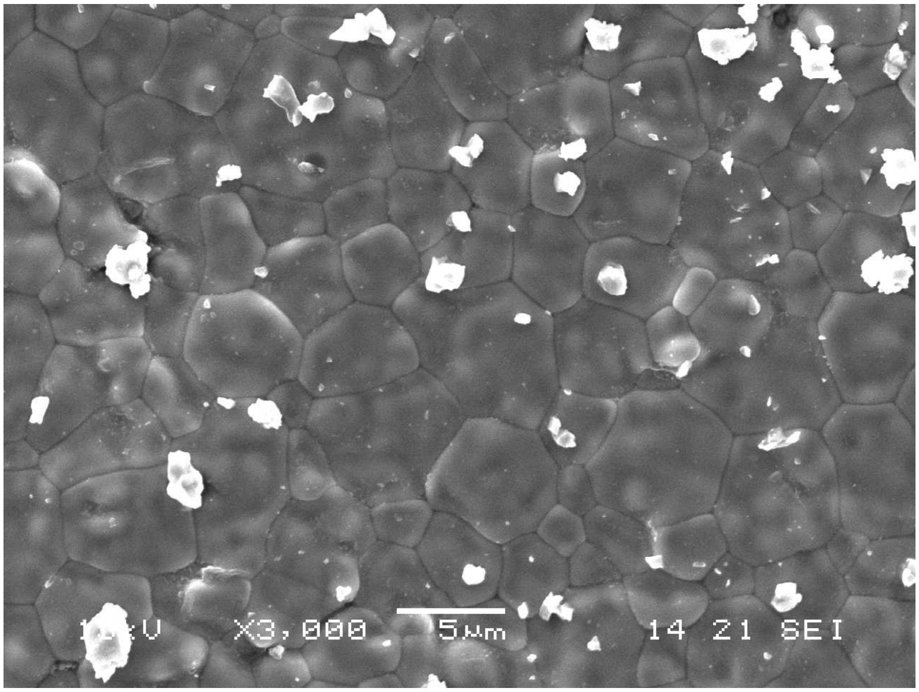

(a)

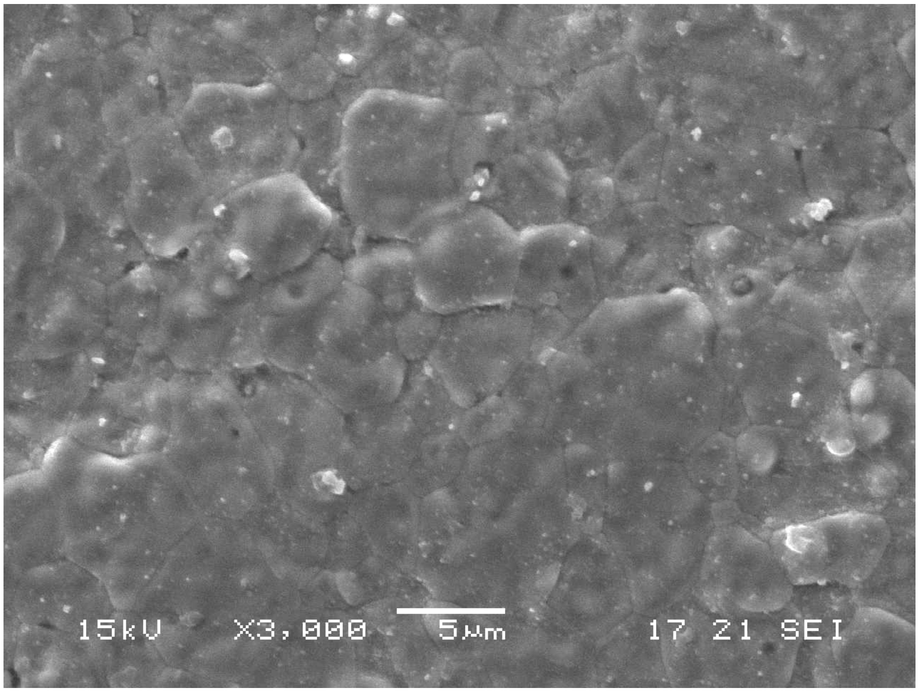

(b)

Figure 8.9 SEMs of the outside YSZ surface of the asymmetric tube fabricated via the new colloidal deposition method: (a) freshly fabricated; (b) reduced at 850 ^{o}C 20 sccm H_2 for 30 min

Figures 8.10 a, b & c showed the cross-section SEM of the fabricated asymmetric dense YSZ/porous YSZ-NiO membrane, the reduced dense YSZ/porous YSZ-Ni membrane, and the dense YSZ/porous YSZ membrane after leaching out the Ni using 50 vol.% HNO_3 aqueous solution at 50 ^{o}C, respectively. A careful check of Fig. 8.10a showed that the fabricated asymmetric membrane actually consisted of three layers, i.e., dense pure YSZ layer (~ 10 μm thickness), porous YSZ-NiO layer 1 (40 - 10 μm thickness), and porous YSZ-NiO layer 2 (~ 1000 μm thickness). The porous YSZ-NiO layer 2 has more uniform pores than that of the YSZ-NiO layer 1. EDX showed that no Ni was found in the dense YSZ layer, whereas obvious Ni was detected in the porous YSZ-NiO layer 1. After H_2 reduction the porosity of the fabricated asymmetric membrane increased from 16% to 25% which was lower than the theoretical value of 32% assuming total reduction of NiO and no Ni sintering during reduction process. The lower experimental porosity suggested in-situ aggregation of Ni particles or partially re-oxidation of Ni into NiO during the cooling down process. As showed in Fig. 8.10b, the pure YSZ layer was dense, while the YSZ-NiO layers were porous. The pore size distribution of YSZ-NiO layer 2 was more uniform than that of the YSZ-NiO layer 1 (Fig. 8.10b). After leaching Ni out of the base no porosity difference between these two layers were detected but the layer 1 contained lots of big pores (Fig. 8.10c), which suggested that the differences between YSZ-NiO layer 1 and YSZ-NiO layer 2 were mainly caused by the NiO distribution among the YSZ network. During co-sintering of the YSZ/YSZ-NiO object, the gas escaped from the YSZ-NiO layer 1 need to penetrate through the YSZ-NiO layer 2 because the pure YSZ layer has high particle packing density and was finally sintered to dense. Therefore, there exist some local sites within the YSZ-NiO layer 1 which have enough high pressure to push the NiO out and redistribute within the layer 1 resulting large pores and decreasing the number of pores. Figures 8.11 a, b & c showed the inner surface SEMs of the freshly fabricated, H_2 reduced, and Ni leaching out membranes, respectively.

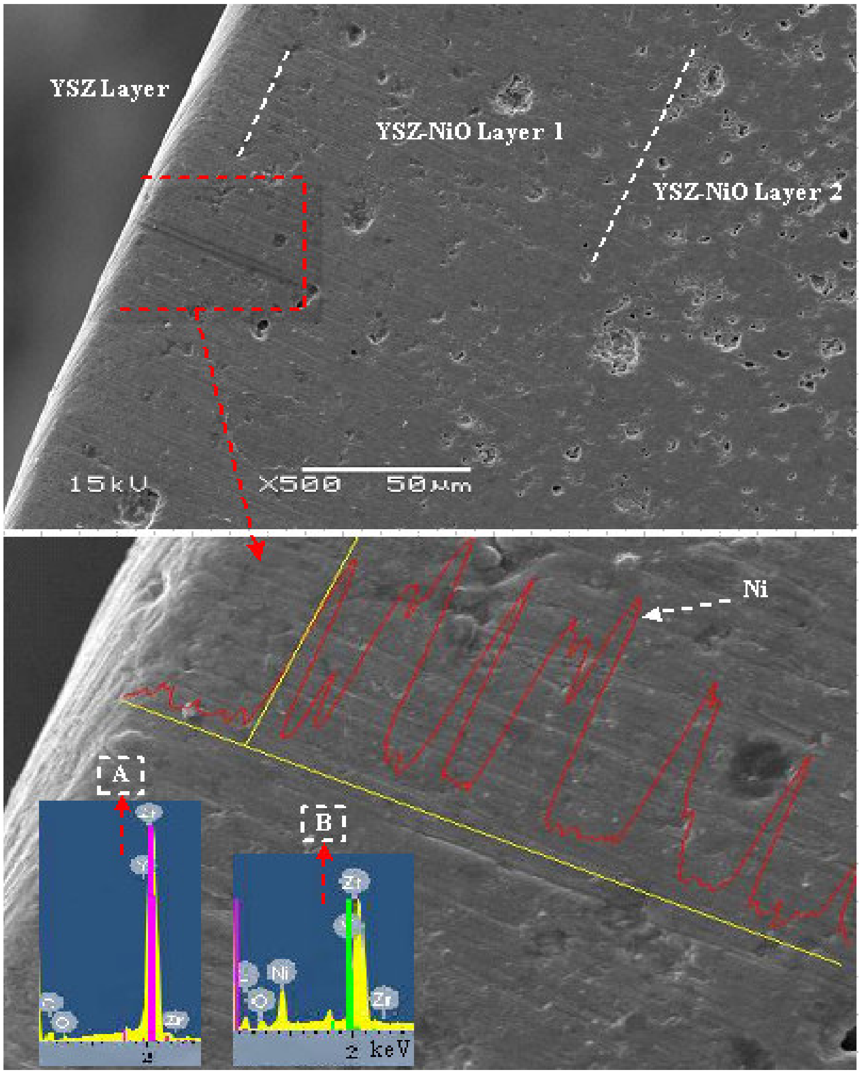

(a)

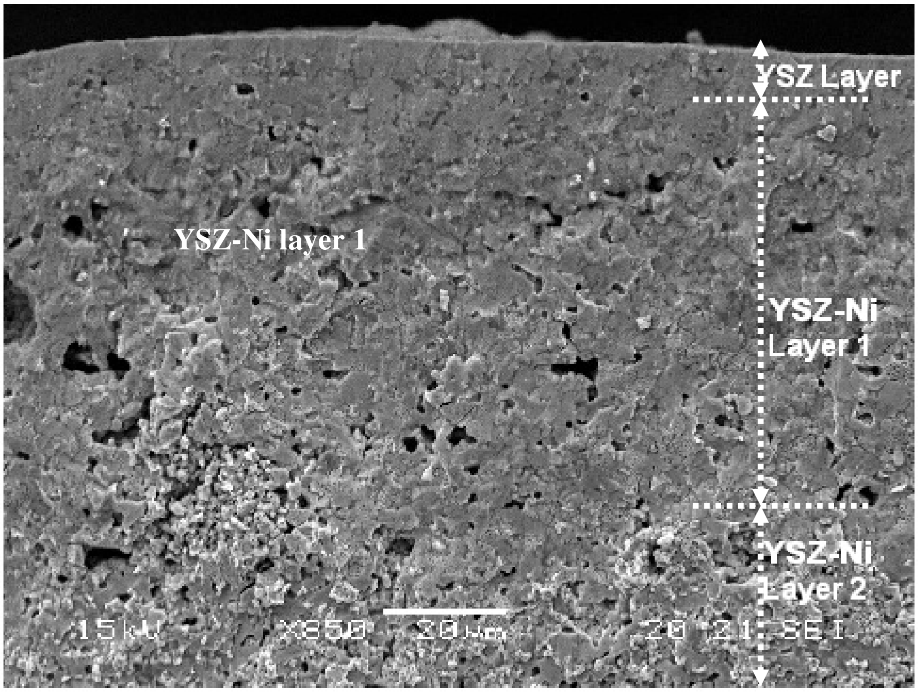

(b)

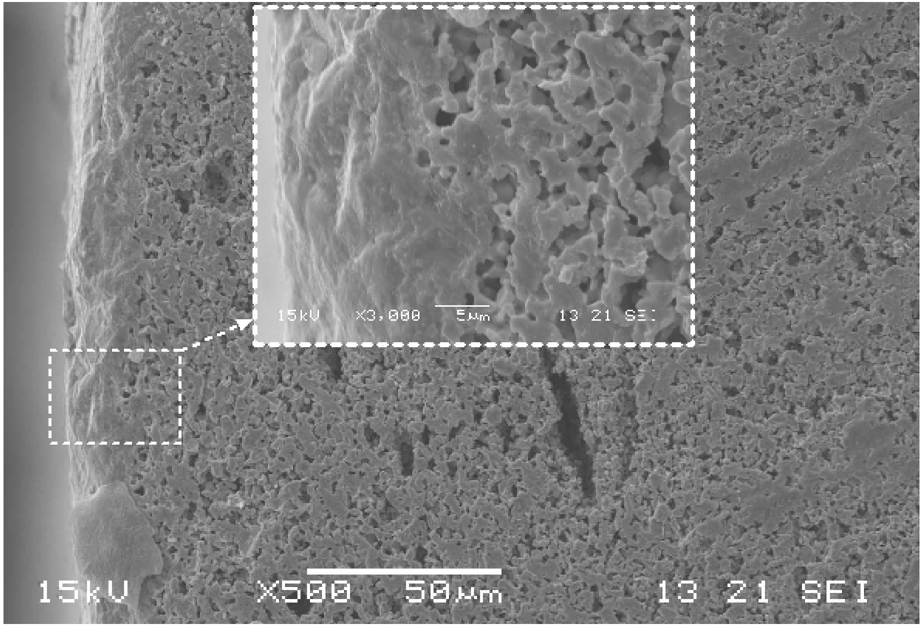

(c)

Figure 8.10 Cross-sectional SEMs of: (a) freshly produced; (b) after H_2 reduction; (c) after Ni leached out

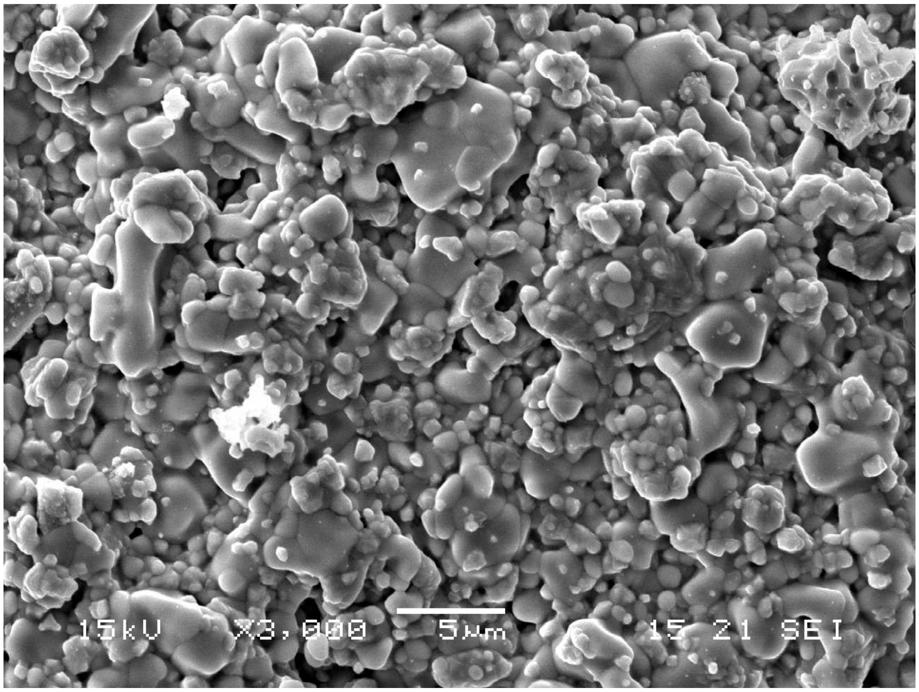

(a)

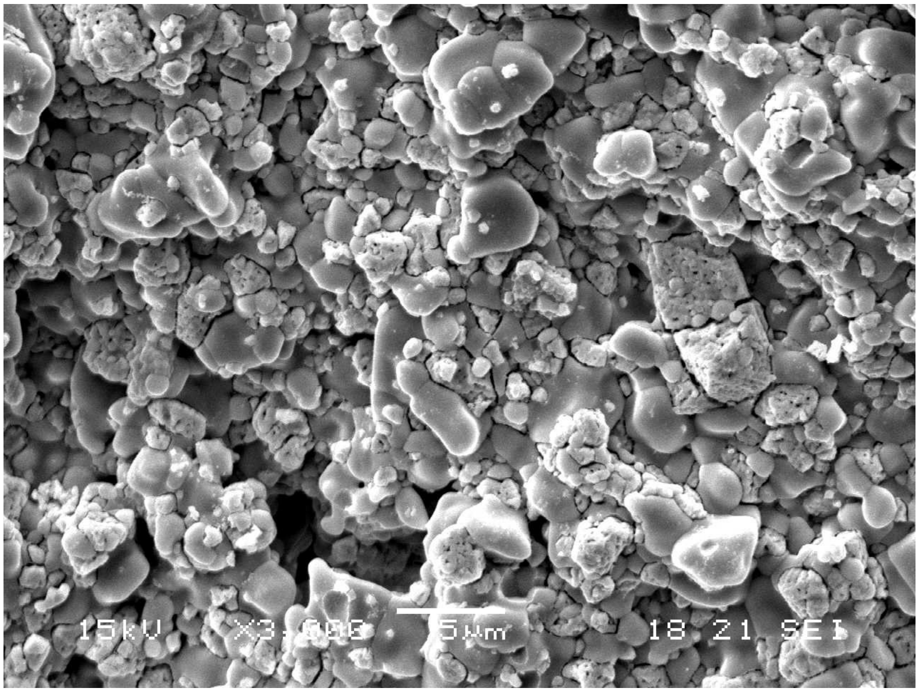

(b)

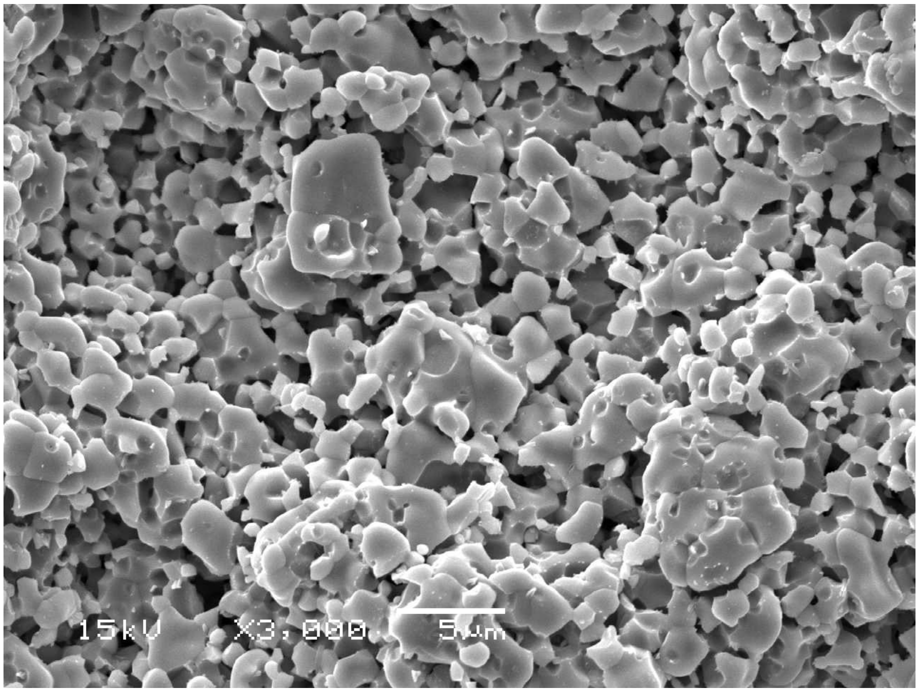

(c)

Figure 8.11 Inner surface SEMs of: (a) freshly produced; (b) after H_2 reduction; (c) after Ni leached out

8.3.3 Methane reforming via membrane reactor

Figure 8.12 showed the methane conversion (X_{CH4}), CO selectivity (S_{CO}), and H_2 selectivity (S_{H2}) within reaction temperature range from 623 to 850 ^oC. X_{CH4}, S_{CO}, and S_{H2} increased with the increase of the reaction temperature. Raising temperature significantly increased the methane conversion and H_2 selectivity, while the increase of CO selectivity was not so significant especially when the temperature was lower than 750 ^oC. At 850 ^oC high methane conversion (>90%), CO selectivity (> 90%), and H_2 selectivity (> 80%) were achieved. The overall electrochemical reaction of the methane within the membrane reactor can be written as Eq. 8.2 (Mogensen and Kammer, 2003).

$$CH_4 + O^{2-} \rightarrow CO + 2H_2 + 2e^- \qquad (8.2)$$

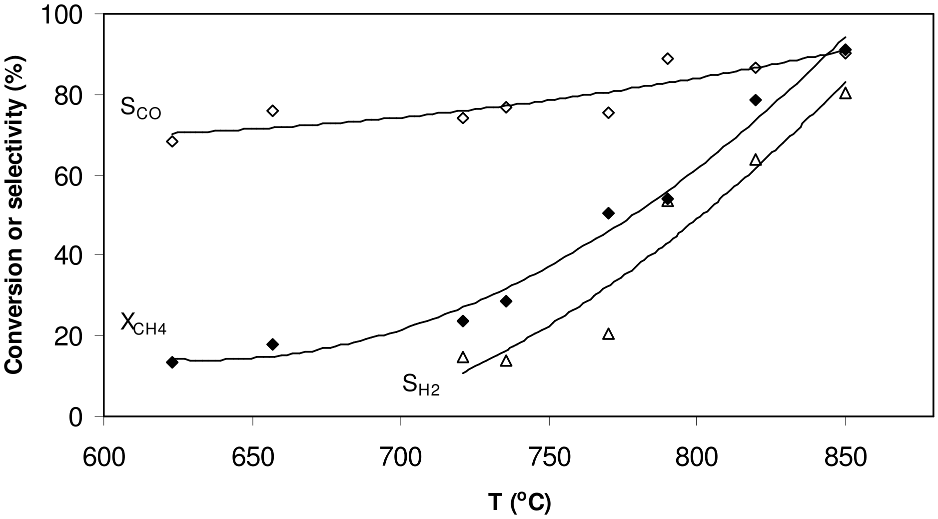

Figure 8.12 POM results within the measuring temperature range

During the methane activation process, an incident CH_4 molecule was first adsorbed on the catalyst surface and then subsequently dissociated into the surface adsorbed carbon (C_s) and hydrogen (H_s) species ($CH_{4-x,s} \rightarrow CH_{4-x-1,s} + H_s$, x is integer and $0 \leq x \leq 3$). The CO came from the reaction between the formed C_s and surface oxygen species O_s^* such as O, O^-, or O^{2-} ($C_s + O_s^* \longrightarrow CO_s$). Oxidation of the surface adsorbed carbon mono-oxide with O_s^* resulted in CO_2 ($CO_s + O_s^* \longrightarrow CO_{2,s}$). H_2 gas was the result of the combination of two H_s atoms ($H_s + H_s \longrightarrow H_2$). The reaction between the H_s and O_s^* resulted in the steam ($H_s + O_s^* \longrightarrow HO_s$ & $HO_s + H_s \longrightarrow H_2O_s$). From this POM mechanism, it is expected that the methane reforming stability due to the formed carbon filaments can be improved if the deposited carbon being removed in time.

8.3.4 Methane reforming catalyst stability study

Figure 8.13 shows the continuous POM results (5 sccm CH$_4$/30 sccm He, at 850 ^{o}C) over a reaction time span of 90 min. It can be seen that both the methane conversion and the H$_2$ selectivity decreased as the reaction time significantly, whereas the time has no obvious effect on the CO selectivity. Such different trends suggested that the activity of the nickel catalyst decreased as the increase of reaction time due to the coke formation. The carbon filament on the nickel surface brought down the methane conversion and therefore the H/O ratio, which resulted in the decreasing of H$_2$ selectivity. The CO selectivity is not obviously affected by losing the nickel activity since the C/O ratio does not varied significantly. The activity of the nickel catalyst is expected to be recovered if the surface carbon filament can be cleaned up in time. Actually, the COMR has the advantage to remove the carbon filament by the diffused pure oxygen from the air side.

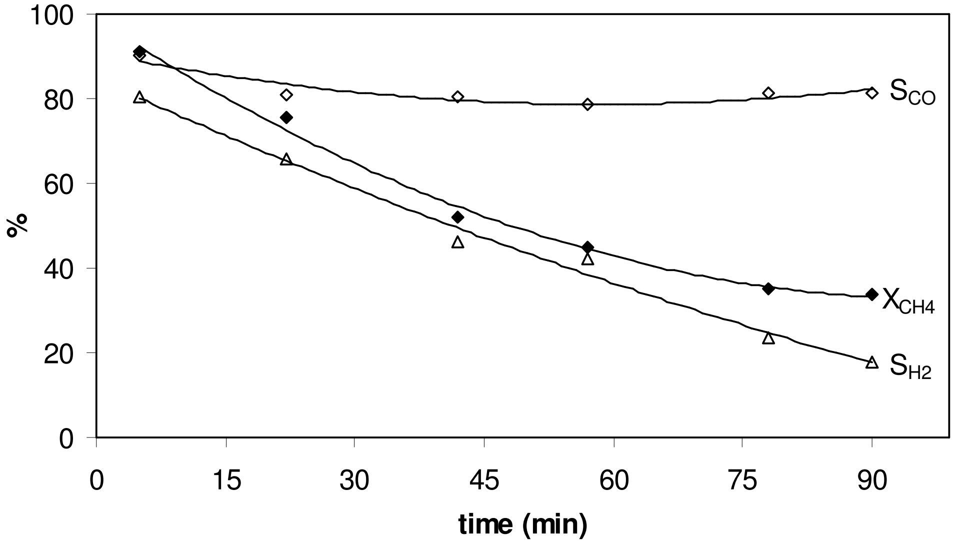

Figure 8.13 Time dependent output of the continuous POM

Figure 8.14 shows the POM results from cyclic operation, in which the CH_4 mixture (5 sccm CH_4/30 sccm He) and pure He gas (30 sccm) is supplied periodically for each 10 min. Fig. 8.14 displays the results while the supplying of CH_4 mixture gas was resumed, but the total reaction time was 200 min. All the methane conversion, H_2 selectivity and CO selectivity remained stable over the reaction course. The deposited carbon on the catalyst surface was effectively scavenged in the intervals when the CH_4 feeding was ceased and thus the POM stability was improved significantly.

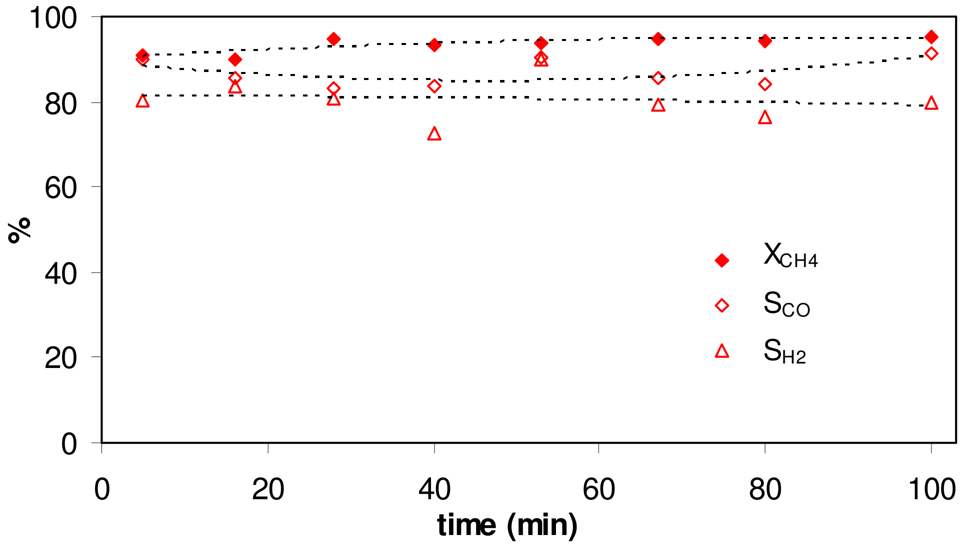

Figure 8.14 Dependence of the results of cyclic POM on reaction time

8.4 Conclusions

A novel low-cost colloidal suspension coating method was invented to manufacture an asymmetric ceramic membrane reactor in this paper. To prevent the voids or cracks caused by the binder removal in the traditional colloidal deposition technology an additional binder-free colloidal suspension coating process was employed. The binder-free colloidal suspension was coated to fill the voids or cracks after pre-firing of the binder-containing colloidal deposition. After co-firing the support and the deposited colloidals an asymmetric thin dense YSZ/thick porous YSZ-NiO membrane was fabricated. The fabricated membrane was found actually to consist of three layers, i.e., dense YSZ layer (~ 10 μm thickness), porous YSZ-NiO layer 1 (40 ~ 80 μm thickness), and porous YSZ-NiO layer 2 (~ 1000 μm thickness). The YSZ-NiO layer 1 has the same NiO concentration as the YSZ-NiO layer 2 but different pore size which was caused by the aggregation of the NiO particles during sintering. The NiO aggregation within the YSZ-NiO layer 1 was more serious due to the dense YSZ layer than that within the YSZ-NiO layer 2, which introduced larger pores.

An asymmetric tubular ceramic membrane reactor (porous LSM80-CGO20/ dense YSZ⊥TiO_2-Pd/porous YSZ-Ni) for methane reforming into syngas was fabricated using the created new low cost fabrication method. The membrane reactor showed high methane conversion (> 90%), CO selectivity (> 90 %), and H_2 selectivity (> 80%) at 850 ^{o}C. It was also found that the fabricated COMR lost its catalytic activity fast due to the unavoidable coke formation on the nickel surface; however, the cyclic feeding of the reactants was found to be able to scavenge the deposited surface carbon filament and thus increased the POM stability significantly.

Chapter 9 A study of methane dissociation mechanism

An accurate understanding of the methane dissociation mechanism is very important for the analysis of the methane reforming performance in POM-COMR. The mechanism figured out could also benefit other important industrial processes such as steam methane reforming. This study employed density function theory (DFT) to carry out theoretical simulation of the methane dissociation rate determination step (i.e., the 1st C-H cracking process). As a result, a new methane 1st C-H cleavage pathway has been proposed, a new theoretical method without fitting parameter to calculate the initial methane thermal sticking coefficients has been developed. The long time debate about whether or not the methane dissociation is the H tunneling process has also been resolved. The way of how to explain the methane reforming conversion at high temperature by this theoretical result has been proposed as well. The theoretically calculated methane dissociation energy barrier and the methane initial sticking coefficients were found to be very close to the experimental data from the literature. The methane dissociation is a new process, which is neither the H tunneling nor the pure traditional “over barrier” process, and the theoretical result can satisfactorily explain the methane conversion measured in Chapter 8.

9.1 Introduction

To date, it has been widely considered that the 1st C-H cleavage of methane was the rate determination step for methane dissociation processes (e.g., POM, SMR, and methane thermal cracking). To understand the methane 1st C-H cleavage mechanism, many theoretical work based on cluster or slab model on Ni(111) surface have been performed; however, the calculated energy barriers were much higher than the molecular beam experimental data measured by Lee et al. (51 kJ/mol) (1987) and Beebe et al. (53 kJ/mol) (1987). The reported theoretical simulations essentially used the same methane 1st C-H cracking pathway, by which the molecular CH_4 adsorbed and dissociated on-top of a single Ni atom (1-fold site) and this was followed by the diffusion of the CH_3 and H species towards the opposite 3-fold sites next to this Ni atom. This Chapter proposed a new methane 1st C-H dissociation pathway on Ni(111) surface, wherein the CH_4 molecule was adsorbed and dissociated on the 3-fold site and the generated H shifted to an adjacent 3-fold site while the CH_3 underwent rotation and diffused to the surface of nickel cluster instead to another site. The calculated energy barrier (52 kJ/mol) was very close to the experimental data (51 ~ 53 kJ/mol).

The comparison of the calculated initial methane sticking coefficients with the experimental data can be used to examine the proposed methane dissociation mechanism; however, there still has no an effective theoretical method to calculate the methane sticking coefficients accurately. Using H tunneling theory, Yang and Whitten (1992) calculated the sticking coefficient on Ni(111) surface, which was found to be only about half of the molecular beam experimental data reported by Beebe et al. (1987). Beebe et al. (1987) calculated the thermal sticking coefficients on Ni(111) surface using empirical formula and the calculated results were found much lower than the experimental data measured by them. In this work, we proposed a new theoretical method without fitting parameter for the mathematical calculation of the initial methane thermal sticking coefficients.

Three decades ago Winters (1976) explained the kinetic isotope effect in methane dissociation process by H tunneling theory. Since then, it has become a long time debate whether the methane dissociation on the H tunneling mechanism or the "over barrier" mechanism described by transition-state theory. Lee et al. (1987) reported one-dimensional H tunneling model and Luntz and Harris (1991 & 1992) developed multi-dimensions H tunneling model; however, much more studies assumed that the methane dissociation on non-tunneling models (Holmblad et al., 1995; Beck et al., 2003; Bukoski & Harrison, 2003; Abbott et al., 2003). One of the reasons why this debate still can not be solved is the fact that the methane dissociation mechanism is still not very clear. Based on the proposed methane 1st C-H cracking pathway, this work also attempted to clarify this debate. In addition, an effective way to explain the industrial level POM results using the proposed new methane dissociation mechanism was also developed in this work.

9.2 Density functional theory calculation

The quantum calculations were performed using density functional theory (DFT) (Payne et al., 1992), Hartwigsen-Goedecker-Hutter pseudopotential (Hartwigsen et al., 1998), the Teter Pade parametrization approximation (LDA) (Goedecker et al., 1996), and a plane-wave basis set with kinetic energy cutoff of 1080 eV, which were implanted in the ABINIT code (Gonze et al., 2002; Goedecker, 1997; Gonze, 1996;

http://www.abinit.org). As an initial study, we ignored the relaxations of nickel surface, C-H bond length, and H-C-H angle. The fcc nickel crystal lattice parameter was fixed as 3.52 Å and the C-H bond length and H-C-H angle in both CH_4 and CH_3 were fixed as 1.09 Å and 109.5°, respectively. A super cell with the dimension of 6 Å × 6 Å × 22.32 Å was used.

9.3 Results and Discussion

The methane dissociation mechanism on $Ni_{1-x}O$ ($0 \leq x \leq 1$) is very dependent on the value of x (Chapter 7). At low x value, the methane dissociation mainly happens on the metallic Ni surface and the 1st C-H cracking is the rate determination step. Figure 9.1 gives an illustration for the role of the interface between the Ni-YSZ phases within a COMR having low oxygen chemical potential on the Ni catalyst surface (such as the membrane reactor tested in Chapter 8), in which the Ni-YSZ interface bridges the combination of $[C]_s$ and $[O]_s$ species.

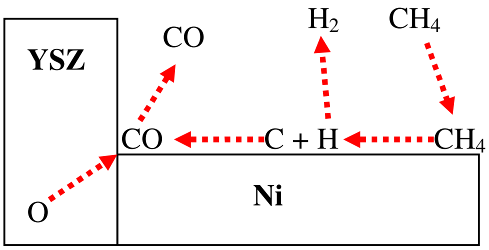

Figure 9.1 The significance of Ni(0)-YSZ interface in POM

9.3.1 The chemical adsorption and disassociation of methane on Ni(111) plane

In the following study, the catalytic dissociation of methane is restricted only on Ni(111) surface as it represents the catalytic activity of the Ni(0) catalyst. The decomposition of the 1st C-H bond on Ni(111) surface is the slowest step compared with the rates for forming the other three adsorbed intermediates $[CH_2]_{ads}$, $[CH]_{ads}$, and $[C]_{ads}$. We propose in this work an alternative path to simulate the real activation process of CH_4 molecule: the molecule touched down initially towards the center of three Ni(0) atoms (labeled 1-3 on Fig. 9.2), which is known as a 3-fold site, and with its approaching to the 3-fold site the CH_4 molecule gave away the first H to an adjacent 3-fold site. Different to this activation path, CH_4 molecule was normally thought to land first at a Ni(0) atom (known as atop site) for undergoing dissociation, and then the generated CH_3 and H species migrate to the two neighboring 3-fold sites respectively. Figure 9.3 portrays in more detail about how the central C atom became more exposure in the course approaching to the 3-fold site, in which the three C-H bonds might wing away from the 3-fold site to coordinate the formation of $[CH_3]_{ads}$.

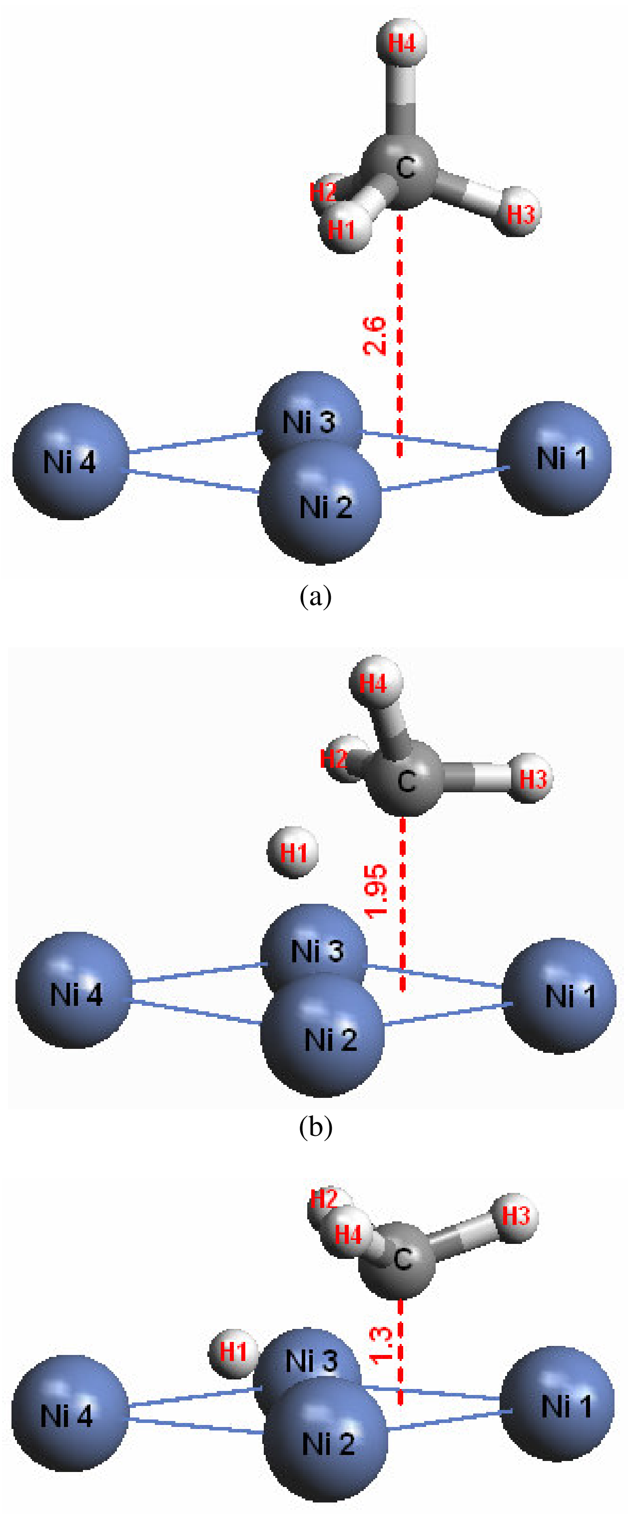

(a)

(b)

(c)

Figure 9.2 The DFT calculated methane 1st C-H cracking states: (a) initial; (b) transition; (c) final

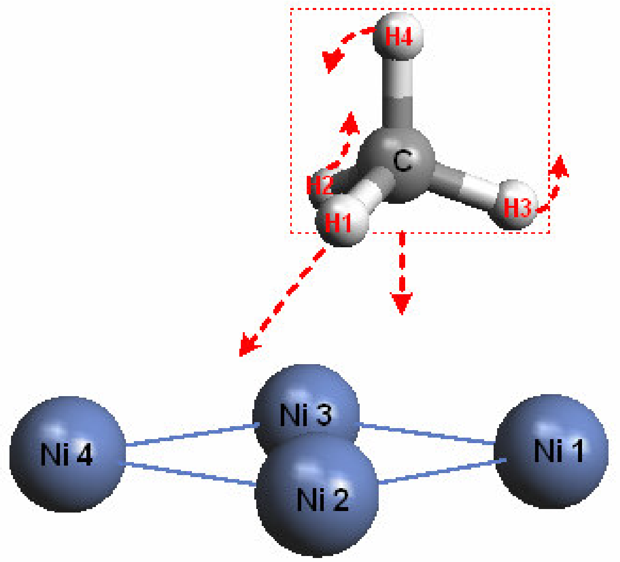

Figure 9.3 The 1st C-H cracking of methane on the 3-fold site

Figures 9.2 a, b, and c show the calculated distances from the central C atom to the 3-fold site, which characterizes the initial adsorption state, transition state, and final state, respectively. In parallel, the calculated change of total energy ($E-E_0$), where E_0 represents the energy of the reference state described by Fig. 9.2a and E represents the sum of energies spent for elongating C-H1 bond and gained for forming Ni1-H1 bond. As predicted, $E-E_0$ exhibited a parabola-like profile versus the H1 shifting distance (viz. describing departure of H1 from C) in Fig. 9.4. Likewise, the simulated activation barrier for the first C-H bond dissociation on the Ni (111) surface was found to be 52 kJ/mol, which is within the experimental measurement range (51 ~ 53 kJ/mol) (Lee et al., 1987; Beebe et al., 1987). Unlike the treatments reported previously, in which $-CH_3$ shifted from atop side to the adjacent 3-fold site and thus ended up with a energy barrier much higher than the experiment-based data, the calculation based on the aforementioned activation mechanism, involving the adsorption and relaxation of the -CH_3 within the 3-fold site, resulted in an energy barrier almost the same as the experimental value.

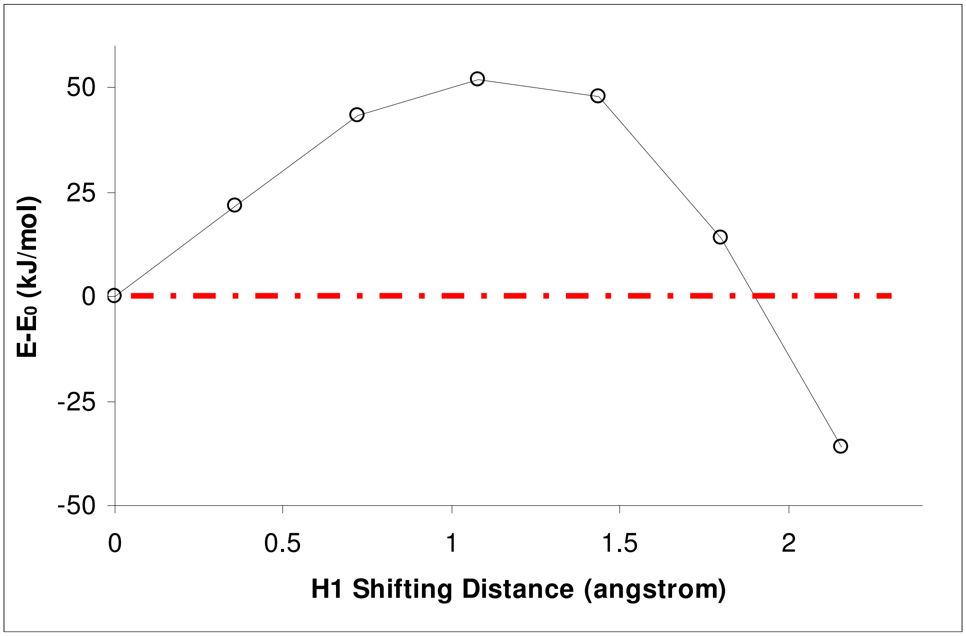

Figure 9.4 The calculated dissociation energy curve for the cleavage of the 1st C-H bond

9.3.2 Calculation of the methane initial thermal sticking coefficients

To check whether the proposed mechanism is proper, we proposed a new theoretical method to calculate the methane thermal sticking coefficients (or initial sticking probabilities) at different temperatures. The relationship between the thermal sticking coefficient, $S_0(T)$, effective factor, α, normalized Boltzmann energy distribution, $F(E) = \frac{1}{kT} e^{-\frac{E}{kT}}$, and the initial dissociation sticking coefficient, $S_0(E)$, could be expressed by Eq (9.3).

$$\boldsymbol{S}_0(\boldsymbol{T}) = \alpha\int_0^\infty \boldsymbol{F}(\boldsymbol{E})\cdot \boldsymbol{S}_0(\boldsymbol{E})d\boldsymbol{E} \tag{9.1}$$

$$\alpha = \boldsymbol{A}_s \cdot \boldsymbol{B}_s \tag{9.2}$$

The value of α is equal to 1/162 and could be broken down into two factors (A_s and B_s). A_s was related to the momentum direction by which methane molecule collides to Ni(111) plane while B_s was connected with the actual sites occupied by a dissociated CH_4 molecule. The CH_4 molecule upon arriving to Ni(111) surface possesses three molecular motion types (viz. the vibrational, translational, and rotational motions), their momentums can be projected to six directions (x, -x, y, -y, z, and -z) with only the direction perpendicular to the catalyst surface, along which C-H bond dissociation is induced. Thus, factor A_s is equal to 1/6 in terms of overall probability. The initial sticking coefficient was the sticking probability at zero carbon coverage. Under this situation there was nil possibility for two H atoms to form a H_2 molecule. After a CH_4 molecule is dissociated into 5 atoms (1 C atom and 4 H atoms), the sites taken by C or H atoms and the sites adjacent to an occupied site can not be used for the dissociated adsorption of another CH_4 molecule due to a higher energy barrier. Therefore, the number of actual occupied sites (i.e., the $1/B_s$ value) was 27 on (111) plane as shown in Fig. 9.5. Hence the α value equals to $\boldsymbol{A}_s \times \boldsymbol{B}_s = \frac{1}{6}\times\frac{1}{27} = \frac{1}{162}$ as asserted above.

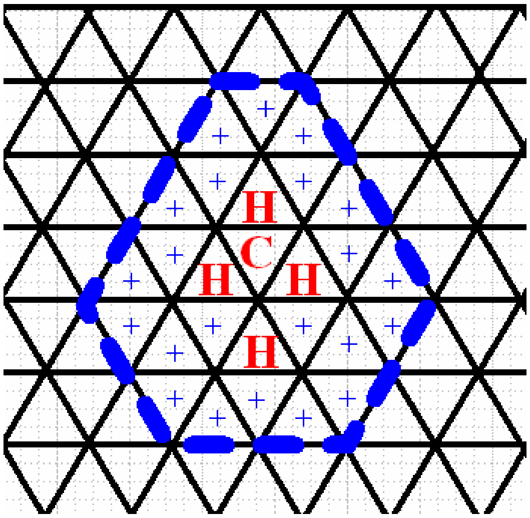

Figure 9.5 Schematic of the actual occupied sites of a dissociated methane molecule

To simplify the calculation of the $S_0(E)$, we designed a rectangular potential well which had the identical height of potential barrier and the area (potential × shifting distance) was equal to that under the parabolic curve of the calculated potential (> 0) ~ H1 (Fig. 9.4). The rectangular potential barrier has a height of 52 kJ/mol and the width of 1.28 Å. In this way, the $S_0(E)$ can be approximately expressed as the one-dimensional transmission probability with energy E either below or over the rectangular potential barrier height (Eq. 9.3).

$$S_0(E) = \left\{ \begin{array}{ll} \left[1 + \dfrac{\left(e^{K_I a} - e^{-K_I a}\right)^2}{16 \dfrac{E}{V_0}\left(1 - \dfrac{E}{V_0}\right)} \right]^{-1} & for \quad E < V_0 \\ \left[1 + \dfrac{\sin^2 K_{II} a}{4 \dfrac{E}{V_0}\left(\dfrac{E}{V_0} - 1\right)} \right]^{-1} & for \quad E > V_0 \end{array} \right\} \qquad (9.3)$$

$$K_I = \sqrt{\frac{2mV_0}{\hbar^2}\left(1-\frac{E}{V_0}\right)} \tag{9.3a}$$

$$K_{II} = \sqrt{\frac{2mV_0}{\hbar^2}\left(\frac{E}{V_0}-1\right)} \tag{9.3b}$$

It can be seen from Fig. 9.6, a good agreement between our calculated methane thermal sticking coefficients with the experimental data measured by Beebe et al. (1987) has been achieved. To the best of our knowledge, the calculated activation energy and the thermal sticking coefficients have been to date the values closest to the experimental data. In brief, both the proposed methane dissociation mechanism and the theoretical method to calculate the thermal sticking coefficients are reasonable.

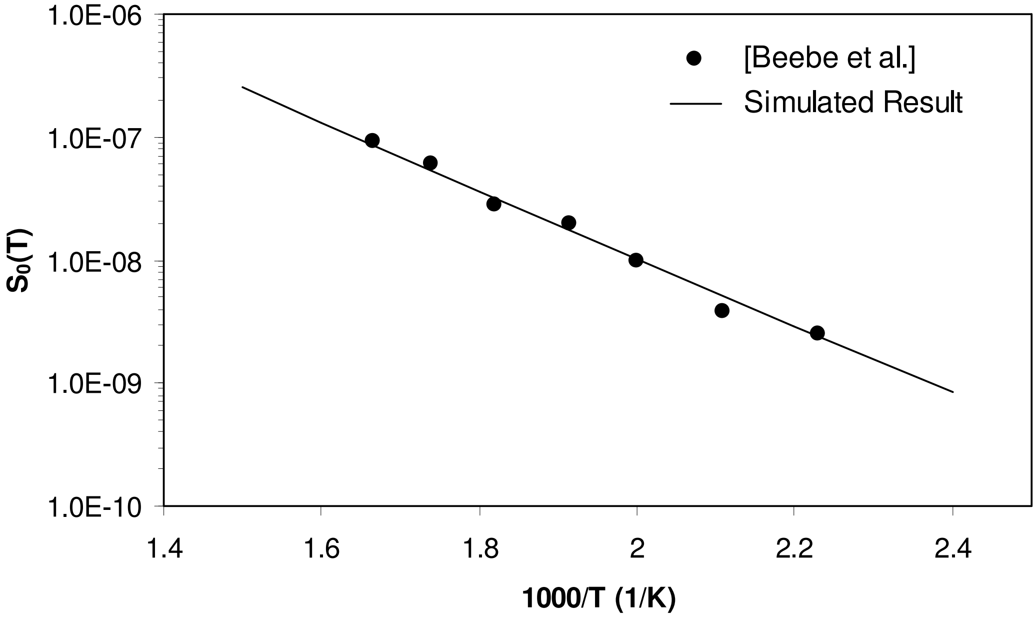

Figure 9.6 A comparison of the calculated methane thermal sticking coefficients with the experimental data

9.3.3 Tunneling, reflection, or "over barrier"?

Up to now, the methane dissociation during the POM process was widely described via the classical transition-state theory in which the rate constant was written in the Arrhenius form because it was generally assumed that at the high reaction temperatures (600 ~ 900 °C) an activated methane molecule could obtain enough energy to deform its shape and totally over the dissociation potential barrier, i.e., the tunneling or reflection phenomena can be neglected and the "over barrier" mode dominates the reaction. Nevertheless, some publications (Lee et al., 1987; Luntz and Harris, 1991 & 1992) suggested that the H tunneling was the final process in the methane 1st C-H bond cleavage. This section attempted to clarify the importance of the tunneling and reflection during the methane 1st C-H cracking process. Figure 9.7 showed the dependence of $F(E)S_0(E)$ on E at 623 °C and 850 °C. Within the testing temperature range, the methane dissociation due to the H tunneling is very small and can be neglected. The reflection part, R(T), is calculated by Eq. (9.5).

$$\boldsymbol{R}(\boldsymbol{T}) = 1 - \frac{\int_{V_0}^{\infty} \boldsymbol{F}(\boldsymbol{E}) \cdot \boldsymbol{S}_0(\boldsymbol{E}) \boldsymbol{dE}}{\int_{V_0}^{\infty} \boldsymbol{F}(\boldsymbol{E}) \boldsymbol{dE}} \tag{9.5}$$

The calculated result within the measurement temperature range was shown in Fig. 9.8. It can be seen that reflection was significant (0.48 ~ 0.53) and can not be ignored. Therefore, neither the H tunneling theory nor the classical "over barrier" transition-state theory can describe exactly the methane dissociation mechanism at the industrial level temperature range. To make a clear description of the methane dissociation, the reflection phenomena needs to be taken into account.

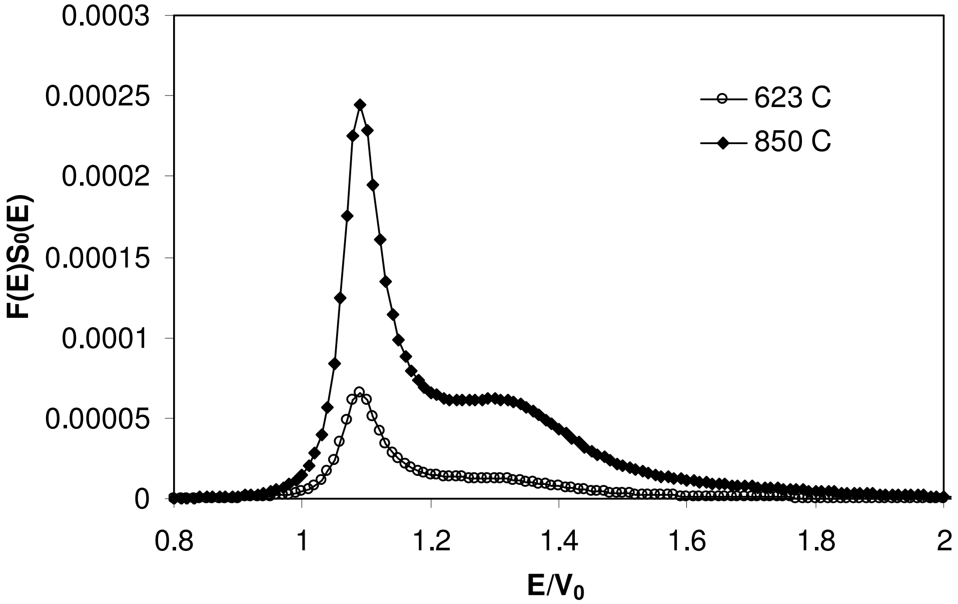

Figure 9.7 Dependence of calculated F(E)S_0(E) on E at different temperatures

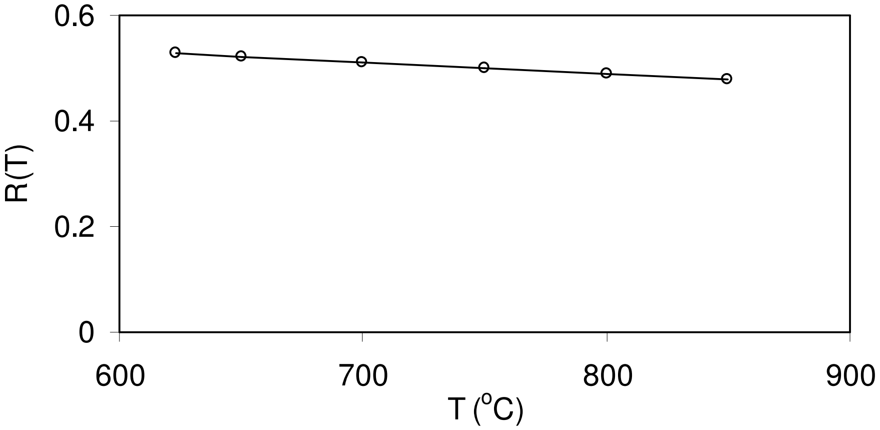

Figure 9.8 The calculated reflection probability at different temperatures

9.3.4 Fitting of the experimental data

In the case of low catalyst surface oxygen chemical potential and that the temperature is the only variable to affect the methane dissociation the methane conversion (X_{CH4}) is determined by the methane initial sticking probability, $S_0(T)$, and the methane conversion is related to the thermal sticking probability by

$$X_{CH4} = \gamma[S_0(T)]^n \qquad (9.6)$$

in which the γ and n are constants.

The value of $S_0(T)$ at different temperature can be calculated from Eqs (9.1) and (9.3) by numerical method. Figure 9.9 showed a good agreement between the experimental data and the calculated methane conversion at different temperature with the parameter value of $\gamma = 1.01108 \times 10^6$ and $n = 1.5471$.

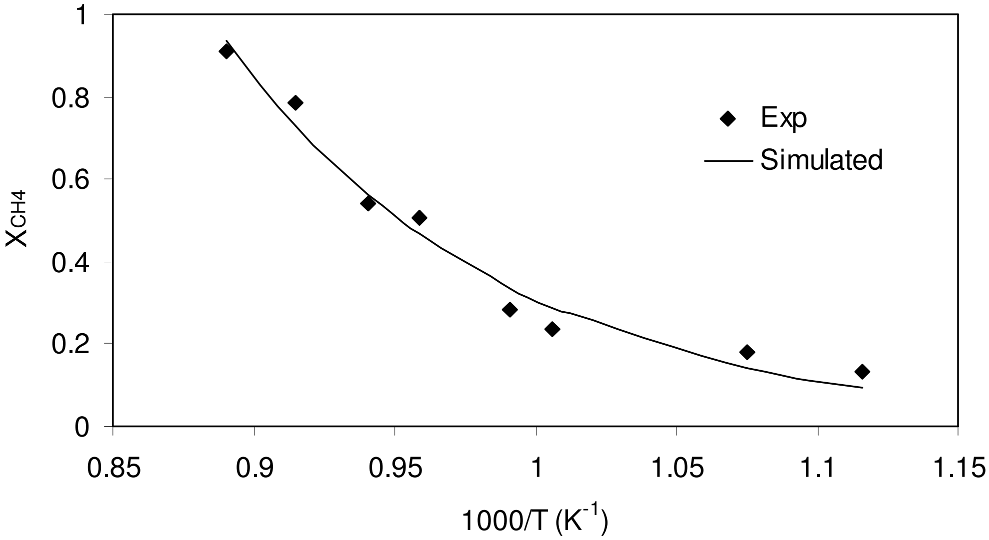

Figure 9.9 Comparison between the measured methane conversion and the simulation results at different temperatures

The widely used Arrhenius equation is much simpler than our method to fit the dependence of the thermally activated methane conversion on the reaction temperature. Actually, a simplification of our method can result in the Arrhenius equation; however, the fitted apparent activation energy by the Arrhenius equation may be higher than the actual energy barrier (V_0). Fitting the same experimental data in Fig. 9.6 by Arrhenius equation gave the apparent activation energy of about 73 kJ/mol, which is much higher than the calculated energy barrier (52 kJ/mol) for the methane 1st C-H cracking. As the decrease of the measurement temperature the apparent activation energy from Arrhenius equation is expected to be close to the actual energy barrier, which may explain why the low temperature molecular beam experimental can give the activation energy very close to the actual dissociation barrier.

9.4 Conclusion

DFT computation of the methane 1st C-H cleavage demonstrates that the complicated methane decomposition process could be simulated using a simple Ni_4-CH_4 cluster model. The calculated dissociation energy barrier was found to be very close to the respective experimental data reported by other authors. During the methane 1st C-H cracking on Ni(111) surface process, the adsorbed CH_4 molecule at the 3-fold site involves in a series of movement simultaneously, i.e., H shift to adjacent 3-fold site, CH_3 rotation, and CH_3 shift to the underlying 3-fold site.

A new theoretical method without fitting parameter was proposed to calculate the initial methane thermal sticking coefficients. Based on the energy barrier and the proposed method, this work calculated the methane initial sticking coefficients under different temperatures, which were found to be very close to the experimental data from literature.

The analysis of the methane dissociation mechanism suggested that neither the H tunneling mechanism nor the pure classical "over barrier" transition-state theory was proper to explain the methane 1st C-H cracking process accurately. The H tunneling process is found to be neglectable, whereas the reflection phenomena (~ 0.5) was significant. Finally, a method to fit the created theory with the dependence of high temperature POM methane conversion on the reaction temperature was proposed and found to be able to fit the experimental data from Chapter 8 well.

Chapter 10 Conclusions and recommendations

10.1 Conclusions

The technically realization of asymmetric tubular COMR (ceramic oxide-electrolyte membrane reactor) in lab-scale offers an initial model to the attempt of integrating the air separation with methane reforming in industrial scale, which will lead to a significant decrease in the cost of producing syngas. Nowadays, the major challenges for the commercially making an asymmetric tubular COMR for POM (partial oxidation of methane) include what is the low cost method (or process) and how to retain stability of nickel catalyst through reducing the extent of coke formation. This thesis presents meaningful laboratory results obtained from studying the above two issues. In this study, the rheology of the ceramic-polymer blend has been studied, five wet-chemistry processing methods have been invented for the preparation of asymmetric tubular COMR, the reaction mechanism of POM at the interface between the electrolyte and anode layers in POM-COMR has been studied using DFT (density function theory), and a scheme of periodically charging methane to POM-COMR has been proposed to overcome coke deposition at nickel catalyst surface and thus to maintain a high POM catalytic stability. The important achievements of this study are highlighted in the following sections:

10.1.1 Rheological study of ceramic-polymer blend

The CeO_2-PEG blends prepared by solution mixing method, in which the CeO_2 fine powders were thoroughly mixed with PEG aqueous solution followed by evaporation of water, were selected for the study of particle effects on viscous flow of the PEG melt under low shear rates. The blends containing as high as 80 wt.% (or 41.6 vol.%) of CeO_2 still exhibit Bingham plastic response and thus the relative viscosities (η_{rel}) of the blends with various volume fractions of CeO_2 (ϕ) at different temperatures were obtained.

It was found that the widely cited Eliers, Mooney, Krieger-Dougherty, and their modified models fit the experimental data poorly. The XRD and DSC analyses of the formulated CeO_2-PEG blends proved the occurrence of strong adsorption of PEG chains on CeO_2 particle surface. The adsorption resulted in the formation of a physical cross-linking network, especially in the high CeO_2-loading blends. In addition, due to the van der Waals (vdw) attractive forces among CeO_2 particles the characteristic infrared absorption band of the PEG (ν_{C-O-C}) undergoes changes in both frequency and intensity with increasing of the CeO_2 volume fraction. Assuming that these two fundamental interactions (adsorption and vdw attraction) are the prevalent forces in the studied ceramic-polymer blending system, a new theoretical model (Eq. 3.9) expressing the relative viscosity (η_{rel}) as the function of ϕ, T, and the geometry/surface states of the ceramic particles (n/B) was established via the Einstein equation and the Arrhenius relationship. In this mathematic model, the activation energy of viscous flow consists of two parts, the barrier due to the presence of vdw attractive forces and the barrier due to formation of the physical network. This mathematic model was found to be able to match well the experimental $\eta_{rel} \sim \phi$ data within the designated range of shear rates and temperatures.

Due to the importance of surfactant to the extrusion of a ceramic-polymer paste, an additional study was also carried out to understand non-ionic surfactant (Tween®-80) effect on lowering down the melt viscosity of the blends. It was found that the added non-ionic surfactant could decrease the relative viscosity of the blend significantly before the lowest critical surfactant concentration. The concept of slippery hydrophobic shell was then proposed to explain the existence of the lowest critical surfactant concentration.

10.1.2 Fabrication of asymmetric tubular COMRs by convenient wet coating/plating methods

In this thesis, five types of wet chemistry based methods have been developed, because of their low-cost merits, to fabricate asymmetric tubular COMRs. Table 10.1 lists the five types of these techniques, the COMRs made, and the composition of sweeping gas.

Table 10.1 Summary of the five techniques developed for the fabrication of asymmetric tubular COMRs

Fabrication technology	COMR	Sweeping gas
Vacuum assisted ceramic-ceramic composite slurry coating	LSCO80-CeO_2/CeO_2	Pure He
Green tube coating & co-sintering	(LSCO80)/CGO20/CeO_2	Pure He
Ceramic-metal composite dip coating & solution plugging	LSM80-Ag(Pd)/YSZ	Pure He
Slurry coating and ESP	LSM80-CGO20/YSZ-Ag/YSZ-Ni(O)	CH_4/He
Two-steps colloidal suspension coating	LSM80-GO20/YSZ ⊥(TiO_2-Pd)/YSZ-Ni(O)	CH_4/He

Method 1: Vacuum was used to increase the LSCO80-CeO_2 mixture packing density on the porous CeO_2 tube surface. The presence of CeO_2 particles in the mixture plays a crucial role in turning the LSCO80-CeO_2 layer into gas-tight and crack-free. The CeO_2 particles (~ 4.7 μm diameter) were used to block the big pores at the surface of CeO_2 tube, while the home-made sub-micron LSCO80 particles were used as the continuous phase during sintering process. It was suggested that the CeO_2 particles in the membrane gave rise to and upheld a LSCO80 network that buffers the thermal-induced stress effectively and thus avoided the crack formation during the high temperature sintering process. The mixture of LSCO80-CeO_2 (1:1 vol) was also found to have the CTE close to that of the pure CeO_2, which also decreased the crack formation possibility. The air separation results showed that the porosity of the porous support has almost no influence on the measured activation energy value, although it shows a significant effect on the oxygen permeation flux, which implies that the surface oxygen exchange on the permeate side is likely the rate-limiting mechanism when measuring the permeation via inert gas sweep method.

Method 2: Green tube coating followed by co-sintering technique has been developed to fabricate the asymmetric tubular (LSCO80/)CGO20/CeO_2 membrane. The COMR was fabricated by the two-step procedure. At the first step, a thin CGO20 (submicron) green layer was coated on the green CeO_2 (~ 4.7 μm diameter) tube surface and sintered at 1600 ^{o}C. It was found that this co-sintering of CGO20/CeO_2 green tube resulted in a special porous/dense/porous structure. At the second step, the LSCO colloidal suspension was coated on the fabricated asymmetric tubular GCO20/CeO_2 membrane surface and went through sintering. The GCO20/CeO_2 fabricated in the 1st step displays a unique sintered structure with a dense GCO20 layer being embedded slightly below the porous tube surface. The coated LSCO80 layer exhibits different surface morphologies resulted from varying its sintering temperature, which give rise to different oxygen permeation activation energy values. The XRD analysis shows that the perovskite LSCO80 and the cubic fluorite CGO20 are stable at the sintering temperatures, although the high sintering temperature causes tetragonal distortion in the LSCO80. Impedance measurement also shows that the reverse effect of the LSCO80 sintering temperature on the oxygen ionic transport and the surface oxygen exchange. The air separation experimental showed that the oxygen permeation was very dependent on the LSCO80 sintering temperature and only the one with the lowest sintering temperature (1100 ^{o}C) lead to a higher oxygen permeation flux than the GCO20/CeO_2 membrane because of its very rough surface morphology.

Method 3: Ceramic-metal composite dip coating and solution plugging were used to fabricate the asymmetric tubular LSM80-Ag(Pd)/YSZ membrane. The porous YSZ support with porosity of 31% was made through extrusion and sintering at 1400 ^{o}C for 30 min. To fabricate a thin and gas-tight layer on the support surface, two steps were employed, which were, firstly, implementation of dual phase metal-ceramic composite (Ag(Pd)-LSM80) coating, and secondly, plugging surface pores of the coating layer by the salt-precursor approach. The presence of Ag(Pd) alloy in the LSM80 phase is essential to assure success of the subsequent pore-closing step. The chemical compatibility and charge transport behavior at the interface between LSM80 and YSZ were investigated. The analysis results show that the occurrence of minor interfacial species generated from sintering the two oxides at 1300 ^{o}C has negligible the oxygen ionic conductivity at the interface. The oxygen permeation of the asymmetric LSM80(S)-Ag(Pd)-LSM80-YSZ membrane reached to 0.35 sccm/cm^2 at 900 ^{o}C.

Method 4: The combination of YSZ suspension slurry coating and electroless silver plating (ESP) was proposed to fabricate the asymmetric tubular COMR, which was equipped with a cathode layer (< 10 μm), the composite of LSM80 and CGO20 oxides, and with an anodic layer (~ 1000 μm), the composite of YSZ and Ni(0). These two electrodes sandwiched a dense electrolyte layer (5-10 μm) composed of YSZ and Ag. The anode is a catalytic layer over which POM takes place and functions in addition as a structural support to the reactor. This membrane reactor successfully coupled the oxygen separation from the air with partial oxidation of methane and realized a high conversion of CH_4 and high selectivity for CO and H_2. A series of studies involving XRD, XPS, TPR, and methane thermal decomposition have been conducted to understand the bilateral cation diffusion between the NiO and YSZ phases. The $Ni_{1-x}O$ located at the interface derived from reduction of the

NiO by CH_4 revealed unique POM catalytic performance. This study suggested that the POM process was very complicated and involved in at least three major reactions as the change of the surface oxygen chemical potential or the membrane reaction temperature.

Method 5: A new two-step colloidal suspension coating method was invented to produce the asymmetric tubular COMR. The conventional slurry coating layer (YSZ in this part) normally has a low powder-packing density due to the presence of organic additives such as polymer binder. The coating layer was to cast a loose YSZ powder packing layer after organics were burnt off and such a powder layer will be converted by sintering to a YSZ layer with lots of voids or cracks in it. For solving this problem, an additional coating by binder-free YSZ colloidal suspension was employed to stuff the YSZ powder layer left behind by removing the organics. After co-firing the coated object a thin and dense YSZ layer was formed on the asymmetric support, thick porous YSZ-NiO tube. This asymmetric membrane reactor consisted of three layers, i.e., the top dense YSZ layer (~ 10 μm thickness), the meddle porous YSZ-NiO layer 1 (40 ~ 80 μm thickness), and the lower porous YSZ-NiO layer 2 (~ 1000 μm thickness). The YSZ-NiO layer 1 has a similar NiO content to the YSZ-NiO layer 2 but different pore size, which was caused by the aggregation of the NiO particles during sintering. A greater extent of NiO aggregation within the YSZ-NiO layer 1 occurred because YSZ particles in layer 1 were packed more tightly than that in layer 2. An asymmetric tubular ceramic membrane reactor (porous LSM80-CGO20/ dense YSZ⊥(TiO_2-Pd)/porous YSZ-Ni) showed high methane conversion (> 90%), CO selectivity (> 90 %), and H_2

selectivity (> 80%) at 850 ^{o}C. It was also found that the fabricated POM-COMR lost its catalytic activity fast due to the unavoidable coke formation on the nickel surface; however, the cyclic feeding of the reactants was found to be able to remove the deposited surface carbon and thus increased the POM stability significantly.

10.1.3 Surface oxygen de-sorption and lattice thermal expansion of LSCO80

The extended Hückel theory (EHT) has been attempted to simulate the LSCO80 surface oxygen de-sorption process. It was found that the calculated activation energy value was close to that determined by air separation using pure He as the sweeping gas, which suggested the simple EHT method be a feasible way to undertake theoretical exploration of the oxygen de-sorption or adsorption on the cubic perovsktie-type metal oxide surface. Both air separation and XRD experimental indicated that that the LSCO80 lattice expanded with the increase of the sintering temperature, which accounted for the influence of the sintering temperature on the COMR oxygen permeation. The DFT simulation of the bulk LSCO80 lattice length at different oxygen vacancy concentration suggested that the low oxygen vacancy concentration (or lower partial oxygen pressure) results in extended LSCO80 bulk lattice length.

10.1.4 Mechanism study of methane dissociation on Ni (111) surface

The mechanism study of POM when it was conjugated with oxygen permeation through membrane suggests that the detailed methane reforming process depend on the catalyst surface oxygen chemical potential. At low catalyst surface oxygen concentration, an adsorbed methane molecule directly dissociates into a series of species (i.e., CH_{4-x} ($1 \le x \le 4$) and H) on the nickel surface and the 1st C-H cracking is the rate determination step. The methane 1st C-H cracking over Ni catalyst surface was simulated using DFT. This work selected Ni(111) surface as the representative lattice index. A new 1st C-H cracking path way was proposed and the calculated activation energy was found to be very close to experimental data from literature. A novel theoretical method to calculate the initial methane thermal sticking coefficient has also been proposed. The calculated sticking coefficients at different temperatures were found to be almost the same as that measured by molecular beam method reported by other authors. A further analysis of the methane dissociation mechanism suggests that the H tunneling process is negligible, whereas the reflection phenomena (~ 0.5) and the "over barrier" part dominate the methane 1st C-H cracking process. In addition, the method how to fit the high temperature POM experimental data within a COMR with the proposed methane dissociation mechanism has also been proposed.

10.2 Recommendations for the future work

On the basis of completion of this PhD research, I would make a few recommendations for the further work for advancing the performance of asymmetric tubular POM-COMR:

10.2.1 Fabrication of the tube support with specific pore structures

Typically the fabricated porous ceramic tubes have random pore channels and pore size distribution because of adopting the conventional powder paste extrusion and sintering of green body. As a result, it has to be very porous (> 30 vol.%) to assure a high gas permeability since torturous and dead-end pore channels were prevalent in the tube body. Moreover, such a high porous structure incurs poor mechanical strength in the tube. In light of this drawback, a future effort to design a porous tube structure which is predominant by straight and more uniform pore channels will be important. Special extrusion die set design or the addition of pore former with special geometry or size can be attempted to control the pore channel shapes and distributions.

10.2.2 Fabrication of cathode sustained asymmetric tubular COMR

The specific surface area of catalyst has a significant effect on the performance of POM. Reducing particle size of Ni(0) clusters embedded in the anodic layer of POM-COMR is expected to promote catalytic stability of POM. It is anticipated that if the present anode-supported POM-COMR is redesigned as cathode-supported POM-COMR it would be easier to achieve a higher extent of nickel-phase dispersion in the anode layer because there is no need to apply a high sintering temperature. For instance, the Ni grains in the YSZ anode support can be redistributed by dissolving in concentrated nitric acid, and followed by impregnation and sintering. The sintering temperature can be varied to control the redistributed catalyst particle size.

10.2.3 Coupling of syngas synthesis with electrical power supply

The COMR fabrication methods developed by this work can also be employed to fabricate SOFC. Turning the internal electronic circuit into external circuit, the fabricated ceramic membranes have the potential to convert methane into syngas and supply electrical power to connected loading simultaneously.

References

Abbott, H.L., A. Bukoski, D.F. Kavulak and I. Harrison. Dissociative Chemisorption of Methane on Ni(100): Threshold Energy From CH_4 ($2\nu_3$) Eigenstate-Resolved Sticking Measurements, J. Chem. Phys., *119,* pp.6407-6410. 2003.

Abrutis, A., A. Bartasyte, G. Garcia, A. Teiserskis, V. Kubilius, Z. Saltyte, V. Faucheux, A. Figueras and S. Rushworth. Metal-organic Chemical Vapour Deposition of Mixed-conducting Perovskite Oxide Llayers on Monocrystalline and Porous Ceramic Substrates, Thin Solid Films, *449,* pp.94-99. 2004.

Adler, S.B. Factors Governing Oxygen Reduction in Solid Oxide Fuel Cell Cathodes, Chem. Rev., *104,* pp.4791-4843. 2004.

Akin, F.T. and J.Y.S. Lin. Oxygen Permeation Through Oxygen Ionic or Mixed-Conducting Ceramic Membranes with Chemical Reactions, J. Membr. Sci., *231,* pp.133-146. 2004.

Alstrup, I. A New Model Explaining Carbon Filament Growth on Nickel, Iron, and Ni-Cu Alloy Catalysts, J. Catal., *109,* pp.241-251. 1988.

Amato, I. Catalytic Conversion Could be a Gas, Science, *259,* pp.311. 1993.

Anderson, H.U. Review of P-type Doped Perovskite Materials for SOFC and Other Applications, Solid State Ionics, *52*, pp.33-41. 1992.

Armstrong, T., F. Prado and A. Manthiram. Synthesis, Crystal Chemistry, and Oxygen Permeation Properties of $LaSr_3Fe_{3-x}Co_xO_{10}$ ($0 \leq x \leq 1.5$), Solid State Ionics, *140*, pp.89-96. 2001.

Badyal, J. P. S., X. Zhang and R.M. Lambert. A Model Oxide Catalyst System for the Activation of Methane: Lithium-doped NiO on Ni(111), Surf. Sci. Lett., *225*, pp.L15-L19. 1990.

Balachandran, U., J.T. Dusek, R.L. Mieville, R.B. Poeppel, M.S. Kleefisch, S. Pei, T.P. Kobylinski, C.A. Udovich and A.C. Bose. Dense Ceramic Membranes for Partial Oxidation of Methane to Syngas, Appl. Catal. A, *133*, pp.19-29. 1995.

Balachandran, U., J.T. Dusek, P.S. Maiya, B. Ma, R.L. Mieville, M.S. Kleefisch and C.A. Udovich. Ceramic Membrane Reactor for Converting Methane to Syngas, Catal. Today, *36*, pp.265-272. 1997.

Baker, R.T., B. Gharbage and F.M.B. Marques. Ionic and Electronic Conduction in Fe and Cr Doped (La,Sr)$GaO_{3-\delta}$, J. Electrochem. Soc., *144*, pp.3130-3135. 1997.

Baran, E.J. Structural Chemistry and Physicochemical Properties of Perovskite-like Materials, Catal. Today, *8*, pp.133-151. 1990.

Barbucci, A., P. Carpanese, G. Cerisola and M. Viviani. Electrochemical Investigation of Mixed Ionic/Electronic Cathodes for SOFCs, Solid State Ionics, *176*, pp.1753-1758. 2005.

Beebe, T.P. Jr., D.W. Goodman, B.D. Kay and J.T. Yates Jr. Kinetics of the Activated Dissociative Adsorption of Methane on the Low Index Planes of Nickel Single Crystal Surfaces, J. Chem. Phys., *87*, pp.2305-2315. 1987.

Beck, R.D., P. Maroni, D.C. Papageorgopoulos, T.T. Dang, M.P. Schmid and T. R. Rizzo. Vibrational Mode-specific Reaction of Methane on a Nickel Surface, Science, *302*, pp.98-100. 2003.

Benbow, J.J., E.W. Oxley and J. Bridgwater. The Extrusion Mechanics of Pastes—the Influence of Paste Formulation on Extrusion Parameters, Chem. Eng. Sci., *42*, pp.2151-2162. 1987.

Bengaard, H.S., I. Alstrup, I. Chorkendorff, S. Ullmann, J.R. Rostrup-Nielsen and J.K. Nørskov. Chemisorption of Methane on Ni(100) and Ni(111) Surfaces with Preadsorbed Potassium, J. Catal., *187*, pp.238-244. 1999.

Bengaard, H.S., J.K. Nørskov, J. Sehested, B.S. Clausen, L.P. Nielsen, A.M. Molenbroek and J.R. Rostrup-Nielsen. Steam Reforming and Graphite Formation on Ni Catalysts, J. Catal., *209*, pp.365-384. 2002.

Besland, M.P., H. Djani-ait Aissa, P.R.J. Barroy, S. Lafane, P.Y. Tessier, B. Angleraud, M. Richard-Plouet, L. Brohan and M.A. Djouadi. Comparison of Lanthanum Substituted Bismuth Titanate (BLT) Thin Films Deposited by Sputtering and Pulsed Laser Deposition, Thin Solid Films, *495*, pp.86-91. 2006.

Boaro, M., J.M. Vohs and R.J. Gorte. Synthesis of Highly Porous Yttria-stabilized Zirconia by Tape-casting Methods, J. Am. Ceram. Soc., *86*, pp.395-400. 2003.

Bouwmeester, H.J.M. and A.J. Burggraaf. Dense Ceramic Membranes for Oxygen Separation. In The CRC Handbook of Solid State Electrochemistry, ed by P.J. Gellings and H.J.M. Bouwmeester, pp.481-553. Boca Raton, FL, CRC Press. 1997.

Bouwmeester, H.J.M. Dense Ceramic Membranes for Methane Conversion, Catal. Today, *82*, pp.141-150. 2003.

Brant, M. C. and L. Dessemond. Electrical Degradation of LSM–YSZ Interfaces, Solid State Ionics, *138*, pp.1-17. 2000.

Bucher, E., W. Jantscher, A. Benisek, W. Sitte, W. Preis, I. Rom and F. Hofer. Transport Properties of $La_{0.4}Sr_{0.6}CoO_{3-\delta}$, Solid State Ionics, *141/142*, pp.375-380. 2001.

Bukoski, A. and I. Harrison. Assessing a Microcanonical Theory of Gas-surface Reactivity: Applicability to Thermal Equilibrium, Nonequilibrium, and Eigenstate-resolved Dissociation of Methane on Ni(100), J. Chem. Phys., *118*, pp.9762-9768. 2003.

Burbidge, A.S. and J. Bridgwater. The Single Screw Extrusion of Paste, Chem. Eng. Sci., *50*, pp.2531-2543. 1995.

Burghgraef, H., A.P.J. Jansen and R.A. van Santen. Electronic Structure Calculations and Dynamics of Methane Activation on Nickel and Cobalt, J. Chem. Phys. *101*, pp.11012-11020. 1994.

Chen, C.C., M.M. Nasrallah and H.U. Anderson. Synthesis and Characterization of YSZ Thin Film Electrolytes, Solid State Ioincs, *70/71*, pp.101-108. 1994.

Chen, C.H., H.J.M. Bouwmeester, R.H.E. van Doorn, H. Kruidhof and A.J. Burggraaf. Oxygen Permeation of La0.3Sr0.7CoO3-δ, Solid State Ionics, *98*, pp.7-13. 1997.

Chen, C.S., B.A. Boukamp, H.J.M. Bouwmeester, G.Z. Cao, H. Kruidhof, A.J.A. Winnubst and A.J. Burggraaf. Microstructural Development, Electrical Properties and Oxygen Permeation of Zirconia-palladium Composites, Solid State Ionics, *76*, pp.23-28. 1995.

Chen, C.S., H. Kruidhof, H.J.M. Bouwmeester, H. Verweij and A.J. Burggraaf. Oxygen Permeation Through Oxygen Ion Oxide-noble Metal Dual Phase Composites, Solid State Ionics, *86-88*, pp.569-572. 1996.

Cheng, J. and A. Navrotsky. Energetics of Magnesium, Strontium, and Barium Doped Lanthanum Gallate Perovskites, J. Solid State Chem., *177*, pp.126-133. 2004.

Cherry, M., M.S. Islam and C.R.A. Catlow. Oxygen Ion Migration in Perovskite-type Oxides, J. Solid State Chem., *118*, pp.125-132. 1995.

Chiang, Y.-M., D.P. Birnie, III and W.D. Kingery. Physical Ceramics: Principles for Ceramic Science and Engineering. pp.101-500, New York: John Wiley & Sons Inc. 1997.

Chiu, R.C. and M. J. Cima. Drying of Granular Ceramic Films: II, Drying Stress and Saturation Uniformity, J. Am. Ceram. Soc., *76*, pp.2769-2777. 1993.

Chu, W.F. Thin- and Thick-film Solid Ionic Devices, Solid State Ionics, *52*, pp.243-248. 1992.

Cima, M.J., J.A. Lewis and A.D. Devoe. Binder Distribution in Ceramic Greenware During Thermolysis, J. Am. Ceram. Soc., *72*, pp.1192-1199. 1989.

Cook, R.L. and A.F. Sammells. On the Systematic Selection of Perovskite Solid Electrolytes for Intermediate Temperature Fuel Cells, Solid State Ionics, *45*, pp.311-321. 1991.

Corriu, R.J.P., P. Gerbier, C. Guérin and B. Henner. From Preceramic Polymers with Interpenetrating Networks to SiC/MC Nanocomposites, Chem. Mater., *12*, pp.805-811. 2000.

Croce, F., R. Curini, A. Martinelli, L. Persi, F. Ronci and B. Scrosati. Physical and Chemical Properties of Nanocomposite Polymer Electrolytes, J. Phys. Chem. B, *103*, pp.10632-10638. 1999.

Deng, Z.Q., W. Liu, D.K. Peng, C.S. Chen, W.S. Yang. Combustion Synthesis, Annealing, and Oxygen Permeation Properties of $SrFeCo_{0.5}O_y$ Membranes, Mater. Res. Bull., *39*, pp.963–969. 2004.

Dissanayake, D., M.P. Rosynek, K.C.C. Kharas and J.H. Lunsford. Partial Oxidation of Methane to Carbon Monoxide and Hydrogen over a Ni/Al_2O_3 Catalyst, J. Catal. *132*, pp.117-127. 1991.

Dissanayake, D., M.P. Rosynek and J.H. Lunsford. Are the Equilibrium Concentrations of CO and H2 Exceeded during the Oxidation of CH4 over a Ni/Yb2O3 Catalyst?, J. Phys. Chem., *97*, pp.3644-3646. 1993.

Dongare, M.K., K. Malshe, C.S. Gopinath, I.K. Murwani and E. Kemnitz. Oxidation Activity and ^{18}O-isotope Exchange Behavior of Nickel Oxide-stabilized Cubic Zirconia, J. Catal., *222*, pp.80-86. 2004.

Du, Y. and N.M. Sammes. Fabrication and Properties of Anode-supported Tubular Solid Oxide Fuel Cells, J. Power Sources, *136*, pp.66-71. 2004.

Du, Y., N.M. Sammes and G.A. Tompsett. Optimisation Parameters for the Extrusion of Thin YSZ Tubes for SOFC Electrolytes, J. Eur. Ceram. Soc., *20*, pp.959-965. 2000.

Endo, A., H. Fukunaga, C. Wen and K. Yamada. Cathodic Reaction Mechanism of Dense $La_{0.6}Sr_{0.4}CoO_3$ and $La_{0.81}Sr_{0.09}MnO_3$ Electrodes for Solid Oxide Fuel Cells, Solid State Ionics, *135*, pp.353-358. 2000.

Feng, M., J.B. Goodenough, K. Huang and C. Milliken. Fuel Cells with Doped Lanthanum Gallate Electrolyte, J. Power Sources, *63*, pp.47-51. 1996.

Ferreira, M.L., N.N. Nichio and O.A. Ferretti. A Semiempirical Theoretical Study of Ni/α-Al_2O_3 and $NiSn/\alpha$-Al_2O_3 Catalysts for CH_4 Reforming, J. Mol. Catal. A: Chem., *202*, pp.197-213. 2003.

Figueiredo, F.M., V.V. Kharton, A.P. Viskup and J.R. Frade. Surface Enhanced Oxygen Permeation in $CaTi_{1-x}Fe_xO_{3-\delta}$ Ceramic Membranes, J. Membr. Sci., *236*, pp.73-80. 2004.

Flint, S. D. and R. C. T. Slade. Comparison of Calcium-doped Barium Cerate Solid Electrolytes Prepared by Different Routes, Solid State Ionics, *77*, pp.215-221. 1995.

Gavalas, G.R., C. Phichitkul and G.E. Voecks. Structure and Activity of NiO/α-Al_2O_3 and NiO/ZrO_2 Calcined at High Temperatures II. Activity in the Fuel-rich Oxidation of Methane, J. Catal. *88*, pp.65-72. 1984.

Ge, X., Y. Liu and X. Liu. Preparation and Gas-sensitive Properties of $LaFe_{1-y}Co_yO_3$ Semiconducting Materials, Sens. Actuators B, *79*, pp.171-174. 2001.

Giannakas, A.E., T.C. Vaimakis, A.K. Ladavos, P.N. Trikalitis and P.J. Pomonis. Variation of Surface Properties and Textural Features of Spinel $ZnAl_2O_4$ and Perovskite $LaMnO_3$ Nanoparticles Prepared via CTAB-butanol-octane-nitrate Salt Microemulsions in the Reverse and Bicontinuous States, J. Colloid Interface Sci., *259*, pp.244-253. 2003.

Goedecker, S., M. Teter and J. Hutter. Separable Dual-space Gaussian Pseudopotentials, Phys. Rev. B, *54*, pp.1703-1710. 1996.

Goedecker, S. Fast Radix 2, 3, 4 and 5 Kernels for Fast Fourier Transformations on Computers with Overlapping Multiply-add Instructions, SIAM J. Sci. Comput. *18*, pp.1605-1611. 1997.

Gonze, X. Towards a Potential-based Conjugate Gradient Algorithm for Order-N Self-consitent Total Energy Calculations, Phys. Rev. B, *54*, pp.4383-4386. 1996.

Gonze, X., J.-M. Beuken, R. Caracas, F. Detraux, M. Fuchs, G.-M. Rignanese, L. Sindic, M. Verstraete, G. Zerah, F. Jollet, M. Torrent, A. Roy, M. Mikami, Ph. Ghosez, J.-Y. Raty and D.C. Allan. First-principles Computation of Material Properties : the ABINIT Software project, Comput. Mater. Sci., *25*, pp.478-492. 2002.

Goodwin, J.W. and R.W. Hughes. The Dynamics and Phase of Concentrated Dispersions, Adv. Colloid Interface Sci., *42*, pp.303-351. 1992.

Goodenough, J.B., A. Manthiram, M. Paranthaman and Y.S. Zhen. Oxide Ion Electrolytes, Mater. Sci. Eng. B, *12*, pp.357-364. 1992.

Goodenough, J.B. Annu. Oxide-ion Electrolytes, Rev. Mater. Res. *33*, pp.91-128. 2003.

Gorte, R.J., J.M. Vohs and S. McIntosh. Recent Developments on Anodes for Direct Fuel Utilization in SOFC, Solid State Ionics, *175*, pp.1-6. 2004.

Gorte, R.J., S. Park, J.M. Vohs and C. Wang. Anodes for Direct Oxidation of Dry Hydrocarbons in a Solid-oxide Fuel Cell, Adv. Mater., *12*, pp.1465-1469. 2002.

Gu, Y. and G. Meng. A Model for Ceramic Membrane Formation by Dip-coating, J. Eur. Ceram. Soc., *19*, pp.1961-1966. 1999.

Guyot, A., F. Chu, M. Schneider, C. Graillat and T.F. McKenna. High Solid Content Latexes, Prog. Polym. Sci., *27*, pp.1573-1615. 2002.

Han, P. and W.L. Worrell. Mixed (oxygen ion and p-type) Conductivity in Yttria-stabilized Zirconia Containing Terbia, J. Electrochem. Soc., *142*, pp.4235-4246. 1995.

Hardy, A., G. Vanhoyland, M.V. Bael, J. Mullens and L.V. Poucke. A Statistical Approach to the Identification of Determinant Factors in the Preparation of Phase Pure $(Bi,La)_4Ti_3O_{12}$ from an Aqueous Citrate Gel, J. Eur. Ceram. Soc., *24*, pp.2575-2581. 2004.

Harizanov, O., A. Harizanova and T. Ivanova. Formation and Characterization of Sol–gel Barium Titanate, Mater. Sci. Eng. B, *106*, pp.191-195. 2004.

Hartwigsen, C., S. Goedecker and J. Hutter. Relativistic Separable Duel-space Gaussian Pseudopotentials from H to Rn, Phys. Rev. B, *58*, pp.3641-3662. 1998.

Hatchwell, C., N.M. Sammes and I.W.M. Brown. Fabrication and Properties of $Ce_{0.8}Gd_{0.2}O_{1.9}$ Electrolyte-based Tubular Solid Oxide Fuel Cells, Solid State Ionics, *126*, pp.201-208. 1999.

Hayashi, H., H. Inaba, M. Matsuyama, N.G. Lan, M. Dokiya and H. Tagawa. Structural Consideration on the Ionic Conductivity of Perovskite-type Oxides, Solid State Ionics, *122*, pp.1-15. 1999.

He, H., Y. Huang, J.M. Vohs and R.J. Gorte. Characterization of YSZ-YST Composites for SOFC Anodes, Solid State Ionics, *175*, pp.171-176. 2004.

He, H., R.J. Gorte and J.M. Vohs. Highly Sulfur Tolerant Cu-ceria Anodes for SOFCs, Electrochem. Solid-State Lett., *8*, pp.A279-A280. 2005.

Hickman, D.A. and L.D. Schmidt. Production of Syngas by Direct Catalytic Oxidation of Methane, Science, *259*, pp.343-346. 1993.

Holmblad, P.M., J. Wambach and I. Chorkendorff. Molecular Beam Study of Dissociative Sticking of Methane on Ni(100), J. Chem. Phys., *102*, pp.8255-8263. 1995.

Holstein, W.L. The Roles of Ordinary and Soret Diffusion in the Metal-catalyzed Formation of Filamentous Carbon, J. Catal., *152*, pp.42-51. 1995.

Hong, L., X. Chen and F. Guo. Fabrication of Dense $La_{0.05}Sr_{0.95}CoO_{3-y}$ Thin Film on Porous MgO and CeO_2 Substrates, Thin Solid Films, *389*, pp.27-33. 2001.

Hong, L. and W. Chua. Fabrication of a Dense $La_{0.2}Sr_{0.8}CoO_{3-\gamma}$/CoO Composite Membrane by Utilizing the Electroless Cobalt Plating Technique, J. Membr. Sci., *198*, pp.95-108. 2002.

Hong, L., F. Guo and J. Lin. From Chelating Precursors to $La_{0.05}Sr_{0.95}CoO_{3-y}$ Oxide, Mater. Res. Bull., *34*, pp.1943-1958. 1999.

Hsu, J.-P., S.-W. Huang, Y.-C. Kuo and S. Tseng. Stability of a Dispersion of Particles Covered by A Charge-Regulated Membrane: Effect of the Sizes of Charged Species, J. Colloid Interface Sci., *262*, pp.73-80. 2003.

Huang, K., M. Feng and J.B. Goodenough. Bi_2O_3-Y_2O_3-CeO_2 Solid Solution Oxide-ion Electrolyte, Solid State Ionics, *89*, pp.17-24. 1996.

Huang, K. and J.B. Goodenough. Wet Chemical Synthesis of Sr- and Mg-doped $LaGaO_3$, A Perovskite-type Oxide-ion Conductor, J. Solid State Chem., *136,* pp.274-283. 1998.

Huang, K. and J.B. Goodenough. A Solid Oxide Fuel Cell Based on Sr- and Mg-doped LaGaO3 Electrolyte: the Role of a Rare-earth Oxide Buffer, J. Alloys Compd., *303-304*, pp.454-464. 2000.

Isenberg, A.O. Energy Conversion via Solid Oxide Electrolyte Electrochemical Cells at High Temperatures, Solid State Ionics, *3/4*, pp.431-437. 1981.

Ishihara, T., H. Furutani, M. Honda, T. Yamada, T. Shibayama, T. Akbay, N. Sakai, H. Yokokawa and Y. Takita. Improved Oxide Ion Conductivity in $La_{0.8}Sr_{0.2}Ga_{0.8}Mg_{0.2}O_3$ by Doping Co, Chem. Mater., *11*, pp.2081-2088. 1999.

Ishihara, T., H. Matsuda and Y. Takita. Doped $LaGaO_3$ Perovskite Type Oxide as a New Oxide Ionic Conductor, J. Am. Chem. Soc., *116*, pp.3801-3803. 1994.

Islam, M.S., M. Cherry and C.R.A. Catlow. Oxygen Diffusion in $LaMnO_3$ and $LaCoO_3$ Perovskite-type Oxides: a Molecular Dynamics Study, J. Solid State Chem., *124*, pp.230-237. 1996.

Irvine, J.T.S., A. J. Feighery, D. P. Fagg and S. García-Martín. Structural Studies on the Optimisation of Fast Oxide Ion Transport, Solid State Ionics, *136–137*, pp.879–885. 2000.

James, M., D. Cassidy, D.J. Goossens and R.L. Withers. The Phase Diagram and Tetragonal Superstructures of the Rare Earth Cobaltate Phases $Ln_{1-x}Sr_xCoO_{3-\delta}$ (Ln = La^{3+}, Pr^{3+}, Nd^{3+}, Sm^{3+}, Gd^{3+}, Y^{3+}, Ho^{3+}, Dy^{3+}, Er^{3+}, Tm^{3+} and Yb^{3+}), J. Solid State Chem., *177*, pp.1886-1895. 2004.

James, M., T. Tedesco, D.J. Cassidy and R.L. Withers. Oxygen Vacancy Ordering in Strontium Doped Rare Earth Cobaltate Perovskites $Ln_{1-x}Sr_xCoO_{3-\delta}$ (Ln = La, Pr and Nd; $x > 0.6$), Mater. Res. Bull., *40*, pp.990-1000. 2005.

Jasinski, P., V. Petrovsky, T. Suzuki, T. Petrovsky and H. U. Anderson. Electrical Properties of YSZ Films Prepared by Net Shape Technology, J. Electrochem. Soc., *152*, pp.A454-A458. 2005.

Ji, Y., J.A. Kilner and M.F. Carolan. Electrical Properties and Oxygen Diffusion in Yttria-stabilised Zirconia (YSZ)–$La_{0.8}Sr_{0.2}MnO_{3\pm\delta}$ (LSM) Composites, Solid State Ionics, *176*, pp.937-943. 2005.

Jin, W., I. R. Abothu, R. Wang and T.-S. Chung, Sol-Gel Synthesis and Characterization of $SrFeCo_{0.5}O_{3.25-\delta}$ Powder, Ind. Eng. Chem. Res., *41*, pp.5432-5435. 2002.

Jitaru, I., D. Berger, V. Fruth, A. Novac, N. Stanica and F. Rusu. Lanthanum Chromites Doped with Divalent Transition Metals, Ceram. Int., *26*, pp.193-196. 2000.

Johnson, S.A., P.J. Ollivier and T.E. Mallouk. Ordered Mesoporous Polymers of Tunable Pore Size from Colloidal Silica Templates, Science, *283*, pp.963-965. 1999.

Jørgensen, M.J., S. Primdahl and M. Mogensen. Characterisation of Composite SOFC Cathodes Using Electrochemical Impedance Spectroscopy, Electrochim. Acta, *44*, pp.4195-4201. 1999.

Juan-Juan, J., M.C. Román-Martínez and M.J. Illán-Gómez. Effect of Potassium Content in the Activity of K-promoted Ni/Al_2O_3 Catalysts for the Dry Reforming of Methane, Appl. Catal. A, *301*, pp.9-15. 2006.

Kaya, C., F. Kaya, B. Su, B. Thomas and A. R. Boccaccini. Structural and Functional Thick Ceramic Coatings by Electrophoretic Deposition, Surf. Coat. Technol., *191*, pp.303-310. 2005.

Kharton, V.V., A.A. Yaremchenko, E.V. Tsipis, A.A. Valente, M.V. Patrakeev, A.L. Shaula, J.R. Frade and J. Rocha. Characterization of Mixed-conducting $La_2Ni_{0.9}Co_{0.1}O_{4+\delta}$ Membranes for Dry Methane Oxidation, Appl. Catal. A, *261*, pp.25–35. 2004.

Kharton, V. V., A. V. Kovalevsky, A. P. Viskup, J. R. Jurado, F. M. Figueiredo,A E. N. Naumovich and J. R. Frade. Transport Properties and Thermal Expansion of $Sr_{0.97}Ti_{1-x}Fe_xO_{3-\delta}$ (x= 0.2-0.8), J. Solid State Chem., *156*, pp.437-444. 2001.

Kilner, J.A. and R.J. Brook. A Study of Oxygen Ion Conductivity in Doped Non-stoichiometric Oxides, Solid State Ionics, *6*, pp.237-252. 1982.

Kim, J. and Y.S. Lin. Synthesis and Oxygen-permeation Properties of Thin YSZ/Pd Composite Membranes, AIChE J., 46, pp.1521-1529. 2000.

Kim, H., C. da Rosa, M. Boaro, J.M. Vohs and R.J. Gorte. Fabrication of Highly Porous Yttria-stabilized Zirconia by Acid Leaching Nickel from a Nickel-yttria-stabilized Zirconia Cermet, J. Am. Ceram. Soc., *85*, pp.1473-1476. 2002.

Koke, J. and M. Modigell. Flow Behaviour of Sem-solid Metal Alloys, J. Non-Newtonian Fluid Mech., *112*, pp.141-160. 2003.

Kozhevnikov, V.L., I.A. Leonidov, E.B. Mitberg, M.V. Patrakeev, A.N. Petrov and K. R. Poeppelmeier. Conductivity and Carrier Traps in $La_{1-x}Sr_xCo_{1-z}Mn_zO_{3-\delta}$ (x = 0.3; z = 0 and 0.25), J. Solid State Chem., *172*, pp.296-304. 2003.

Kratzer, P., B. Hammer and J.K. NØrskov. A Theoretical Study of CH_4 Dissociation on Pure and Gold-alloyed Ni (111) Surfaces, J. Chem. Phys., *105*, pp.5595-5604. 1996.

Lai, W., D. Xie and D.H. Zhang, First-principles Sudy of Adsorption of Methyl, Coadsorption of Methyl and Hydrogen, and Methane Dissociation on Ni(100), Surf. Sci., *594*, pp.83-92. 2005.

Larsen, J.H. and I. Chorkendorff. From Fundamental Studies of Reactivity on Single Crystals to the Design of Catalysts, Surf. Sci. Rep., *35*, pp.163-222. 1999.

Lee, M.B., Q.Y. Yang and S.T. Ceyer. Dynamics of the Activated Dissociative Chemisorption of CH_4 and Implication for the Pressure Gap in Catalysis: A Molecular Beam-high Resolution Electron Energy Loss Study, J. Chem. Phys., *87*, pp.2724-2741. 1987.

Lee, B.W. Synthesis and Characterization of Compositionally Modified PZT by Wet Chemical Preparation from Aqueous Solution, J. Eur. Ceram. Soc., *24*, pp.925-929. 2004.

Lee, J.T. and M. Robert. Phase Transitions of Colloid-Polymer Systems in Two Dimensions, Phys. Rev. E, *60*, pp.7198-7202. 1999.

Lee, Y.-C., M.-H. Liang, C.-T. Hu and I.-N. Lin. Microwave Dielectric Properties of $Ba(Mg_{1/3}Ta_{2/3})O_3$ Materials Synthesized by Inverse-microemulsion Process, J. Eur. Ceram. Soc., *21*, pp.2755-2758. 2001.

Leng, YJ, SH Chan, KA Khor and SP Jiang. Performance Evaluation of Anode-supported Solid Oxide Fuel Cells with Thin Film YSZ Electrolyte, Int J Hydrogen Energy, *29*, pp.1025-1033. 2004.

Lenormand, P., D. Caravaca, C. Laberty-Robert and F. Ansart. Thick Films of YSZ Electrolytes by Dip-coating Process, J. Eur. Ceram. Soc., *25*, pp.2643-2646. 2005.

Levine, I.N. Quantum Chemistry. pp. 652-654, New Jersey: Prentice-Hall International Inc. 2000.

Lewis, J.A. Colloidal Processing of Ceramics, J. Am. Ceram. Soc., *83*, pp.2341-2359. 2000.

Liang, M.-H., S.-Y. Wu, C.-T. Hu and I.-N. Lin. Enhancing the Sinterability of $Ba(Mg_{1/3}Ta_{2/3})O_3$ Dielectrics by Using Chemically—derived Powders, Mater. Chem. Phys., *79*, pp.276-281. 2003.

Li, Y., B. Zhang, X. Xie, J. Liu, Y. Xu and W. Shen. Novel Ni Catalysts for Methane Decomposition to Hydrogen and Carbon Nanofibers, J. Catal., *238*, pp.412-424. 2006.

Lin, Y.S. Microporous and Dense Inorganic Membranes: Current Status and Prospective, Sep. Purif. Technol., *25*, pp.39-55. 2001.

Lin, Y.S., K.J. de Vries, H.W. Brinkman and A.J. Burggraaf. Oxygen Semipermeable Solid Oxide Membrane Composites Prepared by Electrochemical Vapor Deposition, J. Membr. Sci., *66*, pp.211-226. 1992.

Liu, D.-M. Densification of Zirconia from Submicron-sized to Nano-sized Powder Particles, J. Mater. Sci. Lett., *17*, pp.467-469. 1998.

Liu, Y. and L. Hong. Fabrication and Characterization of (Pd/Ag)-$La_{0.2}Sr_{0.8}CoO_{3-\delta}$ Composite Membrane on Porous Asymmetric Substrates, J. Membr. Sci., *224*, pp.137-150. 2003.

Lu, C., W.L. Worrell, C. Wang, S. Park, H. Kim, J.M. Vohs and R.J. Gorte. Development of Solid Oxide Fuel Cells for the Direct Oxidation of Hydrocarbon Fuels, Solid State Ionics, *152-153*, pp.393-397. 2002.

Lu, C., S. An, W.L. Worrell, J.M. Vohs and R.J. Gorte. Development of Intermediate-temperature Solid Oxide Fuel Cells for Direct Utilization of Hydrocarbon Fuels, Solid State Ionics, *175*, pp.47-50. 2004.

Lunsford, J.H. Catalytic Conversion of Methane to More Useful Chemicals and Fuels: A Challenge for the 21st Century, Catal. Today, *63*, pp.165-174. 2000.

Luntz, A.C. and J. Harris. The Role of Tunneling in Precursor Mediated Dissociation: Alkanes on Metal Surfaces, J. Chem. Phys., *96*, pp.7054-7063. 1992.

Luntz, A.C. and J. Harris. CH_4 Dissociation on Metals: a Quantum Dynamics Model, Surf. Sci., *258*, pp.397-426. 1991.

Luntz, A.C. CH_4 dissociation on Ni(100): Comparison of a Direct Dynamical Model to Molecular, J. Chem. Phys., *102*, pp.8264-8269. 1995.

Ma, B. and U. Balachandran. Oxygen Nonstoichiometry in Mixed-conducting $SrFeCoO_{0.5}O_x$, Solid State Ionics, *100*, pp.53-62. 1997.

Maiya, P.S., U. Balachandran, J.T. Dusek, R.L. Mieville, M.S. Kleefisch and C.A. Udovich. Oxygen Transport by Oxygen Potential Gradient in Dense Ceramic Oxide Membranes, Solid State Ionics, *99*, pp.1-7. 1997.

Mazanec, T.J., T.L. Cable and J.G. Frye Jr. Electrocatalytic Cells for Chemical Reaction, Solid State Iomcs, *53-56*, pp.111-118. 1992.

Mitberg, E.B., M.V. Patrakeev, I.A. Leonidov, V.L. Kozhevnikov and K.R. Poeppelmeier. High-temperature Electrical Conductivity and Thermopower in Nonstoichiometric $La_{1-x}Sr_xCoO_{3-\delta}$ (x = 0.6), Solid State Ionics, *130*, pp.325-330. 2000.

Mitchell, B.J., J.W. Richardson Jr., C.D. Murphy, B. Ma, U. Balachandran, J.P. Hodges and J.D. Jorgensen. Phase Stability of $SrFeCo_{0.5}O_y$ Under Synthesis and Annealing Conditions, J. Eur. Ceram. Soc., *22*, pp.661–671. 2002.

Mitterdorfer, A. and L. J. Gauckler. Identification of the Reaction Mechanism of the Pt, O_2(g)|yttria-stabilized Zirconia System: Part II: Model Implementation, Parameter Estimation, and Validation, Solid State Ionics, *117*, pp.203-217. 1999.

Mizusaki, J., I. Yasuda, J. Shimoyama, S. Yamauchi and K. Fueki. Electrical Conductivity, Defect Equilibrium and Oxygen Vacancy Diffusion Coefficient of $La_{1-x}Ca_xAlO_{3-\delta}$ Single Crystals, J. Electrochem. Soc., *140*, pp.467-471. 1993.

Mogensen, M., N. M. Sammes and G. A. Tompsett. Physical, Chemical and Electrochemical Properties of Pure and Doped Ceria, Solid State Ionics, *129*, pp.63-94. 2000.

Mogensen, M. and K. Kammer. Conversion of Hydrocarbons in Solid Oxide Fuel Cells, Annu. Rev. Mater. Res., *33*, pp.321-331. 2003.

Montinaro, D., V.M. Sglavo, M. Bertoldi, T. Zandonella, A. Aricò, M. Lo Faro and V. Antonucci. Tape Casting Fabrication and Co-sintering of Solid Oxide "Half Cells" with a Cathode–electrolyte Porous Interface, Solid State Ionics, *177*, pp.2093-2097. 2006.

Myers, D. Surfaces, Interfaces, and Colloids: Principles and Applications. pp.5, New York: VCH Publishers. 1991.

Nakahira, A., F. Nishimura, S. Kato, M. Iwata and S. Takeda. Green Fabrication of Porous Ceramics Using an Aqueous Electrophoretic Deposition Process, J. Am. Ceram. Soc., *86*, pp.1230-1232. 2003.

Nakamura, T., G. Petzow and L.J. Gauckler. Stability of the Perovskite Phase $LaBO_3$ (B = V, Cr, Mn, Fe, Co, Ni) in Reducing Atmosphere I. Experimental Results, Mat. Res. Bull., *14*, pp.649-659. 1979.

Okada, A. Ceramic-matrix Composites. In Handbook of Advanced Ceramics, vol. II: Processing and Their Applications, ed by S. Somiya, F. Aldinger, N. Claussen, R.M. Spriggs, K Uchino, K. Koumoto and M. Kaneno, pp. 417-444. Elsevier Academic Press. 2003.

Otsuka, K., M. Hatano and T. Komatsu. Synthesis of C_2H_4 by Partial Oxidation of CH_4 over LiCl/NiO, Catal. Today, *4*, pp.409-419. 1989.

Pan, X. L., N. Stroh, H. Brunner, G. X. Xiong and S. S. Sheng. Deposition of Sol–gel Derived Membranes on γ-Al_2O_3 Hollow Fibers by a Vacuum-assisted Dip-coating Process, J. Membr. Sci., *226*, pp.111-118. 2003.

Park, J.-H. and R.N. Blumenthal. Electronic Transport in 8 mole Percent Y_2O_3-ZrO_2, J. Electrochem. Soc., *136*, pp.2867-2876. 1989.

Park, S., R. Craciun, J.M. Vohs and R.J. Gorte. Direct Oxidation of Hydrocarbons in a Solid Oxide Fuel Cell I. Methane Oxidation, J. Electrochem. Soc., *146*, pp.3603-3605. 1999.

Park, S., J.M. Vohs and R.J. Gorte. Direct Oxidation of Hydrocarbons in a Solid-oxide Fuel Cell, Nature, *404*, pp.265-267. 2000.

Patrakeev, M. V.,E. B. Mitberg,A. A. Lakhtin,I. A. Leonidov, L.Kozhevnikov,V. V. Kharton,M. Avdeev and F. M. B. Marques. Oxygen Nonstoichiometry, Conductivity, and Seebeck Coefficient of $La_{0.3}Sr_{0.7}Fe_{1-x}Ga_xO_{2.65+\delta}$ Perovskites, J. Solid State Chem., *167*, pp.203–213. 2002.

Payne, M.C., M.P. Teter, D.C. Allan, T.A. Arias and J.D. Joannopoulos. Iterative Minimization Techniques for Ab Initio Total-energy Calculations: Molecular Dynamics and Conjugate Gradients, Rev. Mod. Phys., *64*, pp.1045-1096. 1992.

Pechini, M. P. Method of Preparing Lead and Alkaline Earth Titanates and Niobates and Coating Method Using the Same to Form a Capacitor, US Patent No. 3330697. 1967.

Periana, R.A., D.J. Taube, E.R. Evitt, D. G. Loffler, P.R. Wentrcek, G. Voss and T. Masuda. A Mercury-Catalyzed, High-Yield System for the Oxidation of Methane to Methanol, Science, *259*, pp.340-343. 1993.

Petrovsky, V., T. Suzuki, P. Jasinski, T. Petrovsky and H. U. Anderson. Electrochem. Low-Temperature Processing of Thin-Film Electrolyte for Electrochemical Devices, Electrochem. Solid-State Lett., *7*, pp.A138-A139. 2004.

Prettre, M., C. Eichner and M. Perrin. Catalytic Oxidation of Methane to Carbon Monoxide and Hydrogen, Trans. Faraday Soc., *43*, pp.335-340. 1946.

Puetz, J., F.N. Chalvet and M.A. Aegerter. Wet Chemical Deposition of Transparent Conducting Coatings in Glass Tubes, Thin Solid Films, *442*, pp.53-59. 2003.

Quemada, D. and C. Berli. Energy of Interaction in Colloids and Its Implications in Rheological Modeling, Adv. Colloid Interface Sci., *98*, pp.51-85. 2002.

Rangarajan, S., G. Qi, N. Venkataraman, A. Safari and S.C. Danforth. Powder Processing, Rheology, and Mechanical Properties of Feedstock for Fused Deposition of Si_3N_4 Ceramics, J. Am. Ceram. Soc., *83*, pp.1663-1669. 2000.

Rice, R.W. Ceramic Fabrication Technology. pp. 3, New York: Marcel Dekker Inc. 2003.

Ritchie, J.T., J.T. Richardson and D. Luss. Ceramic Membrane Reactor for Synthesis Gas Production, AIChE J., *47*, pp.2092-2101. 2001.

Rostrup-Nielsen, J.R. Production of Synthesis Gas, Catal. Today, *18*, pp.305-324. 1995.

Sahu, A. K., A. Ghosh, A. K. Suri, P. Sengupta and K. Bhanumurthy. Studies on Chemical Compatibility of Lanthanum Strontium Manganite with Yttria-stabilized Zirconia, Mater. Lett., *58*, pp.3332-3336. 2004.

Sammells, A.F., R.L. Cook, J.H. White, J.J. Osborne and R.C. MacDuff. Rational Selection of Advanced Solid Electrolytes for Intermediate Temperature Fuel Cells, Solid State Ionics, *52*, pp.111-123. 1992.

Schaak, R.E. and T.E. Mallouk. Perovskites by Design: A Toolbox of Solid-State Reactions, Chem. Mater., *14*, pp.1455-1471. 2002.

Sear, R.P. Phase Separation in Mixtures of Colloids and Long Ideal Polymer Coils, Phys. Rev. Lett., *86*, pp.4696-4699. 2001.

Setoguchi, T., M. Sawano, K. Eguchi and H. Arai. Application of the Stabilized Zirconia Thin Film Prepared by Spray Pyrolysis Method to SOFC, Solid State Ionics, *40/41*, pp.502-505. 1990.

Shao, Z., W. Yang, Y. Cong, H. Dong, J. Tong and G. Xiong. Investigation of the Permeation Behavior and Stability of a $BaBi_xCo_{0.2}Fe_{0.8-x}O_3$-δ Oxygen Membranes, J. Membr. Sci., *172*, pp.177-188. 2000.

Shao, Z., H. Dong, G. Xiong, Y. Cong and W. Yang. Performance of a Mixed-Conducting Ceramic Membrane Reactor with High Oxygen Permeability for Methane Conversion, J. Membr. Sci., *183*, pp.181–192. 2001.

Shojai, F. and T.A. Mäntylä. Structural Stability of Yttria Doped Zirconia Membranes in Acid and Basic Aqueous Solutions, J. Eur. Ceram. Soc., *21*, pp.37-44. 2001.

Sirman, J.D. and J.A. Kilner. Surface Exchange Properties of $Ce_{0.9}Gd_{0.1}O_{2-x}$ Coated with $La_{1-x}Sr_xFe_yCo_{1-y}O_{3-\delta}$, J. Electrochem. Soc., *143*, pp.L229-L231. 1996.

Sitte, W., E. Bucher and W. Preis. Nonstoichiometry and Transport Properties of Strontium-substituted Lanthanum Cobaltites, Solid State Ionics, *154/155*, pp.517-522. 2002.

Srinivasan, S., R. Mosdale, P. Stevens and C. Yang. Fuel Cells: Reaching the Era of Clean and Efficient Power Generation in the Twenty-first Century, Annu. Rev. Energy Environ., *24*, pp.281-328. 1999.

Steele, B.C.H. Material Science and Engineering: the Enabling Technology for the Commercialization of Fuel Cell Systems, J. Mater. Sci., *36*, pp.1053–1068. 2001.

Stoneham, A.M. Theory of Defects in Solids: Electronic Structure of Defects in Insulators and Semiconductors. pp.141-144, New York: Oxford University Press. 1985.

Swider, K.E. and W.L. Worrell. Electronic Conduction Mechanism in Yttria-stabilized Zirconia-titania under Reducing Atmospheres, J. Electrochem. Soc., *143*, pp.3706-3711. 1996.

Tan, L., X. Gu, L. Yang and W. Jin. Influence of Powder Synthesis Methods on Microstructure and Oxygen Permeation Performance of $Ba_{0.5}Sr_{0.5}Co_{0.8}Fe_{0.2}O_{3-\delta}$ Perovskite-type Membranes, J. Membr. Sci., *212*, pp.157-165. 2003.

Teraoka, Y., H.M. Zhang, K. Okamoto and N. Yamazoe. Mixed Ionic-electronic Conductivity of $La_{1-x}Sr_xCo_{1-y}Fe_yO_{3-\delta}$ Perovskite-type Oxides, Mat. Res. Bull., *23*, pp.51-58. 1988.

Thompson, M.A. and M.C. Zerner. A Theoretical Examination of the Electronic Structure and Spectroscopy of the Photosynthetic Reaction Center from Rhodopseudommas Viridis, J. Am. Chem. Soc., *113*, pp.8210-8216. 1991.

Thompson, M.A., E.D. Glendening and D. Feller. The Nature of K^+/crown Ether Interactions: a Hybrid Quantum Mechanical-molecular Mechanical Study, J. Phys. Chem., *98*, pp.10465-10476. 1994.

Thompson, M. A. and G. K. Schenter. Excited States of the Bacteriochlorophyll B Dimmer of Rhodopseudomonas Viridis: A QM/MM Study of the

Photosynthetic Reaction Center that Includes MM Polarization, J. Phys. Chem., *99*, pp.6374-6386. 1995.

Thompson, M. A. QM/MMpol: a Consistent Model for Solute/solvent Polarization. Application to the Aqueous Aalvation and Spectroscopy of Formaldehyde, Acetaldehyde, and Acetone, J. Phys. Chem., *100*, pp.14492-14507. 1996.

Tichy, R.S. and J.B. Goodenough. Oxygen Permeation in Cubic $SrMnO_{3-\delta}$, Solid State Sci., *4*, pp.661-664. 2002.

Tsai, C.-Y., A.G. Dixon, W.R. Moser and Y. H. Ma. Dense Perovskite Membrane Reactors for Partial Oxidation of Methane to Syngas, AIChE J., *43*, pp.2741-2750. 1997.

Uhland, S.A., R.K. Holman, S. Morissette, M.J. Cima and E.M. Sachs. Strength of Green Ceramics with Low Binder Content, J. Am. Ceram. Soc., *84*, pp.2809-2818. 2001.

Venkataraman, A., V.A. Hiremath, S.K. Date and S.D. Kulkarni. A New Combustion Route to γ-Fe2O3 Synthesis, Bull. Mater. Sci., *24*, pp.617-621. 2001.

Vente, J.F., S. McIntosh, W.G. Haije and H.J.M. Bouwmeester. Properties and Performance of $Ba_xSr_{1-x}Co_{0.8}Fe_{0.2}O_{3-\delta}$ Materials for Oxygen Transport Membranes, J. Solid State Electrochem., *10*, pp.581-588. 2006.

Wan, J., J.H. Zhu and J. B. Goodenough. $La_{0.75}Sr_{0.25}Cr_{0.5}Mn_{0.5}O_{3-\delta}$ + Cu Composite Anode Running on H_2 and CH_4 Fuels, Solid State Ionics, *177,* pp.1211-1217. 2006.

Wandekar, R.V., B.N. Wani and S.R. Bharadwaj. Effect of Ni Substitution on the Crystal Structure and Thermal Expansion Behaviour of $(La_{0.8}Sr_{0.2})_{0.95}MnO_3$, Mater. Lett., *59*, pp.2799-2803. 2005.

Wang, H., Y. Cong and W. Yang. Investigation on the Partial Oxidation of Methane to Syngas in a Tubular $Ba_{0.5}Sr_{0.5}Co_{0.8}Fe_{0.2}O_{3-\delta}$ Membrane Reactor, Catal. Today, *82*, pp.157–166. 2003.

Wennerström, H. The van de Waals Interaction Between Colloidal Particles and Its Molecular Interpretation, Colloids Surf. A, *228*, pp.189-195. 2003.

Will, J., A. Mitterdorfer, C. Kleinlogel, D. Perednis and L.J. Gauckler. Fabrication of Thin Electrolytes for Second-generation Solid Oxide Fuel Cells, Solid State Ionics, *131*, pp.79-96. 2000.

Winters, H. F. The Kinetic Isotope Effect in the Dissociative Chemisorption of Methane, J. Chem. Phys., *64*, pp.3495-3500. 1976.

Yamazoe, N. and Y. Teraoka. Oxidation Catalysis of Perovskites-relationships to Bulk Structure and Composition (Valency, Defect, etc.), Catal. Today, *8*, pp.175-199. 1990.

Yang,H. and J.L. Whitten. Reaction of Chemisorbed CH and H on Nickel, J. Chem. Phys., *91*, pp.126-136. 1989.

Yang, H. and J.L. Whitten. Ab Initio Chemisorption Studies of CH_3 on Ni (1 1 1), J. Am. Chem. Soc., *113*, pp.6442-6449. 1991.

Yang, H. and J.L. Whitten. Dissociative Chemisorption of CH_4 on Ni(111), J. Chem. Phys., *96*, pp.5529-5537. 1992.

Yaremchenko, A.A., M.V. Patrakeev, V.V. Kharton, F.M.B. Marques, I.A. Leonidov and V.L. Kozhevnikov. Oxygen Ionic and Electronic Conductivity of $La_{0.3}Sr_{0.7}Fe(Al)O_{3-\delta}$ Perovskites, Solid State Sci., *6*, pp.357–366. 2004.

Yokokawa, H. Understanding Materials Compatibility, Annu. Rev. Mater. Res., *33*, pp.581–610. 2003.

Zanetti, M., T. Kashiwagi, L. Falqui and G. Camino. Cone Calorimeter Combustion and Gasification Studies of Polymer Layered Silicate Nanocomposites, Chem. Mater., *14*, pp.881-887. 2002.

Zhang, J. and L. Gao. Synthesis and Characterization of Nanocrystalline Tin Oxide by Sol–gel Method, J. Solid State Chem., *177*, pp.1425-1430. 2004.

Zhang, T. S., J. Ma, S. H. Chan, P. Hing and J. A. Kilner. Intermediate-temperature Ionic Conductivity of Ceria-based Solid Solutions as a Function of Gadolinia and Silica Contents, Solid State Sci., *6*, pp.565-572. 2004.

Zhao S. and R.J. Gorte. The Effect of Oxide Dopants in Ceria on n-Butane Oxidation, Appl. Catal. A, *248*, pp.9-18. 2003.

Zhao, S. and R.J. Gorte. A Comparison of Ceria and Sm-doped Ceria for Hydrocarbon Oxidation Reactions, Appl. Catal. A, *277*, pp.129-136. 2004.

Zhou, Z., P.J. Scales and D.V. Boger. Chemical and Physical Control of the Rheology of Concentrated Metal Oxide Suspensions, Chem. Eng. Sci., *56*, pp.2901-2920. 2001.

Zhu, D.C., X.Y. Xu, S.J. Feng, W. Liu and C.S. Chen. La_2NiO_4 Tubular Membrane Reactor for Conversion of Methane to Syngas, Catal. Today, *82*, pp.151-156. 2003.

Zhu, J., J.G. van Ommen and L. Lefferts. Reaction Scheme of Partial Oxidation of Methane to Synthesis Gas over Yttrium-stabilized Zirconia, J. Catal., *225*, pp.388-397. 2004.

Zhu, J., J.G. van Ommen, H.J.M. Bouwmeester and L. Lefferts. Activation of O_2 and CH_4 on Yttrium-stabilized Zirconia for the Partial Oxidation of Methane to Synthesis Gas, J. Catal., *233*, pp.434-441. 2005.

Appendix A Kröger Vink notation

In the Kröger Vink notation (Chiang et al., 1997) a defect is described by three parts, in which the main body, subscript and superscript identify the defect type (i.e., a vacancy “V” or an ion “B”), the defect site (e.g., normal lattice site or interstitial site “i”) and the effective charge (i.e., dot (·) represents positive charge and dash (′) is the negative), respectively. Some examples within the thesis include:

1) $V_O^{\cdot\cdot}$: lattice oxygen vacancy with two positive effective charge;
2) O_O^x: lattice oxygen with zero charge;
3) $O_i^{''}$: interstitial oxygen with two negative charge;
4) e': electron with one negative charge;
5) $h^{\cdot}$: hole with one positive charge;
6) $B_B^{\cdot}$: lattice B (B = Fe, Co, or other transition metal ions) with one positive charge;
7) $B_B^{'}$: lattice B with one negative charge;
8) B_B^x: normal lattice B state;
9) $Y_{Zr}^{'}$: doped Y in ZrO_2 lattice Zr site with effective one negative charge.

Appendix B Extended Hückel theory

The extended Hückel theory (EHT) deals with the valence-electron Hamiltonian ($\boldsymbol{\hat{H}_{val}}$) as the sum of one-electron Hamiltonians ($\boldsymbol{\hat{H}_{eff}(i)}$) (Stoneham, 1985):

$$\boldsymbol{\hat{H}_{val}} = \sum_i \boldsymbol{\hat{H}_{eff}(i)} \tag{B.1}$$

The calculated energy term of EHT (E_{val}) is taken as the sum of one-electron energy term (e_i):

$$E_{val} = \sum_i e_i \tag{B.2}$$

$$\hat{H}_{eff}(i)\phi_i = e_i\phi_i \tag{B.3}$$

where the molecular orbital (MOs) (ϕ_i) are expressed as linear combinations of the valence AOs (atomic-orbitals), f_r:

$$\phi_i = \sum_r C_{ri} f_r \tag{B.4}$$

The values of e_i and C_{ri} are determined by Eqs. (B.5) and (B.6), derived from the variation method:

$$\det\left(H_{rs}^{eff} - e_i S_{rs}\right) = 0 \tag{B.5}$$

$$\sum_s \left[\left(H_{rs}^{eff} - e_i S_{rs}\right) C_{si}\right] = 0 \tag{B.6}$$

where coulomb integral (S_{rs}) and the bond integral (H_{rs}^{eff}) are defined as

$$S_{rs} \equiv \int f_r^*(i) f_s(i) d\tau_i \tag{B.7}$$

$$H_{rs}^{eff} = \int f_r^*(i) \hat{H}_{eff}(i) f_s(i) d\tau_i \tag{B.8}$$

The Wolfsberg, Helmholz and Hoffmann approximation gives the value of H_{rs}^{eff} in cases of $r \neq s$:

$$H_{rf}^{eff} \approx \frac{1}{2} K \left(H_{rr}^{eff} + H_{ss}^{eff} \right) S_{rs} \tag{B.9}$$

Appendix C Density functional theory

For a many-body system, the Kohn-Sham ground–state electronic energy, E_0, can be written as (Payne et al., 1992)

$$\boldsymbol{E}_0 = \int \rho(\boldsymbol{r})\boldsymbol{v}(\boldsymbol{r})\boldsymbol{dr} + \frac{1}{2}\iint \frac{\rho(\boldsymbol{r}_1)\rho(\boldsymbol{r}_2)}{\boldsymbol{r}_{12}}\boldsymbol{dr}_1\boldsymbol{dr}_2 + \overline{\boldsymbol{T}}_s[\rho] + \boldsymbol{E}_{xc}[\rho] \qquad \text{(C.1)}$$

where $\rho(\boldsymbol{r})$ is the electronic density and $\rho(\boldsymbol{r}) = \sum_{i=1}^{n} \left|\psi_i(\boldsymbol{r})\right|^2$, $\psi_i(\boldsymbol{r})$ is the wave function of electronic state *i*, $\boldsymbol{v}(\boldsymbol{r})$ is the potential energy of interaction between electron and nuclei ($\boldsymbol{v}(\boldsymbol{r}_i) = \sum_{\alpha} \frac{\boldsymbol{Z}_\alpha}{\boldsymbol{r}_{i\alpha}}$), $\overline{\boldsymbol{T}}_s[\rho]$ is the average ground-state electronic kinetic energy of the fictitious reference system which assumes none electron interactions and the same electronic density as that of the real system ($\overline{\boldsymbol{T}}_s[\rho] = -\frac{\hbar^2}{2\boldsymbol{m}} < \psi_s \left| \sum_i \nabla_i^2 \right| \psi_s >$), and $\boldsymbol{E}_{xc}[\rho]$ is the exchange-correlation energy functional.

Once the electronic density $\rho(\boldsymbol{r})$ is determined, the ground-state energy can be calculated from equation 2 because the system ground-state is solely dependent on its electronic density. $\rho(\boldsymbol{r})$ can be obtained through solving the self-consistent Kohn-Sham (KS) equations:

$$\left[-\frac{\hbar^2}{2\boldsymbol{m}}\nabla^2 - \sum_{\alpha}\frac{\boldsymbol{Z}_\alpha}{\boldsymbol{r}_\alpha} + \int \frac{\rho(\boldsymbol{r}')}{\left|\boldsymbol{r}-\boldsymbol{r}'\right|}\boldsymbol{dr}' + \boldsymbol{V}_{xc}(\boldsymbol{r})\right]\psi_i(\boldsymbol{r}) = \varepsilon_i\psi_i(\boldsymbol{r}) \qquad \text{(C.2)}$$

where the $\boldsymbol{V}_{xc}(\boldsymbol{r})$ is the exchange-correlation potential and $\boldsymbol{V}_{xc}(\boldsymbol{r}) = \frac{\delta \boldsymbol{E}_{xc}}{\delta \rho}$, ε_i is the Kohn-Sham eigenvalue.

Assuming that the exchange-correlation energy functional is purely local and $\rho(\boldsymbol{r})$ varies extremely slowly with position, the local-density approximation (LDA) gives

$$\boldsymbol{E}_{xc}[\rho] = \int \rho(\boldsymbol{r})\varepsilon_{xc}(\rho)\boldsymbol{dr} \tag{C.3}$$

$$\boldsymbol{V}_{xc}[\rho] = \varepsilon_{xc} + \rho \frac{\partial \varepsilon_{xc}}{\partial \rho} \tag{C.4}$$

in which ε_{xc} is the exchange-correlation energy per electron in a homogeneous electron gas with $\rho(\boldsymbol{r}) = \boldsymbol{k}$, where *k* is some constant value.

The wave functions $\psi_i(\boldsymbol{r})$ are usually expanded in terms of a set of orthonormal basis functions. In a periodic solid each electronic wave function can be written as a sum of plane waves:

$$\psi_i(\boldsymbol{r}) = \sum_{\boldsymbol{G}} \boldsymbol{c}_{i,\boldsymbol{K}+\boldsymbol{G}} \exp\left[\boldsymbol{i}(\boldsymbol{K}+\boldsymbol{G})\cdot \boldsymbol{r}\right] \tag{C.5}$$

where *K* is the *K* points in *K*-space, G is the reciprocal lattice vector and the summation of *K* and *G* is called the wave vector. In order to expand the tightly bound core wave functions (orbitals) and follow the rapid oscillations of the wave functions of the valence electrons in the core region, a very large number of plane waves are needed. Fortunately, most physical properties of solids are mainly dependent on the valence electrons. Pseudopotential or effective core potential (ECP) method replaces the original solid by pseudo valence electrons and pseudo-ion cores, which allows the electronic wave functions to be expanded using a much smaller number of basis states and thus makes the K-S equations much simpler to be solved.

Appendix D List of publications

Yin, X., C. Choong, L. Hong and Z.-L. Liu. Crafting $La_{0.2}Sr_{0.8}MnO_{3-\delta}$ Membrane with Dense Surface from Porous YSZ Tube, J. Solid State Electrochem., *10*, pp.643-650. 2006.

Yin, X., L. Hong and Z.-L. Liu. Oxygen Permeation Through the LSCO-80/CeO_2 Ssymmetric Tubular Membrane Reactor, J. Membr. Sci., *268*, pp.2-12. 2006.

Yin, X., L. Hong and Z.-L. Liu. Development of Oxygen Transport Membrane $La_{0.2}Sr_{0.8}CoO_{3-\delta}/Ce_{0.8}Gd_{0.2}O_{2-\delta}$ on the Tubular CeO_2 Support, Appl. Catal. A, *300*, pp.75-84. 2006

Yin, X., L. Hong and Z.-L. Liu. A Study on the Fundamental Ceramic-polymer Interactions in the High CeO_2-loading Polyethylene Glycol Blend, J. Eur. Ceram. Soc., 25, pp.3097-3107. 2005.

Yin, X., L. Hong and Z.-L. Liu. Asymmetric Tubular Oxygen-Permeable Ceramic Membrane Reactor for Partial Oxidation of Methane, J. Phys. Chem. C, 2007 (accepted)

Yin, X., L. Hong and Z.-L. Liu. Fabrication of Asymmetric Ceramic Electrochemical Reactor and Methane Conversion to Synthesis Gas, (prepared for submission to Chem. Mater.)